Study, modeling and design of fixed beam transmitarray antennas at 300 GHz

Orestis Koutsos

DOCTORAT BRETAGNE LOIRE / MATHSTIC

UNIVERSITÉ DE RENNES 1

THÈSE DE DOCTORAT DE

L'UNIVERSITÉ DE RENNES 1

ÉCOLE DOCTORALE N° 601
Mathématiques et Sciences et Technologies de l'Information et de la Communication
Spécialité : *Electronique*

Par
Orestis KOUTSOS

Étude, Modélisation et Conception d'Antennes à Réseaux Transmetteurs à Faisceau Fixe à 300 GHz

Thèse présentée et soutenue à Grenoble, France, le 28/06/2022
Unité de recherche : Institut d'Electronique et des Technologies du numéRique (IETR)

Rapporteurs avant soutenance :

Claire MIGLIACCIO	Professeure, Université de Nice, France
Oscar QUEVEDO-TERUEL	Professeur, Institut royal de technologie KTH, Suède

Composition du Jury :

Examinateurs :	Claire MIGLIACCIO	Professeure, Université de Nice, France
	Oscar QUEVEDO-TERUEL	Professeur, Institut royal de technologie KTH, Suède
	Sérgio MATOS	Professeur associé, ISCTE – Lisbon University Institute, Portugal
	Enrica MARTINI	Professeur associé, Université de Sienne, Italie
Encadrant de thèse :	Antonio CLEMENTE	Ingénieur de Recherche (HDR), CEA-Leti, France
Dir. de thèse :	Ronan SAULEAU	Professeur, Université de Rennes, France

Invité(s) :

Nelson FONSECA	Ingénieur de recherche, European Space Agency (ESA), Pays-Bas
Francesco FOGLIA MANZILLO	Ingénieur de recherche, CEA Leti, France

Table of Contents

Acknowledgements

I would like to express my deepest appreciation to my thesis director, Prof. Ronan Sauleau, Professor at the University of Rennes 1. It has been a great honor that you trusted me to carry out this work. Your knowledge, experience and constructive criticism were essential for the success of the thesis, which allowed me to grow more as a researcher and an engineer.

I am extremely grateful to my supervisor, Dr. Antonio Clemente, Research Engineer at CEA-Leti. Your insightful guidance, your endless enthusiasm and your constant motivation have been essential to achieving these results. It has been a pleasure working with you, both in a professional and a friendly manner.

This endeavor would not have been possible without Dr. Francesco Foglia Manzillo, Research Engineer at CEA-Leti. Your valuable comments and brilliant remarks have been extremely helpful. I also thank you for having accepted to participate to the defense of the thesis. I will never forget our collaboration and, most important, our friendship.

I would like to thank Prof. Oscar Quevedo-Teruel, Professor at the KTH Royal Institute of Technology in Stockholm (Sweden), and Prof. Claire Migliaccio, Professor at the University of Nice Sofia-Antipolis (France), for having accepted to evaluate the thesis manuscript and to be part of the jury. Their valuable comments have been very useful. I also acknowledge the remaining members of the jury for having accepted to examine this thesis, Prof. Enrica Martini, Prof. Sergio Matos, and Dr. Nelson Fonseca.

I would like to address my acknowledgment to Dr. Christophe Delaveaud, Head of the Laboratory Antenna, Propagation and Inductive Coupling (LAPCI), for his availability, providing me with all the necessary tools to work under great conditions.

Many thanks to Dr. Mattieu Caillet, Research Engineer at CEA-Leti, for assisting me with all the measurements throughout these years. His experience and technical support were essential for extracting correctly all the results for my thesis.

I would like to extend my thanks to all the other members of the LAPCI for their sympathy and their interest in my research activity.

I would like to give special thanks to my parents, Panagiotis and Maria, and to my brother, Odysseas, for their constant support and encouragement. I would not be here

without them.

I would like to finish these acknowledgments by thanking my wife, Alexandra, for her love and her endless support to follow my dreams. Words can not express how grateful I am to you.

Orestis

List of Figures

List of Tables

RÉSUMÉ EN FRANÇAIS

En raison de la rareté des ressources spectrales et de la nécessité d'une large bande passante pour les communications à haut débit de nouvelle génération, la région inexploitée autour de 300 GHz est très attractive. À ces fréquences, le principal défi pour de telles applications consiste à atténuer les pertes de propagation accrues en réalisant des antennes à gain élevé, efficaces et à large bande. Cependant, les contraintes de fabrication limitent souvent les performances de l'antenne, résultant ainsi en technologies coûteuses avec une résolution plus élevée. Jusqu'à présent, les antennes les plus performantes s'appuyaient sur des technologies telles que la céramique cuite à basse température (LTCC) et le micro-usinage silicium sur isolant (SOI).

Parmi les solutions existantes, les antennes à réseaux transmetteurs sont des candidats pertinents. Ils combinent les avantages des architectures alimentées spatialement avec des processus de fabrication planaires. En principe, le réseau transmetteur transforme l'onde sphérique entrante d'une (ou plusieurs) source focale en une onde plane, rayonnant à un angle donné, habituellement dans le champ lointain. Chaque élément périodique, appelé cellule élémentaire, fournit un déphasage spécifique pour compenser le retard de phase spatiale et orienter le faisceau. La valeur du déphasage est réglée en modifiant la géométrie des couches métalliques constitutives de chaque cellule élémentaire. Dans cette procédure, il est également important de contrôler l'amplitude de la transmission, afin de minimiser la perte de gain due aux réflexions et d'améliorer la bande passante de gain.

Ainsi, la clé de la haute performance, compte tenu d'un processus de fabrication à faible coût à 300 GHz, est l'approche de conception de la cellule élémentaire. Parmi plusieurs architectures proposées, les réseaux transmetteurs anisotropes peuvent offrir des performances améliorées et des fonctionnalités supplémentaires. Plus précisément, la cellule élémentaire représentée sur la Figure 1 atteint un rendement élevé sur une bande passante relativement large en utilisant seulement trois couches métalliques : deux grilles polarisées orthogonalement et un rotateur de polarisation à l'intérieur. Cette conception, appelée polariseur linéaire asymétrique (ALP), a été initialement proposée comme un convertisseur de polarisation à 90° à des fréquences optiques. En optimisant uniquement la couche intermédiaire, des surfaces de déphasage pour la manipulation de front d'onde et

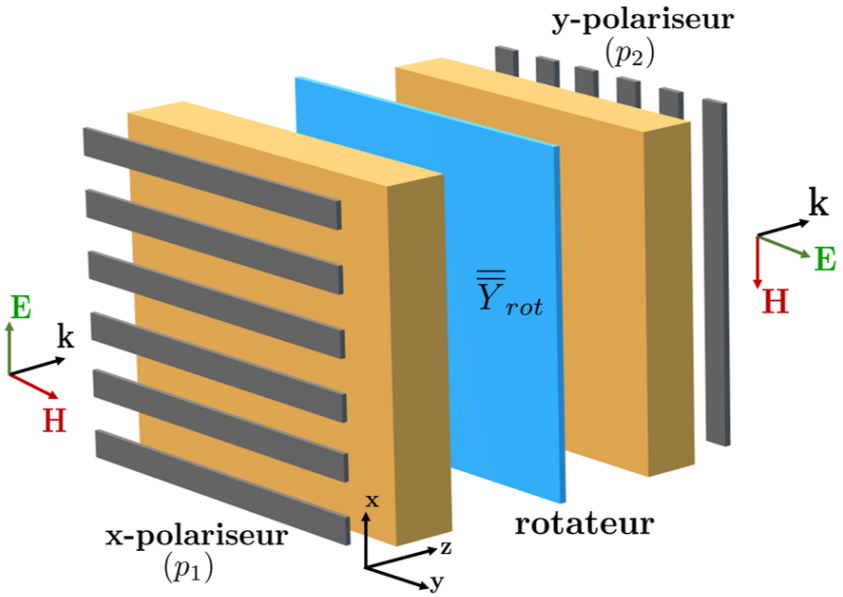

(a)

Figure 1: Vue éclatée de la cellule élémentaire ALP. Le rotateur (couleur bleue) est modélisé de manière générique comme une admittance de feuille anisotrope bidimensionnelle, décrite par une matrice d'admittance 2×2, $\overline{\overline{Y}}_{rot}$. Les polariseurs (couleur grise) sont orientés orthogonalement. Les couches sont entrelacées par deux substrats diélectriques (couleur orange).

des antennes à réseaux transmetteurs à haute résolution de phase peuvent être réalisées.

Bien que quelques conceptions d'antennes à réseaux transmetteurs ALP, fabriquées avec un processus circuit imprimé (PCB) standard, aient été démontrées à des fréquences sub-THz, leurs performances restent quelque peu médiocres, en absence d'une approche théorique rigoureuse pour l'analyse et la synthèse de ces éléments. Par conséquent, seuls des processus paramétriques aveugles ont été employés, sans fournir aucun aperçu sur la conception optimale de cette cellule élémentaire. Compte tenu également des contraintes de fabrication strictes de la technologie PCB à 300 GHz, la tâche devient plutôt difficile.

Dans ce travail de thèse, un modèle théorique basé sur des feuilles d'admittance en cascade pour l'étude et la conception des cellules élémentaires ALP est présenté. Le modèle proposé et la méthodologie de conception sont augmentés par l'utilisation d'un circuit équivalent à quatre ports, en tenant compte de l'anisotropie de la structure. De plus, en appliquant une simple transformation de coordonnées au niveau du rotateur, une expression pratique pour la matrice d'admittance du rotateur est constatée, en négligeant le facteur de couplage. Une expression sous forme fermée du coefficient de transmission en fonction de deux valeurs d'admittance, à savoir Y_u et Y_v, peut être trouvée. Ces valeurs

illustrent le rotateur dans son système cristallin. L'expression de forme fermée peut démontrer de manière précise que la cellule ALP peut atteindre à la fois une transmission presque parfaite et une couverture de phase complète, par opposition aux conceptions de cellules élémentaires symétriques. Pour un scénario théorique simple, la relation entre les deux valeurs d'admittance, Y_u et Y_v, pour une transmission parfaite est exprimée par

$$Y_u Y_v = (\varepsilon_r/\eta_0)^2 \,, \tag{1}$$

où ε_r est la permittivité des substrats et η_0 est l'impédance d'onde en espace libre.

Une fois les propriétés des polariseurs et des substrats fixées, une procédure de synthèse se focalisant uniquement sur la couche rotatrice est possible. Une conception de réseau transmetteur 3-bit adaptée à la fabrication de PCB a été réalisée. La taille périodique de la cellule a été fixée à une demi-longueur d'onde à 300 GHz. Deux substrats de type Astra MT77 ont été utilisés. Pour surmonter les contraintes strictes et atteindre les paires d'admittance ciblées, quatre conceptions de rotateurs différentes ont été utilisées, comme le montre la Figure 2(a). Les quatre cellules élémentaires restantes sont facilement obtenues en reflétant les rotateurs par rapport à l'axe des x. Les topologies finales des cellules ont été optimisées en utilisant le simulateur commercial Ansys HFSS. La bande passante de transmission commune de -1 dB pour ces éléments est de près de 85 GHz, ou 30% à la fréquence centrale. Sur cette bande, les déphasages relatifs entre les états de phase adjacents sont très proches de 45°, avec des variations absolues maximales de 10°.

En outre, une conception de réseau 4-bit adaptée au processus de lithographie au quartz a été synthétisée, comme démontrée par la Figure 2(b). La précision de fabrication améliorée permet d'utiliser un type de rotateur, dont les propriétés sont réglées par les angles ϕ_g et ϕ_{off}. La bande passante de transmission commune -1 dB couvre au moins 110 GHz, ou 40% à la fréquence centrale. Les déphasages relatifs entre les états de phase adjacents sont très proches de $22,5°$. La résolution de phase plus élevée et la taille périodique réduite, cette fois-ci un quart-longueur d'onde, peuvent améliorer le gain de l'antenne et permettre une forme de faisceau plus précise. Les couples d'admittance des rotateurs réalisés sont très proches des valeurs visées, démontrant une erreur dans la phase de transmission inférieure à 5°, par rapport à la conception théorique. Ces résultats prouvent l'efficacité de la procédure de conception et de synthèse de la cellule unitaire proposée pour réaliser des réseaux transmetteurs rentables même à 300 GHz.

Afin de faciliter l'étude et la conception d'antennes à réseaux transmetteurs de grande

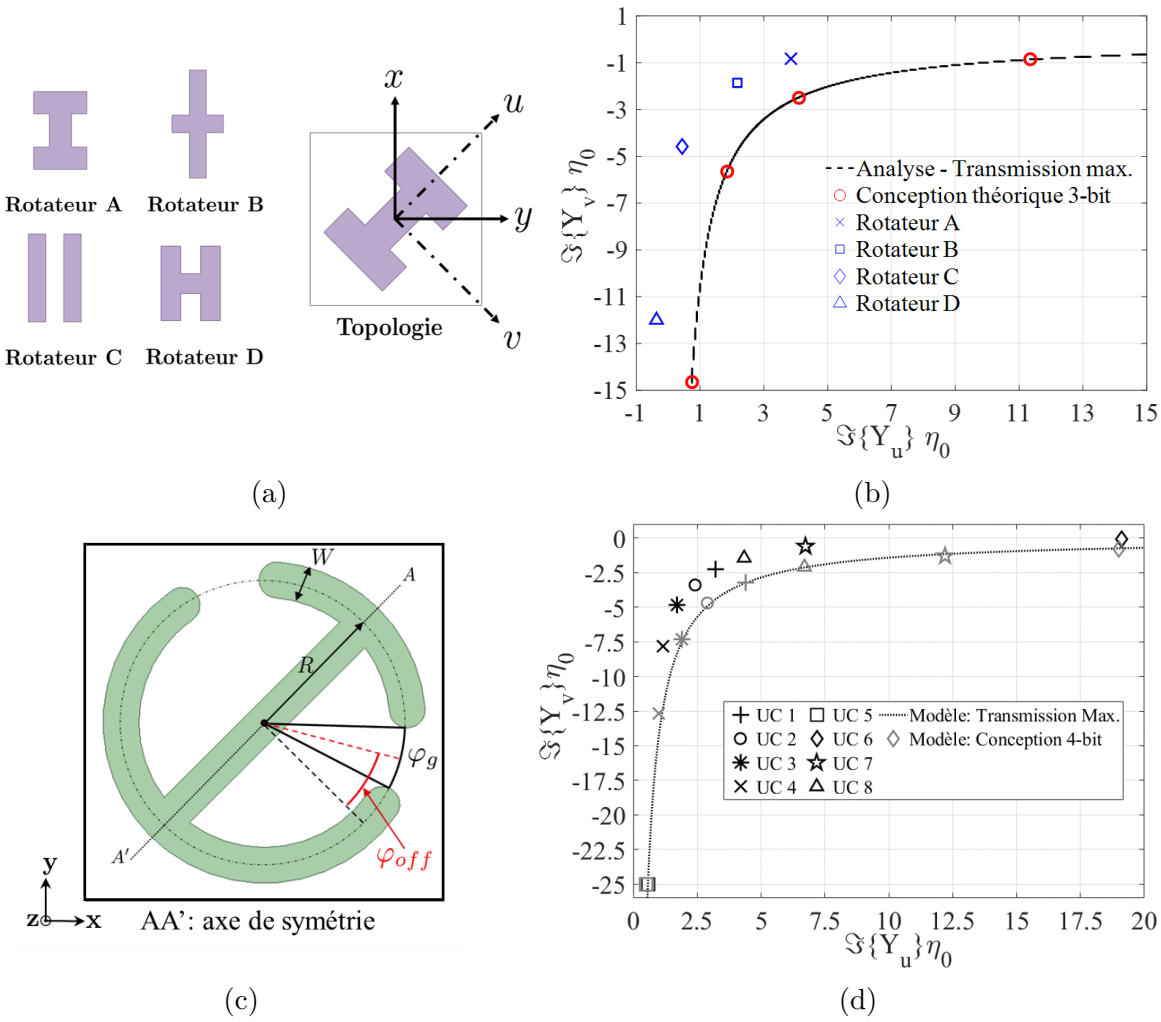

Figure 2: Conceptions de rotateur pour les réseaux transmetteurs PCB 3-bit (a) et quartz 4-bit (c) proposés, avec une taille périodique d'une demi-longueur d'onde et d'un quart-longueur d'onde, respectivement, à 300 GHz. Les résultats de la procédure de synthèse pour les conceptions sont présentés en (b) et (d), respectivement. La courbe en pointillés à chaque graphique est l'expression (1), calculée pour chaque cas.

ouverture, deux méthodes semi-analytiques ont été employées. La première méthode combine une technique de lancer de rayons avec la théorie classique des réseaux d'antennes, y compris les caractéristiques de rayonnement en champ lointain des éléments constitutifs (source focale et cellules élémentaires). La deuxième méthode est basée sur l'application du théorème d'équivalence de surface, où les courants équivalents sur le réseau transmetteur sont construits sous une approximation d'optique physique. Les deux méthodes incluent des techniques de simulation hybrides, permettant une description relativement précise du rayonnement en champ lointain et une réduction significative des coûts de calcul. Le

choix optimal de chaque approche dépend de la description du problème. La première méthode est généralement plus rapide et fournit des résultats précis une fois que la source focale est placée suffisamment loin du réseau transmetteur. La deuxième méthode permet d'utiliser une source plus compliquée, placée à proximité, assurant une performance de l'effet de débordement plus précise. Cependant, cela prend plus de temps et la précision dépend du pas de discrétisation.

Quatre prototypes de PCB, comprenant les rotateurs de la Figure 2(a), ont été fabriqués pour des applications d'antenne à 300 GHz. Ils ont été étudiés et optimisés en utilisant l'approche par lancer de rayons. Parmi eux, deux ont été synthétisés pour atteindre des performances de bande passante et du gain ciblées basées sur les exigences du système définies dans le projet "NEXT5G".

Plus précisément, le prototype illustré dans la Figure 3(a) est basé sur 3600 cellules élémentaires (taille 30 × 30 λ^2 à 300 GHz) et il a été réalisé pour obtenir des performances à large bande. Le réseau transmetteur est illuminé par une source focale de type cornet avec un gain nominal de 20 dBi. Cette dernière est placée à 55 mm de l'ouverture du réseau (F/D = 1,83). L'antenne démontre un gain mesuré de 37,0 dBi à 290,9 GHz, correspondant à une efficacité d'ouverture de 47,2%. L'efficacité d'ouverture maximale est 48,6% à 279,4 GHz, proche de la fréquence centrale (280 GHz), et elle est supérieure à 40,0% entre 250 et 300 GHz. La bande passante de gain de -1 dB est d'environ 56 GHz (19,0%), de 264 à 320 GHz, et la bande passante de gain de -3 dB est supérieure à 80 GHz (> 29,0%).

Le prototype de la Figure 3(c) est basé sur 19600 cellules élémentaires (taille 70 × 70 λ^2 à 300 GHz) et il a été réalisé pour obtenir un gain ultra-élevé pour les communications de liaison longue portée. Le réseau transmetteur est illuminé par une source focale de type cornet avec un gain nominal de 10 dBi, placée à 42 mm de l'ouverture du réseau (F/D = 0,6). Le gain maximal mesuré est 43,4 dBi à 286,9 GHz, correspondant à une efficacité d'ouverture de 39,0%. La bande passante de gain est relativement faible, couvrant environ 17 GHz (6,0%) à -3 dB de gain. Cependant, c'est plus que suffisant pour permettre des débits de données proches de 100 Gbps, grâce au fonctionnement à haute fréquence. La largeur de faisceau à mi-puissance est d'environ 1 degrés dans la largeur de la bande de gain de -3 dB et le niveau des lobes secondaires est inférieur à -22 dB et -17 dB dans les plans H et E, respectivement. La discrimination de polarisation croisée est supérieure à -40 dB dans toute la bande.

La perte de gain de tous les prototypes par rapport à un réseau transmetteur idéal est

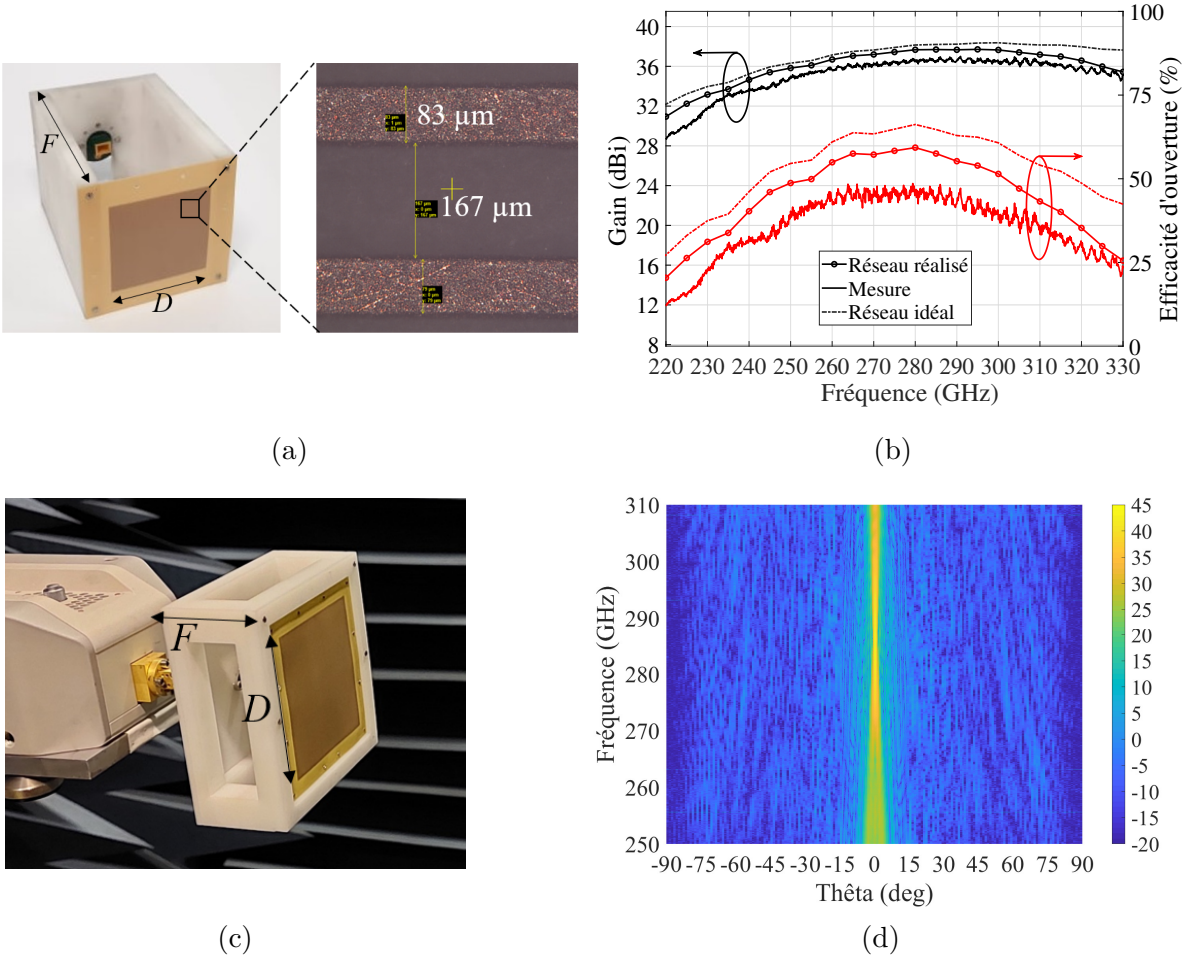

Figure 3: (a) Photographie du prototype basé sur 3600 cellules élémentaires. (b) Gain de crête et efficacité d'ouverture en fonction de la fréquence de ce prototype. (c) Photographie du prototype basé sur 19600 cellules élémentaires, monté sur un convertisseur de fréquence. (d) Diagramme de rayonnement du deuxième prototype en fonction de la fréquence et de l'angle d'élévation dans le plan H.

inférieure à 2 dB, comme illustré à la Figure 3(b) pour le prototype correspondant. Pour un réseau idéal, il est considéré comme une lentille antireflet avec une compensation de phase parfaite, avec la même taille et l'illumination par rapport à chaque cas. Ce résultat démontre la conception efficace de réseaux transmetteurs à faible coût basés sur le modèle de cellule ALP proposé.

Afin d'évaluer la différence de performance du gain entre les résultats simulés et mesurés, une configuration simple a été utilisée pour la caractérisation de la transmissivité des cellules élémentaires. Les résultats expérimentaux ont démontré presque la même différence de phase relative entre les cellules par rapport aux résultats de simulation.

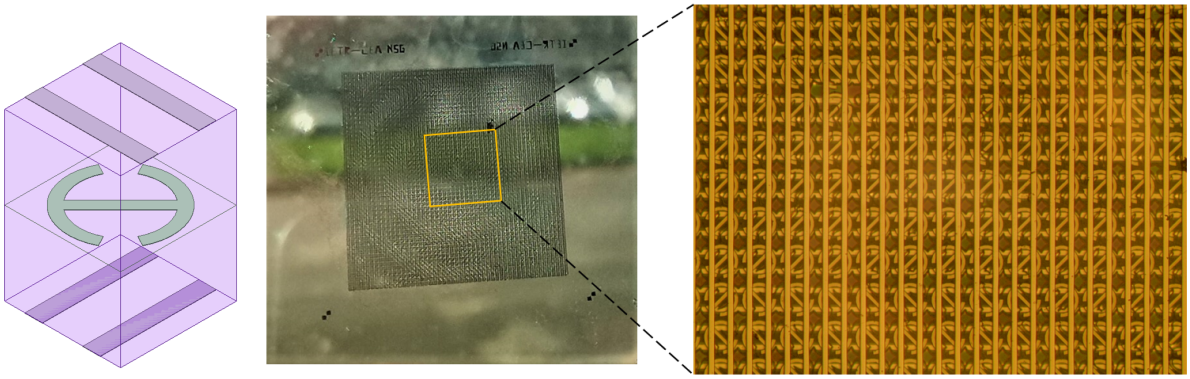

(a) (b)

Figure 4: (a) Vue 3D schématique de la cellule de quartz. (b) Photographie du prototype basé sur 2500 cellules élémentaires.

Enfin, deux réseaux de quartz de même taille ont été fabriqués à l'IETR et seront caractérisés dans un avenir proche. Les deux réseaux ont été synthétisés avec les mêmes propriétés d'illumination (source focale et distance focale), mais en utilisant une méthode semi-analytique différente. L'objectif est de comparer les performances du rayonnement entre les deux méthodes et de valider la conception du quartz. Néanmoins, la fabrication réussie a déjà démontré le premier réseau transmetteur à quartz à 300 GHz (cf. Figure 4(b)).

General Introduction

The following dissertation describes the research work carried out over a period of three years (April 2019 − March 2022) and took place at CEA-LETI (Laboratory of Electronics and Information Technology), within the Laboratory of Antenna, Propagation and Inductive Coupling (LAPCI) in collaboration with IETR (Institut d'Electronique et des Technologies du numéRique), Rennes, France. The work was supported by the National Research Agency (ANR) through the project "NEXT5G", under grant ANR 18-CEA25-0009-01. "NEXT5G" is a fundamental research project that aims to develop next-generation system concept for future data-rate needs up to 1 Tbps and disruptive antenna technologies at sub-THz bands.

Due to the scarcity of electromagnetic spectrum resources and the need for high data-rate communications to meet future demands, the unexploited sub-THz region of the millimeter-wave (mmWave) band is very attractive for "beyond 5G" applications. The major challenge for the antenna designers is to mitigate the high path loss by realizing high-gain, efficient and wideband antennas. However, at these frequencies, the design features are so small that the fabrication constraints often limit the maximum achievable performance, encouraging for more expensive, high-resolution technologies.

Several antenna architectures have been studied and presented as solutions for such scenarios. Among the antenna architectures that are suitable for such scenarios, transmitarray (TA) antennas are one of the best candidates. In particular, they do not require lossy feed networks, thanks to the spatial feeding mechanism, and they do not suffer from feed blockage, making them suitable for near-field excitation. Moreover, the TA is compatible with planar fabrication processes, such as standard printed circuit board. These characteristics allow the design of a low-cost, low-profile antenna with high aperture efficiency and beamforming capabilities in the sub-THz region.

The efficient design of sub-THz TAs using low-cost processes remains very challenging, typically requiring vias and numerous stacked metal layers. Despite a few novel reported architectures, proposed as a solution to enhance the performance, there is still a lack of rigorous procedures for the optimal design. In most cases, a large number of parameters (e.g. geometrical features and material properties) has to be simultaneously optimized,

with the only objective of achieving small reflection losses. This blind parametric process does not provide any insight on the optimal design and it becomes less efficient as the phase resolution of the TA increases. Therefore, the procedure can be time-consuming and does not guarantee to reach the maximum achievable performance. This thesis addresses these issues and it is organized as follows.

Chapter 1 presents an overview of high-gain sub-THz technologies, suitable for high-speed wireless communications. A more detailed state-of-the-art on TA antennas is reported. Their key characteristics over alternative antennas are highlighted by providing a general comparison of the radiation performance and the fabrication process.

Chapter 2 presents two methods for the theoretical modelling and the design of TA antennas. The first method combines a ray tracing technique with classical array theory, while the second approach is based on the application of the surface equivalence theorem, where the equivalent currents on the TA are constructed under a physical optics approximation. Both methods include hybrid simulation techniques, allowing for a relatively accurate description of the far-field radiation and a significant reduction of the computational cost.

In Chapter 3, a cascaded sheet admittance approach for the design of three-layer anisotropic TAs, named as asymmetric linear polarizers, is presented. A circuit model is derived to describe the anisotropic behavior of the periodic element, called unit-cell. A closed-form expression for the transmission coefficient is found, proving that the selected unit-cell can achieve both nearly perfect transmission and full phase coverage. Two unit-cell designs are realized, one suitable for a standard printed circuit board (PCB) manufacturing and another for a quartz lithography process, both presented in the end of this Chapter.

Based on the ray tracing approach of Chapter 2 and the unit-cell model of Chapter 3, four TA prototypes are designed and fabricated PCB, as reported in Chapter 4. In addition, large arrays of identical unit-cells that compose the antenna prototypes, are fabricated for a quasi-optical characterization of their transmissivity.

Two TA prototypes fabricated by lithography process on a quartz substrate are presented in Chapter 5. The prototypes leverage the high fabrication accuracy to achieve higher phase resolution compared to the PCB designs. Each prototype is designed using a different antenna model of Chapter 2, in order to compare the far-field radiation performance between the two methods.

General conclusions and perspectives are finally drawn.

Chapter 1

State-of-the-art on high-gain sub-THz antenna technologies

1.1 Introduction

This chapter presents a general overview on advanced antenna technologies for high-gain applications in the sub-THz region of the millimeter-wave (mmWave) band. The main application interest is to enable high data-rates for next-generation wireless communications at 300 GHz, which is the objective of the NEXT5G project. A general state-of-the-art on classical and advanced antennas for high-gain applications is presented in section two. A more detailed state-of-the-art on the transmitarray antenna, which is the main topic of the thesis, is reported in section three. Finally, conclusions about future transmitarray technologies and their fabrication process are drawn.

1.2 Application overview

1.2.1 High-speed wireless communications

The development of wireless networks with ultra-high data-rate capabilities has been a hot topic in recent years. This system concept can solve the ongoing problem of the increasing mobile data traffic. The continuous urban sprawl as well as various emerging applications in the frame of 5G wireless communication have been accelerating this trend. The 5G subscription uptake is expected to be even faster than 4G. For instance, according to the Ericsson Mobility Report of November 2021 [1], about 4.4 billion 5G subscriptions will be reached by 2027, accounting for 49% of all mobile subscriptions. In the future, several use cases are anticipated to be active concurrently in the same operator network. This will require a degree of flexibility and scalability even higher than the 5G network.

The wireless connectivity for all communication links changes every year in a manner

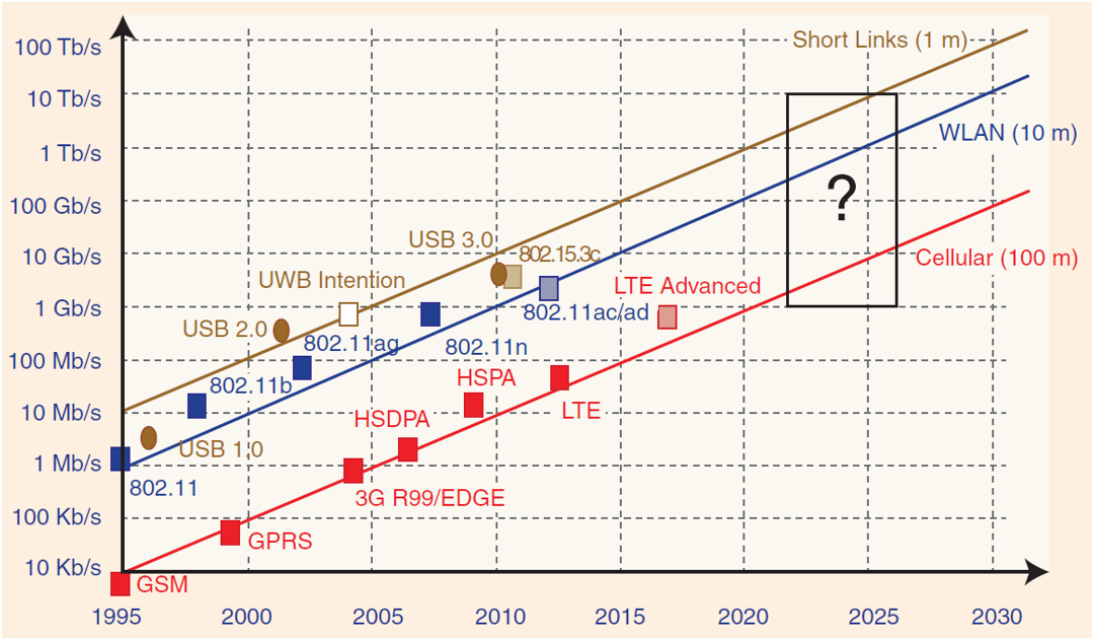

Figure 1.1: Wireless roadmap of standards and their achievable data rates at time of their market introduction (from [2]).

reminiscent of Moore's Law. As shown in Figure 1.1, it can be predicted that in 2025 the cellular links, from the cell to the mobile device (i.e. user equipment), will require up to 10 Gbps data-rate. The indoor WLAN links will require up to 1 Tbps data-rate, respectively.

The maximum achievable data-rate depends on the type of modulation, the signal-to-noise ratio (SNR) and the frequency bandwidth. Therefore, to further increase this parameter, the most effective and straightforward approach is enabling wide bandwidth. However, the additional availability of spectrum for cellular usage in the lower frequencies has already become scarce. For this reason, the unexploited spectrum in the higher end of the mmWave frequencies, around 300 GHz, could provide potentially the answer to these bandwidth requirements.

NEXT5G: Beyond 5G system concept at 300 GHz

"NEXT5G" is a fundamental research project that aims to develop "Beyond 5" system concept for future data-rate needs up to 1 Tbps and disruptive antenna technologies at 300 GHz. These objectives fit with the 2018 Call of the National Research Agency (ANR): Challenge 7 "information and communication Society", axis no. 6 "High performance communication infrastructures" and axis no. 7 "Micro and nanotechnologies for data and

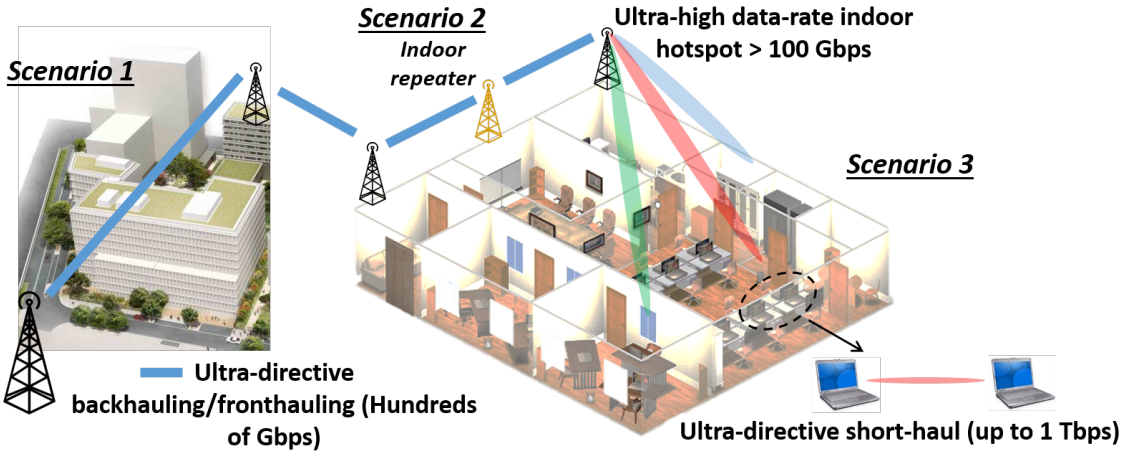

Figure 1.2: NEXT5G system architecture vision with three use case scenarios.

communication processing".

Axis 7-6

[...] The prospect of a proliferation of the connected objects, if it increases the potential for innovative applications, imposes new paradigms of communication, data processing and data storage (potentially massive). [...] The infrastructures must be able to achieve high levels of performance and efficiency while being open and agile to adapt both to scaling issues and to diverse and dynamic application requirements. [...]

The project is based on a strong applicative background addressing three identified scenarios, as shown in Figure 1.2. The first scenario considers a sub-THz point-to-point connection with a single beam and is most relevant for stationary outdoor connections with large range (up to 300 meters) and high capacity requirements, up to several hundreds of Gbps. In this case, the sub-THz beam needs limited steering capability to compensate the misalignment between two antennas in direct link. The second scenario considers a link composed of a transmitting and a receiving backhauling[1], with an intermediate passive repeater. This kind of device can be an extremely low cost solution to allow the

1. The **backhaul** portion of the network comprises the intermediate links between the core network and the small subnetworks.

transmission of the sub-THz electromagnetic wave from a room to another room, or from the outdoor to the indoor without using any power amplifier. Finally, the third scenario is dedicated to the indoor connectivity at sub-THz frequency and is composed of two sub-scenarios. One is an indoor short-range hotspot and the other is an indoor short-haul. In the case of the indoor short-range hotspot, two objects or devices are interconnected by an extremely high-speed wireless link with a data rate up to 1 Tbps. The link distance is less than 5 meters and can be implemented by considering an ultra-low profile fixed-beam antenna on both devices having a gain around 25 to 30 dBi. In the indoor short-haul scenario, the system is very similar to an access point with extremely high data rate (in the order of 100 Gbps).The selected antenna should have a gain around 20 to 25 dBi. Beam-steering capability in a field of view of $\pm 45^{\circ}$ can be required (not completed).

Some initial link budget approximations were In order to assess potential link distances, system bandwidths, bit rates and a support for mobility with respect to physical characteristics, like free space loss and molecular absorption, of the propagation medium.

1.2.2 Other applications

In addition to the bandwidth performance, another advantage of sub-THz is the very small wavelength. This can provide high spatial resolution and good penetration depth for different materials, enabling applications such as imaging, remote sensing, material characterization and biological detection.

Imaging

Imaging systems have shown promise for detecting concealed person-borne threats because of their centimeter-scale spatial resolution in three dimensions at standoff ranges of many meters [3]. Shortening the image acquisition time is one of the main challenges. This can be done by employing THz Radar systems using different techniques [4]–[6], focusing mainly on further reducing the acquisition time.

Remote sensing

Remote sensing can be divided into two types of methods: passive remote sensing and active remote sensing. Some examples of such applications are personal health monitoring systems and explosive detection. These are related to the detection and the monitoring of the physical characteristics of an area by measuring the scattering radiation, typically

from a satellite or an aircraft. Moreover, due to the spectral signature of the interstellar dust cloud, astronomers are very interested for THz sensor technology, related to gas sensing. All these applications require systems and techniques that must achieve high spatial resolution [7]–[9].

Material characterization

The study and characterization of materials can be achieved through THz spectroscopy. This process can give access to the complex refractive index of a wide variety of materials, such as dielectrics, semiconductors, liquids and superconductors. The techniques are similar to imaging applications.

1.3 High-gain sub-THz antenna technologies

At sub-THz frequencies, the antenna designer typically strives to achieve very high performance while on the verge of the chosen fabrication process. Many of the same design techniques used at lower frequencies are still applied, but fabrication constraints impose significant limitations on the type of structure that can be used. This forces the designer to consider unique fabrication processes or completely new antenna structures [10]. This becomes more significant in case of developing high-gain ($>$ 30 dBi) systems with beamforming capabilities. For instance, horn antennas dominate sub-THz and THz systems [11]–[13], but they lack of beam steering and beam shaping functionalities, which are necessary for system concepts like the one reported previously.

Several antenna technologies at frequencies beyond 100 GHz are reported below. The selected state-of-the-art architectures are known for achieving high gain and high radiation efficiency, making them suitable for high-speed communications. A brief description of the fabrication process and the employed materials for each prototype is given, to assess the cost for each design approach.

1.3.1 Dielectric lens antennas

Dielectric lenses are considered a milestone technology for focusing and collimating systems, creating the base for the majority of the antenna solutions existing at the mmWave band. Despite their somewhat limited beamsteering capability, they remain very attractive candidates, as they can achieve high-gain with very high aperture efficiency. Moreover,

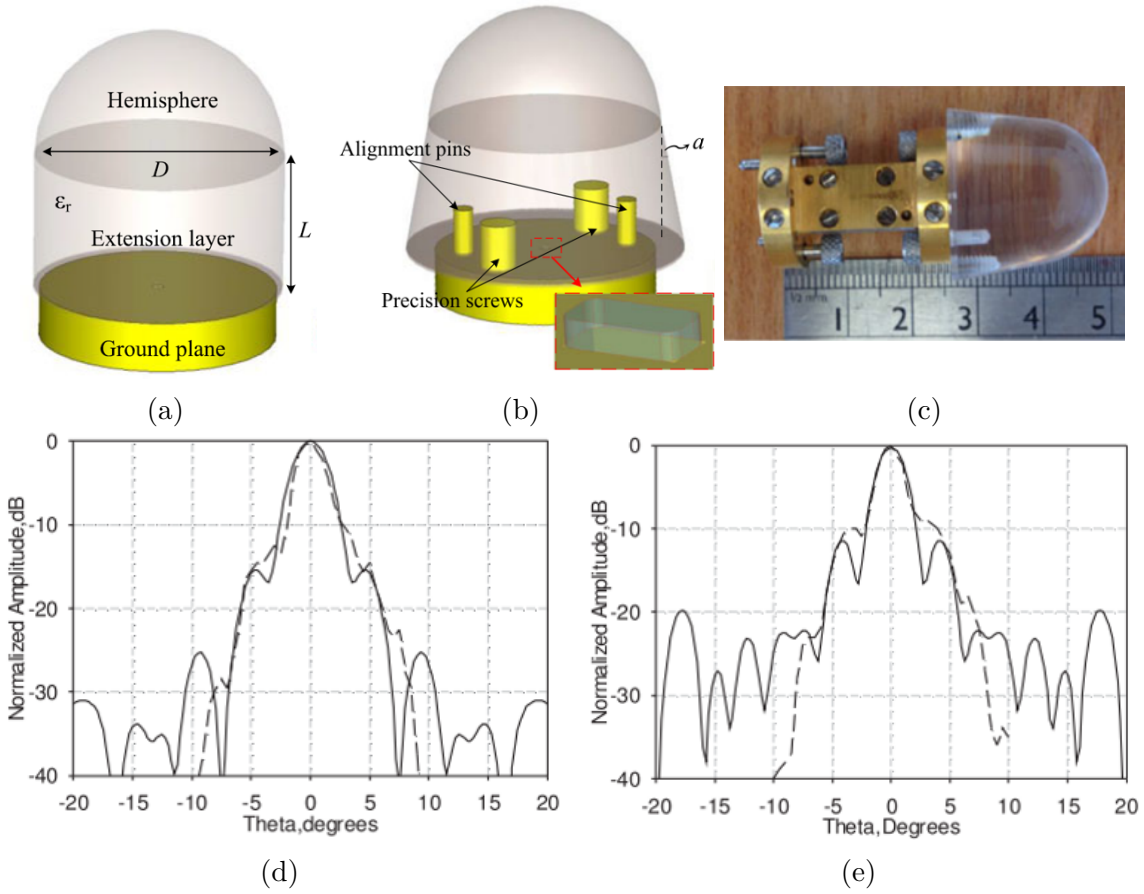

Figure 1.3: (a) Initial geometry of dielectric lens antenna. (b) Proposed antenna geometry incorporated with the WR-3 flange, showing in zoom the air pocket. (c) photograph of the lens prototype mounted on the flange. (d),(e) Radiation pattern of the prototype at 290 GHz in the H-plane and E-plane, respectively.

at sub-THz frequencies, dielectric lenses can offer better manufacturability, while their weight and size become a minor issue.

In 2017, a dielectric lens antenna with an integrated waveguide-based feed and an optimized tapered extension at 290 GHz has been proposed [14]. The hemispheric dielectric lens, shown in Figure 1.3, has been fabricated by classical computer numerical control (CNC) milling technique using Rexolite ($\varepsilon_r = 2.53$) as dielectric material. The optimum diameter D and the corresponding extension L have been selected based on full-wave studies. In addition, by etching off an air pocket at the bottom of the dielectric lens and directly over the waveguide aperture, a broadband matching response is produced. Thanks to this technique and the relatively low relative permittivity, a broadband matching over the operating band of the WR-3 waveguide is achieved. Specifically, the reflection coefficient is less than -14 dB over the entire bandwidth and it is less than -20 dB between

270 and 310 GHz. Finally, the purpose of making a tapered extension is to minimize the spillover effect and the internal reflections. This results in decreasing the sidelobe level and increasing the total directivity by 2 dB.

The experimental characterization of the prototype demonstrated 29 dBi gain at 290 GHz, corresponding to approximately 21.5% aperture efficiency. The relative 3 dB gain bandwidth is 30% (230 - 310 GHz) and the peak measured gain is 30 dBi in this region. These results show that the antenna is compatible with waveguide-based automotive radar and communication systems at 300 GHz.

A circularly polarized (CP) plastic lens antenna for high-speed communications at 180 GHz was recently reported in [15]. The choice of CP was to enhance the wireless link efficiency, especially in scenarios with moving terminals, as it minimizes the loss due to polarization misalignment. The entire antenna system comprises three components; a truncated elliptical plastic lens, a polarizer and a leaky-wave (LW) feed source, shown in Figures 1.4(a) and (b).

The lens is fabricated by a standard milling technique using high-density polyethylene (HDPE). This plastic material was chosen due to its very low loss properties ($\tan\delta = 3.4 \times 10^{-4}$). A quasi-analytic technique based on multilayer spectral Green's function (SGF) combined with a numerical Floquet modes' solver is used to optimize the lens aperture efficiency and axial ratio (AR). The feeding mechanism is a combination of a linearly polarized leaky-wave (LW) feed [16] with an add-on polarizer placed on top of that. An air cavity between the LW element and the polarizer is added, to increase the effective area of the antenna and, therefore, its directivity. The polarizer is based on a dielectric-grating concept [17], using three substrate layers. A triangular longitudinal section gear cutter is used for a milling tool. HDPE was initially used as material, but it was discarded after several trials, as it is too soft to be milled in this particular geometry. Topas material was chosen as the second best candidate, exhibiting also small losses ($\tan\delta = 1.2 \times 10^{-3}$).

The CP lens antenna has been used and characterized for beam steering applications. In order to perform the beam steering, the feed has been displaced off-focus, as explained in [16]. Figure 1.4 shows some experimental results for different steered beams, compared to simulation results. The peak gain for the broadside case is higher than 31 dBi in the entire frequency region. The corresponding aperture efficiency is more than 75% over 44% relative bandwidth. The axial ratio (AR) is less than 3 dB over 35% relative bandwidth, in the region $140 - 200$ GHz. The sidelobe level (SLL) is lower than -15 dB up to 200 GHz for the broadside case. These results demonstrate a very efficient and wideband antenna

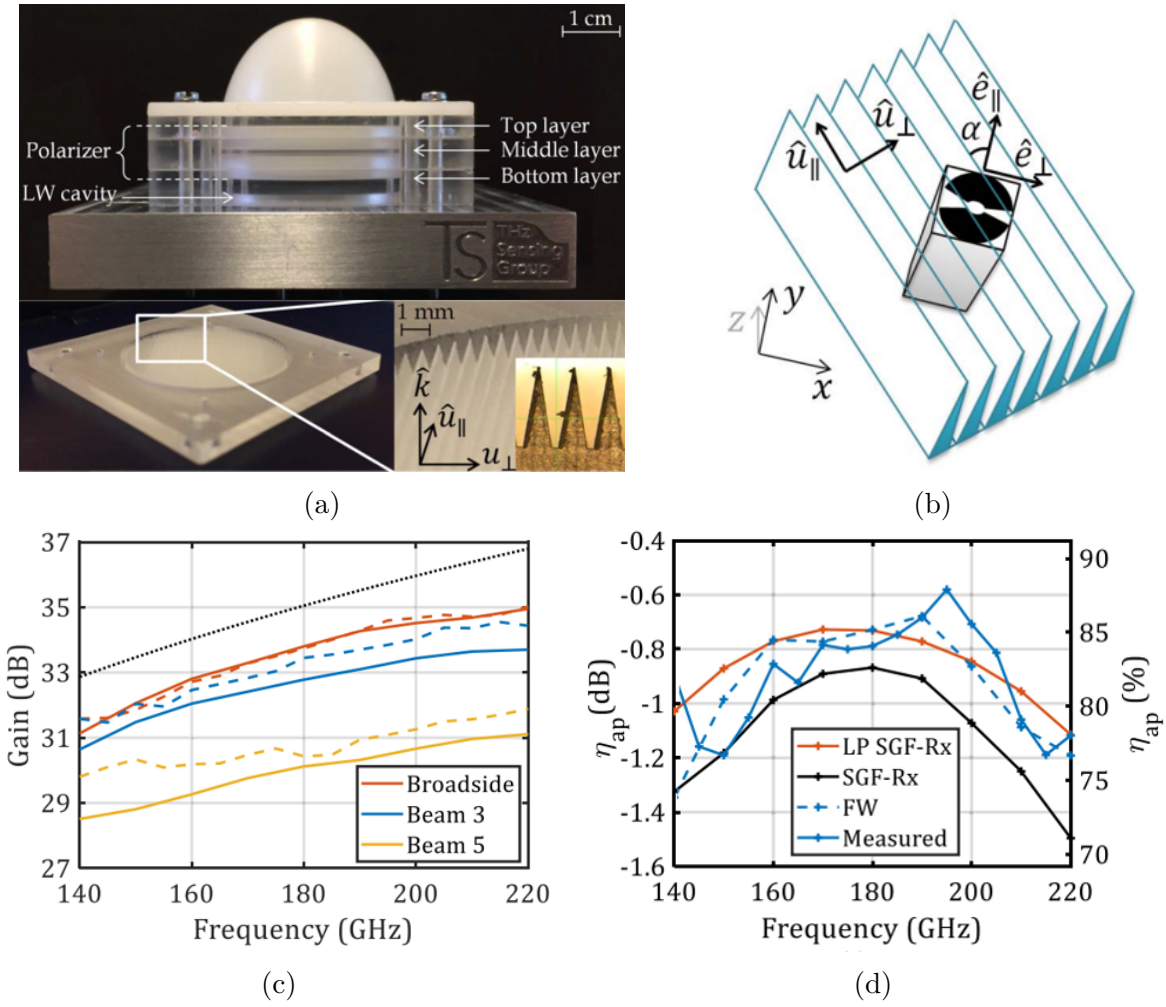

Figure 1.4: (a) CP antenna prototype [15] (top) and bottom polarizer layer with side view of the pyramidal gratings (bottom). (b) Waveguide cross-section and double slot with polarizer grid on top, oriented with 45° angle with respect to the double slot linear polarization $\hat{e}_{||}$. (c) Maximum gain versus frequency for three CP beams; broadside, 8.4° (beam 3) and 16° (beam 5). Full-wave simulations are in solid line and measurements are in dashed line. (d) Broadside aperture efficiency versus frequency. In red, the SGF simulations for linear polarization (LP) are reported for reference.

design, proving that it remains one of the best candidates for high-gain applications at sub-THz frequencies. On the downside, although it was possible to use standard milling techniques for the lens and the polarizer at 180 GHz, the choice of the material is important for the fabrication process and the minimization of losses. Therefore, at higher frequencies, a trade-off between accuracy of technology and material losses could be unavoidable. Finally, even though this antenna was used for beam steering applications, the steering agility remains somewhat limited.

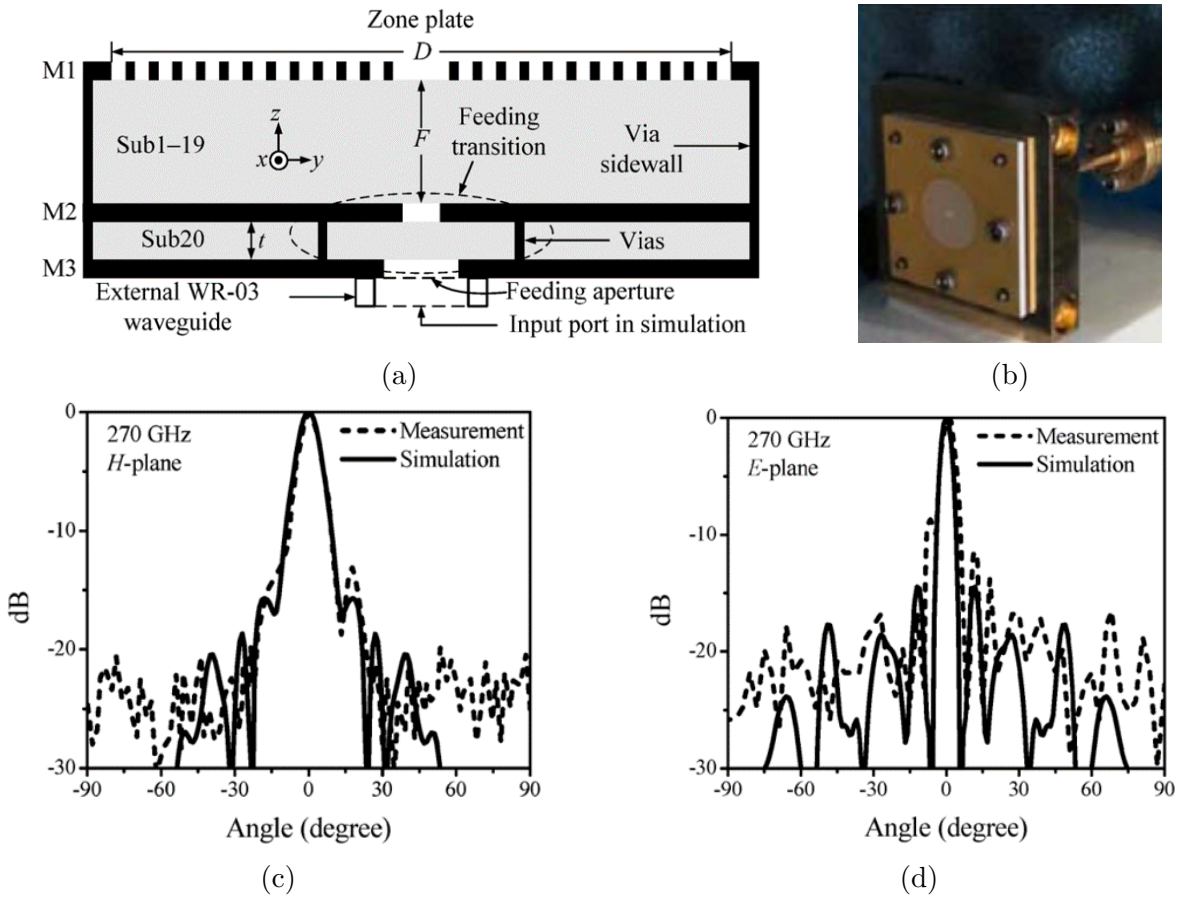

Figure 1.5: (a) Cross-sectional view of the prototype in [18], (b) antenna prototype, and radiation pattern at 270 GHz in the (c) H-plane, and (d) E-plane.

1.3.2 Fresnel Zone Plate antennas

Fresnel Zone Plates (FZPs), or Fresnel lenses, are an alternative to hemispherical dielectric lenses. The FZP can be realized by discretizing the area into rings (Fresnel zones) or into unit-cells exhibiting a specific thickness. In either case, the aim is to compensate the spatial phase delay between the focal source and the FZP, providing a collimating beam. Such antenna systems feature the merits of planar surface, reduced weight, and ease of construction. On the other hand, the phase compensation mechanism is related to the spatial phase delay that is frequency dependent. Therefore, their gain bandwidth can be limited in many cases.

A compact cavity-backed FZP antenna for high-gain applications at 270 GHz has been proposed in 2013 [18]. The FZP design is integrated in low-temperature co-fired ceramic (LTCC) and is based on the rings design approach. As shown in Figure 1.5, the entire

antenna structure consists of twenty substrate layers and three metal layers. Two rows of vias are positioned along the circumference of the circles to form an electric sidewall. In the feeding transition, a double-row via fence is used to minimize the leakage from the via sidewall. The double-row is used because the minimum via diameter and pitch available in LTCC process are electrically large at 270 GHz. The final structure exhibits very low profile, with a focal-to-diameter (F/D) ratio equal to 0.12.

The maximum measured gain of this prototype is 20.8 dBi at 270 GHz and the measured gain is greater than in 17.8 dBi in $266.2 - 275.3$ GHz. Due to a small discrepancy in the estimated relative permittivity and the loss tangent, a frequency shift and a gain drop between measured and simulated gains was observed. A better agreement was found when the relative permittivity was changed from 5.9 to 5.65 and the loss tangent from 0.002 to 0.004. The measured aperture efficiency is about 7% at 270 GHz, which is low due to the increased dielectric loss. Finally, the measured SLLs in H-plane is below -13 dB at 270 GHz. The measured E-plane radiation pattern is not symmetrical. Specifically, the peak SLL in left side and right side is -9 dB and -12 dB, respectively, at 270 GHz. According to the authors, this deterioration attributes to the fabrication tolerance that causes the asymmetry of the antenna structure. Possible reasons include the varied radii and locations of the metallic rings as well as misalignment of the slot on the ground plane M2 along the E-plane axis.

A 3-D printed FZP lens approach at 60 GHz and 275 GHz is reported in [19]. Only the sub-THz prototype is presented here for the sake of our discussion. This time, the design approach is based on tuning the thickness of the unit-cells. Moreover, periodic antireflection structures with different permittivity than the rest of the unit-cell are added in the design, as shown in Figure 1.6. This modification reduces the impedance mismatch at the air-dielectric interface, improving the transmission coefficient. However, in the case of the sub-THz FZP prototype, the typical fabrication accuracy is 0.1 mm, according to the specification of the 3-D printer Stratasys Objet 30. Therefore, the antireflection structure is added only on the bottom side. The chosen ratio F/D for this prototype is 0.47.

The peak measured gain is about 27.5 dBi at around 235 GHz, corresponding to approximately 21% aperture efficiency. However, as shown in 1.6b the measured gain shifts downward by about 20 GHz and suffers from a 2 dB drop compared to the simulated one. This is attributed to the uncertainties in dielectric property, fabrication errors, and alignment error of the measurement system. Finally, the SLLs are below -22 dB and -27

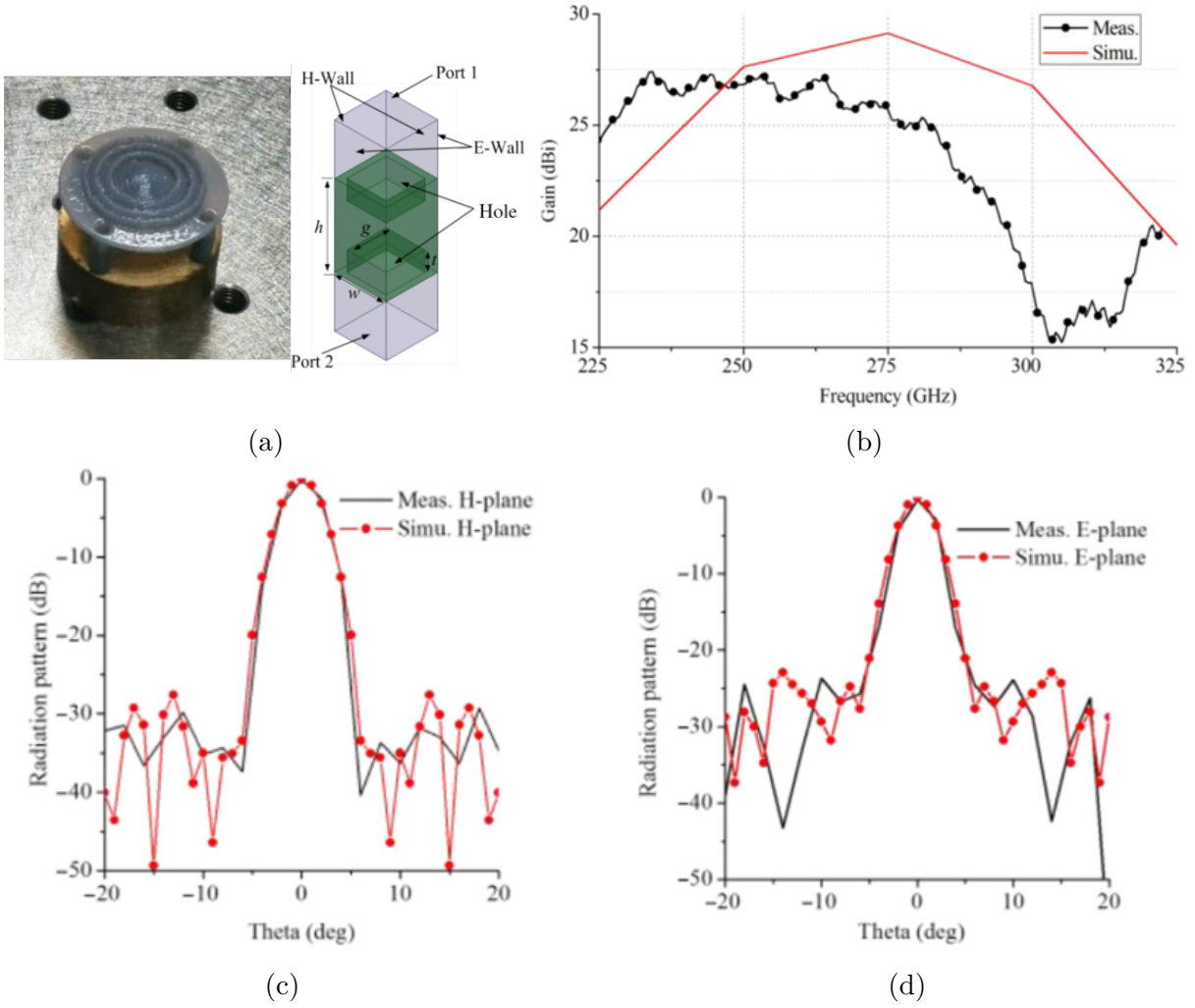

Figure 1.6: (a) Model of the prototype in [19], with its unit-cell design that includes holes as antireflection structures. (b) Measured and simulated gain versus frequency. (c) H-plane, and (d) E-plane radiation pattern at 250 GHz.

dB in the E- and the H-plane, respectively.

A recent FZP antenna prototype achieving dual-band operation at 75 and 120 GHz has been reported in [20]. As shown in Figure 1.7, the proposed dual-band single-polarization FZP is realized by merging two single-band FZP metalens antennas operating at distinct frequency bands into a shared aperture. Simply placing the rings together would destroy the performance of FZP metalens antenna at both bands. Instead, the concentric rings are realized using different double-screen grids. The prototype is fabricated using DragonFly 2020 PRO, an integrated additively manufactured electronics (AME) technique. The focal length is set to 30 mm for both bands, resulting in an F/D equal to 0.5.

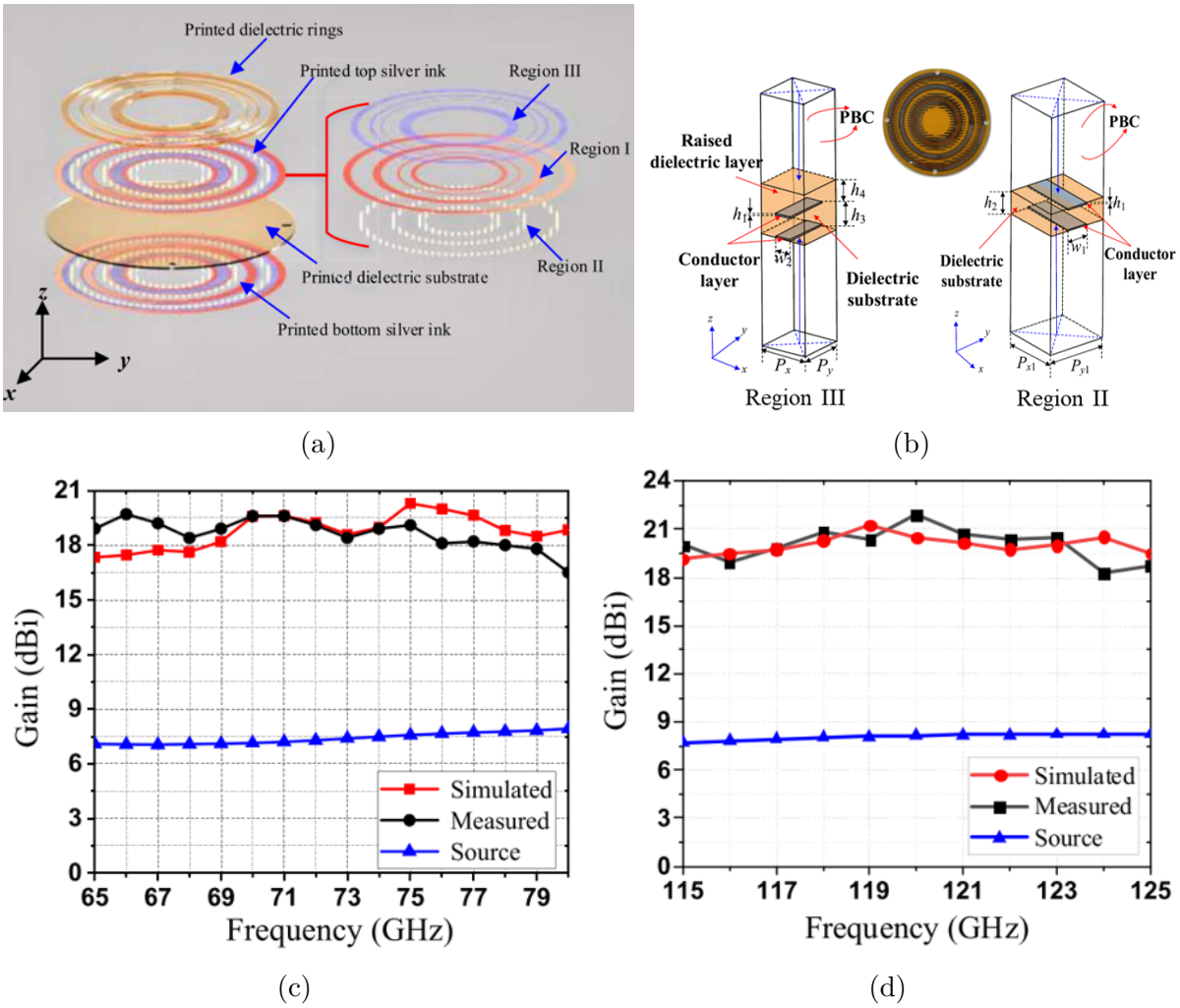

Figure 1.7: (a) Expanded view of the proposed structure in [20]. (b) View of the prototype and its two grid-based uni-cells for the dual-band operation. Simulated and measured gain versus frequency at (b) 75 GHz, and (c) 120 GHz.

The measured gains at the two frequency regions are 20.3 dBi at 75 GHz and 21.9 dBi at 120 GHz, respectively. The corresponding aperture efficiency is 4.8% and 2.7%, respectively. The low efficiency is expected, due to the design. The metallic FZP lens antenna uses only two states for the phase correction (0° and 180°), while 50% energy is reflected backwards. On the other hand, this dual band design is realized using only two metal layers, easing the fabrication process. Finally, the SLLs are kept lower than - 10 dB in both frequency regions.

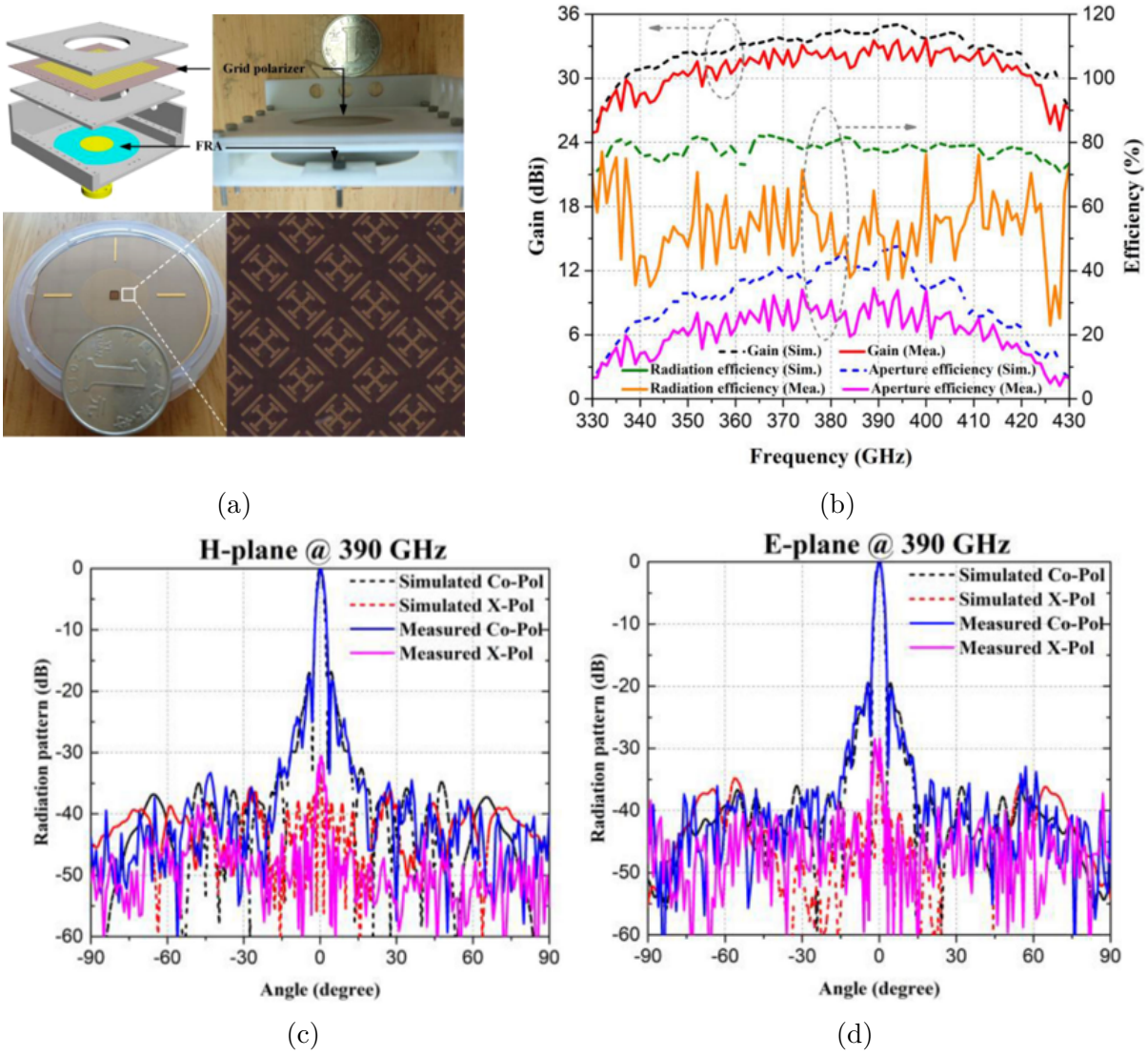

Figure 1.8: (a) View of the prototype in [21], (b) gain and aperture efficiency versus frequency, and radiation pattern at 390 GHz for (c) H-plane, and (d) E-plane.

1.3.3 Reflectarray antennas

Reflectarray (RA) antennas are a good alternative to classical reflector antennas. They are less bulky and they can be manufactured by a low-cost planar fabrication process. Nevertheless, the research on sub-THz RA design is still at an early stage.

A quartz-based folded RA antenna operating at 400 GHz has been reported at 400 GHz [21]. It consists of a classical horn antenna as the feed source, a main RA fabricated by lithography process on a quartz substrate, and a grid polarizer implemented by the

printed circuit board (PCB) technology, used for the folded configuration, as shown in Figure 1.8(a). The quartz lithography allows for the design of subwavelength size elements on the RA, with a minimum conductor width and spacing down to 10 μm. The THz components are sensitive to the substrate characteristics, which are not readily available from the manufacturer. Therefore, the material parameters of the quartz and the PCB substrate have been extracted using a THz-TDS system developed by Menlo Systems GmbH. The measured dielectric constant of the quartz decreases slowly from 3.785 to 3.773 as the frequency increases from 325 to 500 GHz, while the loss tangent fluctuates within a small range from 3.66×10^{-3} to 4.77×10^{-3}. The corresponding PCB substrate, chosen as Taconic TLY-5, has also a stable relative permittivity of 2.253 ± 0.001 within $325 - 500$ GHz, while the loss tangent is between 9.43×10^{-3} and 1.11×10^{-3}. Moreover, thanks to the use of the polarizer, the final focal distance is reduced by half.

The experimental characterization of this prototype demonstrated about 33.66 dBi peak gain at 400 GHz, as shown in 1.8(b). The measured 3 dB gain is $357 - 421$ GHz, corresponding to 16.45% of relative bandwidth. The maximum measured aperture efficiency is 34.51% at 389 GHz and it is equal or more than 20% between 360 and 410 GHz. Finally, the measured SLL is lower than -20.5 dB and -16.7 dB at 390 GHz in the E- and H-plane, respectively, while the cross-polarization discrimination is less than -28 dB in both planes.

1.3.4 Advanced quasi-optical antennas

At sub-THz frequencies, quasi-optical beamforming networks can be a good alternative to classical beamforming networks, delivering compact, directive, and low loss antennas. They can integrate 1-D reflectors or lenses in parallel plate waveguide (PPW) technology, thus reducing the total volume and mass of the system but limiting the beamforming to one plane.

A leaky-wave (LW) fed quasi-optical array antenna, fabricated using silicon on insulator (SOI) wafer micromachining process, has been reported in [22]. The antenna, shown in Figure 1.9, is divided into two main components: the radiation part, a dielectric-filled parallel plate waveguide (PPW) loaded with periodic slots forming a LW array; and the quasi-optical hollow PPW beamforming network, namely a pillbox structure. The final device consists of a stack of 3 chips completely metallized with gold, which was found to be the minimum needed to implement such system. Two of the three chips have high aspect ratio membranes, making their fabrication very challenging and where the mono-

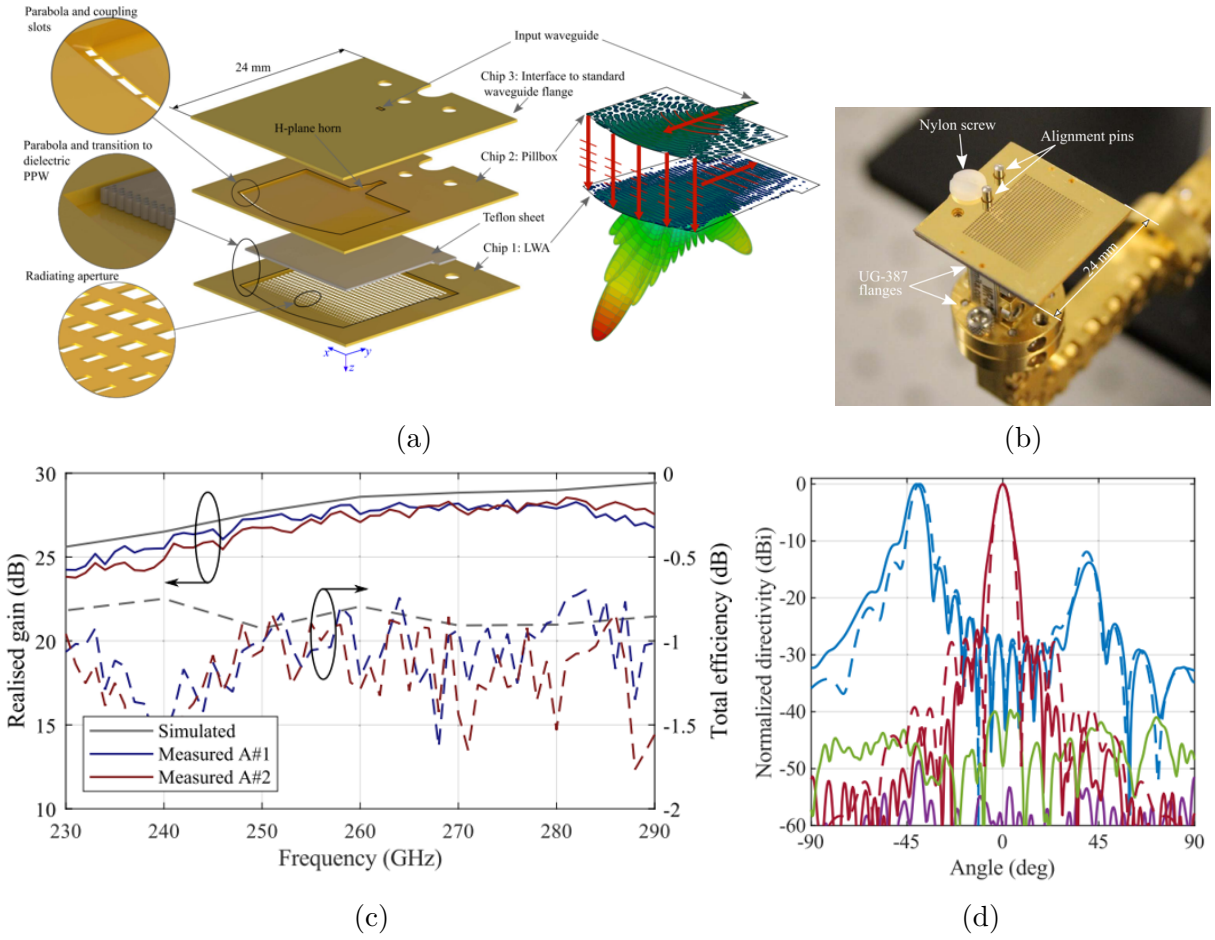

Figure 1.9: (a) CAD drawing of the antenna in [22] showing the three-chip structure, the integrated dielectric substrate and a conceptual representation of the field propagation from chip 2 to chip 3 at the right side. (b) Antenna prototype mounted on the waveguide. (c) Gain and radiation efficiency of two antenna prototypes compared to simulated values. (d) E-plane (blue lines) and H-plane (red lines) co-polarized radiation pattern at 260 GHz. The corresponding cross-polarized pattern is shown with purple lines (E-plane) and green lines (H-plane).

crystalline structure of the silicon wafers is a requirement for the membranes not to break. In addition, silicon micromachining allows for accurate perforations in these membranes, which are used for coupling between the PPW layers and for the LW array radiation. Thanks to the feeding mechanism, the antenna exhibits an ultra-low profile, as shown in Figure 1.9(b).

Two antenna prototypes were fabricated (referred to as A#1 and A#2) and measured. The maximum measured gain is close to 28 dBi at 282 GHz, as shown in Figure 1.9(c). The 3 dB gain bandwidth is about 50 GHz in the observed region, corresponding to approximately 19% of relative bandwidth. The average radiation efficiency is about -1 dB

(80%) with a -1.9 dB (65%) worst case. In the measured E-plane cuts the main beam scans from -75° at 230 GHz to -30° at 290 GHz. The H-plane cuts are always aligned with the main beam pointing direction, and the SLL is kept below -20 dB as designed. One radiation pattern is shown in Figure 1.9(d).

1.3.5 Corporate-feed array antennas

An alternative approach to quasi-optical beamforming networks is using corporate-feed arrays. Corporate-feed array antennas can provide high gain and broadband operation. However, at sub-THz frequencies they require waveguide-based beamforming networks with increasing complexity as the number of elements of the array increases. The geometrical complexity of these networks makes their fabrication extremely challenging at THz frequencies, due to the small features and the high uniformity required to achieve a good performance.

In 2017, the first waveguide array antenna above 300 GHz was reported in [23]. The antenna, shown in Figure 1.10, is constituted of five thin laminated plates, M1 to M5, bonded together and forming two parts of the antenna. The first part is a corporate feeding network in the lower layer and the second one is an array of radiating slots in M5. The two parts are coupled by an array of coupling slots in M3. For the fabrication, bonded thin laminated metallic plates have been adopted. These plates require high etching accuracy because of the sever fabrication tolerance in the 350 GHz band. A deep reactive ion etcher (DRIE) micromachining process was adopted to allow coping with these constraints. It uses dry etching technique, giving high etching accuracy and allowing maintaining vertical sidewalls. In addition, it allows easy integration with others chips components in the system.

A 16 × 16 array has been fabricated and tested. The aperture size is about 11×11 mm^2 with a total thickness of only 1 mm, resulting in an ultra-low profile structure. The directivity, gain, and realized gain in simulation and measurement at the antenna broadside direction versus frequency are compared in Figure 1.11(b). The realized gain is around 29.5 dBi at 350 GHz, corresponding to about 43% of aperture efficiency. The 3 dB gain bandwidth is 44.6 GHz, which is about 14% of relative bandwidth. Good agreement between simulated and measured radiation patterns is obtained in both planes. The measured half-power beamwidth (HPBW) is about 4.1° at 350 GHz. The corresponding SLLs are lower than -13.2 dB in both planes.

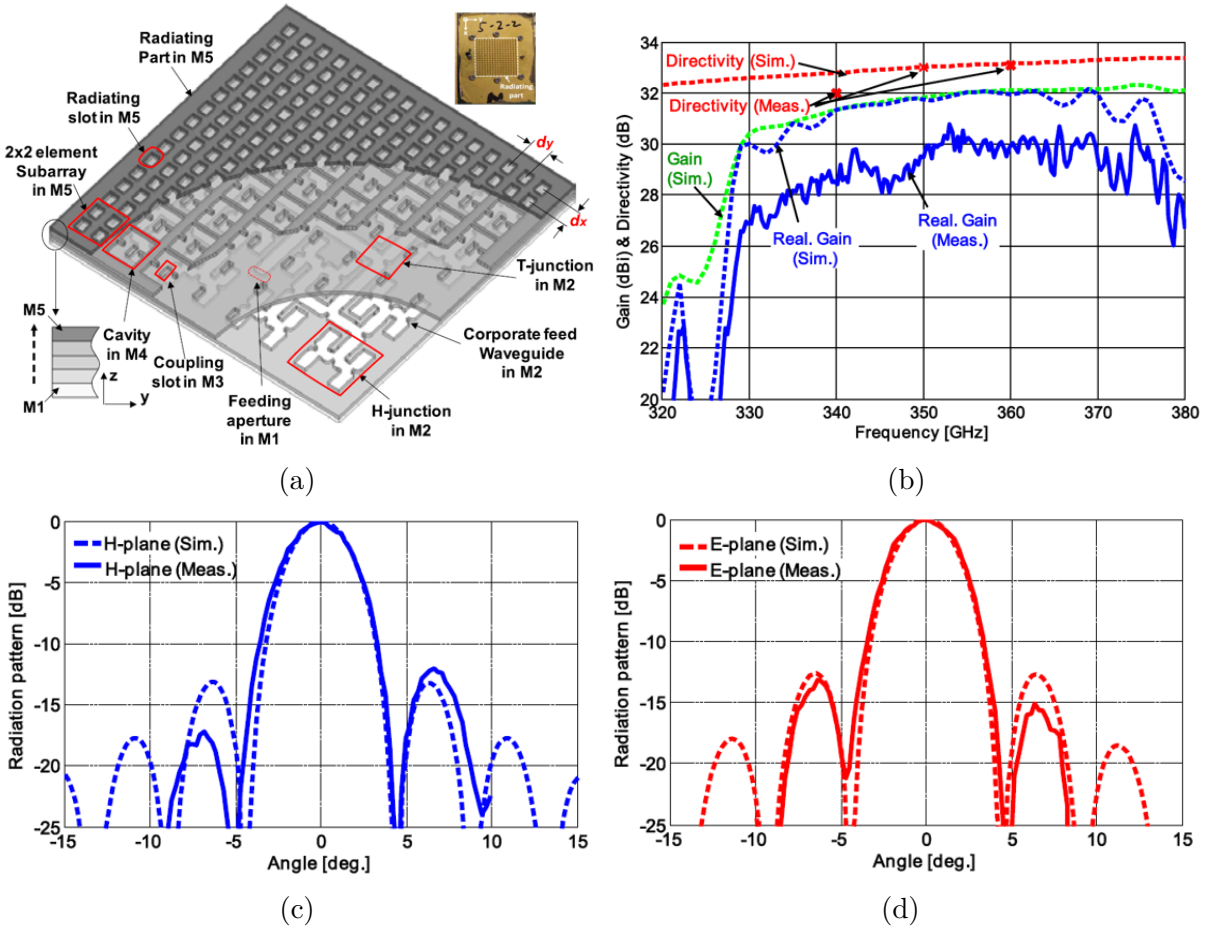

Figure 1.10: (a) 3D-view of the corporate-feed slotted waveguide array antenna in [23]. (b) Directivity, gain, and realized gain versus frequency. (c) and (d) Radiation pattern at 350 GHz in the H- and E-plane, respectively.

Another prototype, similar to the one in [23], has been recently reported in [24]. Using again a SOI micromachining process, the authors managed to improve the radiation performance, both in bandwidth and gain loss, compared to [23]. As shown in Figure 1.11(b), the best-case antenna exhibits a gain that ranges between 36 and 38.2 dBi, showing a total radiation efficiency of around 60%. The 3 dB relative bandwidth is around 25% in the observed region.

1.4 Transmitarray antennas: state-of-the-art

In this section, a more detailed description of the transmitarray (TA) antenna is presented. The research on this antenna technology has been spreading rapidly in the last decade,

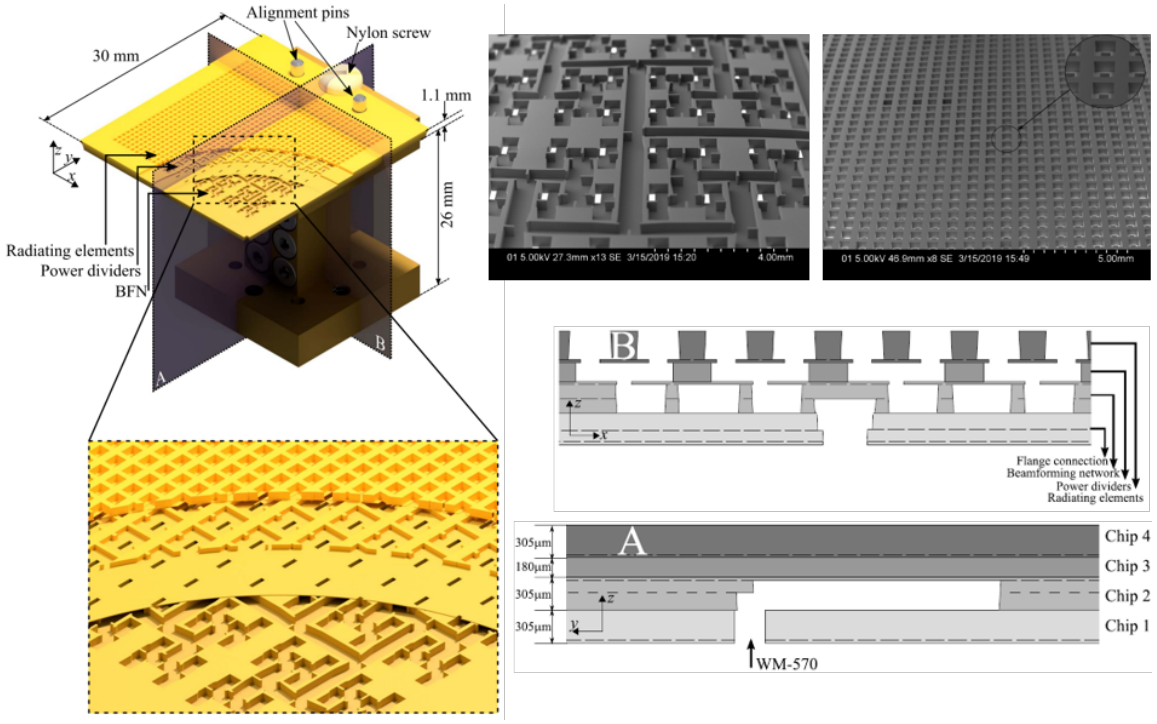

(a)

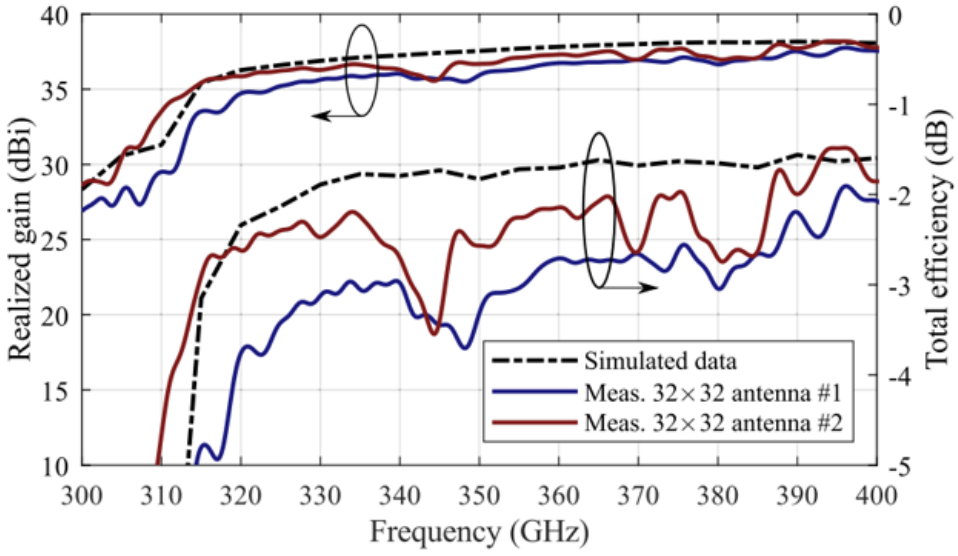

(b)

Figure 1.11: (a) CAD drawing of the antenna on the left, reported in [24]. Two SEM images of the H-tree beamforming network in chip 2 and the radiating coupling slots are shown on top right. Two cross-sections of cutting planes A and B are shown on the bottom right. Plane A shows the input waveguide and the stepped E-bend. Plane B shows the beamforming network, the power dividers and the radiating elements. (b) Gain and total efficiency of the 32×32 prototype in [24].

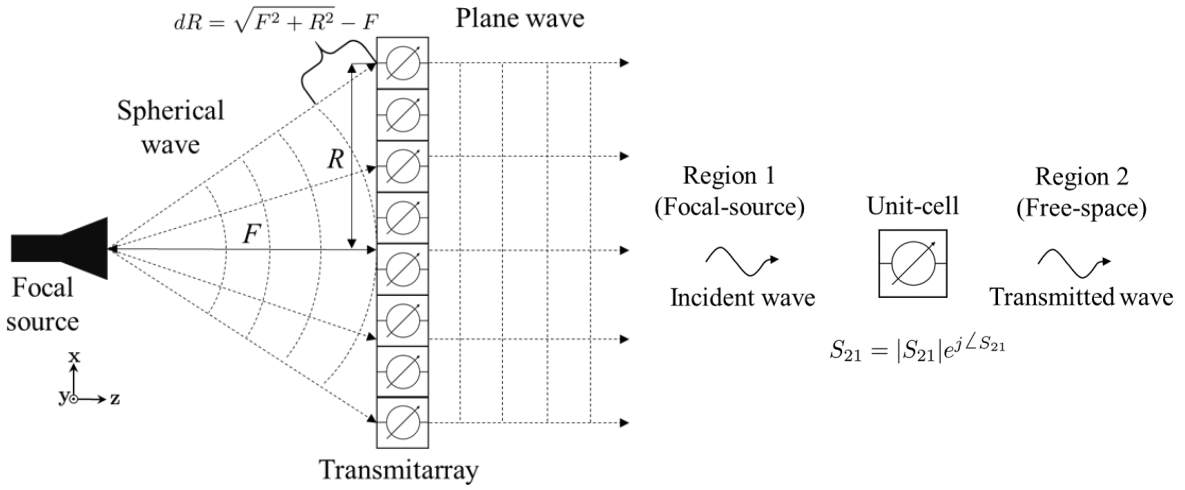

(a) (b)

Figure 1.12: (a) Operating principle of the transmitarray antenna, (b) transmitarray unit-cell.

with numerous prototypes operating in the whole mmWave band. For the purposes of this study, we will focus at high-frequency TA antennas, mainly in the sub-THz region.

1.4.1 Operating principle

A schematic view of the general structure is shown in Figure 1.12. The transmitarray consists of a planar arrangement of unit-cells with the same thickness, composing a two-dimensional artificial lens. Typically, the unit-cell comprises two or more metal layers separated by air or bonded together with some dielectric material. A detailed categorization of the unit-cell design is reported later. Compared to the classical dielectric lenses and Fresnel lenses, transmitarrays are less heavy, less bulky, they do not suffer from inherent reflection losses and the artificial lens can be realized using cost-efficient planar fabrication processes. The focal source is usually a low- or mid-gain element, such as an open-ended waveguide or a small aperture horn, illuminating the transmitarray in relatively close proximity.

In principle, the transmitarray transforms the incoming spherical wave of the focal source to a plane wave, radiating at a given angle in far-field. Unlike RA antennas, there is no feed blockage from the source, which can enable near-field illumination approaches for more compact and efficient systems. Each unit-cell provides a specific phase shift to compensate for the spatial phase delay. In total, the phase shift depends on both

the differential path dR of the spherical wavefront and the steering angle, leading to a unique solution of the phase distribution at each case. The value of the phase shift is tuned by modifying the geometry of the constituent metal layers of each unit-cell. Nevertheless, it is crucial to control also the magnitude of transmission in the design approach, in order to minimize the gain loss due to reflections and improve the gain bandwidth. Another performance issue related to the unit-cell is the number of selected phase shift states, expressed by the phase quantization. For instance, the 1-bit (two states) transmitarray exhibits about 3 dB of quantization losses compared to a perfect phase compensation design (360°) in linear polarization [25]. On the other hand, a 3-bit (eight states) design exhibits less than 0.3 dB of quantization losses [26], making it a satisfying trade-off between loss and unit-cell complexity.

Except for the unit-cell properties, the maximum performance of the transmitarray antenna depends on the illumination, which is controlled by the focal distance and the focal source. For a given feed, the focal distance is selected as a trade-off between spillover losses and illumination tapering in order to maximize the antenna gain. Usually, the focal source is selected with a trade-off between total volume occupancy and gain bandwidth performance. A more directive (higher gain) source leads to a larger focal distance, but also increases the gain bandwidth, as the the differential path dR becomes less sensitive in frequency. The directivity of the focal source is usually in the range between 10 - 20 dBi, leading to a focal-to-diameter ratio between 0.5 and 2.

1.4.2 Fixed beam transmitarrays

The case of passive unit-cells for fixed-beam transmitarray (TA) antennas is discussed here. In general, there is no strict categorization of the TA design, but, for the sake of this discussion, it will be based on the design approach of the unit-cell. According to the literature, the design approach can be categorized into two broad groups; the antenna-filter-antenna (AFA) elements and the frequency-selective-surface (FSS) structures. A third design approach, originating from the FSS design that provides anisotropic transmission, has been derived recently. The latter structure is called asymmetric linear polarizer (ALP) and is presented here separately.

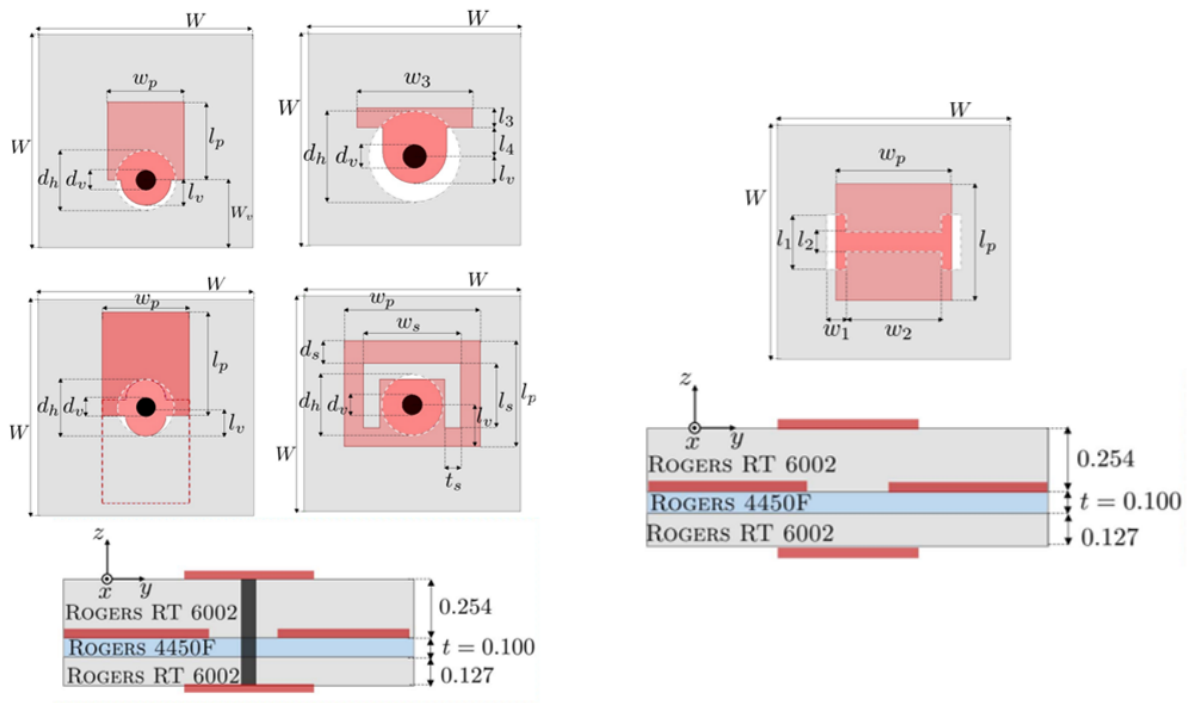

(a) (b)

Figure 1.13: Design and stack-up of the two types of unit cells in [29]. (a) Via-connected patches and (b) aperture-coupled patches. Dimensions of the stack-up are in millimeters.

Antenna-Filter-Antenna (AFA)

At frequencies below 100 GHz, the most common unit-cell architecture is the antenna-filter-antenna (AFA). It comprises two antenna elements, usually patch geometries, physically connected using a metallized via. The design approach is simple and relatively easy to incorporate active components (e.g. PIN diodes) for later reconfigurable designs. Some passive AFA prototypes with high phase resolution (3-bit), good radiation performance and low-cost fabrication process can be found at frequencies between 30 and 100 GHz [26]–[28].

At sub-THz frequencies, the fabrication constraints hinder the achievement of optimal unit-cell performance in the AFA. To cope with this problem, a hybrid design approach was presented at D-band [29]. The authors combined AFA unit-cells comprising either vias- or aperture-coupled radiating elements, demonstrating a 3-bit transmitarray based on five different unit-cell topologies, shown in Figure 1.13. A 20×20 λ^2 TA antenna with an $F/D = 0.75$ was synthesized at 140 GHz. The measured peak gain is about 33 dBi at around 153 GHz, with 33.6% aperture efficiency. The 3 dB gain bandwidth lies between

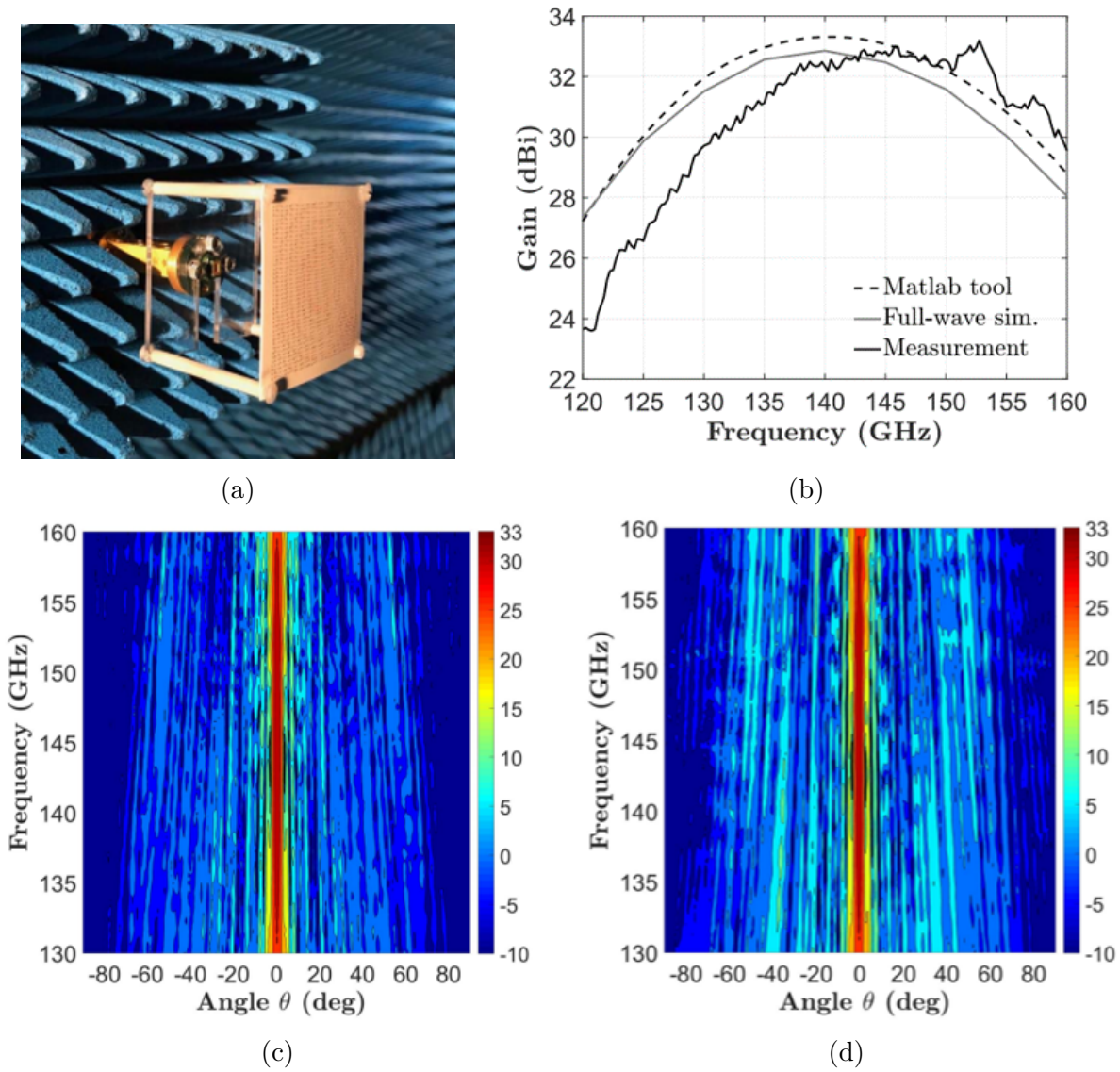

(a) (b) (c) (d)

Figure 1.14: (a) Antenna prototype in [29]. (b) Measured and simulated gain versus frequency. Measured gain pattern (in dBi) as a function of frequency and elevation angle for (c) H-plane and (d) E-plane.

130 and 160 GHz, corresponding to a 19.8% relative bandwidth. The aperture efficiency is greater than 25% between 133 and 154 GHz and reaches a maximum of 38.3% at 144 GHz. As shown in Figure 1.13(c) and (d), the beam characteristics are very stable in the band. However, the strong impact on the metallized via diameter and alignment lead to a frequency shift of about 5 GHz (3.6% at 140 GHz), shown in Figure 1.13(b). Nevertheless, the antenna prototype fulfills the initial bandwidth specification.

To improve the radiation performance and reduce the impact of the fabrication con-

straints, a high-resolution technique for the design of AFA at D-band was reported in [30]. A low temperature co-fired ceramic (LTCC) process was used to enhance the unit-cell design. The phase shift mechanism is based on a wideband substrate integrated waveguide (SIW) aperture-coupling phase delay, as shown in Figure 1.15(b). The fabrication technique allows for the design of a structure comprising seven metal layers and multiple vias, which is able to achieve full phase coverage (360°) and very low insertion loss in the whole D-band (110 − 170 GHz). The final antenna system has a ratio F/D equal to 1.866 due to the high gain and the edge taper of the selected focal source. The measured gain of the proposed TA prototype is 33.12 dBi at 140 GHz, which is the central frequency. The measured 1 dB gain bandwidth lies in the region 138 − 153 GHz, which is equivalent to 10.7% at 140 GHz, while the measured 3 dB gain bandwidth is between 124-158 GHz (24.29%). The measured aperture efficiency is 46.82% at 140 GHz and the maximum one is 50.12% at 142 GHz. Therefore, the results prove that the transmitarray technology can potentially reach radiation performance close to that of classical dielectric lenses, using high-resolution technologies.

Frequency-Selective Surface (FSS)

As shown before, the impact on the metallized via diameter and alignment in the AFA design becomes a major issue at sub-THz frequencies. An alternative and more general design approach is based on the frequency-selective surface (FSS) concept. The FSS unit-cells are via-less and comprise multiple metal layers, separated by air gap or dielectric spacers. Instead of synthesizing and optimizing patch geometries, the synthesis procedure is more arbitrary, employing equivalent admittance values to describe the metal layers and tune the transmission coefficient of the unit-cell [32]. Several FSS TAs have been demonstrated at frequencies lower than 100 GHz, achieving good radiation performance [33]–[35] and enabling useful functionalities [36], [37].

A two-layer FSS TA operating at W-band was reported in [31]. The simple design concept, as shown in Figure 1.16, enables a via-less standard printed circuit board process. Three different slot geometries are used to tune the phase of transmission. In order to enhance the bandwidth performance, some of the central elements were removed, as shown in Figure 1.16(b). The final prototype achieves a peak gain of 24.5 dBi at 97.7 GHz, corresponding to 46.1% aperture efficiency. The 3 dB relative gain bandwidth is about 15% in the observed region. Despite the good radiation efficiency, the structure is relatively narrowband, considering also the total size of the TA. Moreover, removing elements to

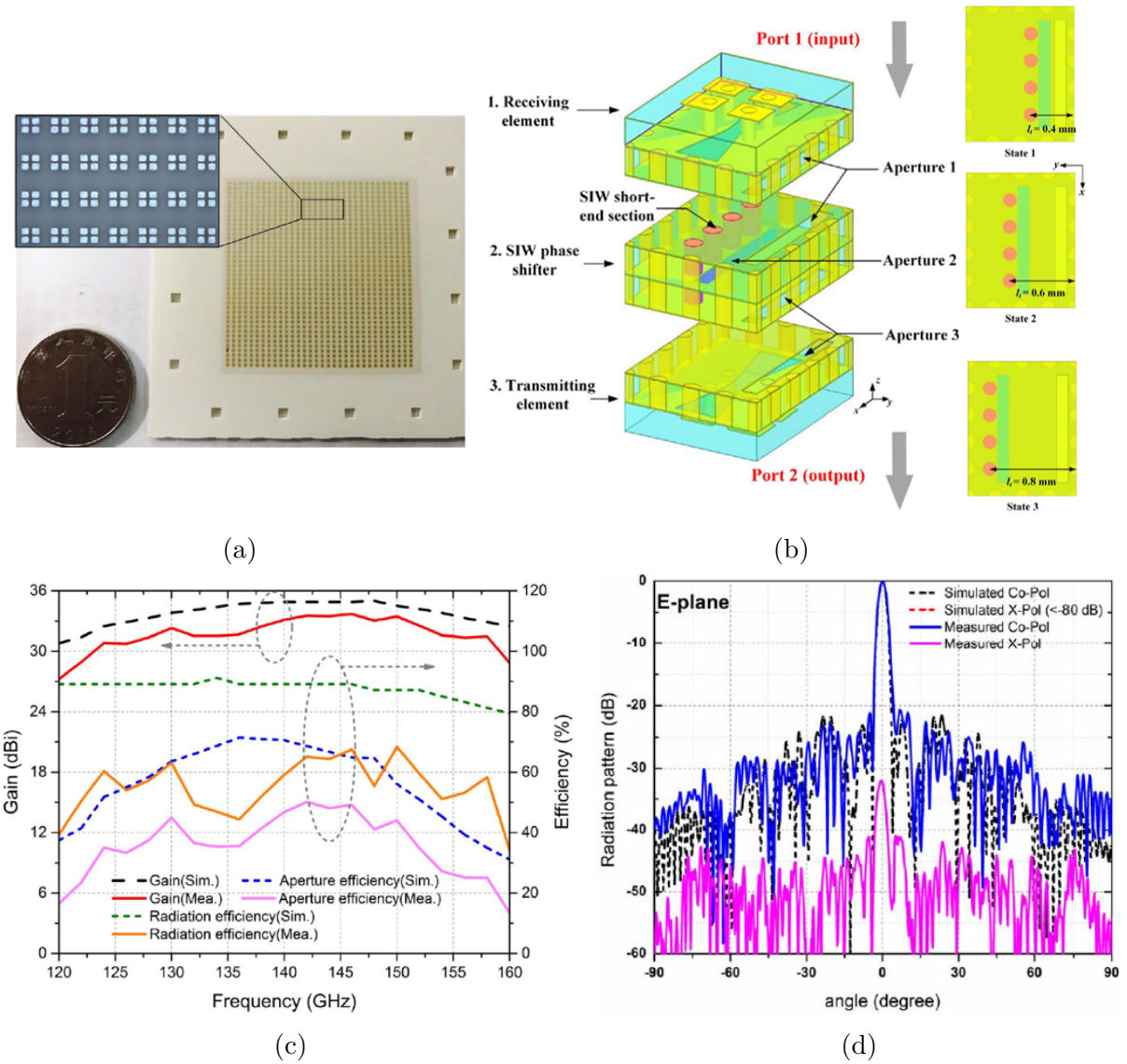

Figure 1.15: (a) Photograph of the fabricated TA in [30] with a SEM view. (b) Expanded view of the unit-cell, including the phase shifting principle of the SIW structure. (c) Simulated and measured gain and corresponding efficiency within frequency band of interest. (d) Measured and simulated E-plane radiation pattern at 140 GHz.

enhance the gain is generally not the best solution, as it limits the beamforming capability, especially in case of synthesizing more complicated radiation patterns.

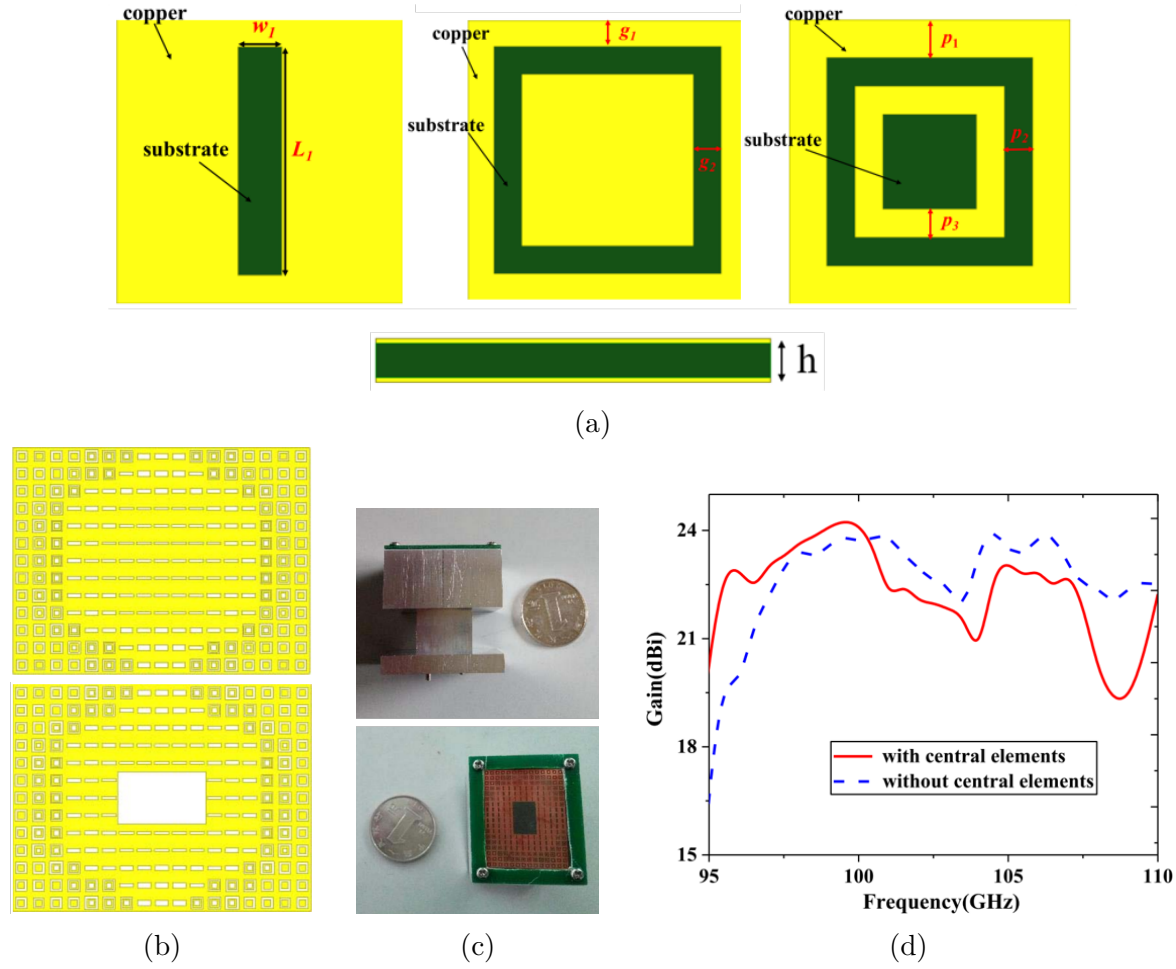

Figure 1.16: (a) Unit-cell geometries of the TA reported in [31]. (b) Structure of the TA surface with (top) and without (bottom) central elements. (c) Side view (top) and front view (bottom) of the prototype without central elements (d) Comparison of gain performance with and without central elements.

Asymmetric Linear Polarizer (ALP)

Anisotropic transmitarray designs can offer enhanced performance and additional functionalities. The unit-cell presented in [38]–[42] achieves high efficiency over wide bandwidth using only three metal layers: two orthogonal polarization grids and an inner polarization rotator. This design, also referred to as asymmetric linear polarizer (ALP), was originally proposed as a 90° polarization converter at optical frequencies [43]–[45]. Furthermore, by optimizing only the middle layer, phase-shifting surfaces for wavefront manipulation and TA antennas with high phase resolution can be realized. A few TA designs have been demonstrated using this concept at sub-THz frequencies [46]–[48].

The first ALP-based transmitarray manufactured in standard PCB at 300 GHz was re-

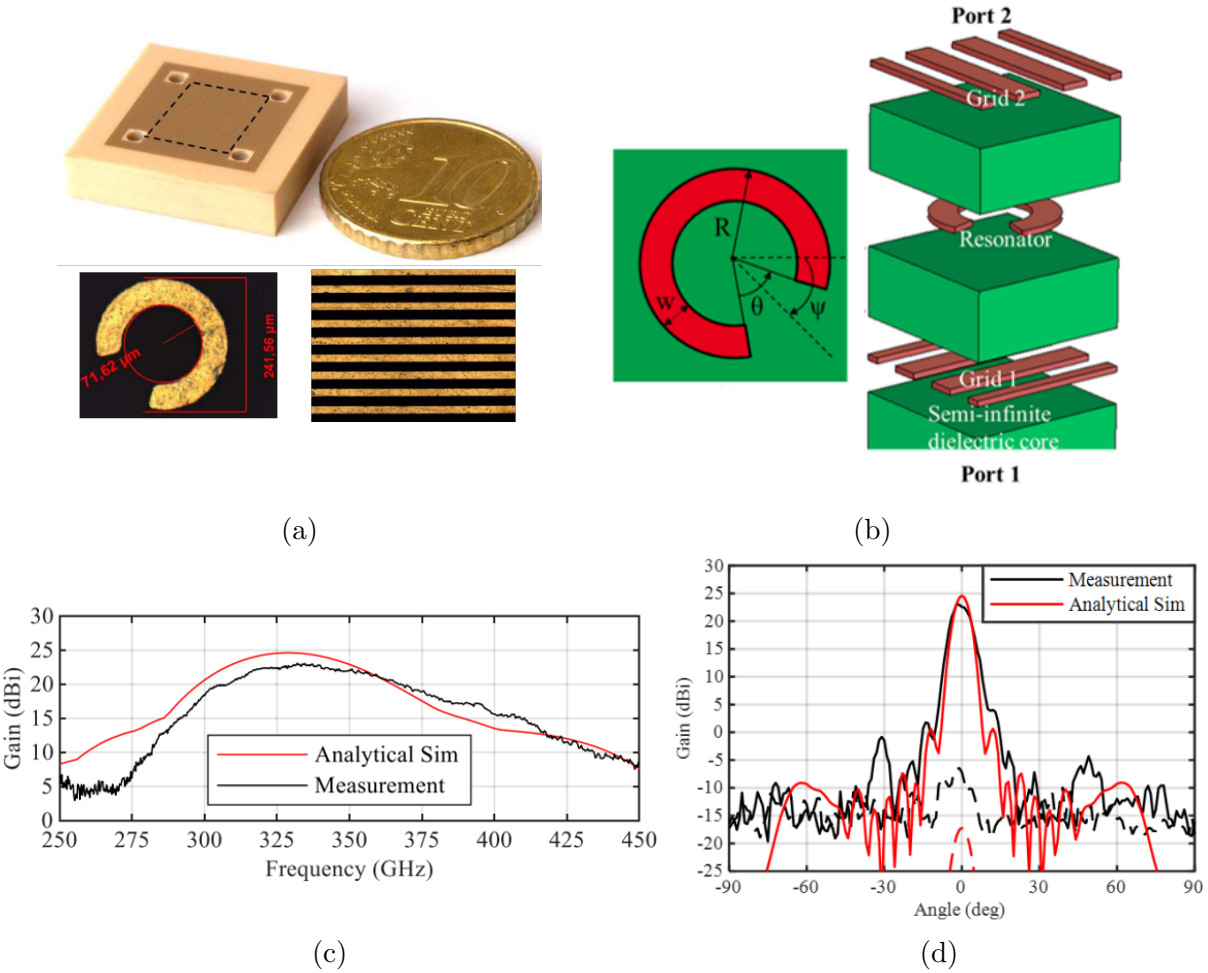

Figure 1.17: (a) Photograph of the prototype reported in [48], showing one rotator unit-cell and the top grid. (b) Geometry of the three-layer unit-cell. (c) Measured and simulated gain versus frequency of the prototype. (d) Measured and simulated E-plane radiation pattern at 332 GHz.

ported in [48]. The entire antenna system (focal source and TA) is integrated in monolithic design, resulting in a compact structure. As shown in Figure 1.17(b), the transmission properties are conveniently controlled by modifying only the middle layer, enabling a 3-bit phase resolution. Each unit-cell topology exhibits more than 44% of relative 1 dB bandwidth in transmission, resulting in 27% common 1 dB bandwidth for the eight selected designs. The measured peak gain for the larger size prototype in [48] is 23.1 dBi at 332 GHz, as shown in Figure 1.17(c). The corresponding aperture efficiency is about 12%. The experimental 3 dB gain bandwidth is 17.2% (308.7 − 366.6 GHz). The decreased aperture efficiency can be explained partly by the dielectric losses and the frequency shift, which is about 3% compared to simulations. Although this performance is not as good as in the

previous high-gain antennas, it is the first prototype fabricated in PCB that operates at 300 GHz. The relatively simple geometry opens new discussions on the design approach of this element, even when it comes to using standard planar fabrication processes.

1.4.3 Standard fabrication techniques

In general, the fabrication of the transmitarray is based on planar processes. The printed circuit board (PCB) is the most common technology, used in all but the simplest electronic products, as it disposes a relatively simple and low-cost manufacturing process. The board electrically connects all the components using conductive tracks and pads, usually copper material, etched from one or more sheet layers of copper, laminated onto and between sheet layers of non conductive substrates. Based on the existing techniques, the substrate can have a thickness from 64 μm up to 1.5 mm. The pre-preg, used as a bonding film, has typically a thickness of 100 μm, but it can be set lower at 64 μm. The laminated copper has typically a thickness value of 17 or 35 μm, which can be minimized to 9 or 12 μm. The minimum width of the tracks is $70 - 80$ μm, with a tolerance of 10 μm in the over- or under-etching. Lastly, when it comes to the use of vias, the minimum diameter size for standard techniques is 100 μm. It is evident that such fabrication constraints already impose many challenges for the TA design at 300 GHz. The maximum periodic size of the TA unit-cell is half wavelength, which is 500 μm at this frequency. Therefore, the periodicity is about 7 times the minimum width and gap of the conductor.

Another approach is using a lithography process on quartz substrates. The principle consists on metallizing one or several substrates in aluminum or gold and bond them after careful alignment. Typically, the thickness of the substrate is between 100 μm and 200 μm. The roughness of the substrate does not exceed 3 μm to ensure good photolithographic process. The metallization of the substrates is done by depositing the metal and making the pattern with standard etching technique. Alternatively, the metallic pattern can be made first in photoresist using a lift-off process later on for the metallization. Using standard etching techniques, the accuracy of the pattern is around 100 nm or 600 nm, considering dry etching or wet etching, respectively. In the lift-off process, the accuracy is about 200 nm. The thickness of the metal is around 600 nm for the etching techniques and 2 μm for the lift-off process. Finally, in the case of multilayer quartz structures, the alignment accuracy can be up to 2 μm, while the bonding is done with some thermally activated photoresist technique.

1.4.4 Low-profile transmitarray antennas

The main drawback of TA antennas is the relatively large total volume occupancy. As discussed before, the focal distance is essential for achieving the maximum aperture efficiency. In the best case, the optimal ratio F/D is found between 0.5 – 0.75, assuming monofocal illumination [29], [49]. Therefore, if the transmitarray exhibits, for example, a diameter equal to 20 λ at a central frequency, then the corresponding focal distance is 10 – 15 λ. At 300 GHz, this distance is equal to only 1 – 1.5 cm. Nevertheless, to further reduce this size, while also providing an efficient design, we can modify the focal source or in general the parameters of illumination. Two general methods can be found in the literature. The first one is based on having a focal array and the second one is based on the folded TA architecture.

In the first approach, the focal source is replaced by multisource architectures ([28], [50], [51]) or an array of waveguide [52] and leaky-wave [53] feeds. Evidently, by increasing the number of sub-sources, the focal distance can be further decreased. This comes at the cost of an increased complexity and, by extension, increased fabrication accuracy and cost. As a rule of thumb, if the transmitarray aperture is divided into N sub-arrays, assuming N focal sources, the focal distance can be reduced by about $\sqrt{N}$ compared to the monofocal case.

As an example, a quad-feed based architecture proposed in [28] is shown in Figure 1.18(a). The focal array is composed of four identical elongated horns disposed in a 2 × 2 array configuration. The profile of the single element elongated horn has been optimized with a polynomial function in order to achieve a quasi-uniform illumination on the TA, minimize the spill-over and increase the transmitarray bandwidth. The final ratio F/D is equal to 0.28, which is about half compared to the single-feed focal system. The proposed antenna presents a measured maximum gain of 32.6 dBi with an aperture efficiency of 39.5%, while the corresponding 3 dB gain bandwidth is more than 10 GHz, covering almost all the region of interest.

Another example of the multisource approach is a phased-array-antenna-fed (PAA-fed) transmitarray, which was proposed in [50]. As shown in Figure 1.18(c), the phased-array can provide 1D beam scanning performances while reducing the total profile. Specifically, the proposed architecture features a ratio H/D equal to 0.375, encompassing 57.5%/44.6% peak simulated/measured aperture efficiencies in the broadside direction. The maximum measured gain drop is 3.71 dB up to ±30° and the beam crossover is about 2 dB.

Folded transmitarray antennas (FTAs) are an alternative to the multisource concept.

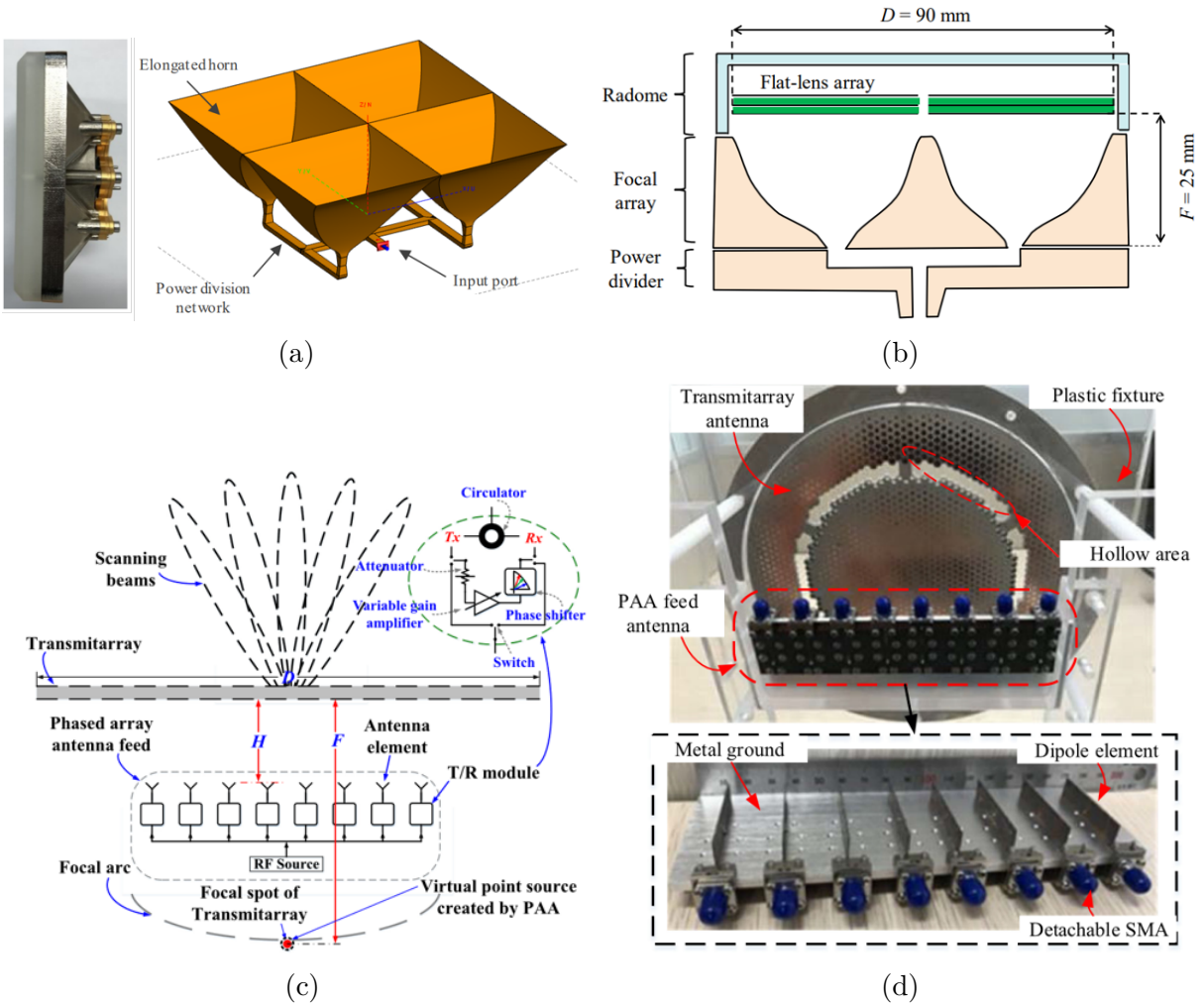

Figure 1.18: (a) Photograph of the quad-feed prototype reported in [28] with a schematic view of the focal array and (b) view of the proposed feed with the radome and the power division network. (c) Schematic view of the PAA-fed transmitarray reported in [50]. (d) Photograph of the PAA-fed prototype.

This approach is preferable when simple fabrication processes are used. Prerequisite for the proper operation is the use of anisotropic transmitarrays, combined with a simple reflector added on the level of the source, which will provide a polarization conversion [39], [54], as shown in Figure 1.19(c). Based on simple ray tracing, the final ratio F/D will be reduced by a factor of three, compared to the unfolded configuration. Thanks to the simple design concept, several prototypes with additional functionalities, such as dual-band [55], [56] or multibeam [57] operation, have been proposed recently.

Finally, some preliminary studies combining the folded and the multisource concepts have been recently presented. For example, in [58], a quadruple feed has been integrated

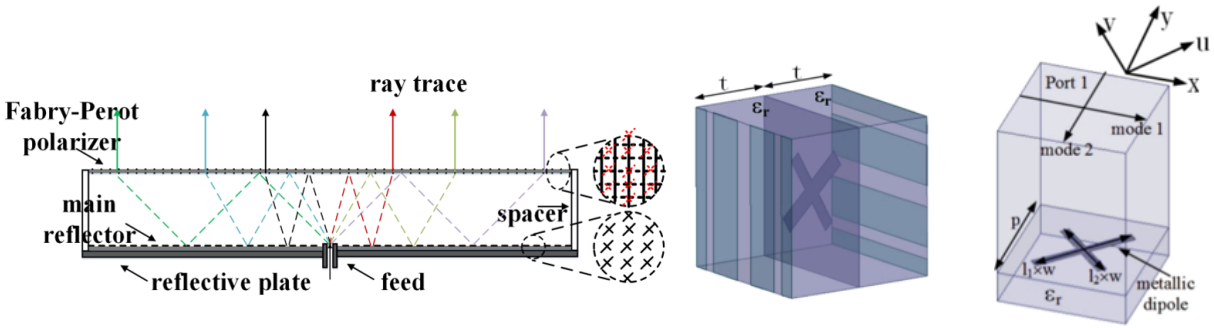

(a) (b) (c)

Figure 1.19: (a) Scheme of the folded transmitarray reported in [39]. The structure comprises (b) the ALP unit-cell, named here as Fabry-Perot polarizer, and (c) the reflector unit-cell.

in the reflector, allowing for the reduction of the antenna height by nearly six times, compared to the single-feed TA.

1.5 Comparison of the antenna technologies

As shown before, there are different ways to design a high-gain antenna system. However, selecting a convenient architecture that could provide good radiation performance at sub-THz frequencies is not a simple task.

Dielectric lenses remain the best choice for achieving high-gain, providing maximum aperture efficiency, up to $70 - 80\%$. Although it seems possible to use standard milling techniques for the lens, the choice of the material becomes crucial for the total losses and the fabrication process. Their weight and size become a minor issue at sub-THz frequencies, but they remain relatively bulky compared to all the other antenna architectures. In addition, the antenna system is not very agile in beam steering, which is very important for next-generation wireless applications. Therefore, they can be used for large range connections that require limited steering capability. However, if the range increases a lot, then an ultra-high gain is required, which means that a large lens must be fabricated, risking of making the system too bulky and heavy.

Replacing classical lenses with Fresnel lenses could provide a cost-efficient solution, reducing also the total mass and profile of the antenna. However, the corresponding aperture efficiency as well as the gain bandwidth are greatly reduced. Nevertheless, thanks to operating principle, these antennas can provide additional functionalities (e.g. dual band operation) compared to classical lenses.

Corporate-feed array antennas, based on waveguide array feed mechanism, are the best choice for achieving broadband gain, high aperture efficiency and ultra-low profile in the system. However, at sub-THz frequencies they depend significantly on the fabrication process, which to this day remains very expensive. As it was shown, the first prototype reported at 350 GHz in [23] demonstrated about 43% aperture efficiency with 14% relative 3 dB gain bandwidth. In [24], the same architecture using the same technology, i.e. SOI micromachining, was optimized to achieve 61% aperture efficiency and 25% relative 3 dB gain bandwidth. Moreover, the corporate beamforming network is the main contributor to the loss in the waveguide array antenna. This loss is the main limiting factor for the maximum gain that can be achieved with a corporate feed element array. In case of targeting at a higher gain, more elements are needed in the design. Therefore, the maximum theoretical gain might drop, leading to a low aperture efficiency.

The use of reflectarray and transmitarray antennas could be a suitable trade-off for providing a low-cost solution with good radiation performance and beam steering capability. For instance, the TA antenna reported in [29] achieves almost the same aperture efficiency and covers larger gain bandwidth compared to the expensive corporate-feed array antenna in [23]. This performance can be further increased, if a higher resolution technique is employed for the TA, as reported in [30]. Of course, the total profile of the TA antenna remains much larger than the corporate-feed array, but this size becomes a minor issue at sub-THz and it can be further reduced considering some of the low-profile techniques that were mentioned before. Similar conclusions are drawn for RA antennas. Nevertheless, TA antennas are a better candidate, as they avoid feed blockage and they can achieve the same radiation performance if using suitable wideband unit-cells with small reflection losses. The performance of all the aforementioned high-gain antennas are presented in Tables 1.1 and 1.2.

Table 1.1: Performance of existing high-gain sub-THz antenna technologies.

Reference	[15]	[19]	[22]	[24]
Center freq. (GHz)	180	275	260	350
Architecture	Dielectric lens	Fresnel lens	Quasi-optical (LW array)	Corporate-feed (WG array)
Technology	Standard milling	3-D printing	SOI micromachining	SOI micromachining
Aperture size (λ^2)	π (9 × 9)	π (9.6 × 9.6)	12.1 × 13.8	25.6 × 25.6
F/D	∼1	0.47	-	-
Gain (dBi)	34.0 @ 180 GHz	27.5 @ 235 GHz	28.0 @ 282 GHz	38 @ 390 GHz
Aperture eff.	>75.0%	21.0%	25.4%	61%
1 dB Gain bandwidth	-	-	-	-
3 dB Gain bandwidth	35.0%	21%	19%	25%
SLL (dB)	E-plane: -15.0 H-plane: -15.0	E-plane: -22.0 H-plane: -27.0	H-plane: -20.0	E-plane: -13.0 H-plane: -13.0

Table 1.2: Performance of existing sub-THz reflectarray and transmitarray antennas.

Reference	[21]	[29]	[30]	[31]
Center freq. (GHz)	390	145	140	100
Architecture	Reflectarray (Folded)	Transmitarray	Transmitarray	Transmitarray
Technology	Quartz lithography	PCB	LTCC	PCB
Aperture size (λ^2)	π (12.9 $\times$ 12.9)	20 $\times$ 20	18.7 $\times$ 18.7	8 $\times$ 6
F/D	1.07	0.75	1.87	0.8
Gain (dBi)	33.66 @ 400 GHz	33.0 @ 145 GHz	33.4 @ 140 GHz	24.5 @ 97.7 GHz
Aperture eff.	34.5%	38.3%	50.1%	46.1%
1 dB Gain bandwidth	-	11.7%	10.7%	-
3 dB Gain bandwidth	16.45%	19.8%	24.4%	15.0%
SLL (dB)	E-plane: -20.5 H-plane: 16.7	E-plane: -16.3 H-plane: -18.6	E-plane: -21.0 H-plane: -21.0	E-plane: -20.0 H-plane: -22.0

1.6 Reconfigurable arrays at high frequencies

Reconfigurable antenna systems can potentially provide increased channel capacity and reduced interference, leveraging on dynamic beamforming. Much of the recent effort has been focused on the realization of reconfigurable arrays. At lower frequencies, different designs have been proposed, realized by incorporating active components, such as PIN diodes, MEMs and varactor diodes in their unit-cell designs [49], [59]–[62]. At sub-THz frequencies, it is difficult to obtain packaged semiconductors, as the electrical size becomes very small and the parasitic effects remain a formidable challenge. Nevertheless, several methods have been investigated [63], focusing on the material used as tunable components and how to perform a dynamic control at each element.

One solution is using complementary metal–oxide–semiconductor (CMOS), which is scalable and it can provide individual control for each antenna element [64]. A CMOS wafer-scale phased-array with low system noise figure and high data rate was reported in D-band [65], shown in Figure 1.20. The 4×2 array is wire-bonded to a printed circuit board and is composed of IF beamforming receive channels with 5-bit phase and 4-bit gain control, wideband active and LC-based Wilkinson IF combiners, a digital step attenuator and amplifier for variable linearity, and a multiplier chain and distribution networks in the LO path. The final structure can scan efficiently up to ±35° in the elevation plane (E-plane), attaining a measured peak gain of 27.5 dBi, as shown in Figure 1.21(a). However, for each LO frequency the gain bandwidth is relatively narrow, due to material losses, mainly the metal (ohmic) loss, and the feed impedance transition network.

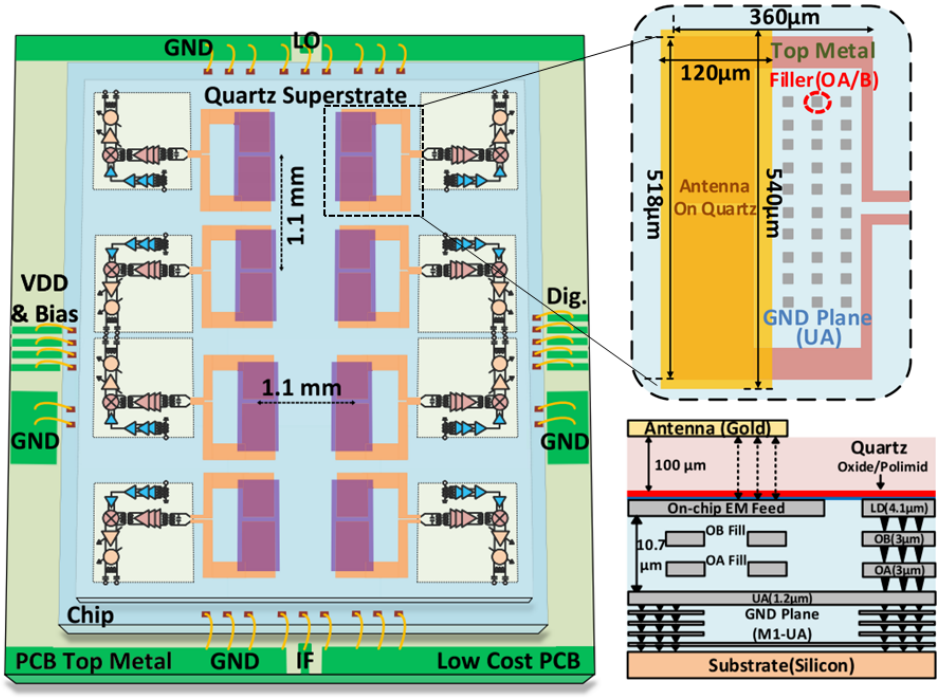

Figure 1.20: Block diagram of the 140 GHz phased-array reported in [65]. The patch antenna unit-cell is depicted on the top right and the stack-up of the structure is shown on the bottom right.

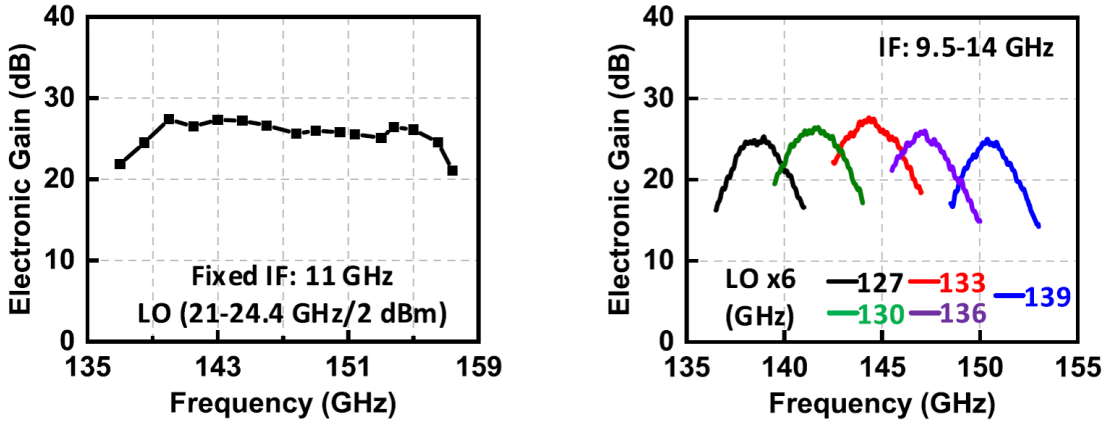

Figure 1.21: Measured gain of the array with (a) fixed IF frequency (11 GHz) and (b) different LO frequencies.

Another antenna based on CMOS technology was reported in [66]. This time, the antenna architecture is based on a metalens concept, conmprising a 2×2-chip structure

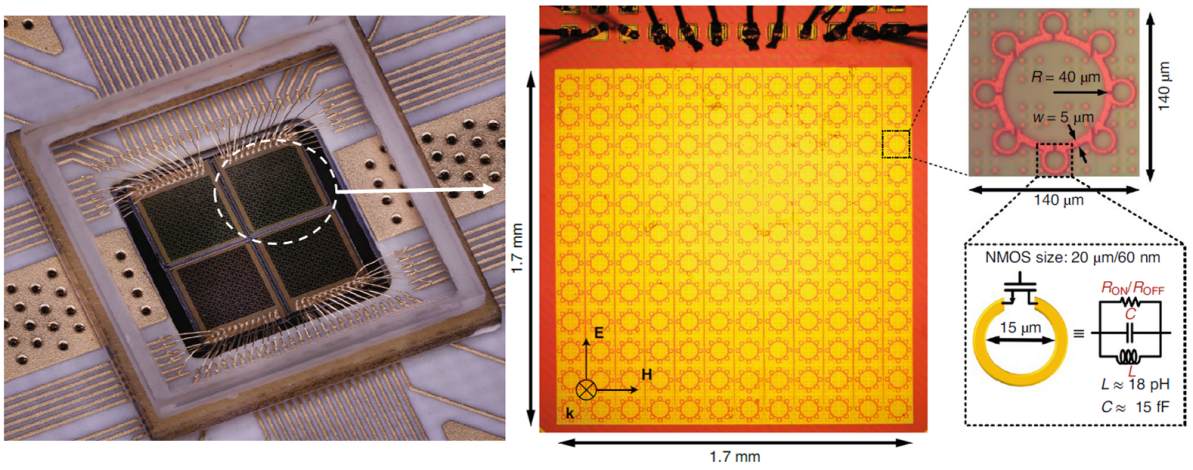

Figure 1.22: Views of the fabricated metalens, reported in [66], showing a single tile chip of meta-elements along with the zoomed-in portion of a single unit cell.

topology, as shown in Figure 1.22. Each chip tile consists of a 12×12 array of subwavelength active meta-elements spaced at $\lambda/7$ of the free-space wavelength. The active element is based on a rapid reconfiguration of a structure that can be programmed to assume various C-shaped split-ring resonator structures with integrated CMOS-based devices. The CMOS switch consists of an n-type metal–oxide–semiconductor (NMOS) transistor. When an incident wave impinges on the metalens, each C-shaped split-ring unit cell will support two symmetric and antisymmetric modes, which depend on the loop length and the CMOS state. Combining both amplitude and phase control, each meta-element can be reconfigured across 256 states (8 bits). Discounting the ones that produce identical amplitude and phase transformations due to symmetry, there remain 84 unique codes for each element. The simulated transmission-amplitude and phase-control map for the 84 states is shown in Figure 1.23, demonstrating amplitude control of -17 dB to -3.5 dB and phase control across 260° at 300 GHz.

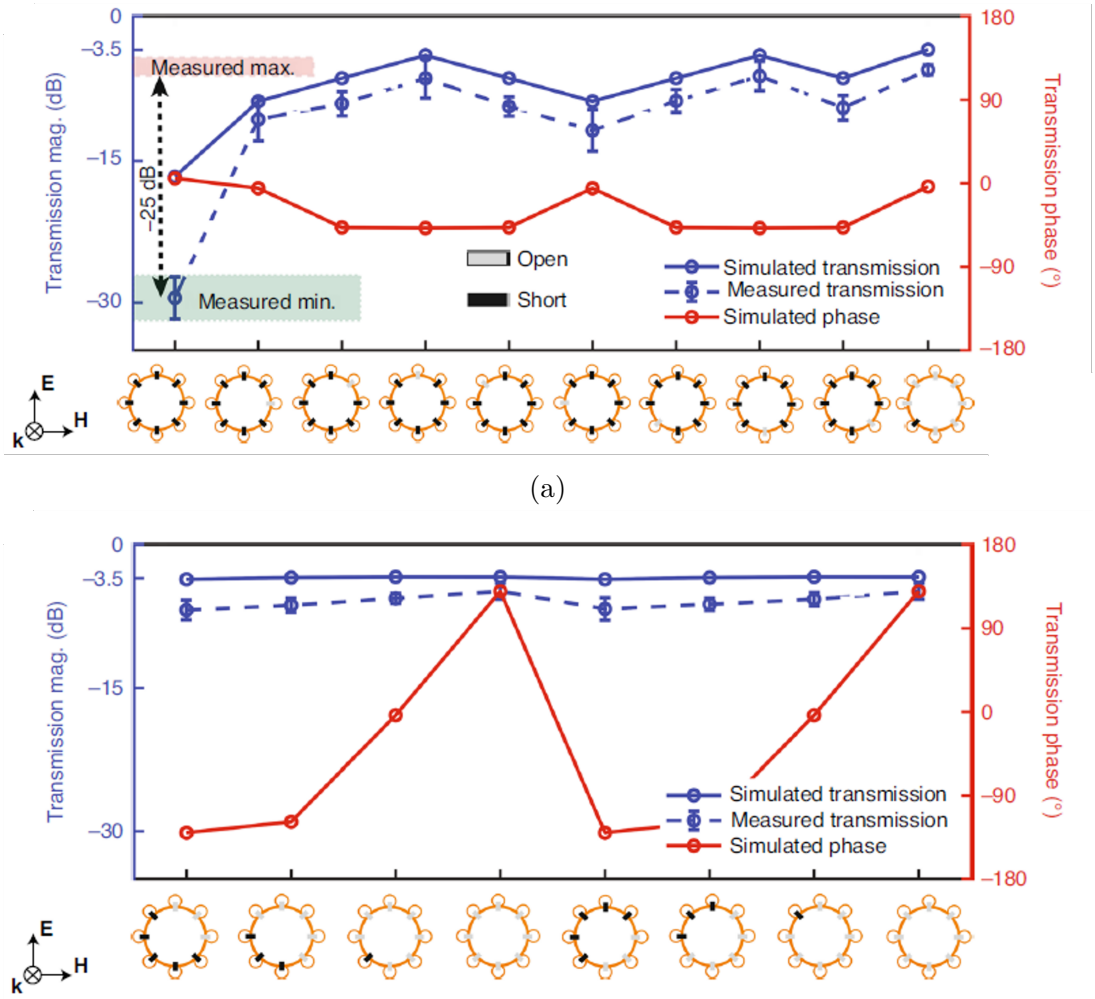

Figure 1.23: (a) Transmission amplitude and phase plot at 300 GHz when the C-shaped split-ring structure is rotated using a single open switch, as shown in the bottom row. (b) Transmission amplitude and phase plot at 300 GHz when the C-shaped split-ring structure is widened by opening multiple switches, as shown in the bottom row.

An alternative approach using phase change materials (PCMs) as a phase transition and achieve the beam-steering. These materials can introduce true reconfigurability as they undergo significant changes in optical properties upon exposure to external stimuli. Examples of PCMs are vanadium dioxide (VO_2) [67], [68] and germanium antimony telluride (GeSbTe) glasses [69], [70]. Figure 1.24 presents an electronically-controlled metasurface that can be placed at the output facet of any millimeter-wave/terahertz/far-infrared electromagnetic radiation source. It consists of a two-dimensional array of reso-

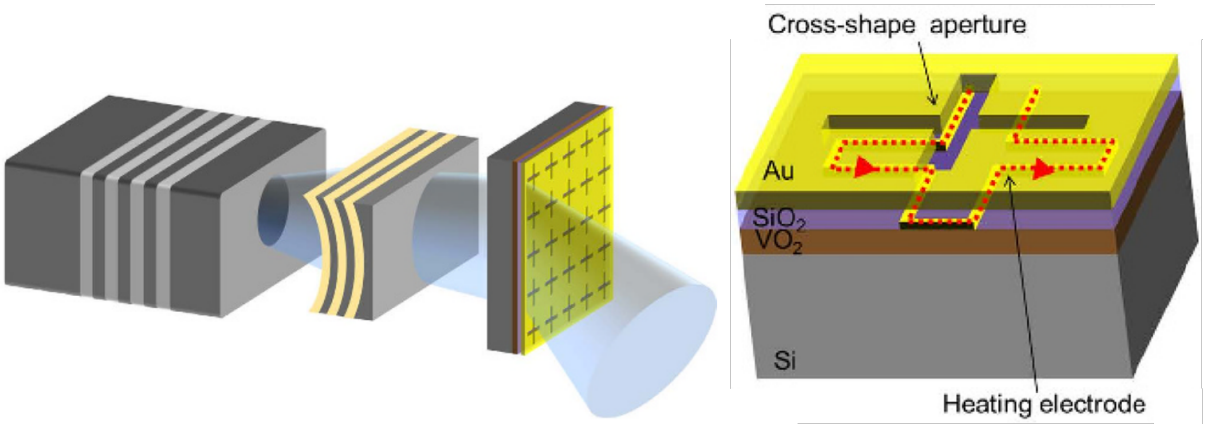

(a) (b)

Figure 1.24: (a) Beam-steering metasurface system using a vertical external cavity surface emitting laser, reported in [67] (b) Metasurface unit-cell comprising VO_2 for a PCM.

nant metasurface unit-cells fabricated on a substrate with electronically-tunable dielectric constant. By controlling the applied current to each individual metasurface unit-cell, its resonance frequency is adjusted and the phase of the transmitted electromagnetic wave through the unit-cell is controlled accordingly.

The method of using PCMs, despite being relatively simple, it lacks the capability of controlling individually each element, which has been the main problem addressed recently. Some preliminary studies on transmitarray [71] and reflectarray [72] architectures have been reported, proposing the integration of patterned GeTe as a PCM. Specifically, in [71], the authors used the AFA unit-cell design to implement theoretically an 1-bit reconfigurable transmitarray. The unit-cell, shown in Figure 1.25(a), comprises two blocks of GeTe on the transmission side. Based on that, a 16×16-element transmitarray was numerically synthesized, exhibiting a peak gain is of 22 dBi at 150 GHz and 1 dB gain bandwidth equal to 16% (24 GHz). Similarly, the work presented in [72] uses the patch geometry shown in Figure 1.25(b) to design a 25×25-element reflectarray, achieving a gain between 15 and 20 dBi for different scanning angles. In both cases, the results are promising, paving the way for future PCM-based and spatially fed architectures.

Finally, a recently proposed idea, which has been only theoretically investigated, was using graphene-based structures. Specifically, as reported in [73], by tuning the chemical potential of the graphene, the phase of the scattered wave, reflected in this scenario, is controlled.

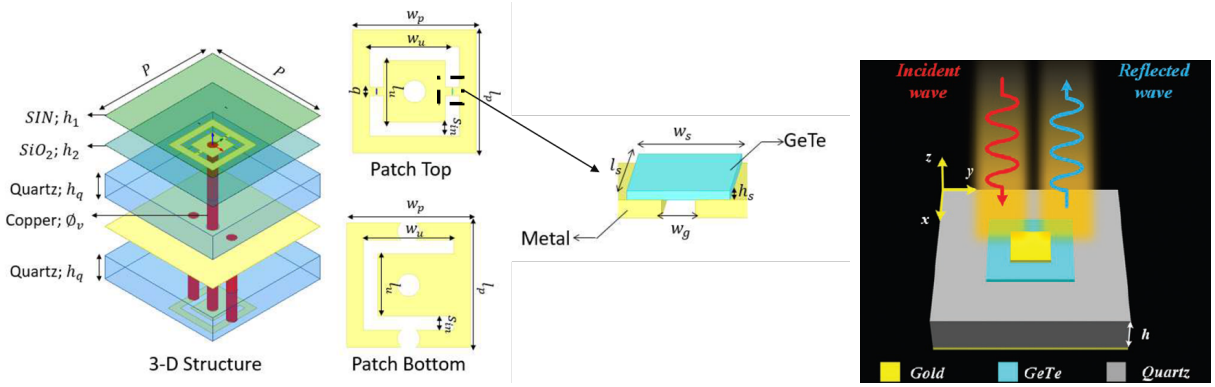

(a) (b)

Figure 1.25: Unit-cell topology integrating patterned GeTe used as a PCM for (a) a transmitarray [71] and (b) a reflectarray [72] design.

1.7 Conclusion

The realization of high-gain antennas at sub-THz frequencies has been already demonstrated through various proposed architectures. Therefore, at first glance, this task does not seem like an insurmountable obstacle. However, the choice of the fabrication process limits significantly the design approach, resulting in several compromises. Advanced antenna technologies, such as corporate-feed array antennas, cannot exist without resorting to expensive manufacturing.

Transmitarray antennas are suitable candidates for low-cost solutions at sub-THz. They already demonstrated good radiation performance, relying on standard planar processes. Despite their volume occupancy, the low-profile solutions at lower frequencies can pave the way for similar methodologies at higher frequencies. However, at 300 GHz, the radiation performance of the existing TA antennas remains somewhat poor.

It has been showed that the ALP unit-cell can attain ideal functionality for a TA design. Further studies on the ALP can potentially improve these results. Therefore, a more rigorous approach for the analysis and synthesis of this class of unit-cells will be reported here, with application to TAs at 300 GHz. Several prototypes will be fabricated, in order to validate the proposed study and stay in line with the objectives of the "NEXT5G" project. Different processes will be considered, in order to assess the antenna and fabrication performance at this frequency region.

Chapter 2

Modelling and design of transmitarray antennas

In this chapter, the theoretical modelling and design of the transmitarray antenna is presented. Two separate methods for the efficient description of the radiated field of transmitarrays are employed. The first method is based on ray tracing technique and classical antenna array theory, employing the far-field characteristics of the focal source and the unit-cells in the design. The second method is based on the application of the surface equivalence theorem, where the equivalent currents on the unit-cells are constructed under a physical optics approximation. To improve the accuracy, both methods employ a mix of analytical modelling and full-wave simulations, adopting specific assumptions and approximations. In both approaches, the objective is to provide a time-efficient solution, which is essential for the analysis and synthesis of electrically large transmitarrays.

2.1 Ray tracing approach

2.1.1 Model description

The following method has been successfully developed in previous works and its accuracy has been already confirmed at mmWave frequencies ([25], [29], [48], [49], [74]). A general scheme of the topology is shown in Figure 2.1. The feed is expressed by a focal point and some radiation pattern, while the transmitarray is modelled as an array of antenna elements. Each antenna element is described by a scattering matrix and two radiation patterns, one in reception and one in transmission.

For a given transmitarray, type of feed and focal distance F, the calculation of the radiated field begins with finding the incident wave on the transmitarray. This is determined

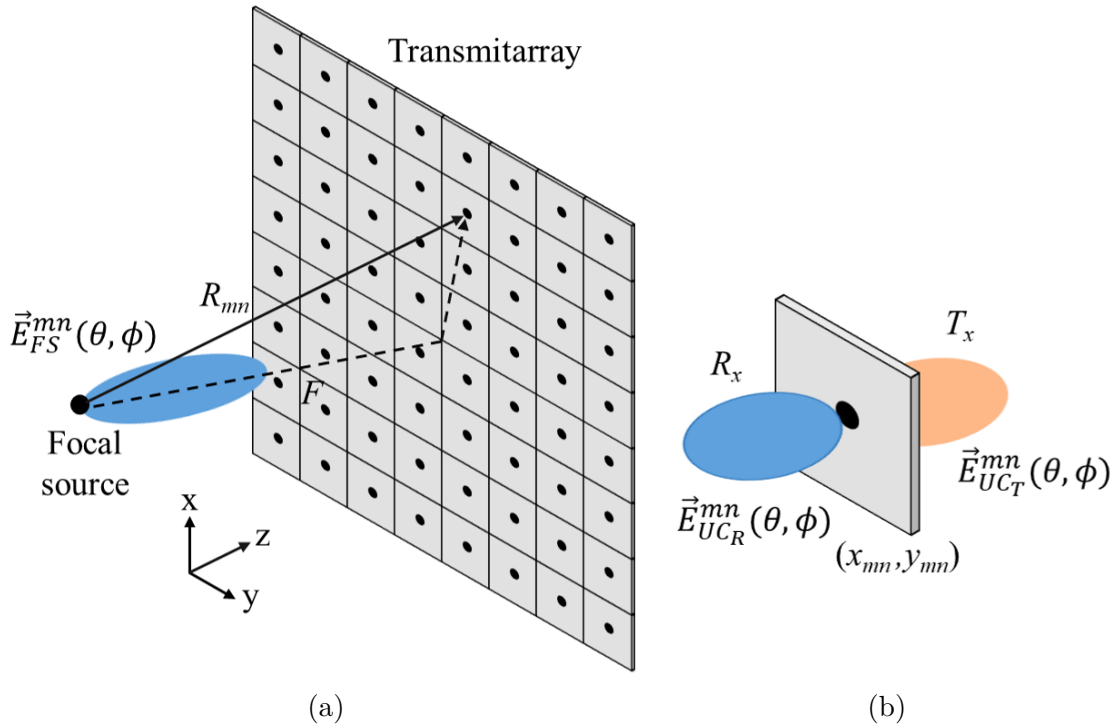

(a) (b)

Figure 2.1: (a) General scheme of the transmitarray antenna using ray tracing technique and (b) unit-cell topology, defined by its scattering matrix and two radiation patterns, one in reception and one in transmission.

by employing the Friis equation between the focal source and each unit-cell as follows

$$\overrightarrow{\alpha}_1^{mn} = \sqrt{P_0}\frac{\lambda}{4\pi R_{mn}} e^{-j\frac{2\pi R_{mn}}{\lambda}} [\overrightarrow{E}_{FS}(\theta,\phi)\cdot \overrightarrow{E}_{UC_R}^{mn}(\theta,\phi)]\,. \tag{2.1}$$

In expression (2.1), P_0 is the input power of the focal source and λ is the wavelength at the frequency of observation. The vectors $\overrightarrow{E}_{FS}(\theta,\phi)$ and $\overrightarrow{E}_{UC_R}^{mn}(\theta,\phi)$ express the far-field quantities of the focal source and the unit-cell in the reception side, respectively. In order to provide a collimating beam, each unit-cell should compensate the spatial phase delay between the source and the transmitarray. In that case, the corresponding phase is equal to

$$\Delta\phi_{sp} = \frac{2\pi R_{mn}}{\lambda} = \frac{2\pi}{\lambda}\sqrt{x_{mn}^2 + y_{mn}^2 + F^2}\,, \tag{2.2}$$

where the center of the reference system is defined on the source point, thus each unit-cell is located at (x_{mn}, y_{mn}, F). Moreover, in order to steer the beam at some angle (ϕ_0, θ_0) in far-field, an additional phase component must be considered. Based on classical antenna

array theory [75], the total phase compensation at each unit-cell will be

$$\psi_{mn} = \Delta\phi_{sp} - \frac{2\pi}{\lambda}(x_{mn}\sin\theta_0\cos\phi_0 + y_{mn}\sin\theta_0\sin\phi_0)\,, \tag{2.3}$$

The phase ψ_{mn} will be also the targeted value in the design process of the unit-cell topologies. Once the total phase distribution is calculated from (2.3), the transmitted wave at each corresponding unit-cell can be simply found as

$$\overrightarrow{\beta}_2^{mn} = S_{21}^{mn}\overrightarrow{\alpha}_1^{mn}\,, \tag{2.4}$$

where S_{21}^{mn} is the transmission coefficient of the employed unit-cell. In reality, only a finite number of unit-cell topologies can be found. This will lead to a forced quantization of the phase distribution, introducing a gain loss. Typically, to minimize that loss, at least eight different unit-cell topologies must be employed. This will result in a 3-bit phase resolution, where the phase difference between the neighboring states must be 45°. The 3-bit phase resolution will lead to less than 0.5 dB of quantization losses.

The power density radiated from the transmitarray at some distance r can be calculated as

$$S(\theta,\phi) = \frac{1}{4\pi r^2}\left|\sum_{m=1}^{M}\sum_{n=1}^{N}[\overrightarrow{\beta}_2^{mn}\overrightarrow{E}_{UC_T}^{mn}(\theta,\phi)]\right|^2\,. \tag{2.5}$$

Therefore, the directivity of the antenna will be equal to

$$D(\theta,\phi) = \frac{S(\theta,\phi)}{P_0/4\pi r^2}\,. \tag{2.6}$$

Finally, the realized gain of the transmitarray antenna can be found as

$$G(\theta,\phi) = \eta_{FS}\,\eta_{SP}\,D(\theta,\phi)\,, \tag{2.7}$$

where η_{FS} is the efficiency of the focal source and η_{SP} is the spillover efficiency. The first parameter is equal to

$$\eta_{FS} = \frac{P_1}{P_0}\,, \tag{2.8}$$

where P_1 is the power radiated from the source. The spillover efficiency will be equal to the ratio of the incident power P_2, collected from the transmitarray, to the power P_1

radiated from the source:

$$\eta_{SP} = \frac{P_2}{P_1}\,. \tag{2.9}$$

The collected power P_2 can be calculated from the following sum

$$P_2 = \sum_{m=1}^{M}\sum_{n=1}^{N} |\,\overrightarrow{\alpha}_1^{mn}|^2\,. \tag{2.10}$$

The total transmitted power is equal to

$$P_3 = \sum_{m=1}^{M}\sum_{n=1}^{N} |\,\overrightarrow{\beta}_2^{mn}|^2\,. \tag{2.11}$$

The difference between P_3 and P_2 represents the dissipation and reflection losses, also called insertion losses, introduced by the unit-cells. The corresponding efficiency is equal to

$$\eta_{IL} = \frac{P_3}{P_2}\,, \tag{2.12}$$

Therefore, the total efficiency of the transmitarray antenna can be found as

$$\eta_{tot} = \eta_{FS}\,\eta_{SP}\,\eta_{IL}\,. \tag{2.13}$$

If all four power quantities are known (P_0, P_1, P_2 and P_3), then a complete power budget estimation is carried out.

2.1.2 Focal Source

The focal source is expressed by a single point, related to the phase center of the feed. The source can be either a real structure or a theoretical one. In the case of a real structure, a 3D finite-element software can be used to calculate the radiation pattern. In this work, two standard gain pyramidal horn antennas, manufactured by Flann Microwave, were used: the Flann 32240-10 and the Flann 32240-20, with a nominal gain of 10 and 20 dBi, respectively. Both horns are mounted on a WR-3 rectangular waveguide and they operate at 220 – 330 GHz, presented later in Chapter 4. Their geometrical dimensions are listed in Table 2.1, based on the scheme of Figure 2.2.

Alternatively, a theoretical source with a cosine radiation can be used. In that case,

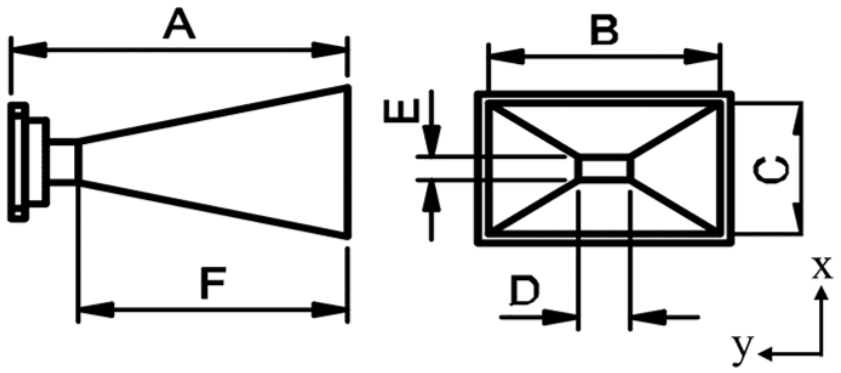

Figure 2.2: Geometry of the employed pyramidal horns from Flann Microwave.

Table 2.1: Geometrical dimensions of the employed pyramidal horn antennas.

Horn model	A	B	C	D	E	F
Flann 32240-10	7.00	1.31	0.95	0.864	0.432	2.00
Flann 32240-20	11.6	4.30	3.00	0.864	0.432	7.40

the radiation intensity is defined as [75]

$$U_{FS}(\theta,\phi) = \frac{n+1}{2\pi}\cos^n(\theta)\,, \tag{2.14}$$

where n is an index that controls the directivity and the beamwidth of the hypothetical source. This is a convenient approach to simplify the analysis and focus on the study of the transmitarray before deriving an actual feed for a focal source. Using the expression (2.14), the directivity can be found as

$$D_{FS}(\theta,\phi) = 4\pi\frac{U_{FS}(\theta,\phi)}{P_{rad}} = 2(n+1)\cos^n(\theta)\,, \tag{2.15}$$

The corresponding half-power beamwidth (HPBW) is equal to

$$\theta_{3-dB} = 2\arccos\left(\sqrt[n]{\frac{1}{2}}\right). \tag{2.16}$$

So, for instance, when $n = 4$, the maximum directivity is equal to 10 dBi and the HPBW is 65.5° and when $n = 49$ they are 20 dBi and $19.2^{/circ}$, respectively. Figure 2.3 shows the radiation pattern of the cosine source for different values of index n, along with the

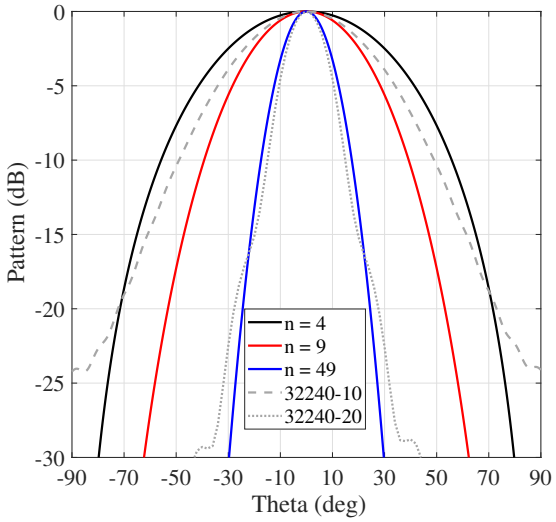

Figure 2.3: Radiation pattern of the theoretical cosine source for different values of index n, along with the two employed pyramidal horns in the E-plane.

pattern of the two employed horns.

2.1.3 Unit-cell

For a given unit-cell geometry, the scattering parameters and the far-field characteristics are calculated using Ansys HFSS. Each type of unit-cell is simulated under an infinite periodic condition, as shown in Figure 2.4. For the study of its scattering parameters, periodic boundaries with Floquet port excitation are used. For the far-field characteristics one of the two ports is replaced by a radiation boundary, to calculate the receiving or the transmitting case of the unit-cell.

As in the case of the theoretical source, the directivity of the unit-cell can be also calculated theoretically. Similar as in (2.15), the corresponding directivity will be

$$D_{UC}(\theta, \phi) = \frac{4\pi dxdy}{\lambda^2} \cos^q(\theta)\,, \tag{2.17}$$

where dx, dy are the unit-cell dimensions and q is an index, typically equal to 1. The expression (2.17) is accurate when the periodical size of the unit-cell remains relatively small, typically less than half wavelength.

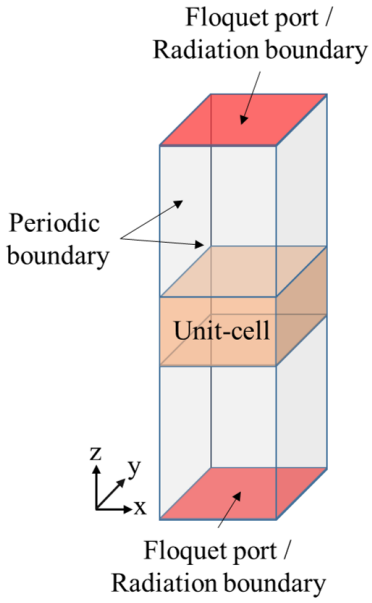

Figure 2.4: Full-wave simulation setup in HFSS, used to calculate the scattering parameters and the radiation patterns of the unit-cells.

2.2 Physical optics approach

2.2.1 Model description

This approach has been already tested for modelling the interaction of an incident electromagnetic field with electrically large objects, demonstrating accurate solutions for the analysis of metascreens [76], which is similar to the case of transmitarray antennas. The geometry of the problem is depicted in Figure 2.5. In this method, the focal source, referred to herein as focal aperture, exhibits a two-dimensional rectangular shape with some input field. Moreover, a spillover area around the transmitarray is defined, in order to take into account the radiated field coming from the source.

For a given field distribution of the focal aperture, the electric and magnetic surface current distributions, $\overrightarrow{J_s}$ and $\overrightarrow{M_s}$, can be found by applying the equivalence theorem [75]. In that case, the transmitted electric and magnetic fields, $\overrightarrow{E_t}$ and $\overrightarrow{H_t}$, at any point of the transmitarray and the spillover area can be constructed under a physical optics approximation, using the following radiation integrals

$$\overrightarrow{E}_t = \frac{jk}{4\pi} \iint \overline{\overline{S}}_{21}(\hat{R})[\frac{e^{-jkR}}{R}(-\overrightarrow{M_s} \times \hat{R} + \eta_0(\overrightarrow{J_s} \times \hat{R}) \times \hat{R})]dS' \,, \tag{2.18a}$$

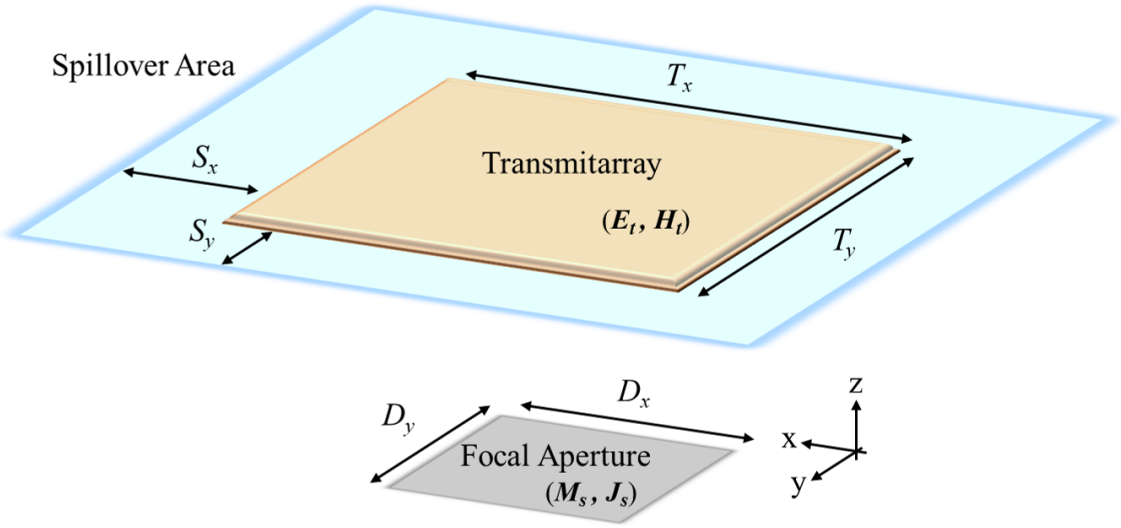

Figure 2.5: Geometry for the calculation of the transmitted field using physical optics.

$$\overrightarrow{H}_t = \frac{jk}{4\pi}\iint[\boldsymbol{n}\overline{\overline{S}}_{21}(\hat{R})\boldsymbol{n}^{-1}][\frac{e^{-jkR}}{R}(\overrightarrow{J_s}\times\hat{R}+\frac{1}{\eta_0}(\overrightarrow{M_s}\times\hat{R})\times\hat{R})]dS' \,. \tag{2.18b}$$

In (2.18), the vector $\hat{R}$ is between the point of observation on the level of transmitarray and each point on the focal aperture. The parameter $\overline{\overline{S}}_{21}$ is the 2×2 transmission coefficient matrix at each point. In the spillover area, the transmission coefficient is equal to the unitary matrix. Finally, the parameter $\boldsymbol{n}$ is the 90° rotation matrix. The derivation of the expressions (2.18) is reported with more details in Appendix A.

As in the previous method, to calculate the phase compensation, the incident wave on the transmitarray must be first found. This is done using the expressions in (2.18), ignoring the scattering matrix. After that, the phase distribution is calculated based on the phase of the incident wave and the steering angle. For instance, if the transmitarray is designed to operate an incoming x-polarized wave, then the phase compensation will be equal to

$$\psi_{mn} = -\angle E_x^{inc} - \frac{2\pi}{\lambda}(x_{mn}\sin\theta_0\cos\phi_0 + y_{mn}\sin\theta_0\sin\phi_0) \,. \tag{2.19}$$

Once the field components of $\overrightarrow{E_t}$ and $\overrightarrow{H_t}$ are known, the radiated field can be calculated using again the equivalence theorem. After certain approximations, the two field

components E_θ and E_ϕ are found, as presented in Appendix A. Then, the gain and the directivity of the transmitarray are calculated as

$$G_\phi = \frac{4\pi|E_\phi|^2}{2\eta_0}\,,\ G_\theta = \frac{4\pi|E_\theta|^2}{2\eta_0}\,, \tag{2.20a}$$

$$D_\phi = \frac{4\pi|E_\phi|^2}{2\eta_0 P_t}\,,\ D_\theta = \frac{4\pi|E_\theta|^2}{2\eta_0 P_t}\,, \tag{2.20b}$$

respectively. In (2.20), the input power P_0 is assumed to be equal to 1 W. The power P_t is the power transmitted from the aperture of the transmitarray and it is equal to

$$P_t = \frac{1}{2}\Re\left\{\iint(\overrightarrow{E}_t^{TA} \times \overrightarrow{H}_t^{TA^*}) \cdot \hat{\boldsymbol{z}} dS\right\} \tag{2.21}$$

To define the complete power budget of the system, the spillover efficiency must be also found. This parameter is calculated as

$$\eta_{SP} = \frac{P_{inc}}{P_0}\,, \tag{2.22}$$

where P_{inc} is the incoming power on the aperture of the transmitarray. The value of P_{inc} can be found using the expression (2.21), where the corresponding field is calculated as in (2.18), ignoring the transmission coefficient.

2.2.2 Focal Aperture

The source can be simulated with a 3D finite-element software. In this method, the Cartesian field components must be exported. A finite plane must be selected in simulation, which should include all the radiated power, in order to satisfy the power conservation and avoid errors in the calculation of the gain. As in the case of the ray tracing technique, to simplify the study, a theoretical field distribution can be assigned first. Three different types of field distribution were considered; a uniform distribution, an open-end waveguide distribution and a pyramidal horn distribution.

For a uniform field distribution, the field components are defined as

$$\overrightarrow{E}_{FA} = A_0\hat{x}\,, \tag{2.23a}$$

$$\overrightarrow{H}_{FA} = \frac{1}{\eta_0}\hat{z} \times \overrightarrow{E}_A \,, \tag{2.23b}$$

assuming that the input field is linearly polarized along x-axis. In case of normalizing the input power to 1 W, the value of A_0 can be calculated from (2.21) on the focal aperture, which will be found as

$$A_0 = \sqrt{\frac{2\eta}{D_x D_y}} \,, \tag{2.24}$$

where η is the wave impedance of the selected medium and the D_x and D_y are the aperture dimensions, as shown in Figure 2.5.

In the case of an open-end rectangular waveguide, the profile of the field can be found from classical waveguide mode theory [77]. For instance, if only the first mode exists, i.e. TE_{10}, then the field components are

$$E_x = 0 \,, \tag{2.25a}$$

$$E_y = \frac{-j\omega\mu\pi}{k_c^2 D_x} A_{10} \sin\frac{\pi x}{D_x} \,, \tag{2.25b}$$

$$E_z = 0 \,, \tag{2.25c}$$

$$H_x = \frac{j\beta\pi}{k_c^2 D_x} A_{10} \sin\frac{\pi x}{D_x} \,, \tag{2.25d}$$

$$H_y = 0 \,, \tag{2.25e}$$

$$H_z = A_{10} \cos\frac{\pi x}{D_x} \,, \tag{2.25f}$$

where D_x and D_y are now the waveguide dimensions, assuming that $D_x > D_y$. In (2.25), the parameter k_c is the cutoff wave number and β is the propagation constant. To normalize the power as in the previous case, using (2.21) the constant A_{10} is found as

$$A_{10} = \frac{2k_c^2}{\pi}\sqrt{\frac{D_x}{D_y \omega\mu\Re(\beta)}} \,. \tag{2.26}$$

Finally, the fields on the aperture of a pyramidal horn are derived by treating the

horn as a radial waveguide. In that case, assuming that the horn is x-polarized, the field is equal to

$$\overrightarrow{E}_A = E_0 \sin\left(\frac{\pi x}{B}\right) exp\left[-\frac{jk}{2}\left(\frac{x^2}{\rho_E} + \frac{y^2}{\rho_H}\right)\right]\hat{x}\,, \tag{2.27a}$$

$$\overrightarrow{H}_A = \frac{1}{\eta_0}\hat{z} \times \overrightarrow{E}_A\,. \tag{2.27b}$$

The parameters ρ_E and ρ_H are the radial distances from the apex to a point on the horn aperture in the E- and H-plane, respectively. Their values can be found using the geometrical dimensions of Figure 2.2 from the following expressions

$$\rho_H = \frac{B\,F}{B - D}\,, \tag{2.28a}$$

$$\rho_E = \frac{C\,F}{C - E}\,. \tag{2.28b}$$

As in the other cases, the value of E_0 must be equal to

$$E_0 = 2\sqrt{\frac{\eta}{B\,C}}\,. \tag{2.29}$$

in order to normalize the power to 1 W. As an example, the field distribution of the Flann 32240-10 horn, calculated from expressions (2.28), is plotted in Figure 2.6.

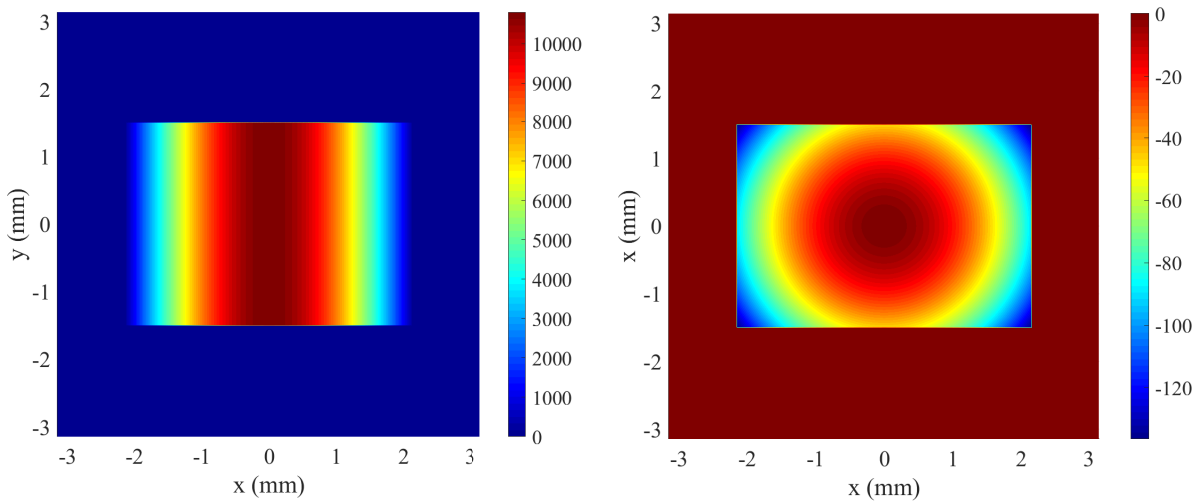

Figure 2.6: Field distribution of horn Flann 32240-10, calculated numerically using expressions (2.28).

2.2.3 Unit-cell

For a given unit-cell geometry, its scattering parameters are calculated using the same full-wave simulation setup as in the previous method, which was discussed in 2.1.3. Normally, the transmission coefficient at each unit-cell changes based on the angle of the incident wave, as expressed in (2.18). Nevertheless, only the nominal case for $\theta = 0°$ was considered in this study, provided that the unit-cell exhibits a relatively small periodical size. This assumption is expected to cause a small discrepancy on the gain level between the theoretical and the realized transmitarray.

2.3 Numerical results and comparison

When a source with a small aperture is placed relatively far away from the transmitarray, both approaches should provide the same results of radiation. On the other hand, when both the focal aperture and the transmitarray are large in size and they are placed in close proximity, then the results should change. To demonstrate that, two theoretical examples are considered. In both cases, the transmitarray is assumed ideal, i.e. a reflectionless lens with perfect phase compensation. The results of some realized transmitarrays will be shown in the other chapters. The size of the unit-cell is set to half wavelength at a central frequency, f_0. A 40×40-element transmitarray (20×20 λ^2) is designed.

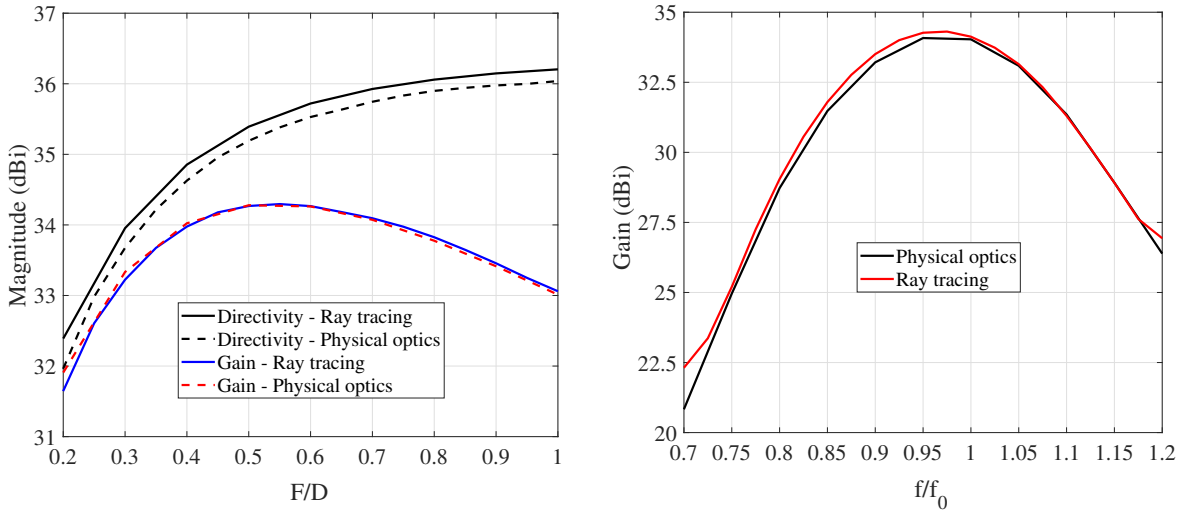

(a) (b)

Figure 2.7: Comparison of the peak gain as a function of (a) the focal distance at f_0 and (b) the frequency when $F/D = 0.55$ between the ray tracing and the physical optics approach, using the 10 dBi Flann horn as a focal source.

In the first example, the transmitarray is illuminated by the 10 dBi gain Flann horn. The aperture of the horn is 1.31×0.95 mm^2, or 1.31×0.95 λ^2 at 300 GHz, which is set as the central frequency. Using the two techniques, a focal and frequency parametric analysis is carried out. The results are shown in Figure 2.7. An almost perfect agreement is observed, where both methods show a peak gain of about 34.2 dBi when $F/D = 0.55$, while the frequency response is the same. For this value F/D the amplitude and phase of the x components of the field are depicted in Figure 2.8. Each pixel represents one unit-cell.

The radiation pattern in the H- and E-plane are shown in Figure 2.9. A perfect agreement between in the position of the nulls and the side lobes is observed. A small discrepancy in the sidelobe level was found, caused by numerical errors in the code. This difference is less than 0.5 dB in the first sidelobe level, thus it can be considered negligible. In Figures 2.9(a) and (b) the spillover area calculated with physical optics was ignored for a better comparison, since it is not modelled in the ray tracing technique. The impact of the spillover radiation is shown in Figure 2.9(c). Finally, the agreement between the two methods also holds when the transmitarray is synthesized to steer the beam at a certain angle. Figure 2.10 shows the synthesized radiation pattern in one plane for four different steering angles. Figure 2.11 shows the corresponding phase distribution for these cases.

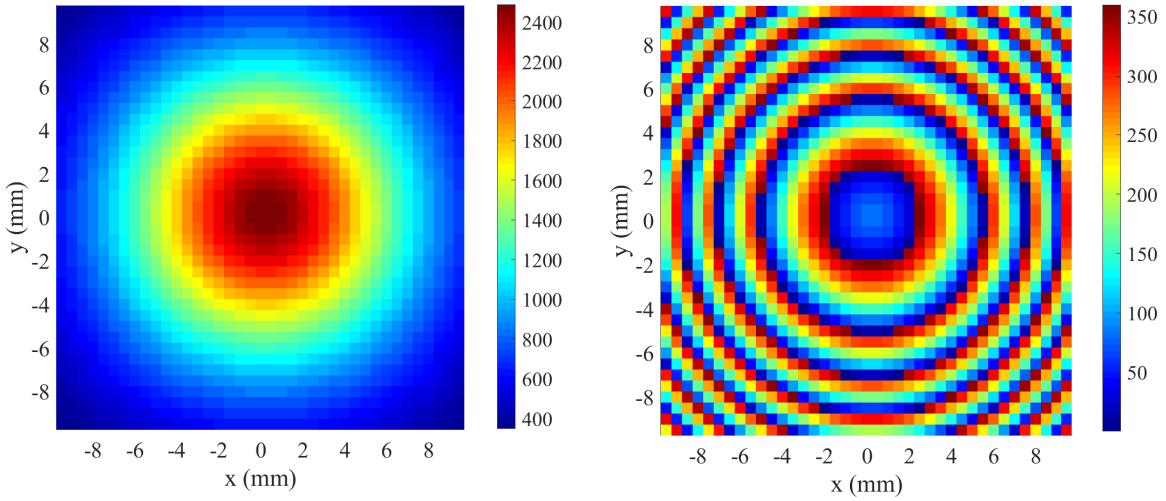

Figure 2.8: (a) Amplitude and (b) phase of x component of the incident field on the transmitarray.

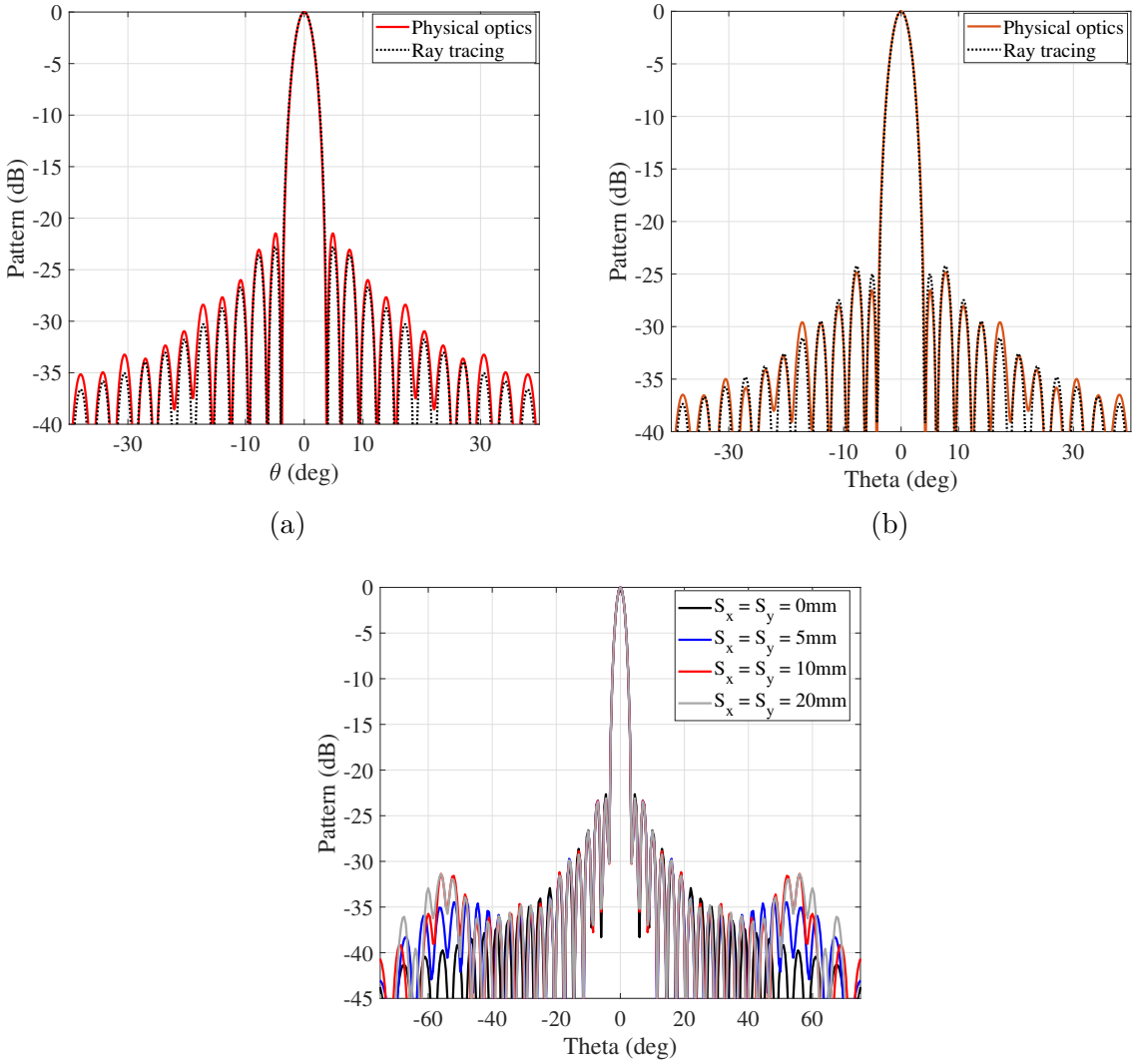

Figure 2.9: Radiation pattern of transmitarray calculated in the (a) H- and (b) E-plane using the two discussed techniques, at the central frequency. (c) Impact of the spillover radiation calculated through the second method.

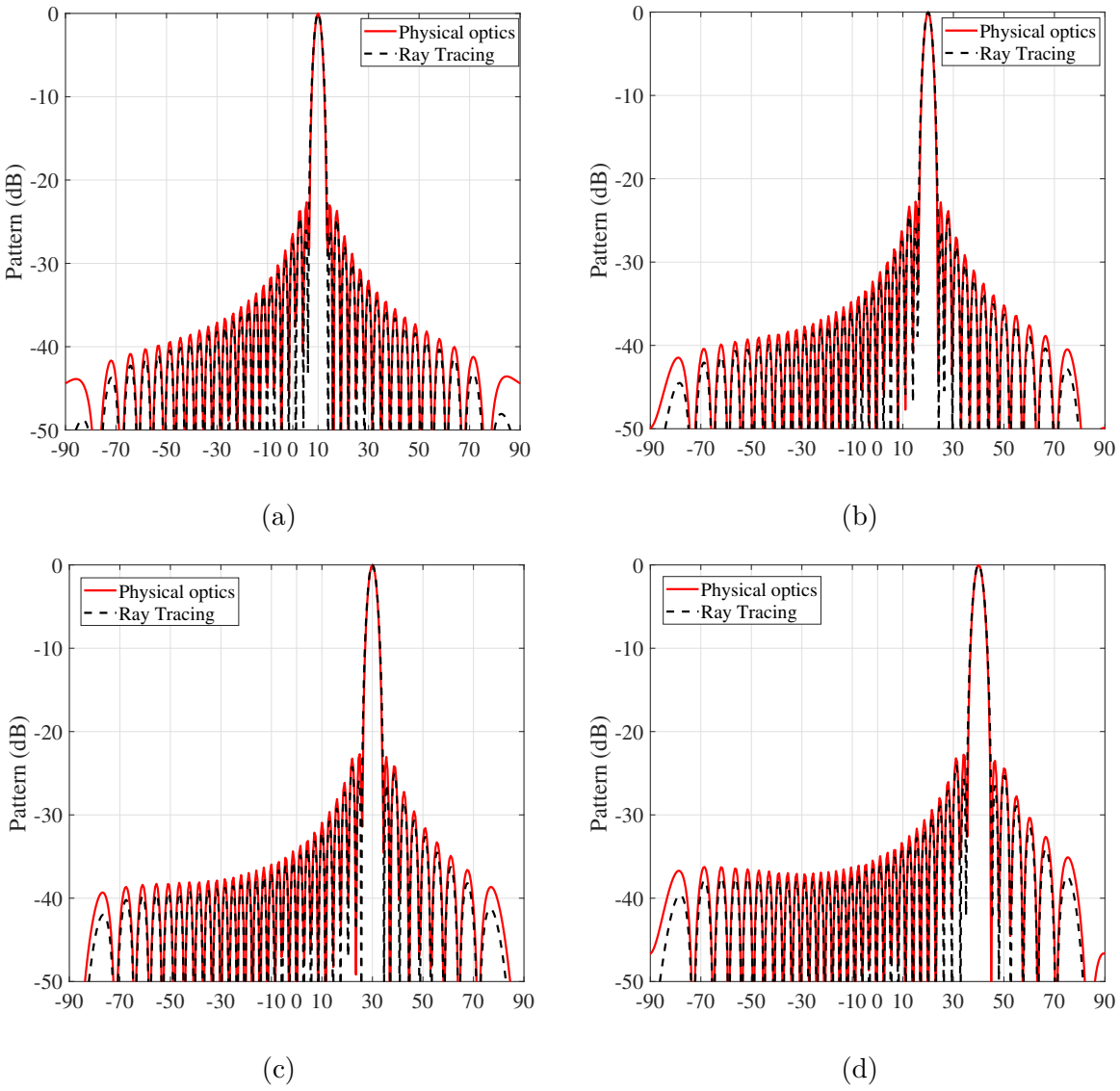

Figure 2.10: Radiation pattern of a theoretical transmitarray calculated using the two discussed techniques for (a) $\theta_0 = 10°$, (b) $\theta_0 = 20°$,(c) $\theta_0 = 30°$ and (d) $\theta_0 = 40°$, while $\phi_0 = 0°$ in all cases.

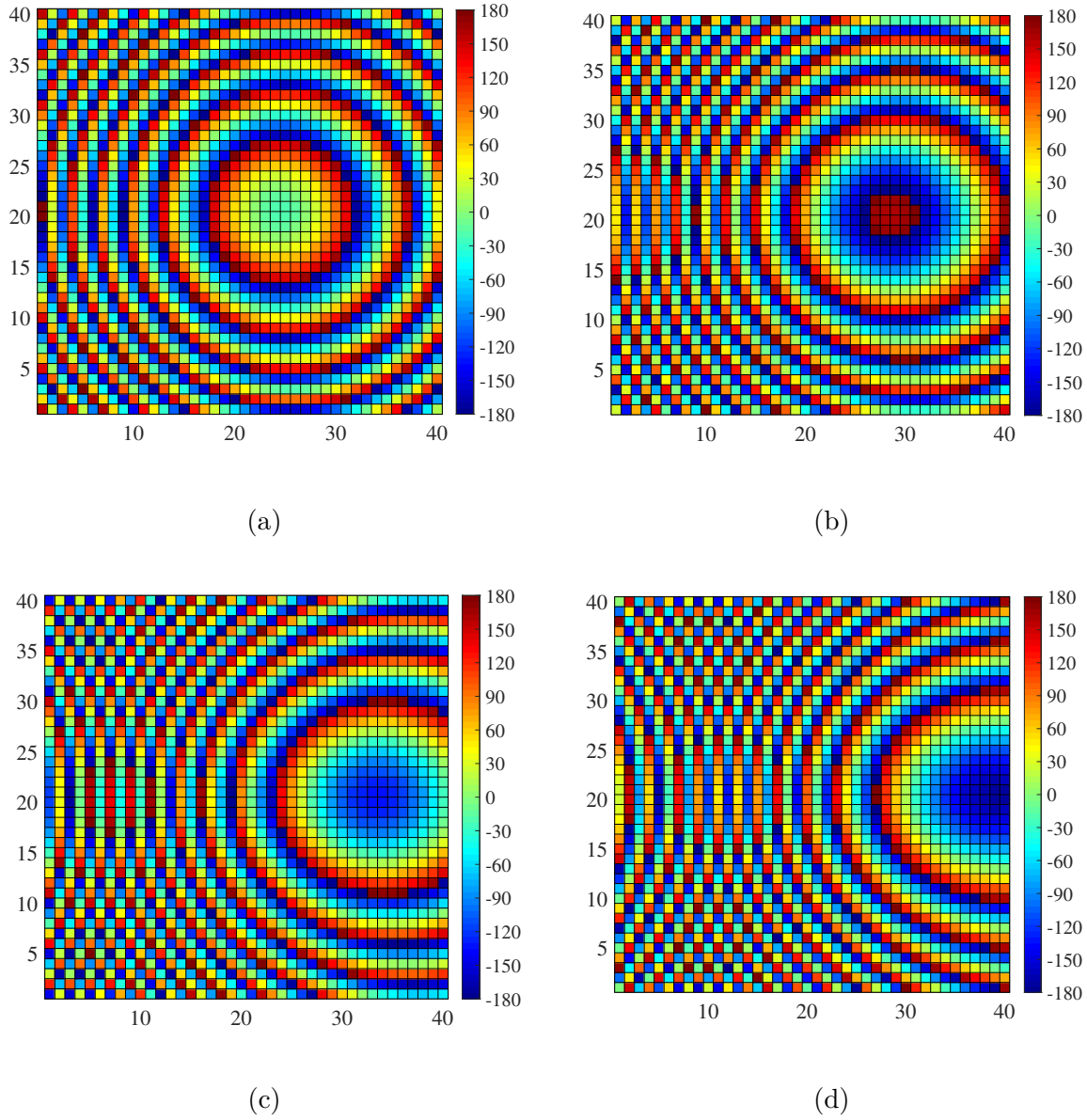

Figure 2.11: Corresponding phase distribution of the transmitarray for the steering angles depicted in Figure 2.10. (a) $\theta_0 = 10°$, (b) $\theta_0 = 20°$,(c) $\theta_0 = 30°$ and (d) $\theta_0 = 40°$, while $\phi_0 = 0°$ in all cases.

In the second example, the transmitarray is illuminated by a theoretical focal aperture of size equal to 10×10 λ^2 at f_0. A uniform field distribution is considered. Due to its large size, the focal aperture exhibits also high directivity, which is about 30 dBi in far-field, with a HPBW less than 4°. Its far-field radiation pattern is used in the ray tracing approach. The results of the focal parametric analysis are shown in Figure 2.12. It can be seen that the solution for achieving maximum gain is the same, when F/D is close to 6, giving a peak of 35 dBi. It is obvious that once the focal distance increases, the results coincide, which is related to the far-field conditions, satisfied in both methods. However, when the focal distance is kept comparable to the transmitarray size ($F/D<2$), a large difference in the peak gain performance is observed. For example, if the F/D is set to 1 ($F = 20\lambda$) the realized gain will be approximately 33 dBi, calculated with physical optics, showing a 3 dB increase compared to the focal aperture. On the other hand, the corresponding value will be about 26 dBi using ray tracing technique, which is not correct. The impact is highlighted through the aperture efficiency of the system, shown in Figure 2.12(b), which is 40% and 5.5%, respectively, calculated with the two methods. Therefore, although the solution for maximum achievable gain is the same, only the physical optics approach can be used in case a low-profile configuration is targeted, considering a relatively large focal aperture. Finally, Figure 2.13 depicts the amplitude and phase of the incident wave, calculated using the two approaches for $F/D = 1$. It can be seen that the physical optics approach takes into account the physical dimensions of the focal source, providing more accurate solutions if the source is placed in close proximity. Nevertheless, this method does not take into account mutual reflections between the source and the transmitarray. Therefore, it is important for the unit-cells to exhibit relatively small reflection losses and for the focal aperture to be well matched, in order to avoid mutual reflections in the real design.

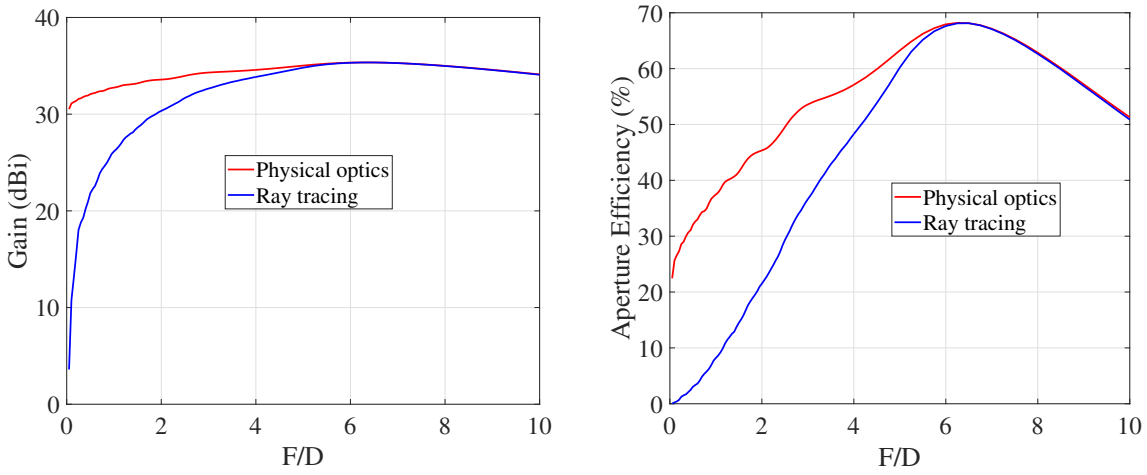

(a) (b)

Figure 2.12: Comparison of the gain (a) and the aperture efficiency (b) as a function of the focal distance, between the ray tracing and the physical optics approach. The transmitarray has a size of 20 $\times$ 20 λ^2 and it is illuminated by a square-shaped focal aperture with size of 10 $\times$ 10 λ^2.

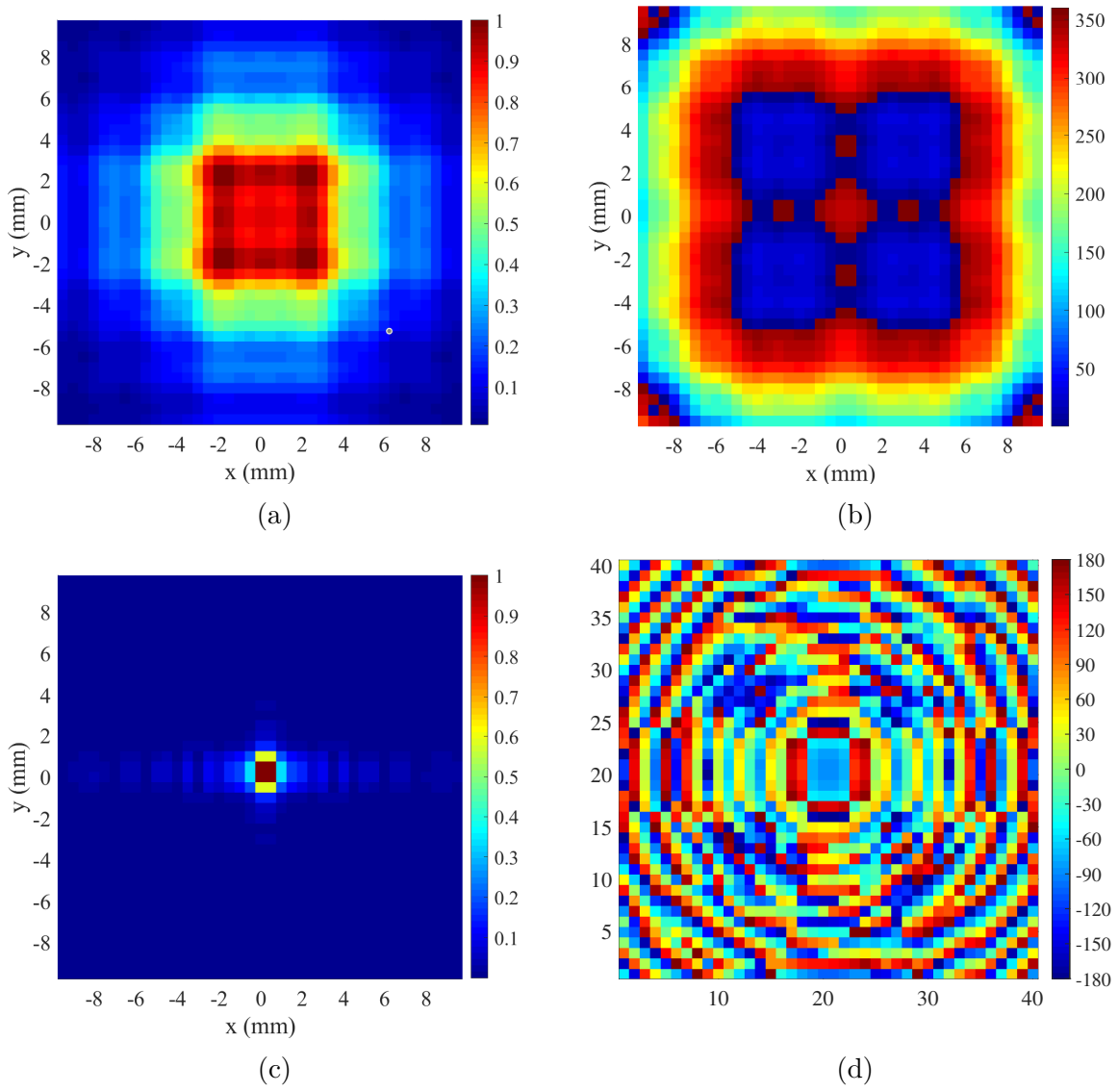

Figure 2.13: (a) Normalized amplitude and (b) phase (deg) of x component of the incident field on the transmitarray using the physical optics technique. (c) Normalized amplitude and (d) phase (deg) of the incident field on the 40×40-elements transmitarray using the ray tracing technique. In both cases the selected F/D is equal to 1.

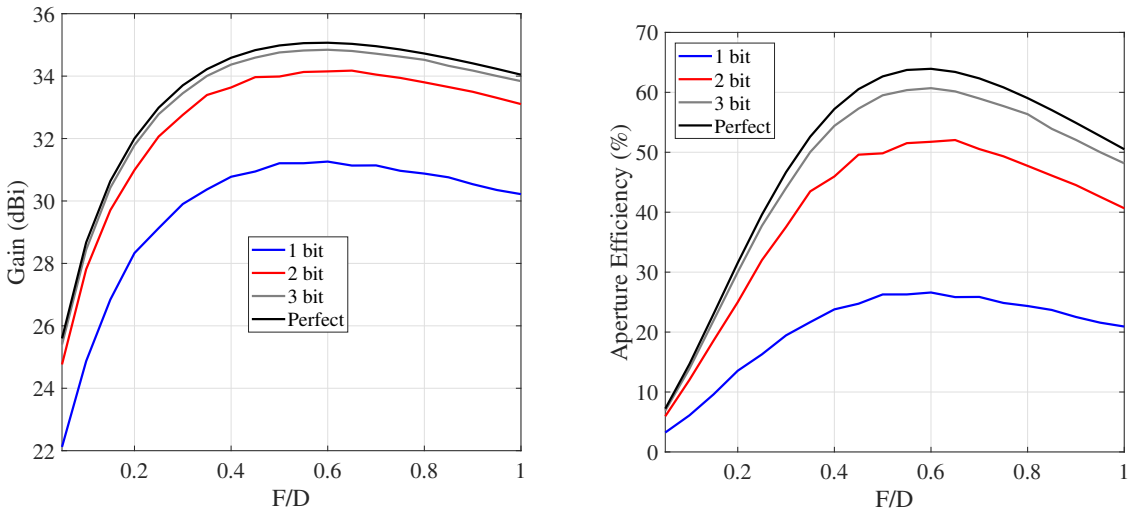

Figure 2.14: (a) Peak gain and (b) aperture efficiency as a function of the focal distance for different cases of phase quantization.

Finally, an important study is to define the problem of phase quantization. In order to ensure that the final design will not exhibit large quantization losses, the transmitarray is examined for different cases of phase resolution. Figure 2.14 shows the results of the simulated peak gain as a function of the focal distance for a 40×40-element transmitarray illuminated by a 10 dBi focal source. In all cases, the unit-cells are considered reflectionless, exhibiting half-wavelength periodical size at the frequency of interest. It can be seen that with a 3-bit phase quantization the quantization losses are kept less than 0.3 dB. Therefore, this will be the minimum targeted resolution for the transmitarray design, as will be presented in the other chapters.

2.4 Conclusion

The theoretical study and modelling of the transmitarray antenna using two separate numerical methods was presented. Both approaches allow for an accurate and time-efficient description of the radiated field, which is essential for electrically large transmitarrays. The ray tracing technique requires very short simulation time with accurate solutions, provided that the focal source exhibits a relatively small size and it is located far enough from the transmitarray, satisfying far-field approximations. The physical optics technique can be more accurate for low-profile designs, taking into account the physical size of both

the source and the transmitarray. This technique also allows for a more accurate representation of the radiation pattern, introducing a spillover area around the transmitarray.

Chapter 3

Modelling and design of anisotropic linear polarizers

3.1 Introduction

As shown in Chapter 1, the key to achieving high performance in transmitarrays (TAs) is the selection of convenient unit-cell designs and the capability to rigorously control and tune their electromagnetic properties. Anisotropic TAs can offer enhanced performance and attractive functionalities, but their design is generally more complicated. Nevertheless, asymmetric linear polarizers (ALPs) have been one of the most commonly employed anisotropic structures, thanks to their high transmissivity over a wide bandwidth and the simple control of their properties using only three metal layers. Despite the increasing number of ALP-based TAs, no theoretical approaches for the analysis and synthesis of their elements have been investigated. Therefore, at sub-THz frequencies their design targeting for maximum performance becomes challenging, especially when it comes to PCB process for their manufacturing.

In this Chapter, a rigorous model based on cascaded sheet admittances to analyze and synthesize the ALP class is presented, with application to TA antennas. The theoretical model and the design methodology are augmented by the use of a circuit model that takes into account the anisotropic properties. A more general analysis of the unit-cell and a quantitative procedure to design it for maximum transmission and phase coverage are thoroughly described.

3.2 Circuit model

A general view of the ALP unit-cell is shown in Fig. 3.1. The structure is periodic in the xy-plane and it comprises three metallic layers. The outer layers are two orthogonal polarization grids, which are assumed identical. The inner layer is an anisotropic sheet that

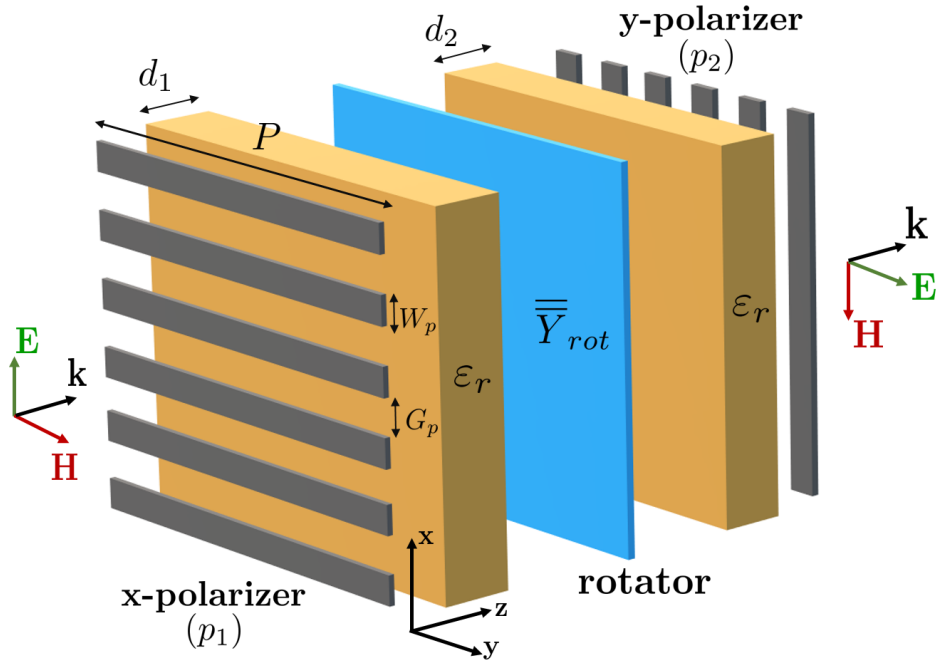

Figure 3.1: Exploded view of the ALP unit-cell with P periodicity, which is the same along the x- and y-axis. The rotator (blue color) is generically modelled as a two-dimensional sheet impedance described by a 2×2 admittance matrix. The polarization grids (grey color) are orthogonally oriented. The layers are interleaved by two dielectric spacers (orange color) of the same permittivity, ε_r.

modifies the polarization of a wave impinging on the unit-cell. Two dielectric spacers of permittivity ε_r and thicknesses d_1 and d_2 interleave the layers. For simplicity, all materials (dielectric, conductor) are considered lossless, homogeneous, isotropic and non-dispersive. The unit-cell is illuminated in either side by a plane wave, x- or y-polarized, propagating along the z-axis. As presented in Fig. 3.1, the structure rotates by 90° the polarization of the incident wave.

The complete scattering phenomenon is modelled by the circuit of Figure 3.2, assuming normal incidence. It is based on the transfer-matrix method (TMM) for cascaded sheets that are expressed by some effective admittance parameters [78]. The employment of a four-port network is necessary in order to take into account the mode coupling induced by the rotator. The spacers are modelled as transmission lines, and for normal incidence the characteristic impedance will be the same for each polarization. Therefore, they are $Z^x_{\varepsilon_r} = Z^y_{\varepsilon_r} = \eta_0/\sqrt{\varepsilon_r}$, where η_0 is the free space impedance, and all the ports have the same generator impedance $Z^x_0 = Z^y_0 = Z_0$. For simplicity, the medium surrounding the unit-cell is assumed to be vacuum ($Z_0 = \eta_0$).

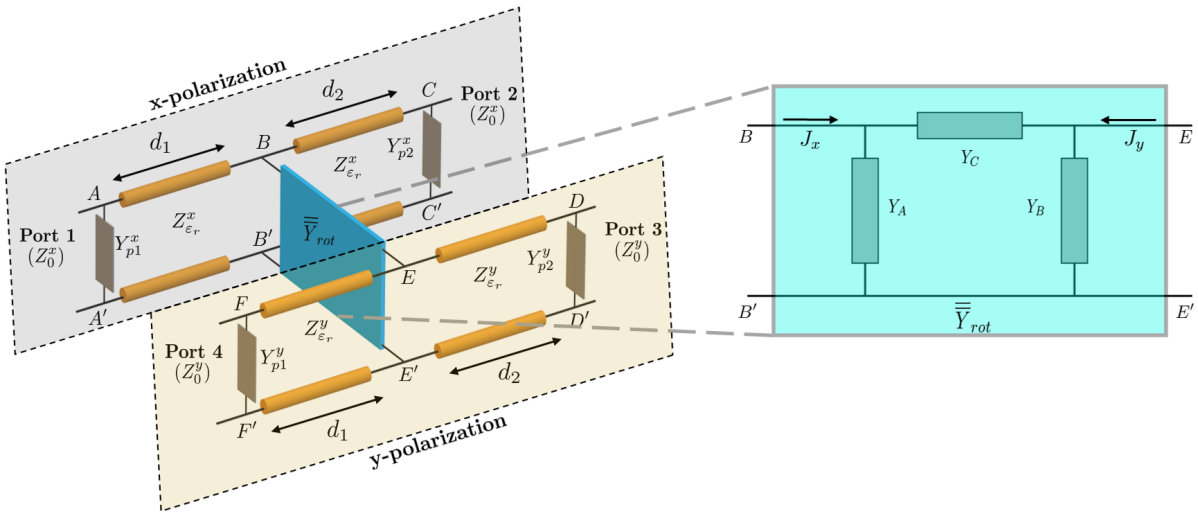

Figure 3.2: Equivalent four-port circuit of the unit-cell. Both polarizers, p_1 and p_2, are represented as a pair of shunt admittances at the ends of x and y transmission lines, respectively. The rotator is modelled by a π-type network, coupling the two transmission lines at BB' and EE'.

Due to the periodical nature of the problem, the circuit representation is accurate when only the dominant mode of the Floquet Waves (FWs) is propagating within the frequency range of observation [79]. Furthermore, the circuit does not take into account any evanescent wave coupling among the stacked layers. All previous assumptions depend on both period and frequency, which can be validated through full-wave simulations. Therefore, in order to obtain accurate results using this model, separations greater than $\lambda/8$ between the layers must be considered and the periodicity of each layer should be equal or less than $\lambda/2$ at the highest operating frequency.

3.2.1 Polarizers

The polarizers act as reflective or transparent surfaces to orthogonal linearly-polarized incident fields. The strip grating, shown in Figure 3.1, has been thoroughly studied in previous works, e.g. [80]–[82], representing an ideal choice for polarizer. The performance is improved when the structure exhibits sub-wavelength periodicity. Here, the two gratings are placed orthogonally, so that the transmitted and reflected fields are parallel to the x- and y-axis, respectively, at the first polarizer.

In the circuit, each grid is seen as a couple of shunt admittances, Y_p^x and Y_p^y, loading the corresponding transmission lines. If the two polarizers are considered identical, then

these parameters are

$$Y_{p1}^{x} = Y_{p2}^{y} = Y_t \,, \tag{3.1a}$$

$$Y_{p1}^{y} = Y_{p2}^{x} = Y_r \,. \tag{3.1b}$$

The value Y_t describes the case of transparency and the value Y_r describes the case of reflection. In general, it is known that Y_t and Y_r exhibit a small capacitive and a finite inductive value, respectively. Nevertheless, in many studies the polarizers are assumed ideal, in order to exploit the polarization properties and simplify the analysis. In that case, the corresponding values are

$$Y_t = 0 \,, \tag{3.2a}$$

$$Y_r \to -\infty \,. \tag{3.2b}$$

The equivalent circuit of Figure 3.2 is valid for any admittance values of the polarizers. Nevertheless, the above approximation can be used to derive a simple analytical expression of the transmission coefficient.

The impedances of the strip grating geometry can be given numerically to good approximation as in [83]:

$$X_L = Z_0 \frac{P_{gr}}{\lambda_0} ln(csc\left(\frac{\pi W_P}{2P_{gr}}\right)) \,, \tag{3.3a}$$

$$X_C = -Z_0 \frac{1}{n^2} \left[\frac{4P_{gr}}{\lambda_0} ln(csc\left(\frac{\pi G_P}{2P_{gr}}\right))\right]^{-1} \,, \tag{3.3b}$$

where $P_{gr} = W_P + G_P$ and $n \approx \sqrt{(1+\varepsilon_r)/2}$ for a capacitive strip grating, which is very accurate in the quasi-static limit [84], [85]. The accuracy of (3.3) depends on the grating periodicity, P_{gr}, which for small values ($P_{gr} \leq \lambda_0/4$) is very good, as shown in Figures 3.3(a) and (b). Hence, the admittances are calculated as $Y_r = -j/X_L = -j/(\omega L_r)$ and $Y_t = -j/X_C = j\omega C_t$. A comparison of the values Y_t and Y_r as a function of frequency is shown in Figures 3.3(c) and (d).

Alternatively, the strip grating can be simulated at a central frequency f_0 using a full-wave solver to export the equivalent parameters L_r and C_t. Then, since it does not exhibit any resonant behavior in frequency, the admittances can be related directly to the parameters L_r and C_t, with almost perfect accuracy compared to simulations.

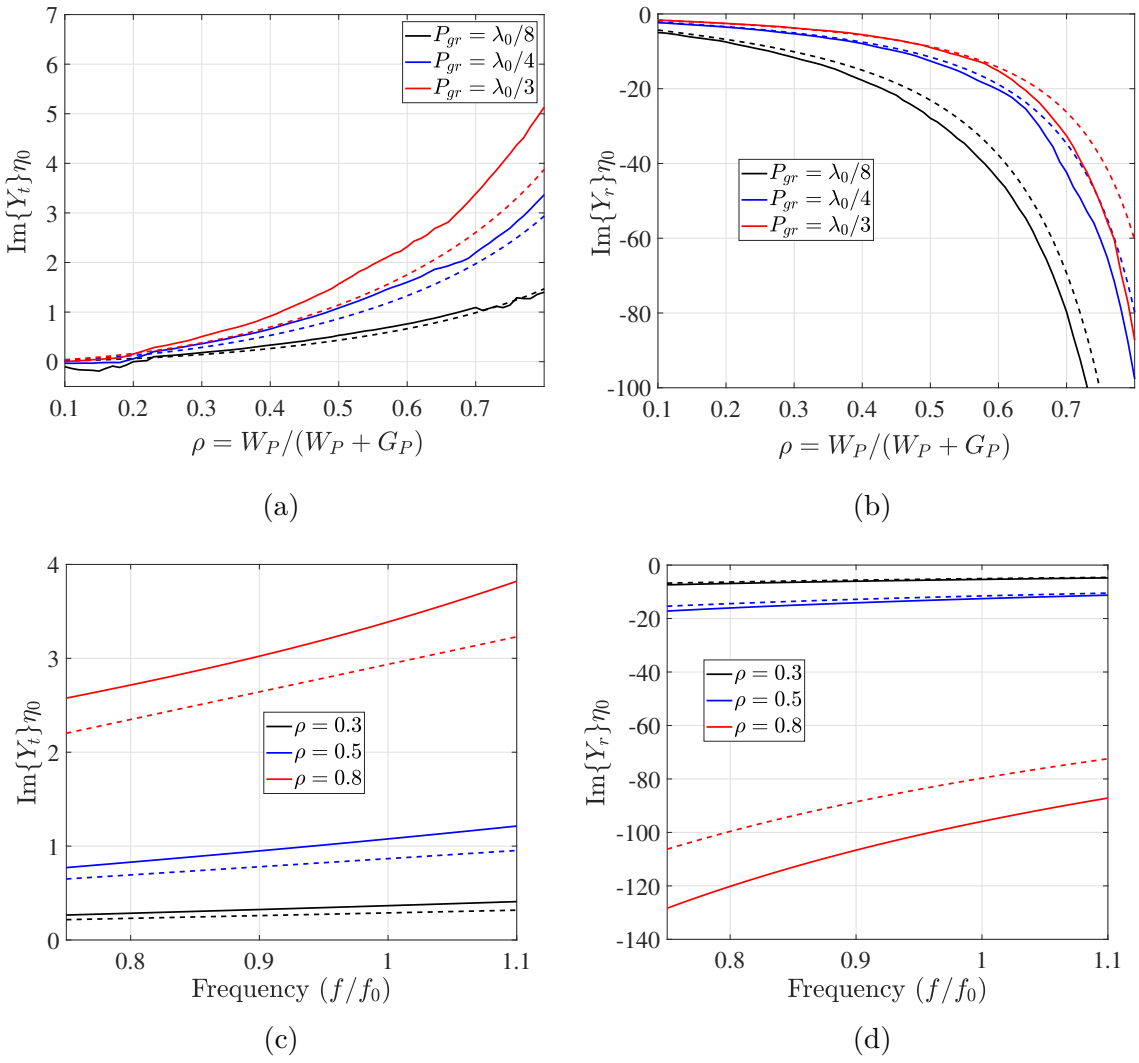

Figure 3.3: Simulated (solid lines) and numerical (dashed lines) normalized admittances Y_t and Y_r using (3.3) of a polarizer that is interleaved between vacuum and some dielectric with relative permittivity $\varepsilon_r = 4$. The values in (a) and (b) are plotted as a function of the filling factor at f_0 and those in (c), (d) are plotted as a function of the frequency for $P_{gr} = \lambda_0/4$.

3.2.2 Polarization rotator

The rotator is coupling the two polarizations in the (x,y) system. The anisotropic behavior of this layer can be described by a 2×2 admittance tensor given by

$$\overline{\overline{Y}}_{rot} = \begin{bmatrix} Y_{xx} & Y_{xy} \\ Y_{yx} & Y_{yy} \end{bmatrix} \tag{3.4}$$

The entries Y_{xy} and Y_{yx} represent the polarization coupling and they are equal by reciprocity. The tensor $\overline{\overline{Y}}_{rot}$ relates the components of the excited surface currents, J_x and J_y, to the average electric field components across the rotator sheet [78]. This relationship can be represented by a π-type circuit [77], placed between the x and y transmission lines, as shown in Figure 3.2. The admittance values of the π-network are

$$Y_A = Y_{xx} + Y_{xy} \tag{3.5a}$$

$$Y_B = Y_{yy} + Y_{xy} \tag{3.5b}$$

$$Y_C = -Y_{xy} \tag{3.5c}$$

3.2.3 Closed-form expression of the transmission coefficient

The overall unit-cell is modelled using five admittance values, namely Y_{xx}, Y_{yy}, Y_{xy}, Y_t and Y_r. Considering the proposed circuit, the main objective is to calculate the scattering coefficient S_{31}, which will be referred to as T^{yx} here, maximize its amplitude and tune the phase. Based on classical network analysis [77], the general expression of this coefficient is calculated as

$$S_{31} \triangleq T^{yx} = (Z_{AA'}^{-1} - Y_t)(1 + S_{11})K_1 K_2^{-1}\,. \tag{3.6}$$

The value $Z_{AA'}$ is the equivalent input impedance at Port 1 when all other ports are terminated by a matched load (Z_0). The value S_{11} is the reflection coefficient at Port 1, also referred as R^{xx}. The expressions K_1 and K_2 are given in Appendix B.

3.2.4 Rotation transformation

If the properties of the polarizers and the spacers are known, then the expression (3.6) is a function of the three admittance entries of the rotator in (3.4). Although in this case the unit-cell can be studied and optimized focusing only on the inner sheet, the analysis remains somewhat complicated. In addition, the synthesis of the admittance tensor and the physical design of the rotator are still problematic, especially due to the coupling factor Y_{xy}, which is hard to control. Therefore, a convenient expression for the admittance tensor

is found by applying a coordinate transformation [86]. It is based on the form invariance of Maxwell's equations under coordinate transformations [87]. In particular, the tensor $\overline{\overline{Y}}_{rot}$ is diagonal in the (u,v) reference system, which is called crystal system and it exists for any passive two-dimensional structure [88]. This can be obtained by rotating the (x,y) system by an angle ϕ, as shown in Figure 3.4(a). The following relationship holds

$$\overline{\overline{Y}}_{rot}^{XY} = \overline{\overline{R}}(\phi)\overline{\overline{Y}}_{rot}^{UV}\overline{\overline{R}}^{T}(\phi)\,, \tag{3.7}$$

where $\overline{\overline{R}}(\phi)$ is the rotation matrix and the superscripts XY and UV indicate the two reference systems. The diagonalized matrix is

$$\overline{\overline{Y}}_{rot}^{UV} = \begin{bmatrix} Y_u & 0 \\ 0 & Y_v \end{bmatrix} \tag{3.8}$$

The three original entries of the rotator admittance can be expressed in terms of the two entries of the diagonalized matrix, yielding

$$Y_{xx} = \cos^2(\phi)Y_u + \sin^2(\phi)Y_v\,, \tag{3.9a}$$

$$Y_{yy} = \sin^2(\phi)Y_u + \cos^2(\phi)Y_v\,, \tag{3.9b}$$

$$Y_{xy} = \sin(\phi)\cos(\phi)(Y_u - Y_v)\,. \tag{3.9c}$$

The entries Y_u and Y_v can be determined from the scattering parameters of the rotator sheet under u- and v-polarized fields. In particular, by simulating the rotator sheet with periodic boundaries at the interface between two semi-infinite media of characteristic impedance $\eta = \eta_0/\sqrt{\varepsilon_r}$, the expressions for the admittances are [77]

$$Y_{u,v} = -\frac{2S_{11}^{u,v}}{\eta(1+S_{11}^{u,v})}\,, \tag{3.10}$$

where $S_{11}^{u,v}$ is the reflection coefficient at each polarization, related to the average incident and reflected field quantities in a periodic environment. Therefore, the admittance parameters can be expressed in the (x,y) system as a function of Y_u, Y_v and ϕ. A proposed circuit representation of this transformation is shown in Figure 3.4(b). The rotation matrix is illustrated using ideal transformers, in order to describe the relationship between

the electric field components in the two coordinate systems. Therefore, from (3.7), the π-circuit in Figure 3.2 can be replaced by the circuit of the rotation matrix and its transpose, placing between them the shunt admittances Y_u and Y_v, as shown in 3.4(c). This concept can be very useful for circuit analysis using simulation platforms.

The impact of the angle of rotation can be studied by focusing on the properties of depolarization of the rotator. If only the π-network is used in the circuit analysis, then from the expressions (3.7) and (3.10) the corresponding depolarization coefficient will be

$$S^{yx/xy} = \sin(2\phi)\frac{(Y_u - Y_v)}{(Y_u + 2\sqrt{\varepsilon_r}/\eta_0)(Y_v + 2\sqrt{\varepsilon_r}/\eta_0)}\,. \tag{3.11}$$

This coefficient has the same value for any combination of ports at different polarizations. In other words, the polarization conversion of a single layer for both reflected and transmitted waves is the same in both regions, assuming reciprocity. Instead of using the π-network, expression (3.11) can be also found as in (3.7), using this time the scattering matrix of the rotator in the (x,y) and the (u,v) systems [88]:

$$\begin{bmatrix} \overline{\overline{S}}^{XY}_{11} & \overline{\overline{S}}^{XY}_{12} \\ \overline{\overline{S}}^{XY}_{21} & \overline{\overline{S}}^{XY}_{22} \end{bmatrix}_{ROT} = \begin{bmatrix} \overline{\overline{R}}(\phi) & \begin{pmatrix} 0 & 0 \\ 0 & 0 \end{pmatrix} \\ \begin{pmatrix} 0 & 0 \\ 0 & 0 \end{pmatrix} & \overline{\overline{R}}(\phi) \end{bmatrix} \begin{bmatrix} \overline{\overline{S}}^{UV}_{11} & \overline{\overline{S}}^{UV}_{12} \\ \overline{\overline{S}}^{UV}_{21} & \overline{\overline{S}}^{UV}_{22} \end{bmatrix}_{ROT} \begin{bmatrix} \overline{\overline{R}}^{T}(\phi) & \begin{pmatrix} 0 & 0 \\ 0 & 0 \end{pmatrix} \\ \begin{pmatrix} 0 & 0 \\ 0 & 0 \end{pmatrix} & \overline{\overline{R}}^{T}(\phi) \end{bmatrix} \tag{3.12}$$

It is clear that, for any pair of admittances, the maximum magnitude of expression (3.11) is found when $\phi = \pm 45°$, which is in agreement with existing ALP designs. For this angle of rotation, the three entries of the π-circuit in (3.5) become

$$Y_A = Y_B = \begin{cases} Y_u, & \text{if } \phi = 45°\,, \\ Y_v, & \text{if } \phi = -45°\,, \end{cases} \tag{3.13a}$$

$$Y_C = \pm(Y_v - Y_u)/2, \;\; \text{for } \phi = \pm 45°\,. \tag{3.13b}$$

Therefore, thanks to the transformation concept, the unit-cell can be analyzed using four admittances, Y_u, Y_v, Y_t and Y_r, instead of five. Finally, the value Y_{xy} vanishes and thus, by fixing the rest of the parameters, expression (3.6) can be completely described only by the two values, Y_u and Y_v, related to the rotator in the crystal system. For the rest of the study, we will consider that the angle of rotation is set for the maximum depolarization.

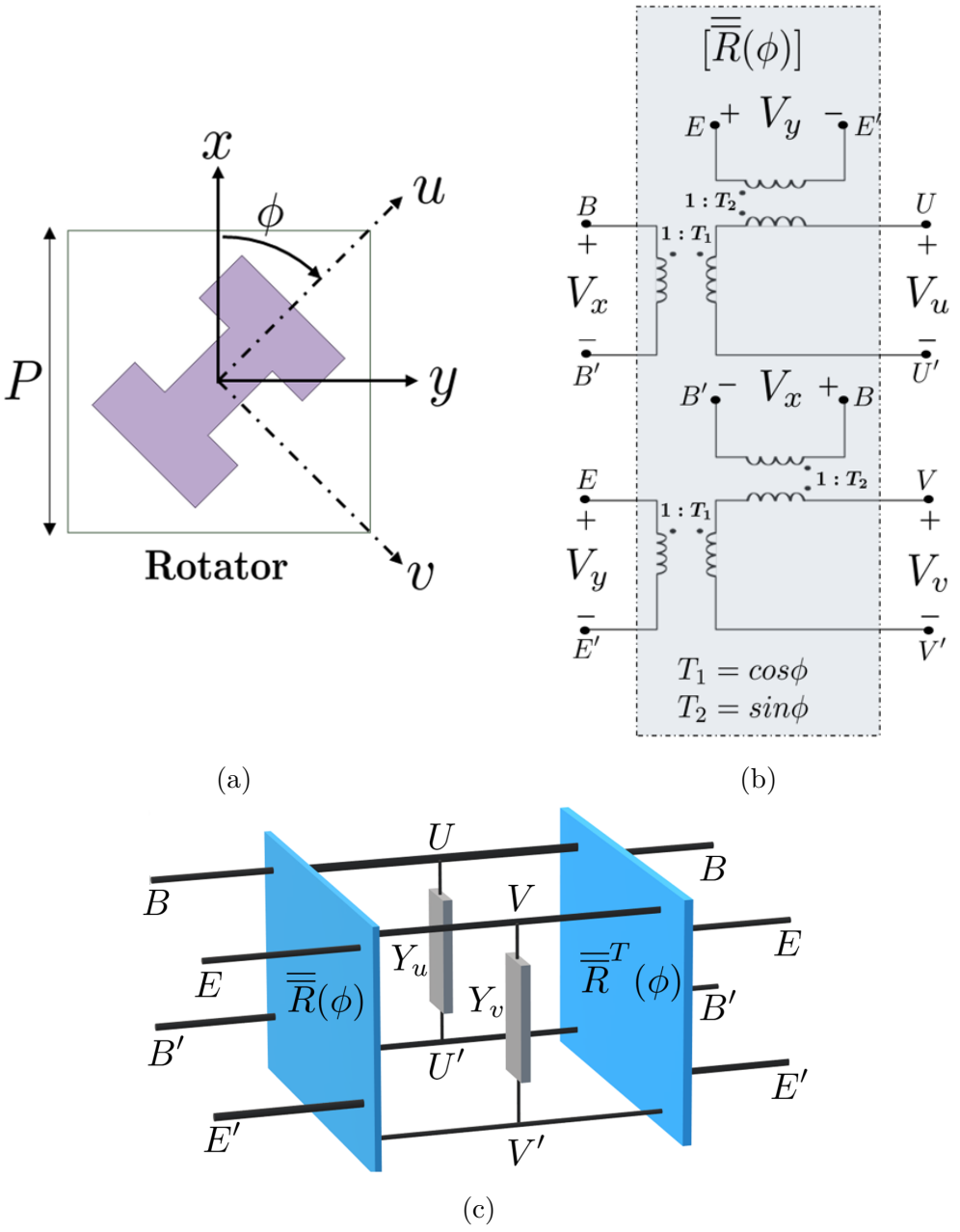

Figure 3.4: (a) Example of a rotator unit-cell design with its reference systems that are necessary to illustrate the diagonalization of $\overline{\overline{Y}}_{rot}$. (b) Equivalent circuit of the rotation matrix, describing the relationship between the electric field components in the two coordinate systems. Ideal transformers are considered for the angle of rotation. The transpose rotation matrix is modelled by a similar network. (c) Total representation of the transformation, which can replace the π-network of Figure 3.2.

3.3 Numerical analysis

3.3.1 Admittance study

To demonstrate the effectiveness of the model, the unit-cell is examined in terms of phase coverage for maximum transmission. Based on the circuit theory, the objective is to calculate the impedance matching condition (IMC) in order to maximize the power transfer from Port 1 to Port 3. After that, the phase of transmission will be studied considering either zero or very low insertion loss (IL).

First, quarter-wavelength spacers are considered, i.e. $d_1 = d_2 = \lambda/4$, where $\lambda = \lambda_0/\sqrt{\varepsilon_r}$, in order to derive a simple closed-form formula for the transmission coefficient. It has been already shown in previous designs that using a thickness close to this value, both wide bandwidth and low insertion loss can be achieved. Furthermore, the two polarizers are assumed ideal using (3.2) and thus a total reflection occurs at ports 2 and 4. Under these assumptions and choosing $\phi = \pm 45°$, expression (3.6) yields

$$T^{yx} = \pm \frac{(Y_v - Y_u)\varepsilon_r Z_0}{\varepsilon_r^2 + Y_u Y_v Z_0^2 + (Y_u + Y_v)\varepsilon_r Z_0} \tag{3.14}$$

The magnitude and phase of (3.14) are plotted in Figures 3.5(a) and (b) as a function of Y_u and Y_v. Assuming lossless materials, each admittance is described by a susceptance. Solving (3.14) for perfect transmission, the following locus is obtained

$$Y_u Y_v = (\varepsilon_r / Z_0)^2 \,. \tag{3.15}$$

As long as the admittance values are defined by (3.15), the unit-cell will exhibit zero insertion loss and cover the whole phase range, from $-180°$ to $180°$. This shows that the anisotropy of the cell can improve the performance for TA design, compared to three-layer designs comprising symmetric FSS, which instead require a certain margin of insertion loss to cover the full phase range [89]. Another interesting observation is that the IMC is satisfied only when $\phi = \pm 45°$. When $\phi \neq \pm 45°$, the behavior of transmission is similar, but the maximum magnitude becomes smaller than one. Lastly, in order to satisfy (3.15), the rotator must exhibit purely capacitive and purely inductive properties for each polarization, respectively, along the crystal axes.

Similar conclusions can be drawn when the spacers exhibit the same thickness but not equal to $\lambda/4$. In particular, if (3.6) is solved for perfect transmission when $d_1 = d_2 = d$,

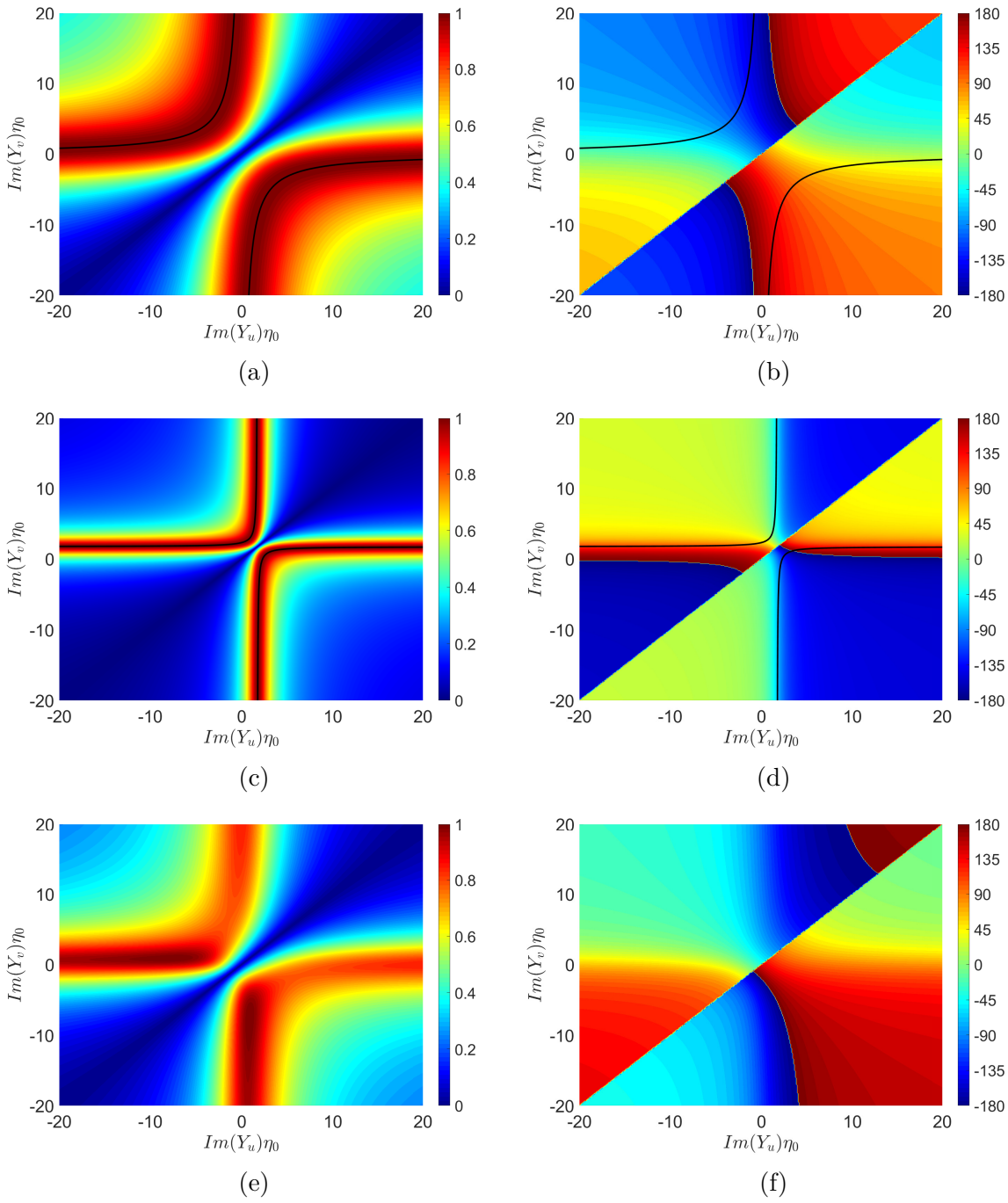

Figure 3.5: Magnitude (a), (c), (e) and phase (b), (d), (f) of T^{yx} as function of the rotator admittances at the crystal axes. The polarizers are assumed ideal. The permittivity and the thickness of the spacers are (a), (b) $\varepsilon_r = 4$, $d_1 = d_2 = \lambda/4$, (c), (d) $\varepsilon_r = 1$, $d_1 = d_2 = \lambda/6$, and (e), (f) $\varepsilon_r = 4$, $d_1 = \lambda/4$, $d_2 = \lambda/6$. The dark solid curves represent the loci for maximum transmission, expressed by (3.15) in (a), (b) and (3.16) in (c), (d).

a similar locus is derived. The expression defines again a hyperbola whose vertices are shifted toward the line $Y_u = Y_v$ as a function of the thickness and the permittivity. For $\varepsilon_r = 1$, the locus can be simplified to

$$(Y_u - jZ_0^{-1}\cot(\beta_0 d))(Y_v - jZ_0^{-1}\cot(\beta_0 d)) = (1/Z_0)^2\,, \tag{3.16}$$

where $\beta_0 = 2\pi/\lambda_0$. An example for $d_1 = d_2 = \lambda/6$ is shown in Figures 3.5(c) and (d). On the other hand, when $d = n\lambda/2$, with $n \in \mathbb{N}$, the problem has no solution and the transmission is zero.

When the two spacers do not have the same thickness, the unit-cell cannot cover all the phase of transmission. For instance, if $d_1 = \lambda/4$ and $d_2 = \lambda/6$, only few solutions are found in the vicinity, covering less than 360° of phase, as shown in Figures 3.5(e) and (f).

3.3.2 Transmission phase limit

A more rigorous description of the transmission performance limits for ALP structures is presented here. This study is an extension of the work presented in [89], where the authors investigated the properties of TA unit-cells comprising identical and symmetric FSS layers. In their approach, the S-parameters of a single FSS layer are represented as a function of its transmission phase. To obtain the overall scattering response for multilayer FSS structures, they used a simple cascaded process. Finally, they demonstrated that the maximum transmission phase range of a three-layer symmetric unit-cell for 1-dB and 3-dB maximum insertion loss are 308° and 360°, respectively. A four-layer unit-cell can achieve full phase range of 360° for only 1-dB insertion loss. The analytical limits of this procedure were generally applicable, independent from the selection of a specific element shape.

Later, the authors in [90] extended this study to symmetric FSS unit-cells using non identical layers. Following the same approach as in [89], they demonstrated full phase coverage for 1-dB insertion loss with only three symmetric and not identical metal layers. Nevertheless, it remains necessary to take into account a margin of insertion loss in order to cover completely the transmission phase. Therefore, for symmetrical topologies, the realization of an almost reflectionless TA can be achieved theoretically only by stacking several metal layers, typically more than four.

In the ALP topology, all layers break the symmetry. Therefore, inspired by the study in [89], each metal layer can be described by a pair of transmission phases, $\angle T_u$ and

$\angle T_v$, in its own crystal system, (u,v). The parameter $T_{u,v}$ is the corresponding complex transmission coefficient, described as

$$T_{u,v} = \cos\left(\angle T_{u,v}\right) e^{j\angle T_{u,v}} \,. \tag{3.17}$$

Assuming again, without loss of generality, that the polarizers are ideal and the spacers are fixed, expression (3.6) can be used as a function of the two transmission phases, $\angle T_u$ and $\angle T_v$, which describe only the rotator. The relationship between the admittances $Y_{u,v}$ and the transmission phases $\angle T_{u,v}$ is calculated by combining (3.10) and (3.17). Assuming that $T_{u,v} = 1 + S_{11}^{u,v}$, which is true for lossless materials in single-mode FW propagation, the following relationship is found

$$Y_{u,v} = -j\frac{2\tan\left(\angle T_{u,v}\right)}{Z_0} \,. \tag{3.18}$$

Therefore, expression (3.15) becomes

$$\tan\left(\angle T_u\right) = -\frac{\varepsilon_r^2}{4}\cot\left(\angle T_v\right), \tag{3.19}$$

and expression (3.16) becomes

$$\left(2\tan\left(\angle T_u\right) + j\cot(\beta_0 d)\right)\left(2\tan\left(\angle T_v\right) + j\cot(\beta_0 d)\right) = -1 \,. \tag{3.20}$$

As shown in Figures 3.6(a) and (b), the unit-cell demonstrates full phase coverage with zero insertion loss. On the other hand, for non equal spacers there is not complete phase coverage, as shown in Figures 3.6(c) and (d). Therefore, the same conclusions are drawn as before, considering a more theoretical representation of the rotator scattering properties. The loci that describe the condition for maximum transmission in (3.19) and (3.20) are illustrated in Figures 3.6(e) and (f), for different properties of the spacers.

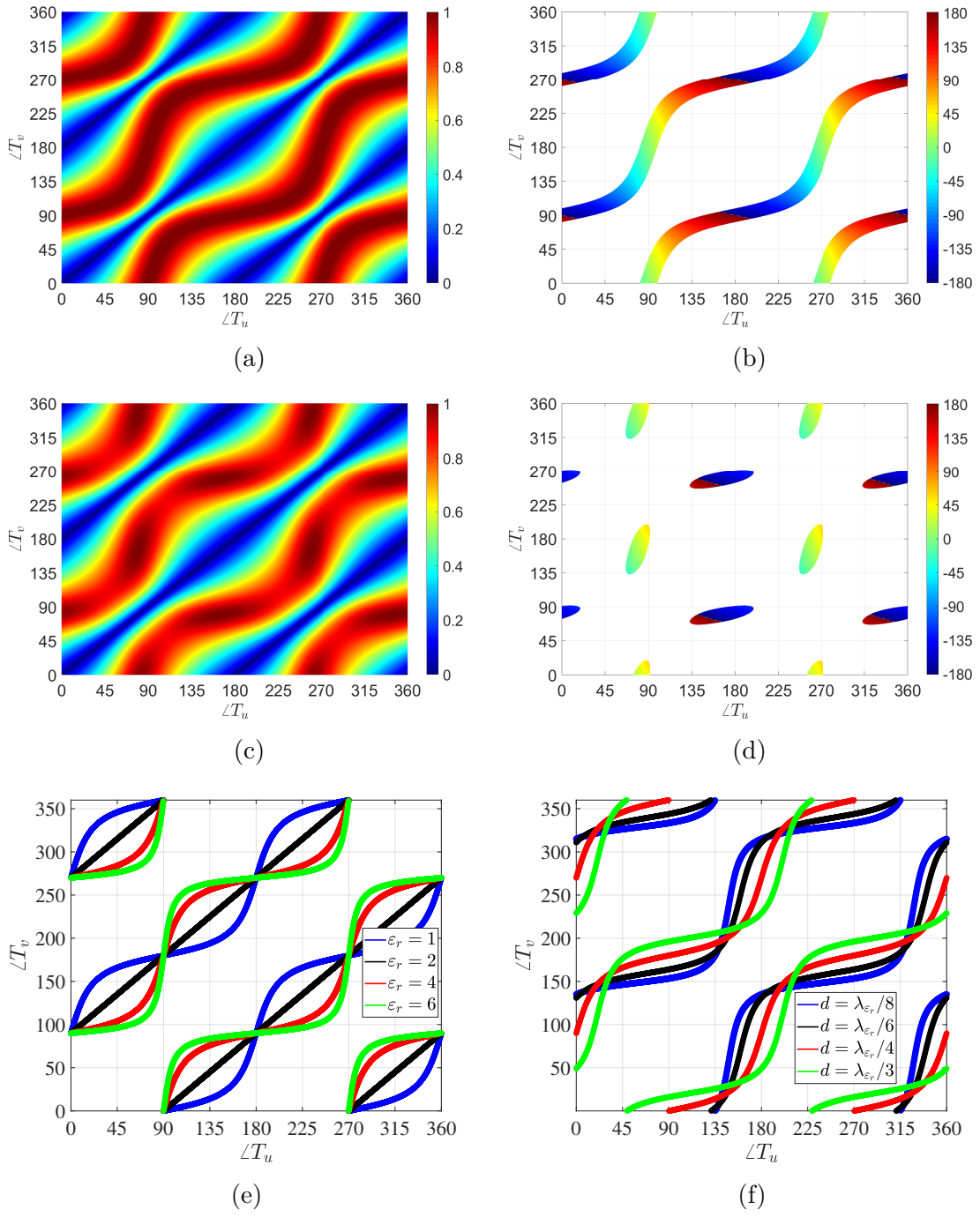

Figure 3.6: Magnitude (a), (c) and phase (b), (d) of T^{yx} as function of the rotator transmission phases calculated at the crystal axes, assuming ideal polarizers. In (b) and (d), only the results of the phase $\angle T^{yx}$ for $|T^{yx}| \leq 0.5$ dB are plotted. Finally, the graph in (e) shows the change of the locus (3.19) when $d_1 = d_2 = \lambda_{\varepsilon_r}/4$ and the graph in (f) shows the change of the locus (3.20) when ε_r=1, for different values of permittivity and spacer thickness, respectively.

3.4 Numerical synthesis

The objective of the synthesis procedure is to realize a set of low-loss unit-cells attaining equispaced transmission phases with applications to TAs. It leverages on the previous model by determining the admittance tensors of the rotator sheets necessary to minimize the insertion loss of the unit-cells and cover the full phase range. Since the procedure is focused mainly on the rotator, it is important to assess first the impact of the other parameters, i.e. the dielectric spacers and the polarization grids. Until now, their properties have been fixed to ease the numerical analysis. Here, in order to derive some guidelines for their design, we study their impact on the transmission bandwidth and the insertion loss, respectively.

First, the effect of the spacers is investigated, assuming that the polarizers are ideal. As it was shown before, they must exhibit the same thickness for maximum performance. The procedure for the calculation of the transmission bandwidth is the following:

- The transmission coefficient T^{yx} is calculated as a function of Y_u and Y_v using (3.6), for several values of permittivity ε_r and thickness d at the design frequency, ω_0.
- For each of these values, the locus of the rotator admittances achieving perfect transmission is found.
- Moving along the locus, a pair (Y_{u0},Y_{v0}) providing a specific value of transmission phase for the unit-cell is selected (e.g. when $\angle T^{yx} = 90°$).
- Assuming that the rotator is non-resonant, the pair (Y_{u0},Y_{v0}) can be modeled as a pure inductance and a pure capacitance when excited by a u- and v-polarized wave, respectively. If $Y_{u0} > 0$ and $Y_{v0} < 0$, the equivalent capacitance and inductance are

$$C_0 = \frac{\Im\{Y_{u0}\}}{\omega_0}\,, \tag{3.21a}$$

$$L_0 = \frac{-1}{\omega_0 \Im\{Y_{v0}\}}\,. \tag{3.21b}$$

Under this hypothesis, the frequency behavior of T^{yx} can be determined. The computed 1-dB transmission bandwidth is plotted as a function of d and ε_r in Figure 3.7(a). The unit-cell can attain almost 100% relative bandwidth when exhibiting approximately quarter-wavelength spacing and a permittivity less than 4. This result is in agreement with previous designs in the literature [48], [91], proving that the structure is considered very broadband. The transmission coefficient of a unit-cell for different values of permittivity

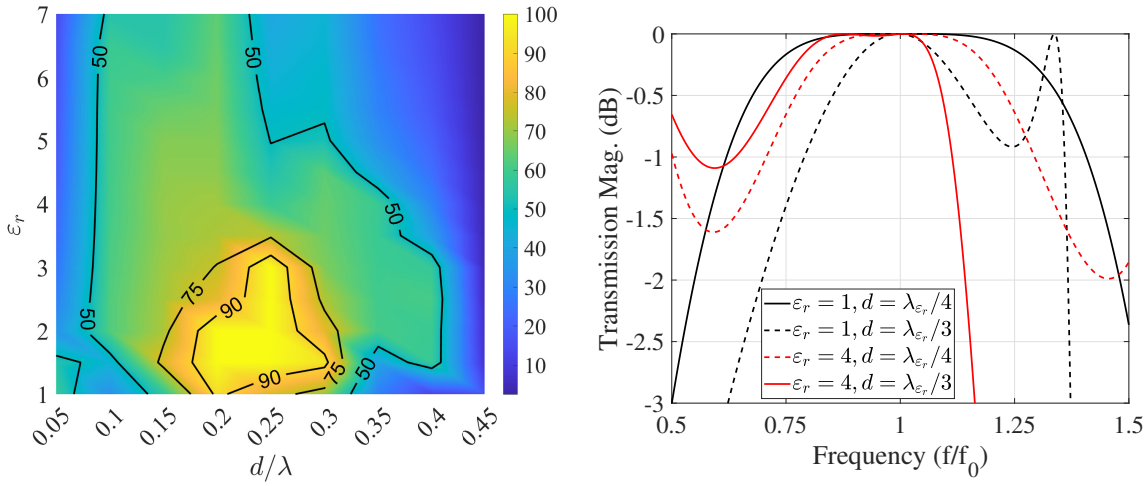

(a) (b)

Figure 3.7: (a) 1-dB relative bandwidth (in %) of the unit-cell as a function of thickness and permittivity of the spacers, assuming ideal polarizers. (b) Transmission coefficient (magnitude) for different values of permittivity and thickness as a function of frequency.

and thickness is plotted in Figure 3.8(b) as a function of frequency.

The effects of the polarization grids can be studied using a similar procedure. The behavior of a grid approaches that of an ideal polarizer as its period decreases [80], [81]. Nevertheless, even for relatively large periods, the mismatch introduced by the real grids with respect to ideal polarizers can be reduced with an appropriate choice of the filling factor $\rho = W_P/(W_P + G_P)$, where W_P is the strip width and G_P is the gap, as shown in Figure 3.1. In order to minimize the insertion loss of the unit-cell, the filling factor should be in the range between 0.2 and 0.4, when the gap is kept at a relatively small value, as shown in Figure 3.8(b).

As an example, a grid with a period of $\lambda_0/4$ and $\rho = 0.32$ is selected, giving $W_P = 0.08\lambda_0$ when $G_P = 0.17\lambda_0$. The sheet admittances of the chosen grid, simulated at the interface between vacuum and a dielectric of permittivity $\varepsilon_r = 4$, are $Y_t = j0.4/\eta_0$ and $Y_r = -j9/\eta_0$, at the center frequency f_0. Almost the same values can be extracted using the expressions (3.3). The transmission coefficient of a unit-cell comprising this grid as polarizer is plotted in Figure 3.8(b) as a function of frequency. The case of ideal polarization grids is also plotted for comparison. It can be seen that the loading effect of the polarization grids introduces also a small frequency shift of transmission coefficient. This can be compensated by slightly tuning, reducing in that case, the thicknesses of the spacers. By choosing $d = 0.22\lambda$, the frequency behavior of the unit-cell with real polarization

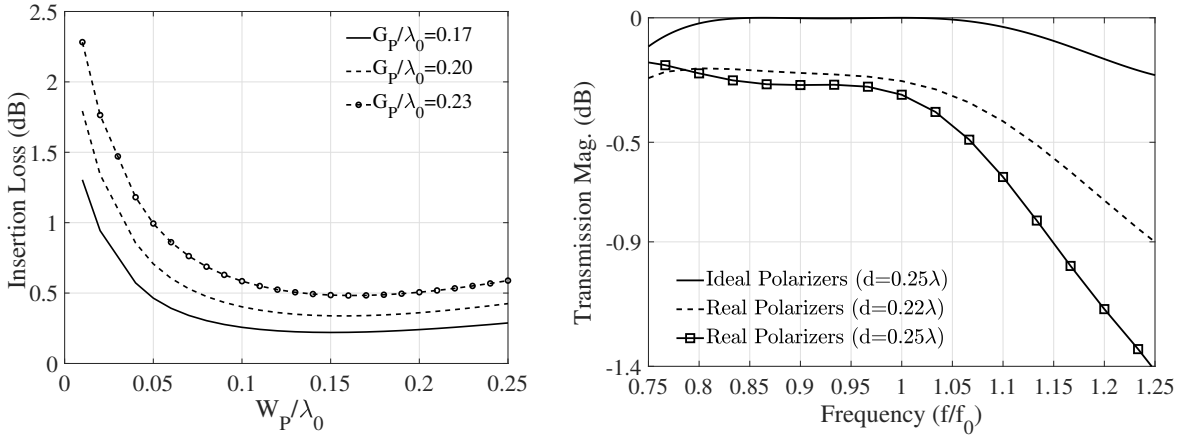

(a) (b)

Figure 3.8: (b) Minimum insertion loss of the unit-cell as a function of the strip width, W_P, for three gap values, G_P. (b) Transmission coefficient (magnitude) as a function of frequency considering ideal and real polarizers.

grids matches the one obtained for ideal polarizers. The insertion loss at f_0 is only 0.25 dB (2.8%), determined by a slight mismatch due to the introduction of the polarization grids.

3.5 Numerical design of transmitarray antenna

To highlight the features of this study, we synthesize a 3-bit TA antenna for broadside radiation at 300 GHz. As an example, we consider a 40 × 40 array with $\lambda_0/2$ element periodicity, illuminated by a theoretical cosine type focal source, as described in Chapter 2, with a gain of 10 dBi and a half-power beamwidth (HPBW) of 65.6°.

First, we calculate the transmission coefficient of the unit-cell as a function of Y_u and Y_v using (3.6) at the design frequency. The thicknesses and relative permittivity of the spacers are fixed to $d = 0.22\lambda$ and $\varepsilon_r = 4$, respectively, while the geometrical parameters of the grids are set to $W_P = 0.08$mm and $G_P = 0.17$mm. Then, the locus of admittance values maximizing $|T^{yx}|$ is numerically found. Moving along the locus, we select 2^N admittance pairs (Y_u^i,Y_v^i), with $i = 1, \ldots, 2^N$ and $N = 3$. These are used for the design of ALP unit-cells achieving a uniform N-bit quantization of the full phase range. The transmission phase $\angle T^{yx}$ as a function of (Y_u, Y_v) and the locus for maximum transmission are plotted in Figure 3.9(a). The pairs of rotator admittances selected to design the 8 unit-cells are indicated with crosses. Their values and the corresponding transmission coefficient are

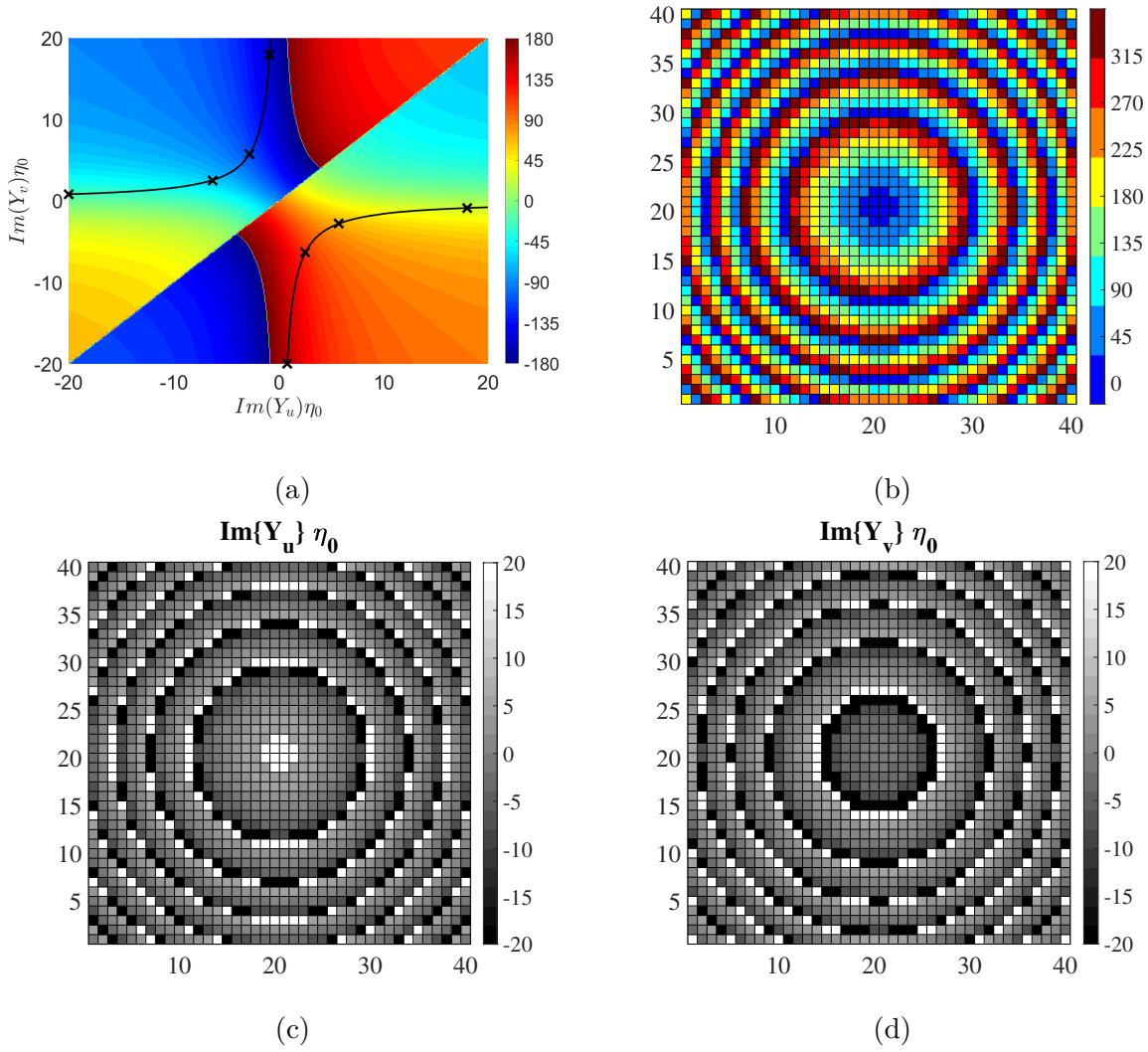

Figure 3.9: (a) Phase of transmission as a function of the admittance pair (Y_u,Y_v) at 300 GHz, including the locus for maximum transmission (-0.25 dB) and the solution points for a 3-bit TA design, marked with crosses. (b) Phase distribution of a 3-bit TA for broadside radiation. (c), (d) Admittance map of the rotator calculated at the crystal axes, based on the results shown in (a).

shown in Table 3.1. By virtue of symmetry, only the branch of the locus in the second or the fourth quarter is needed. Physically, this means that half of the states are obtained when this layer is rotated by $\phi = 45°$, while the other half can be obtained using $\phi =$ -45°. This can be also seen in Table 3.1, where the values of the admittances are reversed between two unit-cells with 180° phase difference.

Following the ray tracing approach of Chapter 2, we calculate the focal distance for maximum gain and aperture efficiency. The far-field radiation pattern of the unit-cells is

Table 3.1: Unit-cell transmission coefficient and rotator admittances for the 3-bit design in Figure 3.9(a).

UC targeted phase (°)	$\angle T^{yx}(°)$	$\lvert T^{yx}\rvert$ (dB)	$\Im\{Y_u\}\eta_0$	$\Im\{Y_v\}\eta_0$
25	25	-0.25	18	-0.9
70	70	-0.25	5.7	-2.8
115	115	-0.25	2.5	-6.3
160	157	-0.25	0.8	-20
205	205	-0.25	-0.9	18
250	250	-0.25	-2.8	5.7
295	295	-0.25	-6.3	2.5
340	337	-0.25	-20	0.8

calculated using the expression (2.17). The optimal focal distance is found at 10 mm, giving an $F/D = 0.5$. The 3-bit phase distribution for broadside radiation is shown in Figure 3.9(b). The peak gain and the aperture efficiency are 35.1 dBi and 64.8%, respectively. The gain loss is about 0.5 dB compared to an ideal TA, taking into account 0.25 insertion loss due to the polarizers and 0.25 dB quantization loss due to the 3-bit resolution. The equivalent admittance map of the rotator for each polarization in the crystal system is illustrated in Figures 3.9(c) and (d). The admittance map of the polarizers is constant, equal to $Y_{p1}^x = Y_{p2}^y = j0.4/\eta_0$ and $Y_{p1}^y = Y_{p2}^x = -j9/\eta_0$.

3.6 Conclusions

A numerical approach for analyzing and designing ALP TAs has been presented. A closed-form expression for the transmission coefficient of the unit-cell was found by modeling it as three cascaded sheet admittances interleaved by two dielectric spacers. A four-port equivalent circuit was derived to accurately describe the anisotropic behavior of the unit-cell and to ease its physical design. We rigorously demonstrated that the selected anisotropic unit-cell can achieve at the design frequency both nearly perfect transmission and full phase coverage, as opposed to standard symmetric FSS designs. It was shown that, following proper design guidelines, the transmission phase can be tuned by varying the inner sheet only. Based on this observation, a procedure to synthesize the admittance tensor of the inner layer and realize multiple low-loss TA unit-cells has been proposed. It requires the optimization of only two admittance parameters.

Chapter 4

Design of transmitarray antennas in Printed Circuit Board

In this chapter, the synthesis of PCB-based anisotropic transmitarrays is reported. Four antenna prototypes are realized, employing the ray tracing technique presented in Chapter 2 and the unit-cell topology presented in Chapter 3. Two of the antenna prototypes were realized to meet certain system requirements, as reported in the "NEXT5G" project. All the prototypes have been tested in anechoic chamber. The transmission properties of the transmitarray unit-cells were also investigated experimentally, using a simple quasi-optical setup. Four arrays of identical unit-cells, each one for a specific phase state, were fabricated for this purpose.

4.1 Printed Circuit Board process

The PCB is a common technology used in all but the simplest electronic products, as it disposes a relatively simple and low-cost manufacturing process. The key features of this fabrication, especially when it comes to the design of transmitarrays, are related to the substrate and the metallization. As mentioned in Chapter 1, the substrate can possess a thickness from 64 μm up to 1.5 mm. The pre-preg, used as a bonding film, has typically a thickness of 100 μm, but it can be set lower at 64 μm. According to the design rules, the laminated copper has a thickness value of 17 or 35 μm, which can be minimized to 9 or 12 μm. Furthermore, special characteristics can be used cutting it down to 5 μm. However, products with special characteristics are considered risky, as the tolerances might lead to fabrication errors or non-realizable structures. In case of using copper with thickness equal to 9 or 12 μm, as done in this work, the minimum width of the tracks is 80 μm, with a tolerance of 10 μm of over- or under-etching. All the prototypes reported in this Chapter were fabricated at CIBEL. The industrial process of this company is separated into three types of characteristics; classical, technical and special. In this work, the prototypes belong

into the second category, where the the minimum width of the tracks is between 80 μm and 110 μm. Lastly, when it comes to the use of vias, the minimum diameter size, using typical characteristics, is 100 μm. The employed substrate material exhibits a relatively small dielectric constant, typically $\varepsilon_r < 4$, with very low permittivity losses. In this work, the selected material was the Astra MT77 from the Isola Group that is known for the ultra low losses[1].

4.2 Unit-cell design

The synthesis procedure of the unit-cell is based on the study of the admittance tensor of the rotator, as described in Chapter 3. The stack-up is shown in Figure 4.1. It comprises two Astra MT77 substrates and a bonding layer with a nominal permittivity equal to $\varepsilon_r = 3$ and relatively low losses ($\tan\delta = 0.0017$). The thicknesses are chosen $h_1 = 0.127mm$ and $h_2 = h_g = 0.064mm$, in order to get a spacer thickness close to $d = 0.22\lambda_{\varepsilon_r}$ at 300 GHz, as demonstrated in Chapter 3.

A key goal of this work was to make the design suitable for standard and low-cost PCB manufacturing. This requirement imposed to use conductor width and spacing larger than 80 μm. For this reason, the geometrical parameters of the grids are set to $W_P = 0.08$mm and $G_P = 0.17$mm, leading to a minimum achievable insertion loss of 0.25 dB, based on the model described in Chapter 3. In order to minimize the quantization losses, a 3-bit phase quantization is considered. For a 3-bit design, 8 rotator admittance pairs, numerically calculated, are used as references for the rotator design. As explained before, by virtue of symmetry, only four of them are eventually needed. In addition, the unit-cell periodicity is set to $P = \lambda_0/2 = 0.5$ mm, in order to avoid grating lobes and, at the same time, ease the integration of controllable devices for future reconfigurable transmitarray designs.

To overcome these strict constraints and achieve the targeted admittance pairs, four different rotator designs were employed. The results of the synthesis procedure and the selected rotator geometries are shown in Figure 4.2. The final rotator geometries have been extracted from full-wave simulations performed in Ansys HFSS, in order to optimize the common frequency bandwidth coverage and get as close as possible to the targeted admittance values. Despite the technological constraints, the admittances of the designed rotators, shown in blue color, are very close to the targeted values obtained from the

1. https://www.isola-group.com/wp-content/uploads/data-sheets/astra-mt77.pdf

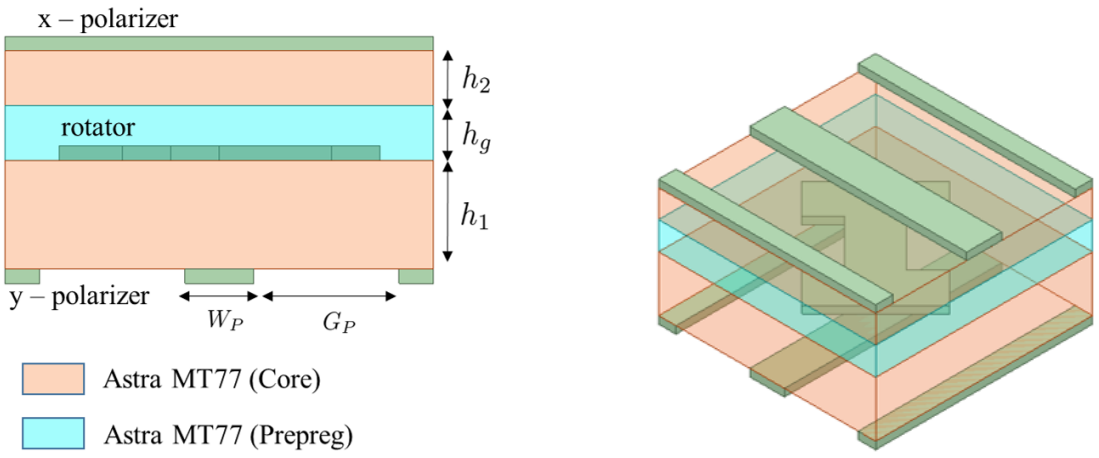

Figure 4.1: (a) Stack-up of the proposed PCB-based ALP unit-cell and (b) 3D view.

synthesis procedure, shown in red color. The phase error is less than 5° for each design, compared to the targeted value, as both pairs (at each phase state) approach the same isodynamic curve of phase $\angle T^{yx}$, as a function of Y_u and Y_v. These results prove the effectiveness of the proposed unit-cell design and synthesis procedure for the realization of low-cost TAs, even at sub-THz frequencies. The remaining four unit-cells are easily obtained by mirroring the rotators with respect to the x-axis. The admittances of the mirrored rotators approach the branch of the optimal admittance locus in the second quadrant. The transmission coefficient of each unit-cell with mirrored rotator is equal in magnitude but shifted in phase by 180° with respect to the corresponding original design.

Table 4.1: Geometrical parameters of the employed rotators.

Layer	Parameter (mm)			
	L_1	L_2	W	G
Rotator A	0.35	0.24	0.1	-
Rotator B	0.5	0.24	0.08	-
Rotator C	0.4	-	0.08	0.08
Rotator D	0.24	0.3	0.08	-

The magnitude and phase of the transmission coefficients of all unit-cells, simulated under normal incidence and enforcing period boundaries, are shown in Figure 4.3. The common 1-dB transmission bandwidth is almost 85 GHz, or 30% at the center frequency. Over this band, the relative phase shifts among adjacent phase states are very close to

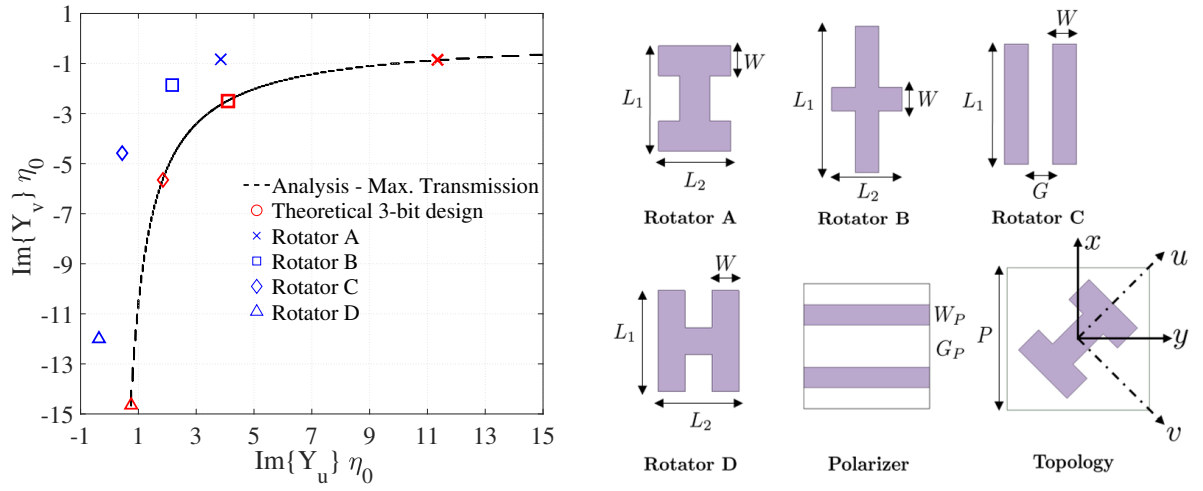

(a) (b)

Figure 4.2: (a) Results of the synthesis procedure of the 3-bit TA at 300 GHz. Due to symmetry, only the fourth quadrant is shown, including four admittances. (b) Rotator designs for the proposed TA, depicted with blue symbols in (a).

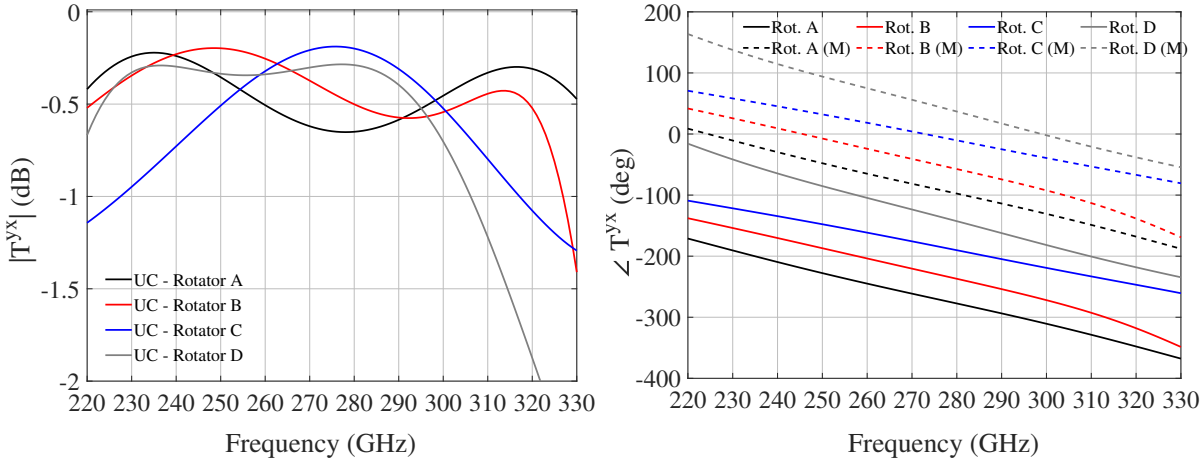

(a) (b)

Figure 4.3: Transmission magnitude (a) and phase (b) of the designed unit-cells, obtained from full-wave simulations. The results when the rotators are mirrored (M) with respect to x-axis are shown in dashed lines.

45°, with maximum absolute variations of 10°.

Finally, the performance of the unit-cells with the four rotator topologies is investigated for oblique angles of incident wave. The transmission magnitude is plotted in Figure 4.4. It can be seen that for angles greater than 10°, strong resonances appear, mainly at

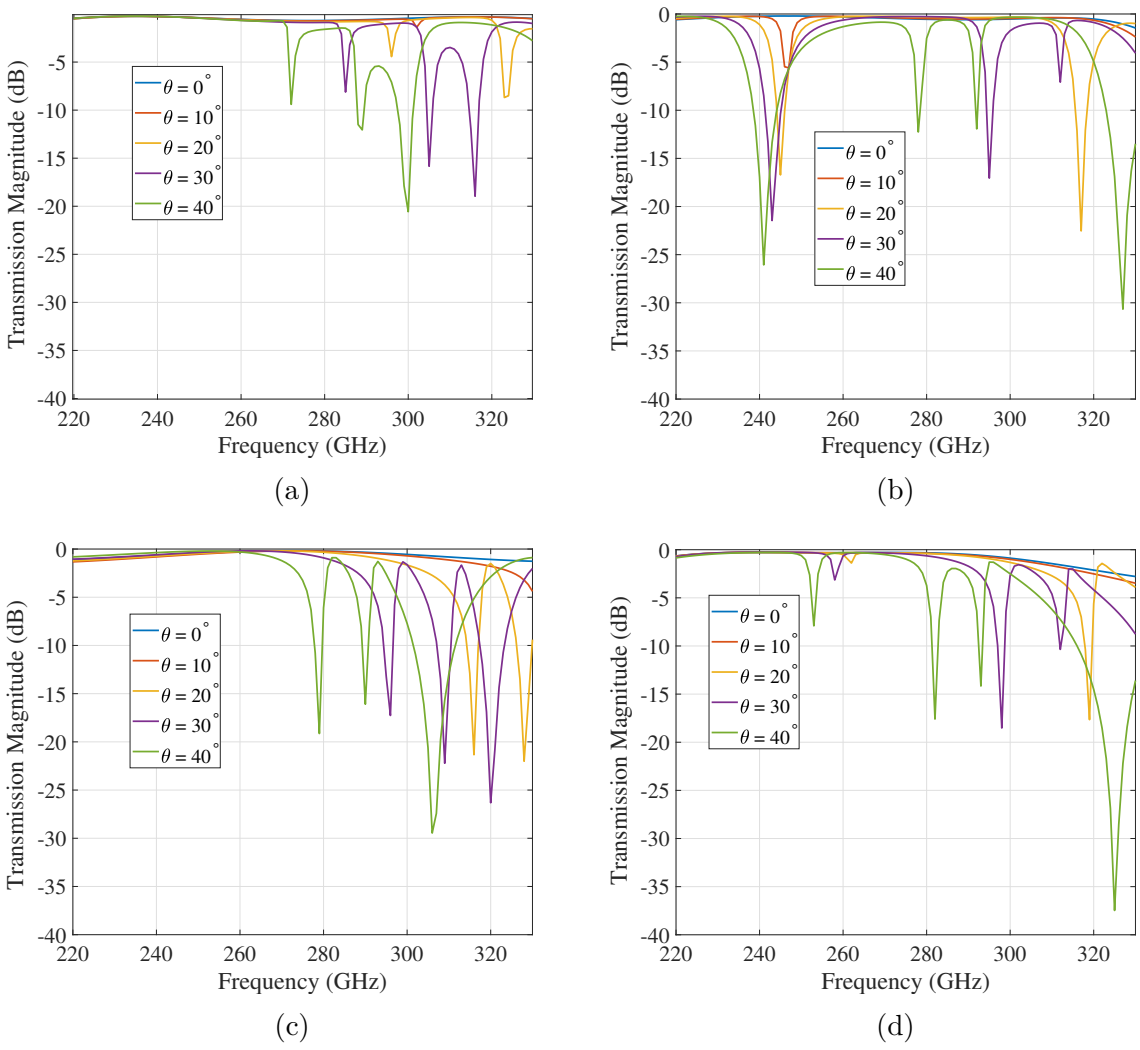

Figure 4.4: Transmission magnitude of the unit-cells in Figure 4.1 comprising the four rotators for different angles of incidence. (a) Rotator A, (a) Rotator B, (a) Rotator C and (a) Rotator D.

higher frequencies. This is caused by the onset of trapped grating lobes in the inner layer [79], leading to a significant magnitude drop. The only way to solve this problem is by reducing the periodical size of the unit-cell and use a substrate with smaller dielectric constant. Nevertheless, the problem is not related to free-space grating lobes, while the final transmitarray is a quasi-periodic structure that is illuminated with a certain edge taper from the focal source. Therefore, the impact will be much smaller. Nevertheless, since the design approaches presented in Chapter 2 were developed considering one nominal angle of incidence ($\theta = 0°$), a difference between simulated and realized radiation performance might be expected.

4.3 Experimental characterization of the unit-cells

A quasi-optical characterization of the transmission coefficient of the unit-cells is presented here. The measurement setup is shown in Figure 4.5(a). Two Flann 32240-20 horns were used, placed at a distance equal to 11 cm. Each material-under-test (MUT) consists of 50×50 unit-cells, with a size equal to 25×25 cm^2. Since the unit-cells exhibit anisotropic transmission, one of the two horns must be rotated by 90° once the MUT is placed, as shown in Figures 4.5(b) and (c). The rotation of the one horn was done manually, which required rotating all the structure together (horn and converter). This action probably introduced some displacement error, attempting to achieve the same link distance between the two setups, as well as a polarization orientation error between the two horns. In the case of the displacement error, both the magnitude and the phase of transmission coefficient are affected. In the case of the polarization orientation error, only the magnitude is affected, where the magnitude drop is related to the magnitude of the orthogonal component of the field between the two horns. Multiple measurements were done, in order to improve the accuracy of the measured results. An alternative approach would be to use other types of antenna, like a Gaussian-beam transmitarray antenna, as reported in [92]. This way, aside from the placement of the MUT, the setup would remain the same in Figures 4.5(b) and (c).

The results of the magnitude and phase of transmission are shown in Figure 4.6. Compared to the simulation results, where infinite periodic condition and Floquet Wave (FW) excitation were used, a magnitude drop is observed. The difference is larger for the unit-cell comprising Rotator A, shown in Figure 4.6(a). Except for the errors mentioned before, the first estimation was that this is caused by fabrication errors, introduced in the etching process of the metal layers, the final thickness of the bonding film and the overall material properties. In reality, most of the discrepancy is due to the different illumination, used in simulation and measurement. Specifically, the measured results include also the impact of the angle of incidence, as was shown before in the unit-cell design. To prove this assumption, a full-wave simulation, with the same setup as in measurement, was done for the unit-cell with Rotator A. As shown in Figure 4.6(a), a better agreement can be observed. However, the simulation required strong computational force and thus only the results for Rotator A were able to be extracted. Nevertheless, the fabricated unit-cell arrays exhibit less than 3 dB of insertion losses in the region of interest, proving that a PCB-based transmitarray design with good performance is possible at sub-THz

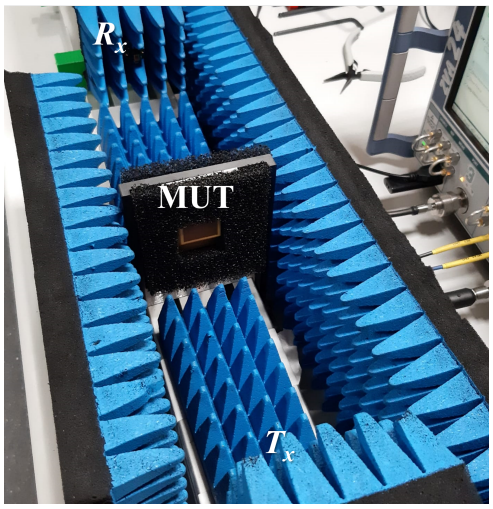

(a)

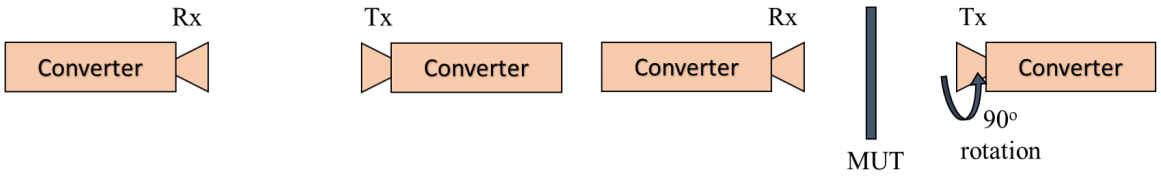

(b) (c)

Figure 4.5: (a) Measurement setup for the characterization of the unit-cells. Schemes of (a) the setup for the reference measurement and (c) the setup for the MUT measurement.

frequencies.

Finally, Figure 4.6(c) shows the relative phase of transmission, using the first unit-cell (Rotator A) as a reference. A very good agreement is observed, while the relative phase shift remains close to 45°. Even if the unit-cells are exhibiting smaller insertion losses, a possible error in the relative phase will deteriorate the performance in the transmitarray design and thus, this is also an important part of characterization.

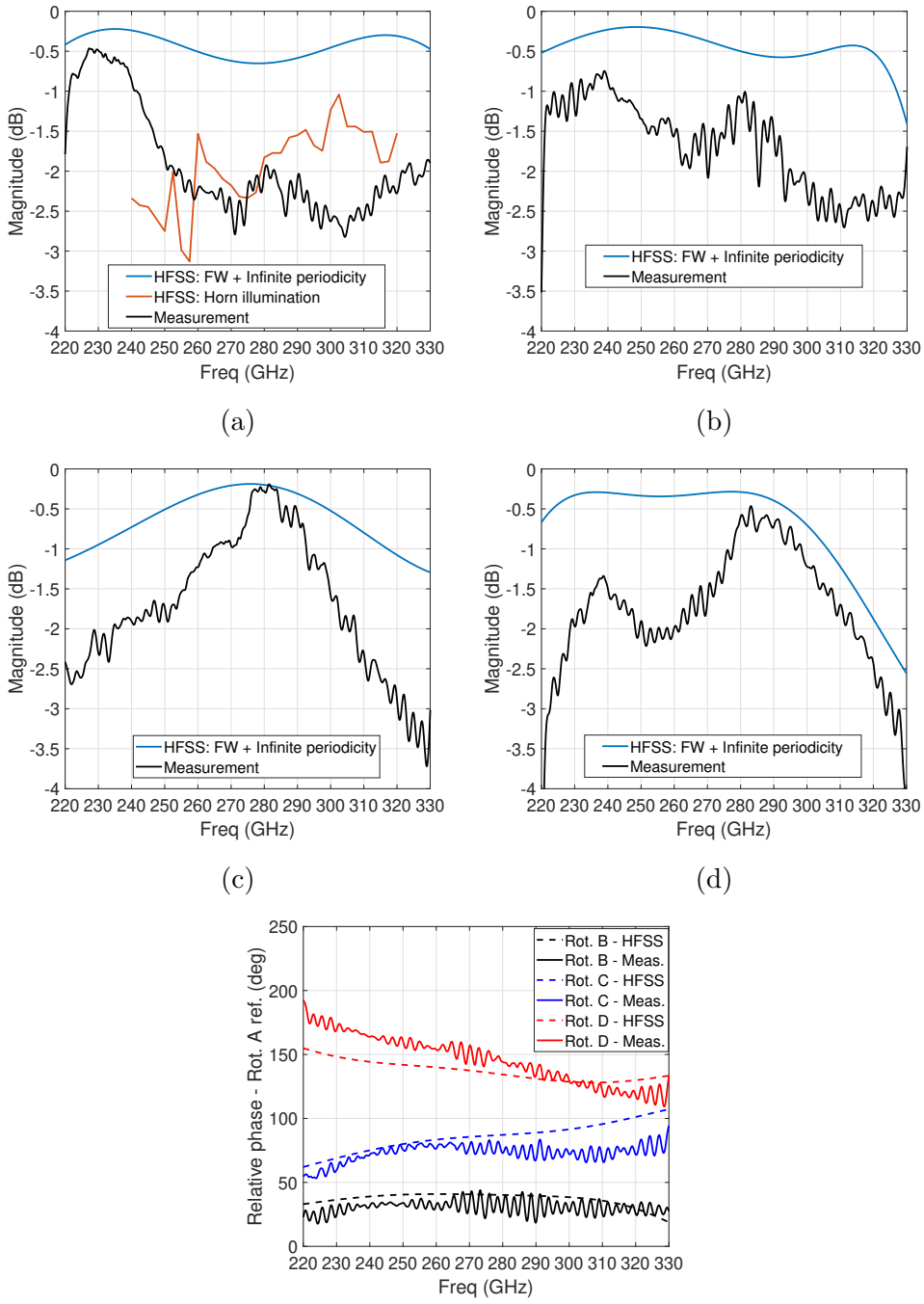

Figure 4.6: Results of the quasi-optical characterization of the transmission coefficient of the 4 types of unit-cells. Magnitude of transmission for (a) Rotator A, (b) Rotator B, (c) Rotator C and (d) Rotator D. (e) Relative phase of transmission, using the unit-cell with rotator A as a reference.

4.4 Design of antenna prototypes

The design of four PCB-based transmitarrays, namely A, B, C and D, comprising the previous rotator topologies is presented here. Two different focal sources were employed, as shown in Figure 4.7(a). They are both standard pyramidal horns, manufactured by Flann Microwave (models 32240), which have been mentioned in Chapter 2. They are copper electroformed on precision mandrels to ensure high accuracy and repeatability in fabrication. Three prototypes were synthesized using the 10 dBi horn, while the fourth one was designed using the 20 dBi horn. A plastic support was used to fix the lens at the selected distance from the horn. For all transmitarrays, the frequency of optimization is set to 280 GHz, which is near the center of the zone of interest. The phase distribution was calculated to steer the beam at broadside.

Prototypes A and B

The first two prototypes consist of a 40×40 elements transmitarray (20×20 λ^2 size at 300 GHz) and the 10 dBi horn (Flann 32240-10) used as a focal source. Despite the same feed and lens size, the two transmitarrays are optimized for a different focal distance. Specifically, prototype A is synthesized to achieve a gain close to the maximum achievable one for this system, while prototype B was designed to provide an improved gain bandwidth compared to prototype A.

Using the ray tracing technique, a parametric analysis on the focal distance is done, as shown in Figure 4.8. The maximum achievable gain is obtained at $F = 11$ mm, leading to a focal-to-diameter ratio $F/D = 0.55$. The simulated gain is 33.3 dBi and the corresponding aperture efficiency is about 48.6% at 280 GHz. This was the selected focal distance to optimize and design prototype A. In case of improving the gain bandwidth, a straightforward approach is to slightly increase the focal distance. This will introduce additional spillover losses, decreasing the maximum gain, but the antenna becomes more wideband [93]. The incident wave on the transmitarray becomes less sensitive to the spatial phase delay, reducing the phase errors that occur at frequencies other than the frequency of optimization. A clear illustration of this impact can be observed at the phase distribution of prototypes A and B through the number of repetitions of one full phase circle (360°), as shown in Figure 4.9. Increasing the phase repetitions on a transmitarray that is optimized at a single frequency results in a more narrowband system. Finally, the selected focal distance for prototype B is $F = 20$ mm ($F/D = 1$), giving a good trade-off between

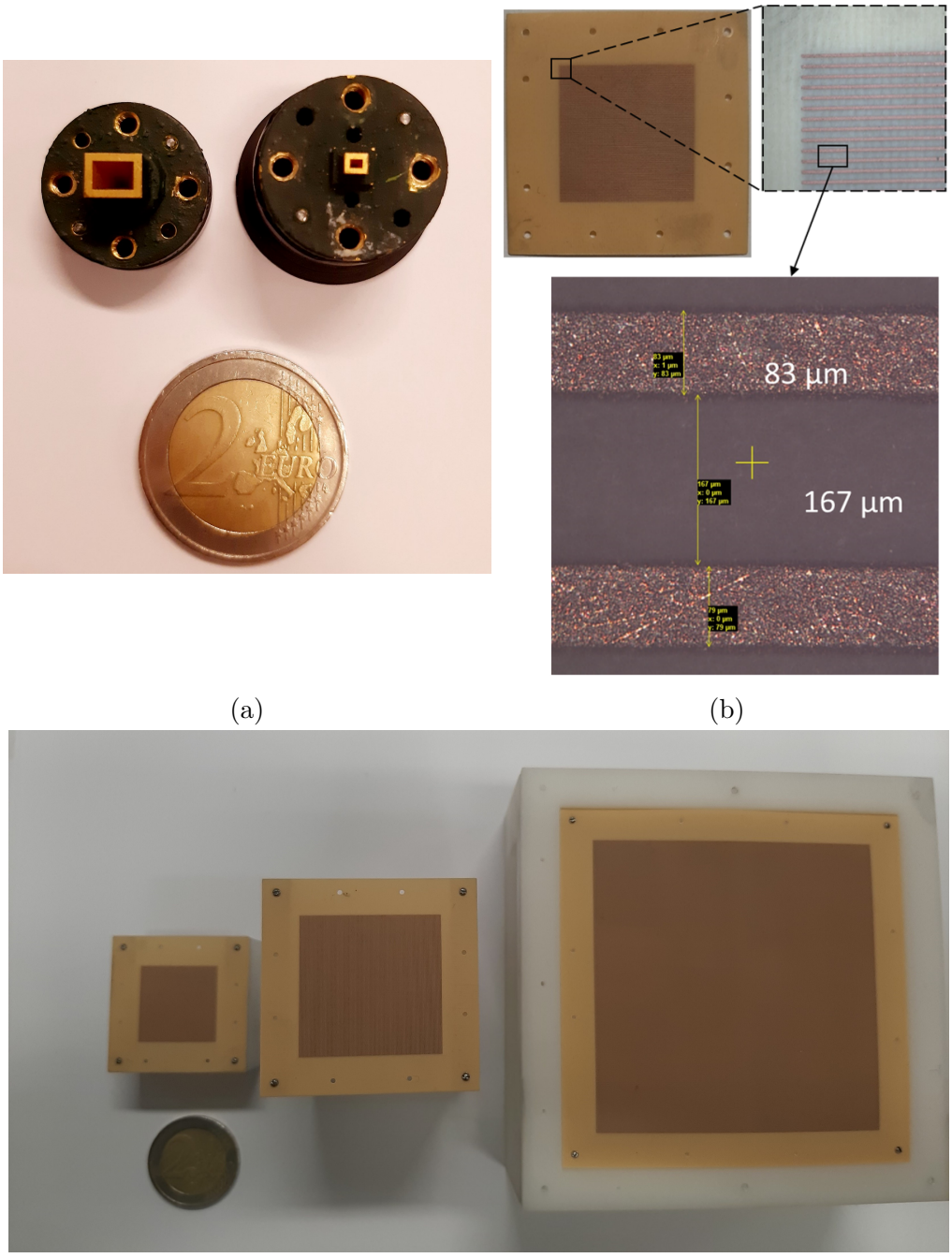

(a) (b)

(c)

Figure 4.7: (a) Photograph of the employed pyramidal horns. Model 32240-10 is shown on the right and model 32240-20 is shown on the left. (b) Close-up view of one of the fabricated transmitarrays. (c) Photograph of the three employed sizes of the four transmitarrays. Prototypes A and B exhibit the same size, shown on the left. Prototype C is shown on the right and prototype D in the middle.

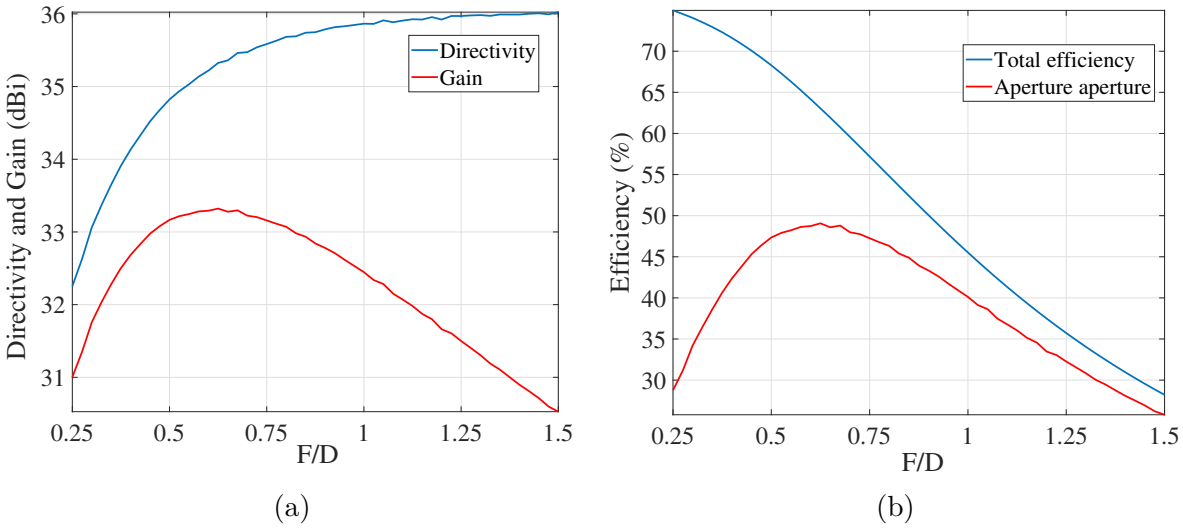

(a) (b)

Figure 4.8: Simulated (a) gain and (b) efficiency as a function of the focal distance for a 40×40 elements transmitarray using a 10 dBi horn.

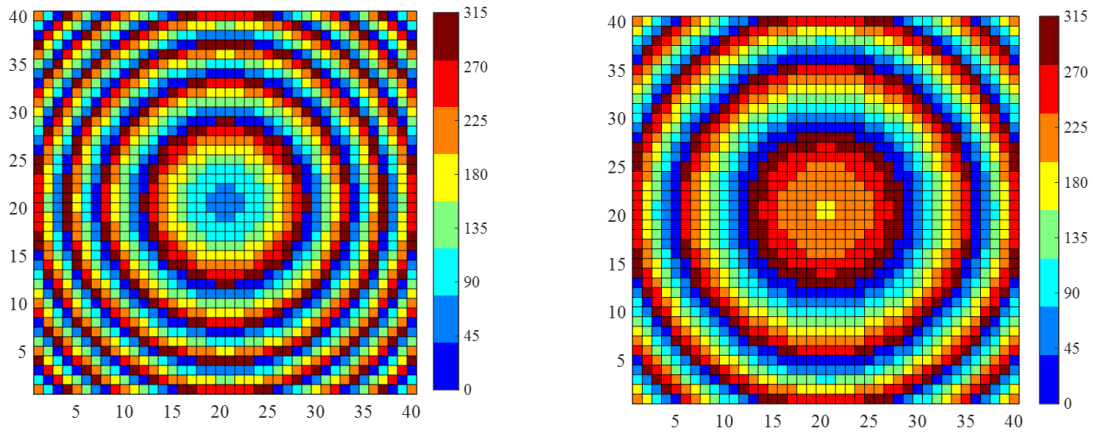

(a) (b)

Figure 4.9: Phase distribution of prototypes (a) A and (b) B, calculated at 280 GHz.

the gain drop and the bandwidth improvement. The simulated gain is 32.4 dBi and the corresponding aperture efficiency is about 40.1% at 280 GHz. For prototype A, the 1 dB and 3 dB gain bandwidth are 30 GHz (10.5%) and 55 GHz (19.3%), respectively. For prototype B they are 45 GHz (15.5%) and 85 GHz (29.3%), respectively.

Prototypes C and D

These prototypes are designed considering the system requirements for the case scenarios of "NEXT5G" project, presented in Chapter 1. Specifically, prototype C is designed for point-to-point backhaul links and stationary outdoor connections of a large range, up to 300 meters. The most important requirement is to achieve an ultra-high gain, more than 40 dBi, providing a beam with extremely small beamwidth and an aperture efficiency as high as possible. The selected transmitarray exhibits a very large size of 140×140 elements (70×70 λ^2 at 300 GHz) and is illuminated by the 10 dBi Flann horn. The selected focal distance for maximum gain is set to $F = 42$ mm, giving $F/D = 0.6$. At this distance, the simulated peak gain and aperture efficiency are about 44.55 dBi and 51.4%, respectively, at 285 GHz.

Prototype D was designed to provide both high gain and wideband operation, in order to enable very high data-rate in the system. The main problem is that for large transmitarrays, the antenna becomes narrowband, due to the reason discussed in Chapter 2 and for prototypes A and B. To overcome this issue, a more directive focal source can be considered, thus the horn Flann 32240-20 is used. Although this will lead to a higher F/D ratio, the problem is minor, thanks to the small design features at very high frequencies. The selected transmitarray for this prototype has a size of 60×60 elements (30×30 λ^2 at 300 GHz), targeting for a gain higher than 35 dBi and close to 40 dBi. The corresponding focal distance to achieve maximum gain is calculated at 55 mm, which gives an $F/D = 1.83$. Finally, the simulated peak gain is about 37.68 dBi at 285 GHz and the aperture efficiency is 59.3% at 280 GHz. The corresponding 1 dB and 3 dB gain bandwidths are 56 GHz (19.0%) and 90 GHz (34.0%), respectively.

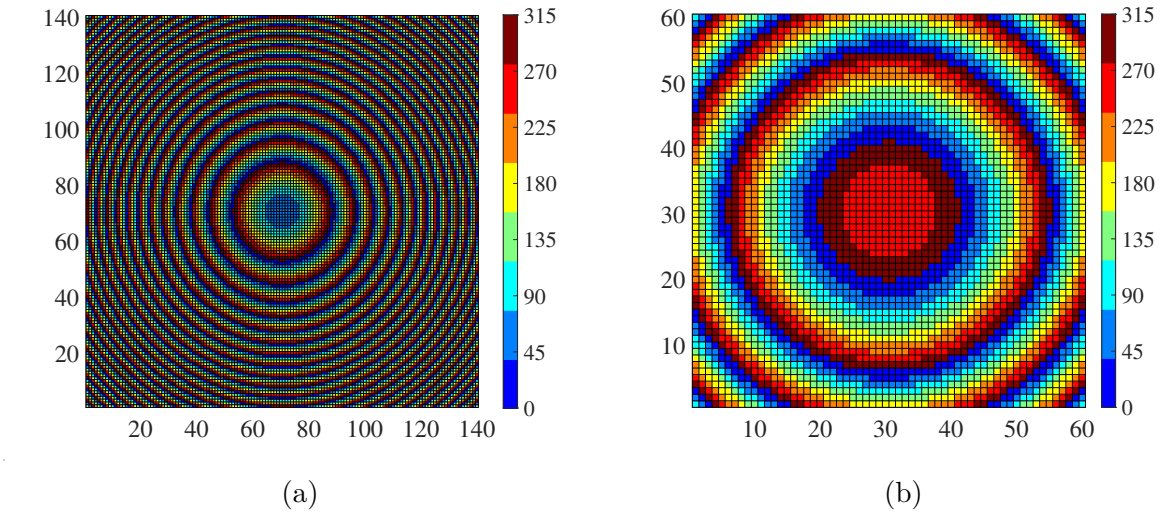

(a) (b)

Figure 4.10: Phase distribution of prototypes (a) C and (b) D, calculated at 280 GHz.

4.4.1 Experimental results

The far-field radiation of all the prototypes was characterized in an anechoic chamber. Since the transmitarray antenna is physically larger than a half-wavelength, the far-field is defined in terms of the Fraunhofer distance. Therefore, the minimum distance is calculated as

$$d_F = \frac{2D_m^2}{\lambda}\,. \tag{4.1}$$

As largest dimension, D_m, we can consider the diagonal of the transmitarray ($D_m{=}\sqrt{2}D$). Nevertheless, the array is not radiating uniformly, due to the illumination, and thus the actual dimension will be smaller. In any case, using the expression (4.1), we can get a safe estimation of the minimum link distance. Prototypes A, B and D were tested in the anechoic chamber shown in Figure 4.11(a). The link distance is about 6 meters. Prototype C was tested in the larger anechoic chamber of CEA Leti, shown in Figure 4.11(b), as its physical size was too large for the smaller chamber. In the second setup, the link distance is about 12 meters. In both cases, the setup is similar, using the same instruments with different cables to cover the link distance. One vector network analyzer (VNA) from Rohde & Schwarz was used. The model is the R&S ZVA24, shown in Figure 4.11(c), with an operating frequency at 24 GHz. Two frequency converters were used for a frequency up-conversion to 220 – 330 GHz. The model is the R&S ZC330, as shown in Figure 4.11(d). Finally, two motion controllers, each one at one end of the link, were used. The motion controller in the T_x side was used to adjust the azimuth angle, either at 0° or at 90°. The

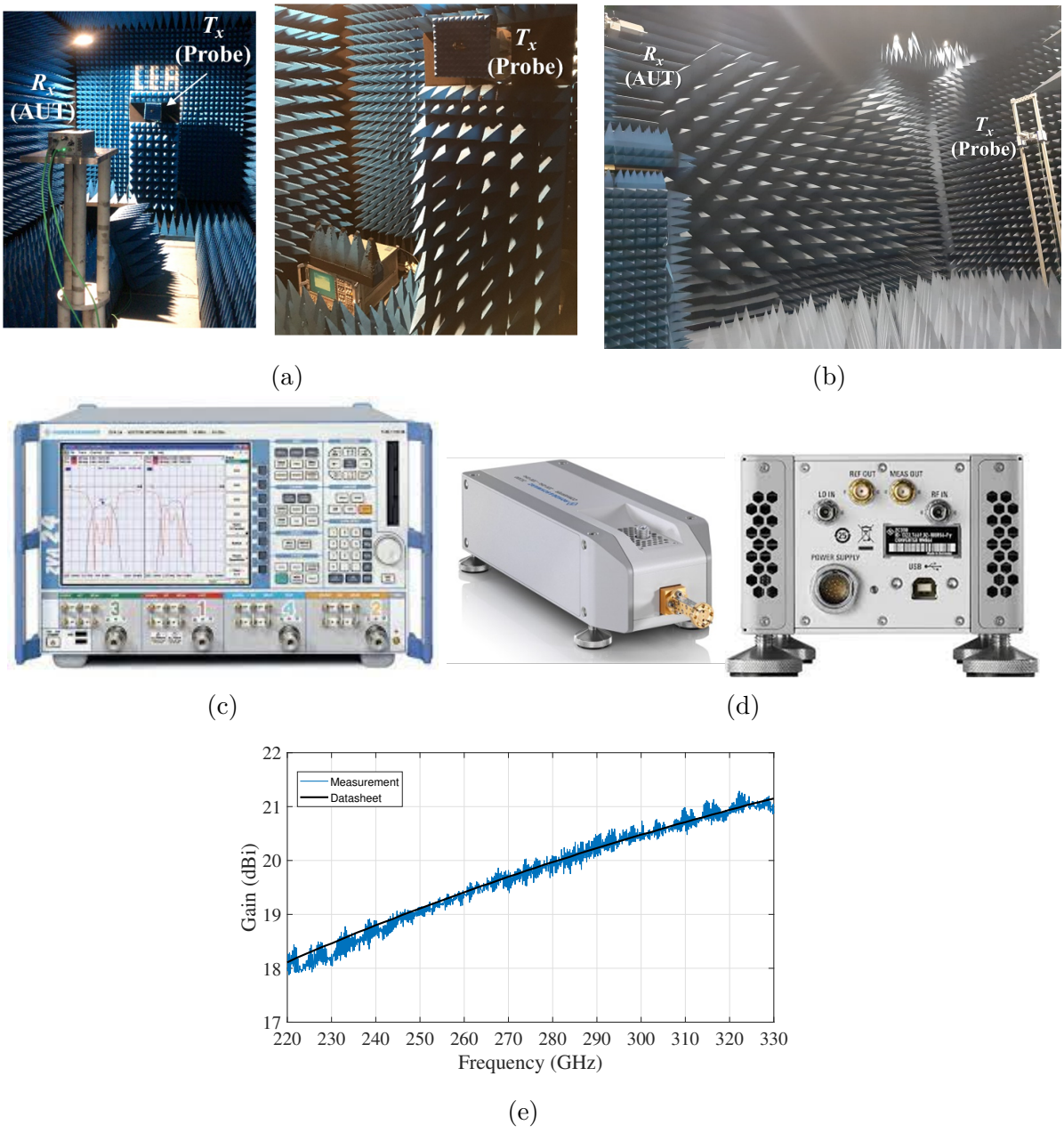

Figure 4.11: (a) Measurement setup of prototypes A, B and D in the small anechoic chamber. (b) Measurement setup of prototype C in the big anechoic chamber. (c) Vector network analyzer and (d) frequency converter, used in the two setups. (d) Measured gain of the 20 dBi Flann horn, used as a reference in the setup.

motion controller in the R_x side was used to scan in the elevation angle and obtain the radiation patterns in the two principle planes, i.e. E-plane and H-plane. Finally, the 20 dBi Flann horn was used as a probe in both sides in the two chambers to calculate the

reference of the system.

The calculation of the absolute gain is based on the calculation of the transmission coefficient between the receiving and the transmitting side. This coefficient is calculated in the VNA as

$$S_{21}^{REF/AUT} = \frac{\beta_2^{REF/AUT}}{\alpha_1}\,, \tag{4.2}$$

where $\beta_2^{REF/AUT}$ is the measured wave on the T_x for each case and α_1 is the measured wave on the R_x. Therefore, the measured gain will be equal to

$$G_{meas}^{co/cross}(\theta, \phi = 0°, 90°) = \left| \frac{S_{21}^{AUT}(\theta, \phi = 0°, 90°)}{S_{21}^{REF}} \right|. \tag{4.3}$$

In expression (4.3), the measured co-polarized gain is calculated having the focal source and the probe orthogonally polarized, due to the anisotropy of the transmitarray. The cross-polarized gain is measured when the two horns are aligned. In total, four patterns, two for each plane, were measured at each prototype.

Prototype A

To validate the ray tracing technique, prototype A was also simulated using Ansys HFSS. The full-wave simulation required about 300 GB of RAM and several days to complete, even for a few frequency points. This highlights the importance of developing accurate and time efficient numerical solutions for large antenna systems.

The peak gain and aperture efficiency are plotted as a function of frequency in Figure 4.12 for all three types of characterization (full-wave simulation, numerical simulation, measurement). A good agreement between full-wave and numerical simulation is found, showing that the impact of the angle of incidence on the transmission properties of the unit-cells is not as significant as in the case of an infinite uniform periodic array. However, a larger frequency shift, about 10 GHz (3.5%), between numerical simulation and measurement can be observed. This was caused by a small error in the focal distance, due to the realized size of the mechanical support. The error is around 0.5 mm, giving $F =$ 11.5 mm approximately. Finally, the antenna exhibits a maximum measured gain of 32.2 dBi at 307 GHz, with an aperture efficiency of 31.8%. The 1 dB and 3 dB relative gain bandwidths are 9.5% and 18.9%, respectively.

The beam shape remains stable between 270 and 330 GHz in the two orthogonal cut planes, as shown in Figure 4.13. The half-power beamwidth (HPBW) is about 3.2° in the

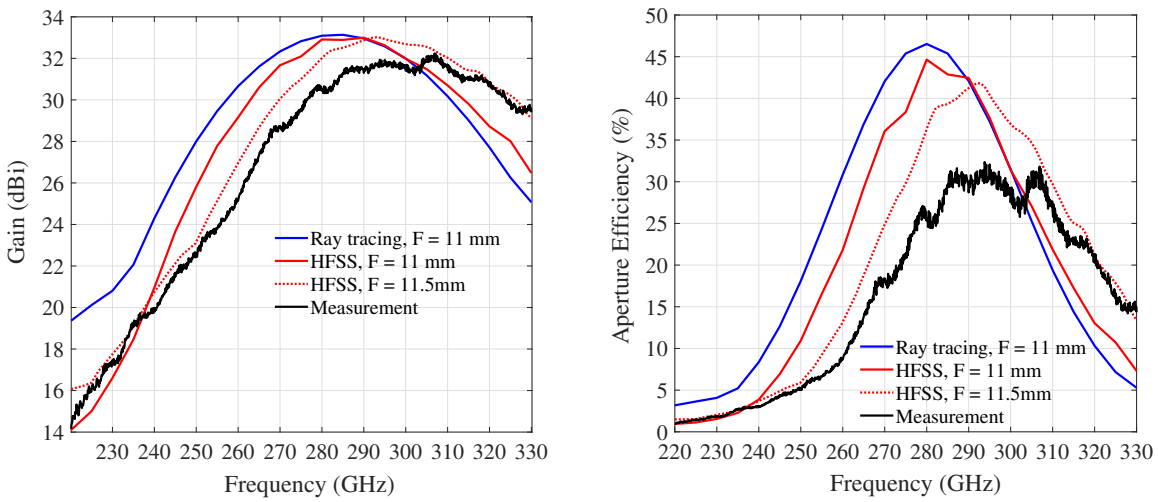

(a) (b)

Figure 4.12: Simulated and measured (a) gain and (b) aperture efficiency of prototype A.

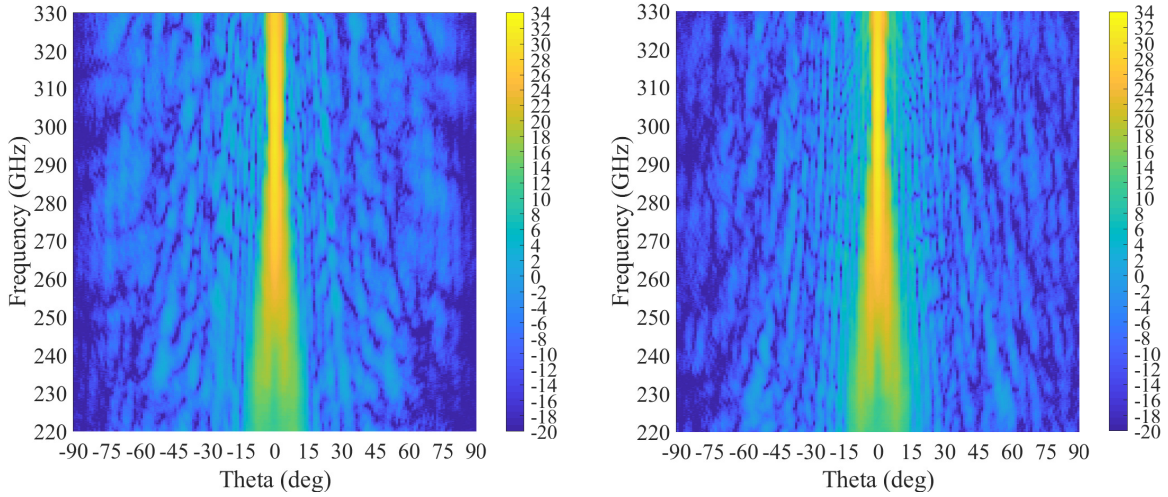

(a) (b)

Figure 4.13: Measured gain of prototype A as a function of elevation angle and frequency in the (a) H- and (b) E-plane.

3 dB gain bandwidth. The radiation pattern at two frequency points is shown in Figure 4.13. The sidelobe level is greater than -22 dB. The cross-polarization discrimination is greater than -30 dB. A comparison of the pattern between the ray tracing technique and the measurements is shown in the other prototypes.

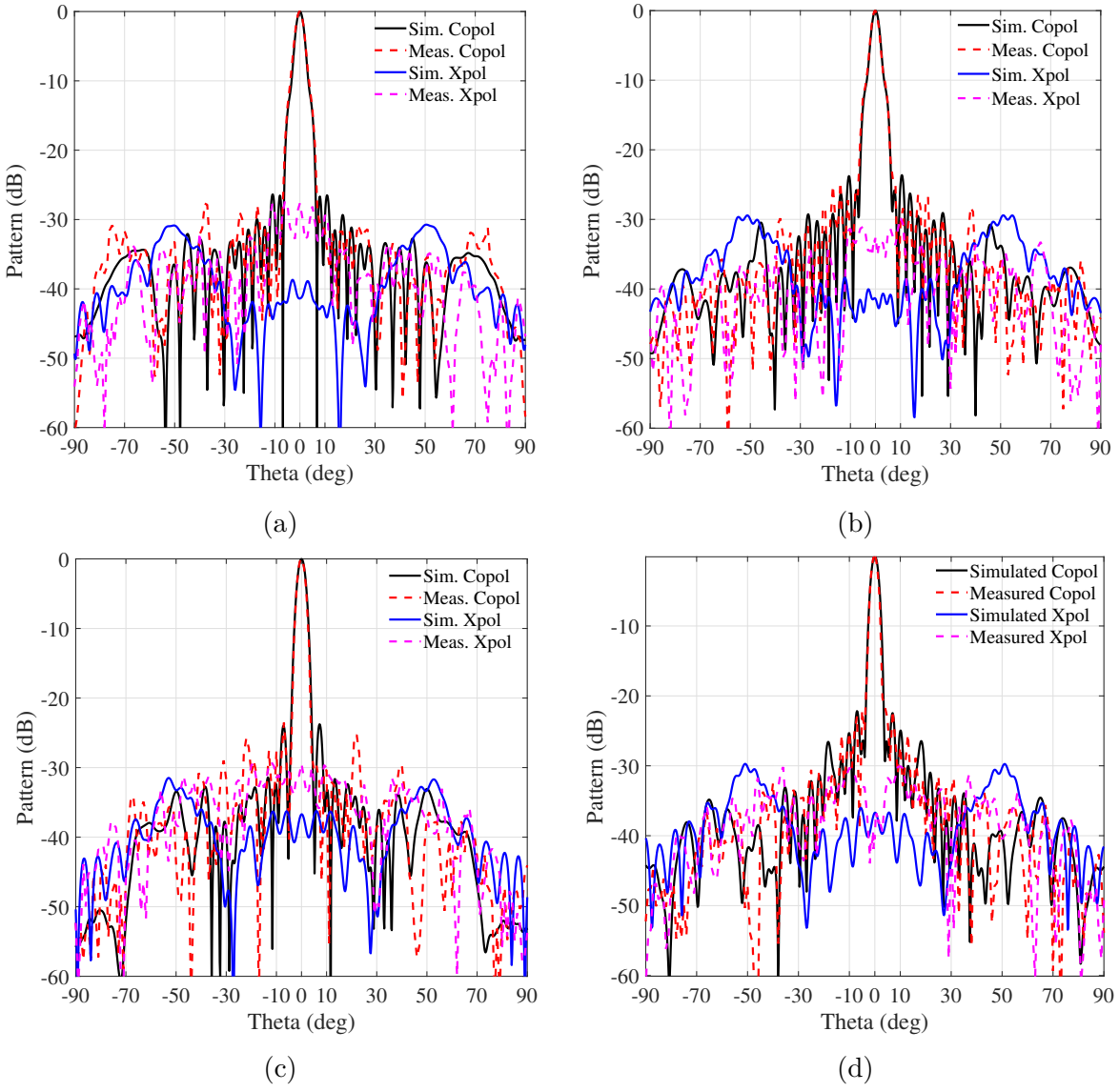

Figure 4.14: Co- and cross-polarized simulated (HFSS) and measured radiation pattern of prototype A. (a) H-plane at 280 GHz, (b) E-plane at 280 GHz, (c) H-plane at 300 GHz and (d) E-plane at 300 GHz.

Table 4.2: Power budget and radiation characteristics of prototype A.

	Simulation	Measurement
Frequency	295 GHz	295 GHz
Focal source gain	10.6 dBi	11.3 dBi
Theoretical directivity of a uniform aperture	36.8 dBi	-
Quantization loss	0.3 dB	-
Broadside directivity	34.5 dBi	-
Spillover loss	1.0 dB	-
Broadside gain	32.9 dBi	31.9 dBi
Power efficiency	69.1%	55.0%
Aperture efficiency	40.4%	32%

Prototype B

A picture of this prototype mounted on the frequency converter is shown in Figure 4.15(a). The peak gain and aperture efficiency as a function of frequency are shown in Figure 4.15(b). The maximum measured gain is 32.2 dBi at 287 GHz, with an aperture efficiency of 36.5%. The antenna attains approximately 29.3 GHz of 1-dB bandwidth and 70.4 GHz of 3 dB bandwidth, which are 10.5% and 25.1% at 280 GHz, respectively. The aperture efficiency is equal or greater than 24% between 265 and 310 GHz. To emphasize this performance, the measured gain is compared in Figure 4.15(b) with an ideal TA, i.e. a reflectionless lens providing perfect phase compensation. It can be seen that the gain loss is only about 1.9 dB in the 3 dB bandwidth.

The gain as a function of the elevation angle and the frequency in the two principle planes is shown in Figure 4.16. The half-power beamwidth is about 3.4° in the 3 dB bandwidth. The radiation pattern at two frequencies is shown in Figure 4.17 for the H- and E-plane cuts. The simulated (ray tracing) and measured results of the patterns are in good agreement and the maximum sidelobe level is about -19 dB and -15 dB in the H- and E-plane, respectively. The good agreement between the simulated and the measured co-polarized radiation patterns validates the ray tracing technique. On the other hand, a difference in the cross-polarized patterns can be observed. This was expected, as the ray tracing technique does not take into account the spillover radiation from the focal source. In this system, the impact of the focal source on the radiation pattern is observed at the cross-polarization, due to the anisotropy of the transmitarray and the polarization conversion. A better agreement between measured and simulated results can be found

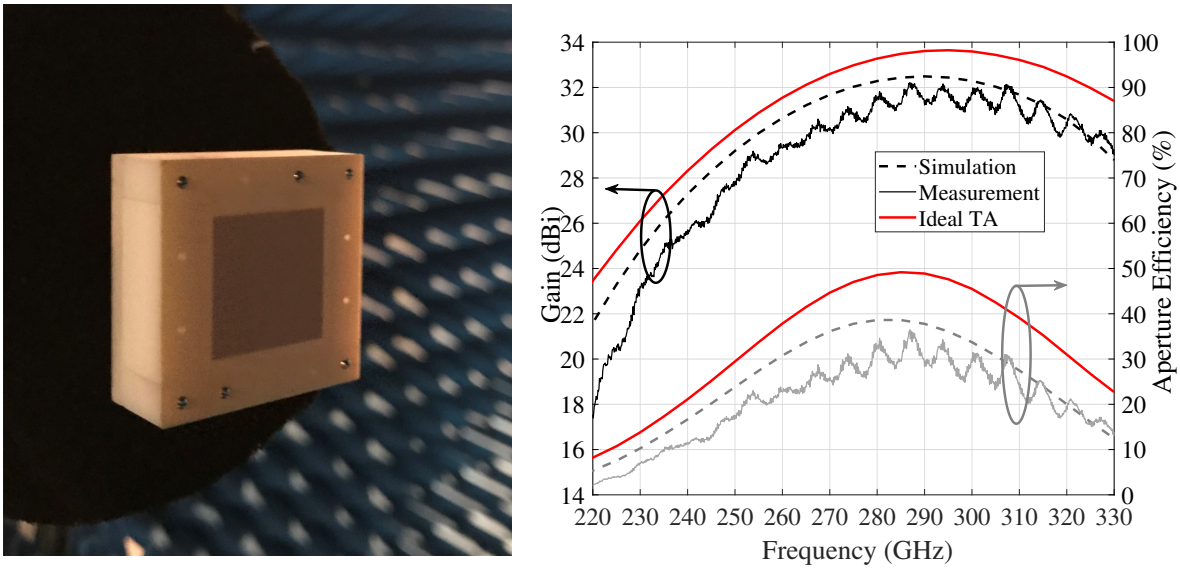

(a) (b)

Figure 4.15: (a) View of prototype B. (b) Simulated and measured results of the gain and aperture efficiency as a function of frequency. The red curve depicts the gain and aperture efficiency of an ideal transmitarray on the same setup, which can be used a a reference for maximum performance.

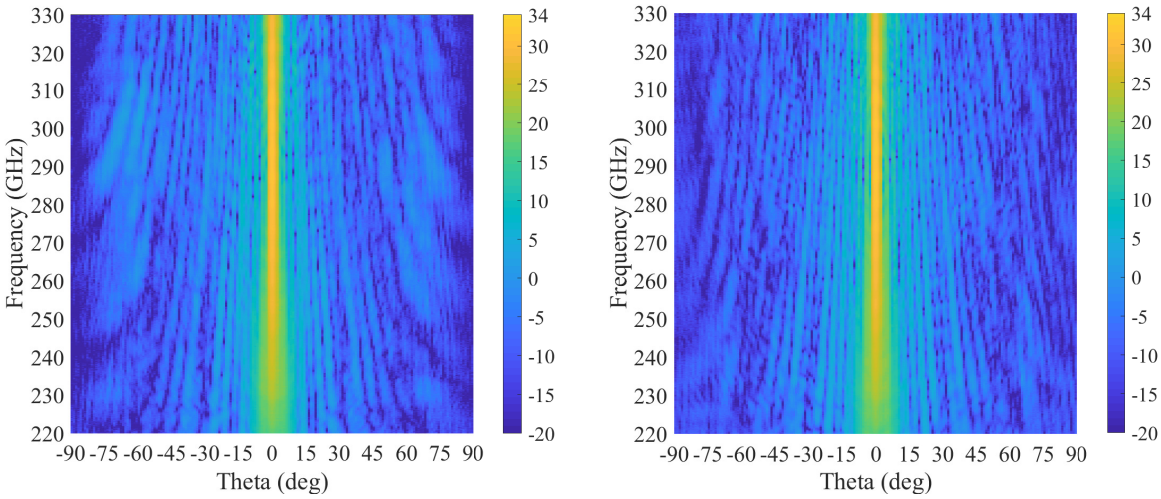

(a) (b)

Figure 4.16: Measured gain of prototype B as a function of elevation angle and frequency in (a) H- and (b) E-plane.

using the physical optics approach, which is presented later in prototype C.

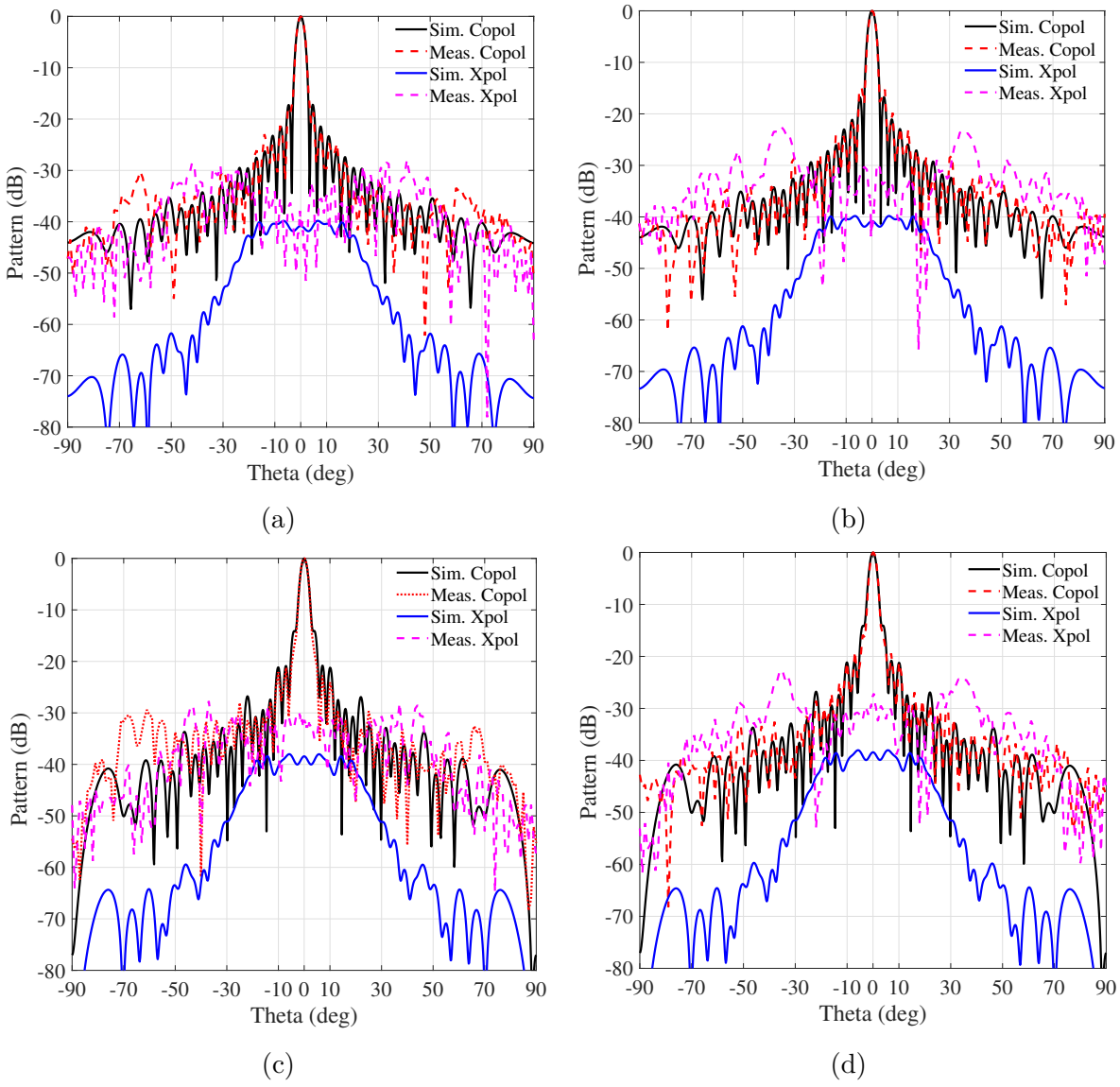

Figure 4.17: Co- and cross-polarized simulated (HFSS) and measured radiation pattern of prototype B. (a) H-plane at 280 GHz, (b) E-plane at 280 GHz, (c) H-plane at 300 GHz and (d) E-plane at 300 GHz.

Table 4.3: Power budget and radiation characteristics of prototype B.

	Simulation	Measurement
Frequency	300 GHz	300 GHz
Focal source gain	10.7 dBi	12 dBi
Theoretical directivity of a uniform aperture	37.0 dBi	-
Quantization loss	0.3 dB	-
Broadside directivity	35.0 dBi	-
Spillover loss	2.8 dB	-
Broadside gain	32.3 dBi	31.7 dBi
Power efficiency	53.7%	46.7%
Aperture efficiency	33.7%	31.5%

Prototype C

A photograph of prototype C is shown in Figure 4.18. To the best of the author's knowledge, this is one of the largest fabricated prototypes reported in this frequency region, exhibiting a size of 70×70 λ^2 at 300 GHz. As mentioned before, the antenna was measured in the large anechoic chamber, in order to satisfy far-field conditions for a more accurate characterization of the radiation pattern and mainly the sidelobe level.

The measured peak gain and the aperture efficiency as a function of frequency are shown in Figure 4.19(a). The maximum measured gain is 43.34 dBi at 284.35 GHz, with an aperture efficiency of 39.0%. The antenna has approximately 10.0 GHz of 1 dB and 17.0 GHz of 3 dB gain bandwidth, which are 3.5% and 6.0% at 280 GHz, respectively. These results demonstrate a narrowband system, which is expected as explained before. Moreover, compared to the ray tracing technique, there is a small frequency shift of 5 GHz (1.7%), which is almost the same as in the case of prototype A, where both prototypes have been synthesized for a similar F/D (0.55 and 0.6). This is expected, as it is related to the modelling of the unit-cells and the phase center of the focal source. Using the physical optics model of Chapter 2, the frequency shift can be further reduced, as shown in Figure 4.18(b). Nevertheless, the results of the ray tracing are still in good agreement.

The measured radiation pattern as a function of both elevation angle and frequency in the two principle planes is shown in Figure 4.19. The main lobe is very stable in the 3 dB gain bandwidth, exhibiting HPBW equal to only 1° in the same region. An introduction of holes in the side walls of the mechanical support was considered, in order to eliminate a small sidelobe level discrepancy, as it was observed in the other prototypes.

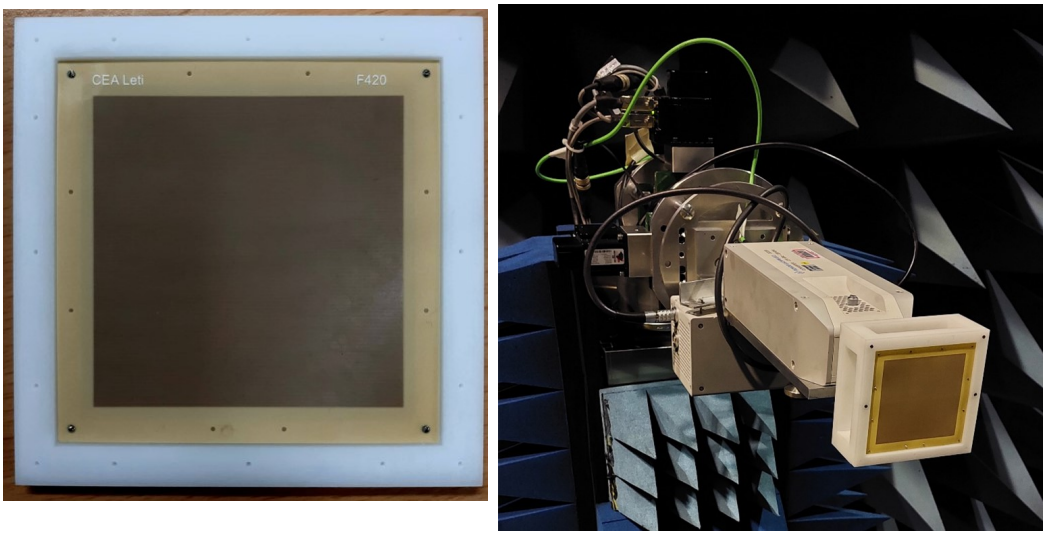

(a) (b)

Figure 4.18: (a) Photograph of the transmitarray used for prototype C and (b) view of the antenna mounted on the setup.

This impact is more obvious in prototype D, as will be presented later. A very good agreement in the co-polarization radiation pattern can be observed in Figure 4.20. The maximum sidelobe level is about -16.7 dB and -22 dB in the H- and E-plane, respectively. Figure 4.21 shows the cross-polarized radiation pattern at 285 GHz. The cross-polarization level is less than -40 dB in both planes. As mentioned in prototype B, there is a difference between the measured pattern and the simulated one using ray tracing technique, caused by the spillover radiation of the focal source. To solve that issue, one way is to superpose the far-field of the transmitarray antenna and the focal source, leading to a somewhat better agreement. Nevertheless, a more rigorous approach is to define a spillover area on the plane of the transmitarray, as explained in the physical optics approach. The results of the cross-polarization pattern including a spillover area are shown in the same Figure. The additional margin area at each side of the transmitarray is set as 10 mm in the simulation.

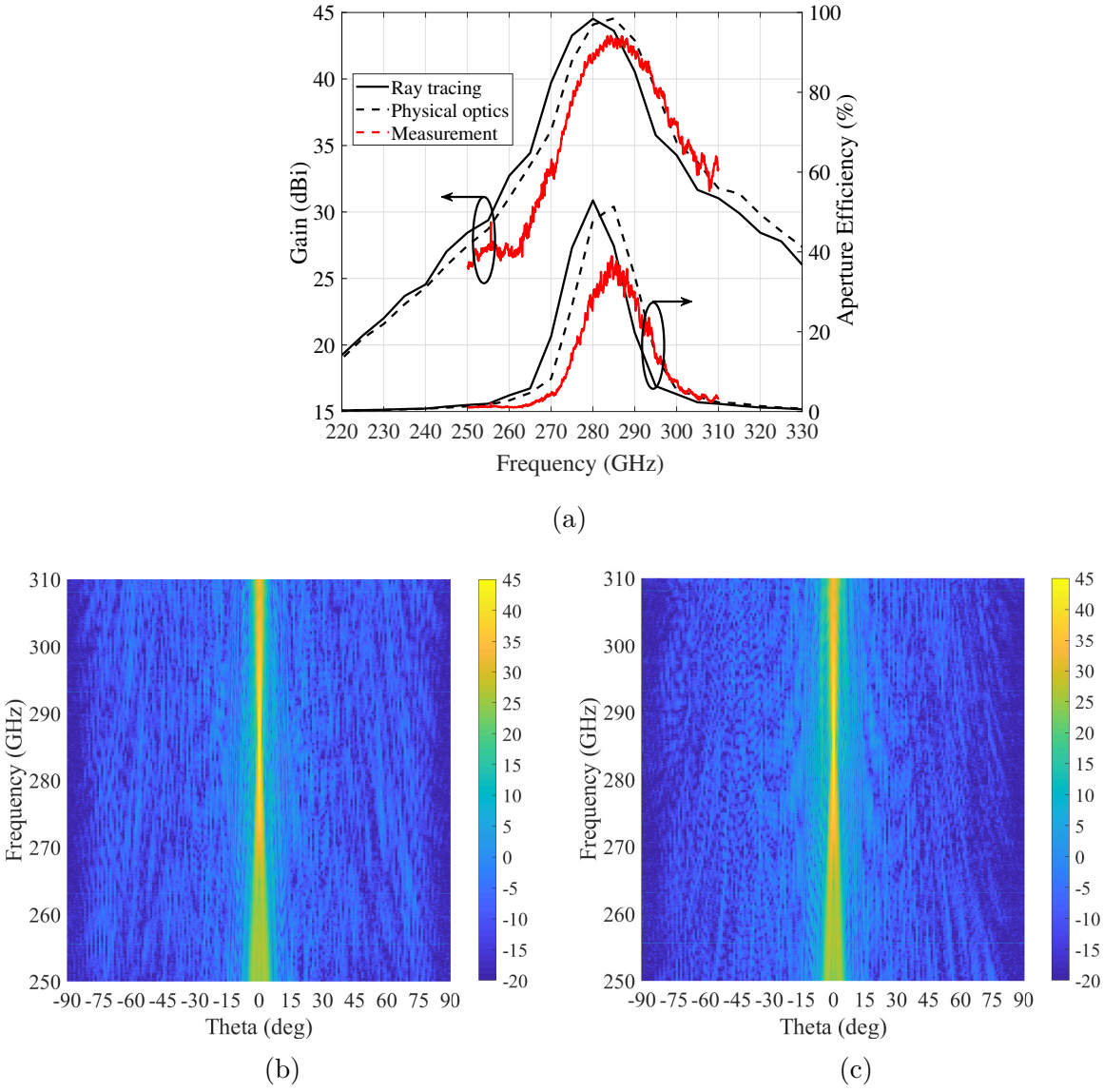

Figure 4.19: (a) Results of the gain and the aperture efficiency as a function of frequency, including a numerical simulation using the physical optics technique. Measured gain of prototype C as a function of elevation angle and frequency in (b) H- and (c) E-plane.

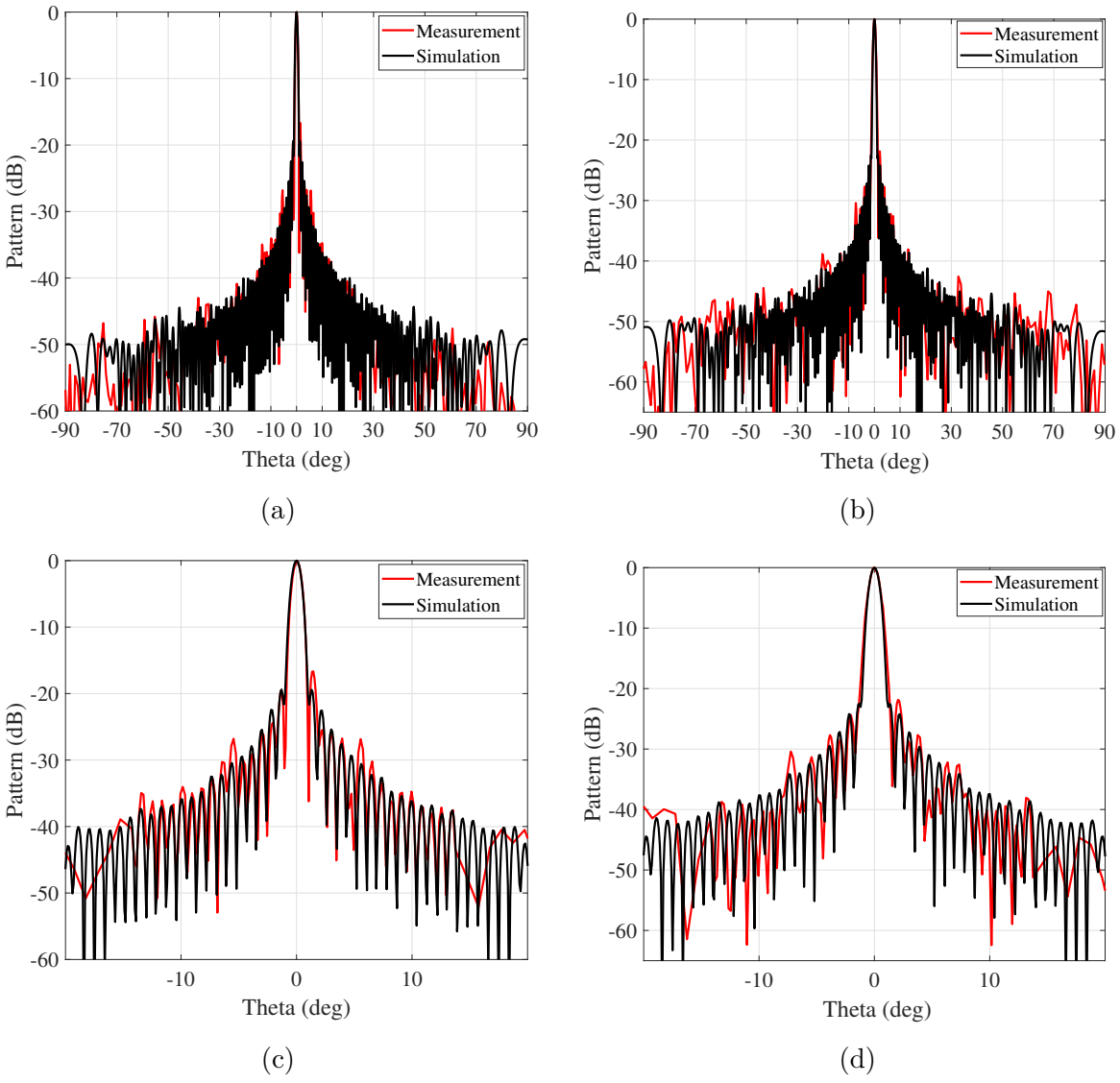

Figure 4.20: Co-polarized radiation pattern of prototype C in (a) H-plane and (b) E-plane at 285 GHz. The same pattern is shown in zoomed view for the (c) H-plane and (d) E-plane, for better comparison.

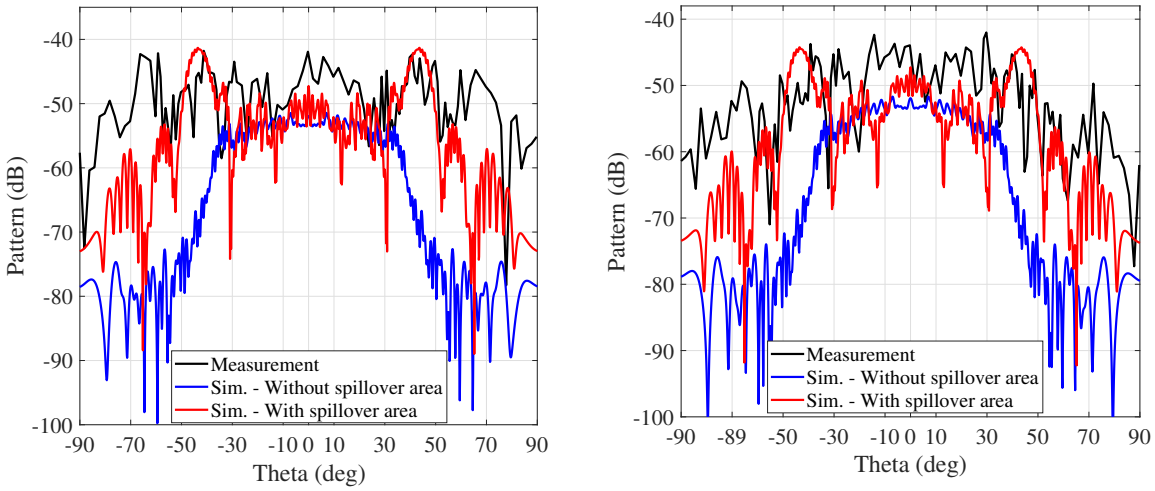

Figure 4.21: Cross-polarized radiation pattern of prototype C in (a) H-plane and (b) E-plane at 285 GHz. Using the physical optics technique and adding a spillover area around the transmitarray, the agreement is improved.

Table 4.4: Power budget and radiation characteristics of prototype C.

	Simulation	Measurement
Frequency	285 GHz	285 GHz
Focal source gain	10.3 dBi	11.3 dBi
Theoretical directivity of a uniform aperture	47.4 dBi	-
Quantization loss	0.3 dB	-
Broadside directivity	45.1 dBi	-
Spillover loss	1.1 dB	-
Broadside gain	44.0 dBi	43.0 dBi
Power efficiency	77.6%	61.6%
Aperture efficiency	45.7%	37.7%

Prototype D

The antenna prototype is shown in Figure 4.22(a). The measured peak gain is 37.0 dBi at 290.9 GHz, with an aperture efficiency of 47.2%, as shown in Figure 4.22(b). The maximum aperture efficiency is 48.6% at 279.4 GHz, which is close to the optimization frequency, and it is more than 40.0% between 250 and 300 GHz. The measured 1 dB gain bandwidth is approximately 56 GHz, from 264 to 320 GHz, which is about 19.0%, and the measured 3 dB gain bandwidth is more than 85 GHz (>30%), demonstrating a very wideband behavior. As showed in prototype B, here the measured gain is only 1.4 dB lower than the value that could be reached using an ideal TA.

The shape of the beam is very stable across the frequency range, as shown in Figure 4.23. The half-power beamwidth (HPBW) is approximately 2° in the 1-dB gain bandwidth, in both principal planes. The radiation pattern at two frequency points is shown in Figure 4.24. The first sidelobe level is about -24.6 dB and -25.8 dB in the H- and E-plane, respectively. A sidelobe level discrepancy between simulation and measurements is observed in the H-plane, caused by the impact of the mechanical support that is placed in this side of the antenna, as shown in Figure 4.22(a). The cross-polarization discrimination is greater than 26.0 dB across the entire band. Due to the mechanical support, the cross-polarization is suppressed in the H-plane and without the existence of the support, the actual level is as the one shown in E-plane. This is confirmed by adding the cross-polarization pattern simulated using the physical optics approach. The spillover area is set to 40 mm at each side of the transmitarray. A very good agreement up to ±40° of elevation angle can be observed. To further improve the results at the region outside of ±40°, the spillover area should be further increased, which will also increase the computational time.

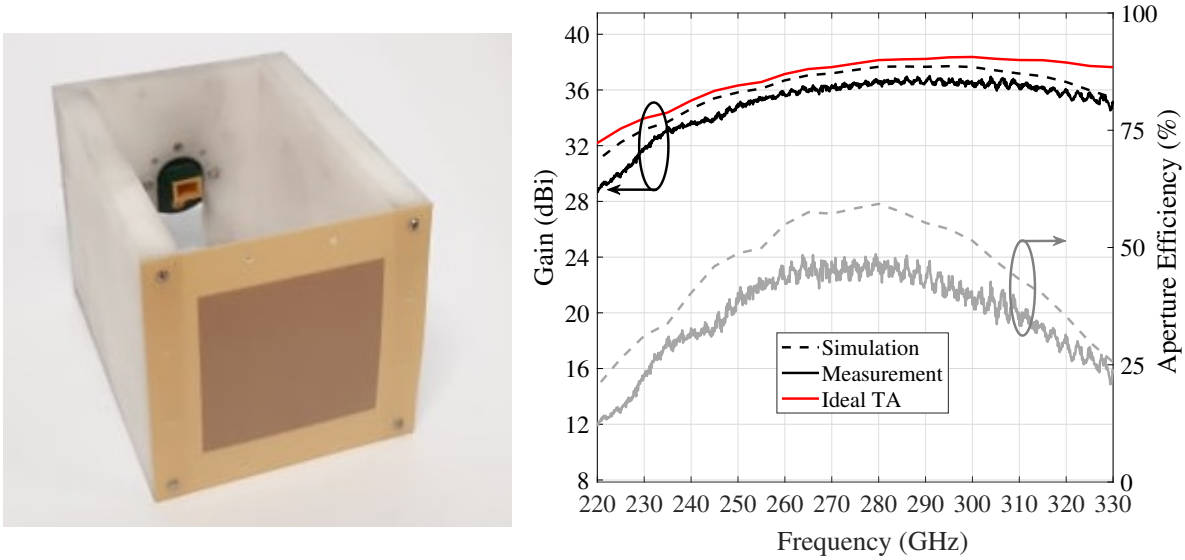

(a) (b)

Figure 4.22: (a) View of prototype D mounted on the horn. (b) Simulated and measured results of the gain and aperture efficiency as a function of frequency.

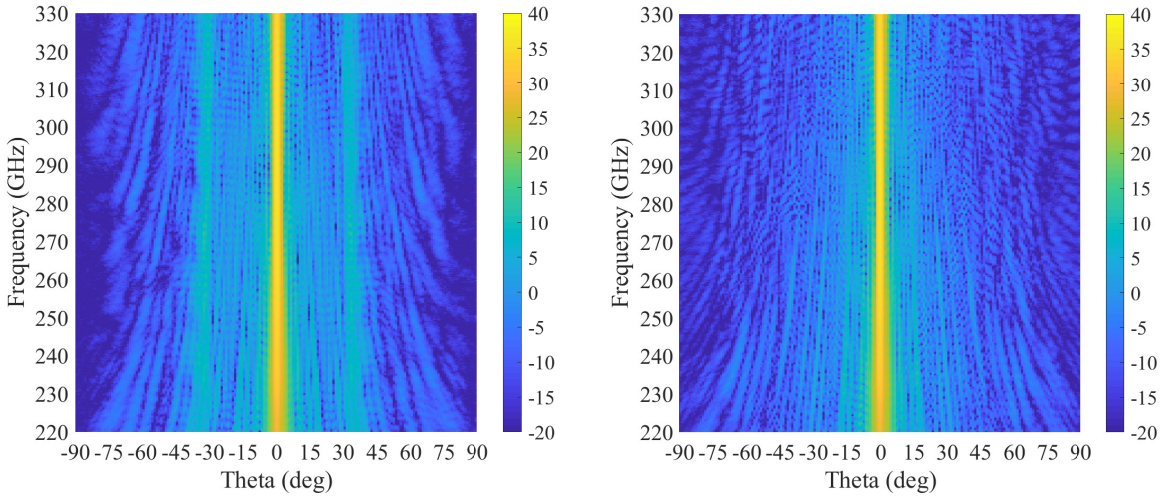

(a) (b)

Figure 4.23: Measured gain of prototype D as a function of elevation angle and frequency in (a) H- and (b) E-plane.

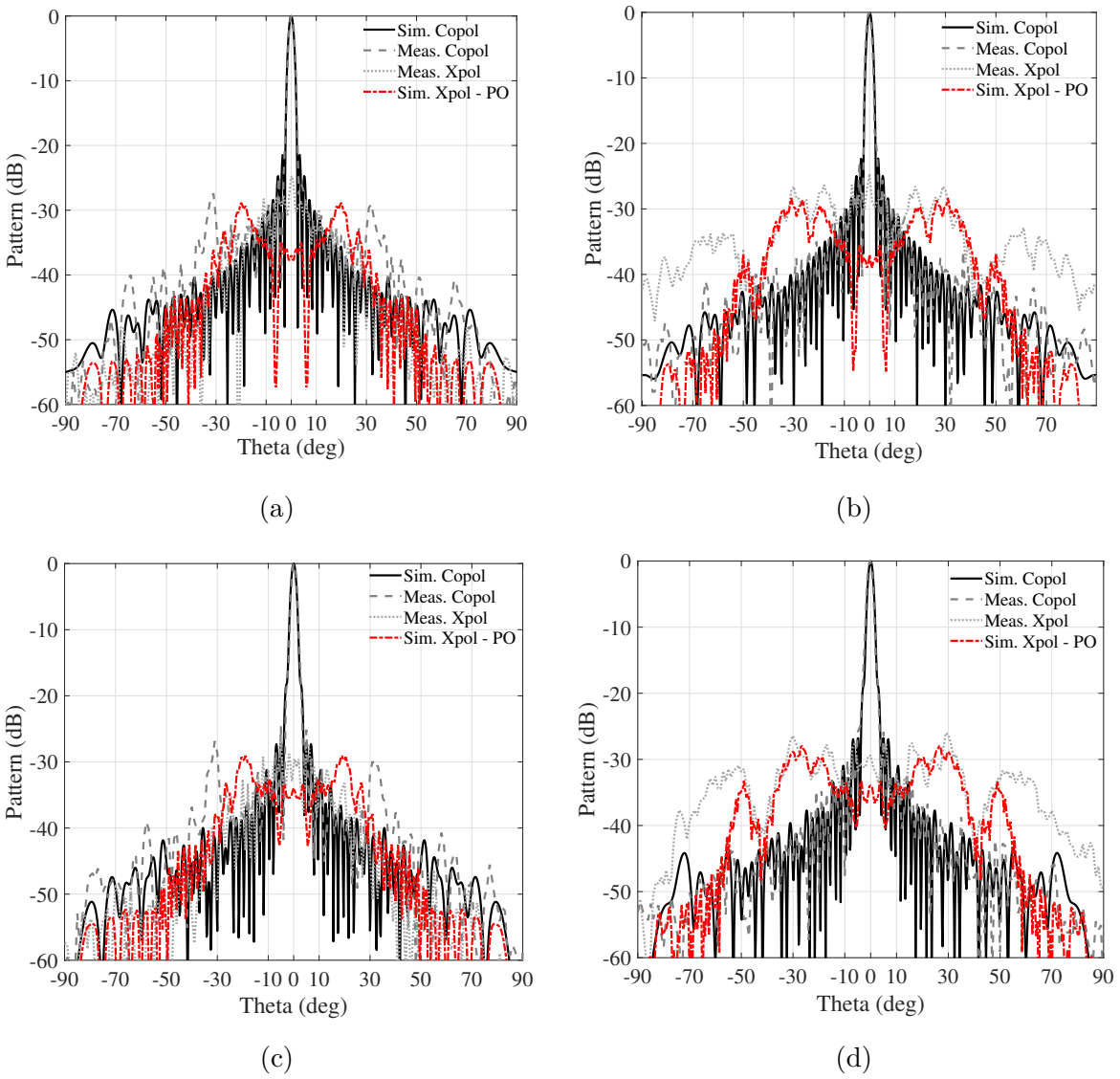

Figure 4.24: Co- and cross-polarized measured radiation pattern of prototype D. (a) H-plane at 280 GHz, (b) E-plane at 280 GHz, (c) H-plane at 300 GHz and (d) E-plane at 300 GHz.

Table 4.5: Power budget and radiation characteristics of prototype D.

	Simulation	Measurement
Frequency	290 GHz	290 GHz
Focal source gain	20.1 dBi	20.1 dBi
Theoretical directivity of a uniform aperture	40.2 dBi	-
Quantization loss	0.3	-
Broadside directivity	39.0 dBi	-
Spillover loss	0.9 dB	-
Broadside gain	37.6 dBi	37.0 dBi
Power efficiency	72.4%	63%
Aperture efficiency	55.2%	47.2%

4.4.2 Comparison

Table 4.6 compares the performance of the four reported antenna prototypes with some state-of-the-art spatially fed antennas (transmitarrays and reflectarrays) at frequencies beyond 100 GHz. All four prototypes attain a state-of-the-art performance, exhibiting a gain up to 43.34 dBi for prototype C and an aperture efficiency more than 30% and up to almost 50% for prototype D. A wideband performance was also obtained with prototype D, which is one of the key goals for antennas used for future wireless communications. The designed transmitarray does not comprise any vias as in the antenna presented in [29] and comprises only three metal layers. Moreover, prototype D outperforms all other antennas, exhibiting the most wideband performance and almost the same aperture efficiency as the D-band antenna fabricated in LTCC, which comprises multiple metal layers (seven) and thousands of vias, as reported in [30].

Table 4.6: Comparison of prototypes with state-of-the-art spatially fed antennas beyond 100 GHz.

Reference	[21]	[29]	[30]	Proto. A	Proto. B	Proto. C	Proto. D
Center freq. (GHz)	390	145	140	280	280	280	280
Architecture	RA (Folded)	TA	TA	TA	TA	TA	TA
Technology	Quartz lithography	PCB	LTCC	PCB	PCB	PCB	PCB
Aperture size (λ^2)	π (12.9×12.9)	20×20	18.7×18.7	18.7×18.7	18.7×18.7	65×65	28.0×28.0
F/D	1.07	0.75	1.87	0.55	1.0	0.6	1.83
Peak gain (dBi)	33.66	33.0	33.4	32.2	32.2	43.34	37.0
Aperture eff.	34.5%	38.3%	50.1%	31.8%	36.5%	39.0%	48.6%
1 dB gain bandwidth	-	11.7%	10.7%	9.5%	10.5%	3.5%	19.0%
3 dB gain bandwidth	16.4%	19.8%	24.4%	18.9%	25.1%	6.0%	34.0%
SLL (dB)	-16.7	-16.3	-21.0	-22.0	-15.0	-16.7	-24.6

4.5 Conclusion

In this chapter, the design, fabrication and experimental characterization of different transmitarray prototypes using standard Printed Circuit Board Technology was presented. All prototypes were synthesized using the ray tracing technique. A good agreement between measured and simulated results was found. The gain difference was consistent between all prototypes, showing that both the fabrication process and the ray tracing approach can be considered reliable. An additional small improvement between measured and simulated gain and radiation patterns was observed in the case of the physical optics approach. This approach lead to a further minimization of the frequency-shift error, improving also the cross-polarized radiation pattern. Leveraged by the model described in Chapter 2 and the final topology, all prototypes exhibit a gain loss equal or less than 2 dB compared to an ideal transmitarray. This was an excellent result, considering that all prototypes exhibit a large size and they were fabricated using a standard printed circuit board process at 300 GHz. Finally, a simple setup for the experimental characterization of the unit-cells was presented. Despite the difference in magnitude between measurements and simulations using infinite periodic condition, all unit-cells exhibit less than 3 dB of insertion losses in the frequency of observation. Moreover, the measured relative phase of transmission remains close to 45°, validating the 3-bit transmitarray design. Possible improvements on the measurement setup of the unit-cells, considering the type of the employed antennas, could further consolidate these results.

Chapter 5

Design of Transmitarray antennas in Quartz Lithography

In this Chapter, a 4-bit anisotropic transmitarray using lithography process on quartz substrate is presented. The study and synthesis of the transmitarray antenna was investigated using both approaches presented in Chapter 2. Two prototypes, each one using a different transmitarray model, were fabricated for future measurements and comparisons. The selected fabrication technology improves the accuracy of the process, enabling a subwavelength periodical unit-cell size, achieving a metalens design concept.

5.1 Unit-cell design

The design leverages a quartz-based lithography process to achieve high fabrication accuracy. The quartz glass substrate does not introduce substrate waves, thanks to the low dielectric constant, enabling high-gain and cost-efficient antennas [21]. Based on this process, the minimum conductor width and spacing can go down to a few μm. This accuracy allows targeting a higher phase quantization (e.g. 4-bit) and a smaller unit-cell size. Having a subwavelength periodical size, the transmitarray becomes less sensitive to the angle of incidence, which could cause problems, as showed in Chapter 4.

The proposed unit-cell architecture is represented in Figure 5.1. The selected rotator is a combination of a dipole and a split circular ring, sandwiched between the two grid polarizers. The optimization process is based again on the unit-cell model of Chapter 3. For a relative permittivity equal to 3.78, the substrate thicknesses are fixed to $h = 144$ µm and the filling factor of both polarizers is fixed to 0.3. The periodic size is set to 200 μm, which is equal to 0.2λ at 300 GHz. The radius of the circular ring and the metallic width are set to 80 μm and 20 μm, respectively, for all rotator designs. The phase of transmission can be controlled by the opening, ϕ_g, and the orientation, ϕ_{off}. As shown in Figure 5.2, this type of rotator is almost ideal for the unit-cell. It can be seen that by

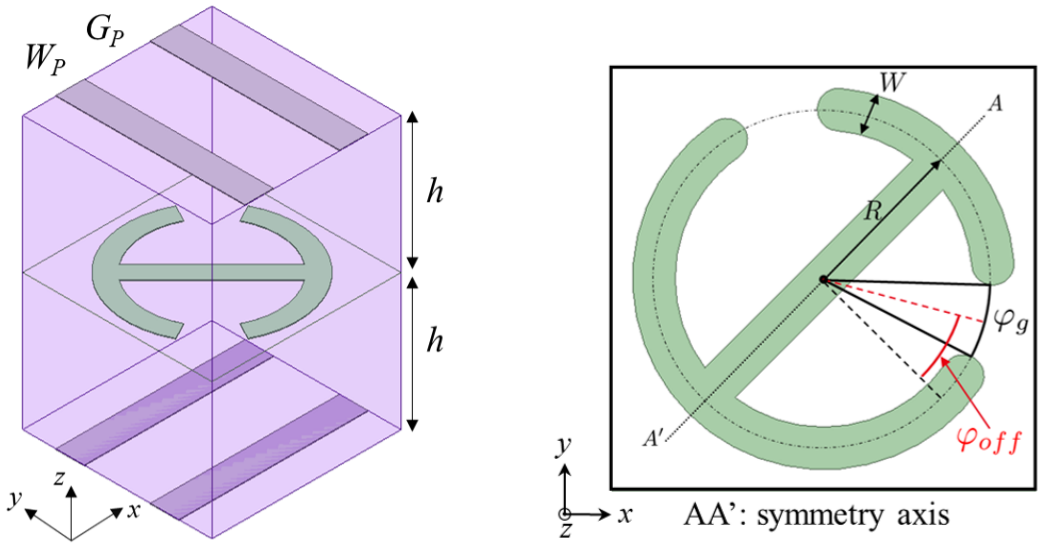

(a) (b)

Figure 5.1: (a) View of the proposed unit-cell design. (b) Rotator geometry.

tuning the two values, ϕ_g and ϕ_{off}, the corresponding magnitude of transmission presents less than 0.5 dB insertion loss for the majority of the results.

Based on these results, eight different rotator topologies are designed. By mirroring the rotator with respect to the y-axis (see Figure 5.1(b)), 16 unit-cells are obtained, resulting in a 4-bit TA. The obtained phase resolution not only improves the antenna gain, but it also enables an accurate pattern shaping, such as the synthesis of focused beams with reduced sidelobe levels (SLLs) [94]. Figures 5.3(a) and (b) show the magnitude and phase of transmission of the final topologies. Their corresponding dimensions are shown in Table 5.1. All unit-cells demonstrate a relative phase error less than 11° (±5.5°) and a wideband performance. The insertion loss is less than 1 dB over a relative bandwidth greater than 40%. Moreover, the 8 unit-cell topologies, described as a function of the rotator admittance pairs (Y_u,Y_v), are shown in Figure 5.3(c). The final designs are compared to a theoretical 4-bit TA with minimum insertion loss. The agreement between theoretical and designed admittance values validates the effectiveness of the model.

Finally, the performance of the unit-cell is also investigated under oblique angles of incident wave. Thanks to the subwavelength periodical size, the magnitude of transmission remains almost uncharged for an incident angle up to 40°, as shown in Figure 5.4.

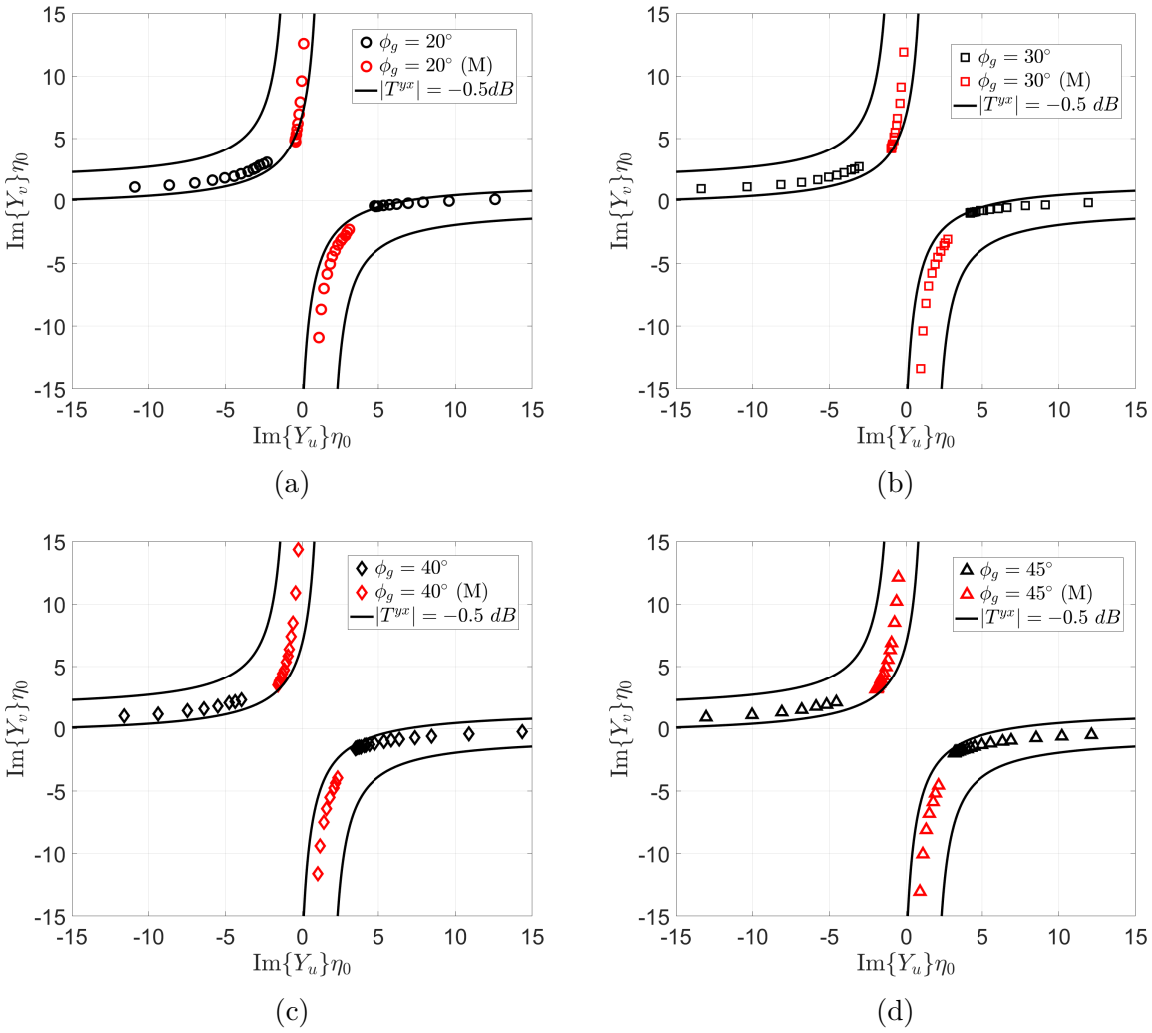

Figure 5.2: Admittance properties in the crystal axes of the rotator in Figure 5.1(b) for different opening angles, ϕ_g, when the offset angle ϕ_{off} varies from 0° to 60°. Most admittance pairs fall in the region where $|T^{yx}| \leq 0.5$ dB, highlighted by the two loci (dark solid curves) at each graph. The results when the rotator is mirrored (M) are depicted with red symbols.

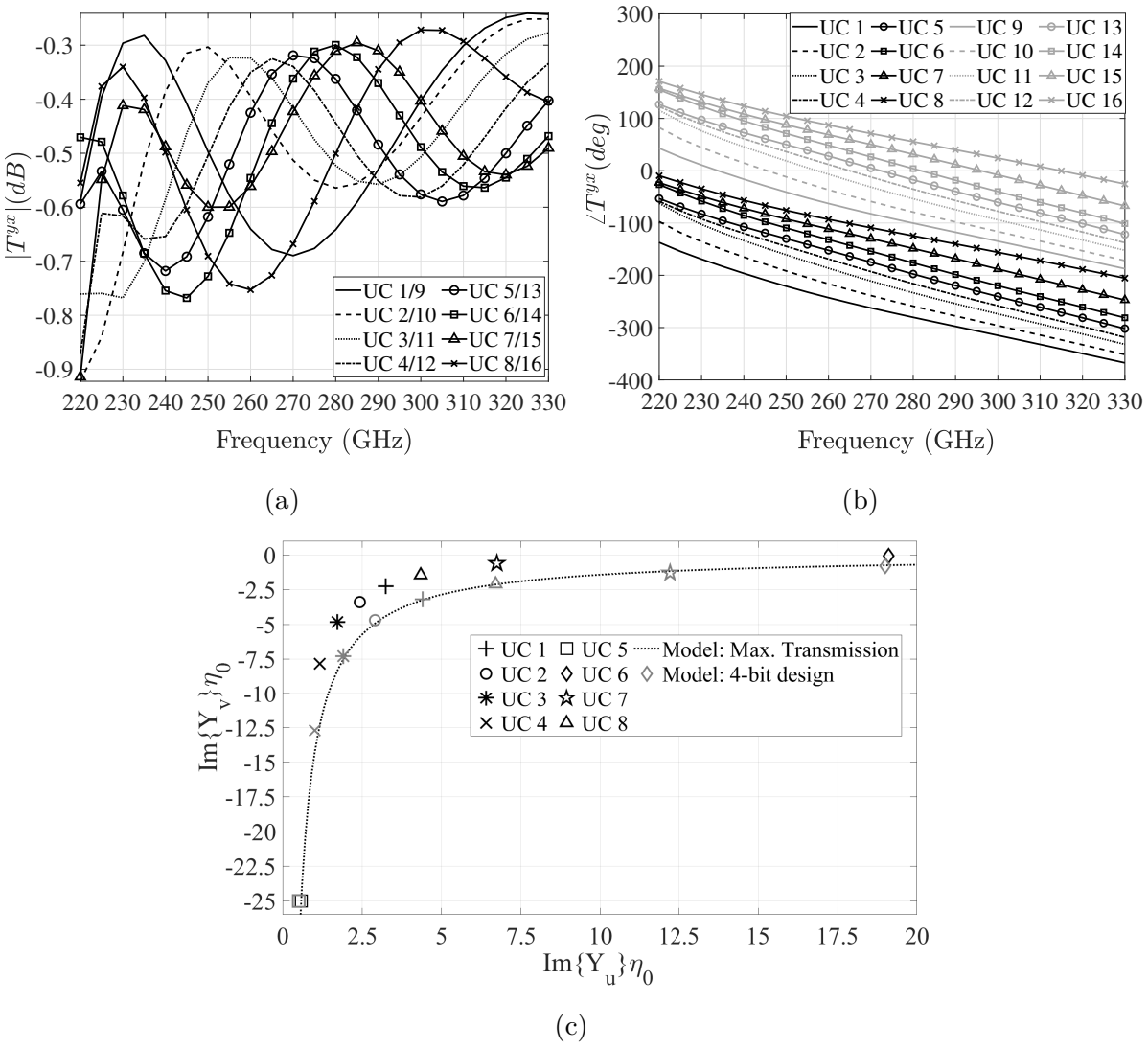

Figure 5.3: Transmission magnitude (a) and phase (b) of the designed unit-cells, obtained from full-wave simulations. (c) Results of the synthesis procedure of the 4-bit TA in quartz, showing only half states in the fourth quadrant.

Table 5.1: Geometrical parameters of the employed rotators.

Unit-cell (no.)	Parameter	
	ϕ_g	ϕ_{off}
1/9	20	60
2/10	25	50
3/11	30	45
4/12	35	40
5/13	35	35
6/14	35	30
7/15	45	30
8/16	45	20

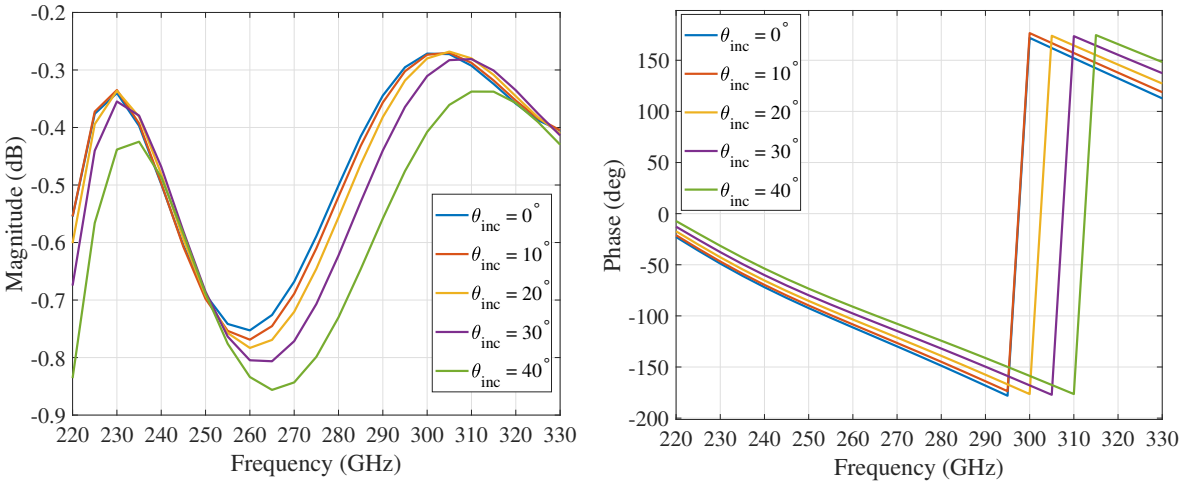

(a) (b)

Figure 5.4: Magnitude (a) and phase (b) of transmission of the quartz unit-cell with $\phi_g = 20°$ and $\phi_{off} = 60°$, for different angles of incident Floquet Wave.

5.2 Prototyping

As mentioned, a quartz-based lithography process was selected to improve the fabrication accuracy and reduce the unit-cell size. One of the two prototypes has been fabricared at IETR (NanoRennes), as shown in Figure 5.5.

The principle of this technology consists on metallizing several quartz substrates in aluminum or gold and bonding them after correct alignment. Therefore, the key points are metallization alignment and bonding. The quartz substrate can be processed from 0,1 to 2 mm thickness. The maximum size of the quartz area cannot exceed 75mm to fit with most IETR's micro fabrication equipment and especially the alignment bonding system. The roughness of substrate cannot exceed 3 μm, in order to ensure good photolithographic process.

For the substrate metallization, several methods can be used. One method is to deposit metal and make the pattern afterwards by standard etching technique. Another one is to first pattern some shapes in photoresist, then metallize these shapes just before releasing the photoresist to perform a so called lift off process. At IETR, the evaporation can be done with Electron Beam deposition (EBD), Ti, Au. The lift off can be performed with standard photoresist (S1818) or thick photoresist (SPR). The etching process can occur in dry etching by ICP-RIE plasma in Cl2 chemistry or in wet etching using acid solutions. The accuracy of the pattern is less than 1 μm and the final minimum size can potentially go down to a few μm, typically 2 – 5 μm, depending on the type of metallization.

In the case of alignment, the layers are aligned using a Suss Microtech MA6 mask aligner with a 2 μm accuracy in back side alignment. It is also possible to use the same equipment for aligning two substrates and clamp them before the bonding step.

Finally, the bonding alignment is realized using the Suss Microtech BA6 bond alignment. Bonding can be done with photoresist thermally activated, using Benzocyclobutene (BCB) or SU-8.

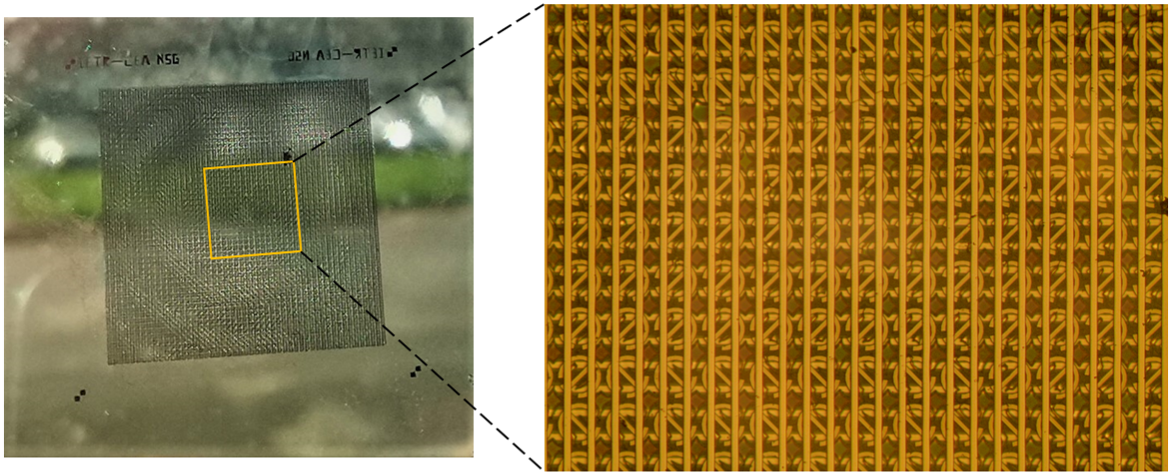

(a)

Figure 5.5: Photograph of one transmitarray prototype fabricated in quartz wafer.

5.3 Antenna design

To demonstrate the performance of the quartz elements, a 50×50 elements transmitarray (size equal to 10×10 mm^2 at 300 GHz) is designed. The 10 dBi gain Flann horn is used as a focal source. Using either the ray tracing or the physical optics technique, the obtained results are the same. Specifically, the F/D ratio that maximizes the aperture efficiency is found equal to 0.5 at 280 GHz. The corresponding gain and aperture efficiency are 27.8 dBi and 54.9%, respectively, as shown in Figure 5.6.The simulated peak gain and aperture efficiency as a function of frequency are plotted in Figure 5.7. The maximum value is about 28.0 dBi at 295 GHz and the corresponding aperture efficiency is about 52.0%. The 1 dB and 3 dB gain bandwidths are about 60 GHz (20%) and 100 GHz (34%), respectively, demonstrating a wideband behavior. Compared to an ideal transmitarray, the gain loss is only 0.5 dB, as shown in Figure 5.7(a). Therefore, this design can reach theoretically almost the maximum achievable performance. The phase distribution calculated with both transmitarray models is depicted in Figure 5.8. Aside from a constant phase difference, the distribution is almost the same in the two approaches.

The radiation pattern as a function of both the elevation angle and frequency for the H- and E-plane are shown in Figure 4. The main lobe is stable in the 3 dB gain bandwidth and its HPBW is about 6°. Finally, the radiation pattern at two frequency points is plotted in Figure 5.10, The first sidelobe level in the H- and E-plane is 23.2 dB and 25.1 dB, respectively. The spillover radiation of the focal source is included in the

Table 5.2: Theoretical power budget and radiation characteristics of quartz transmitarray.

Frequency	295 GHz
Focal source gain	1
Theoretical directivity of a uniform aperture	30.8 dBi
Quantization loss	0.2
Broadside directivity	29.8 dBi
Spillover loss	1
Broadside gain	28.0 dBi
Power efficiency	65%
Aperture efficiency	52.0 %

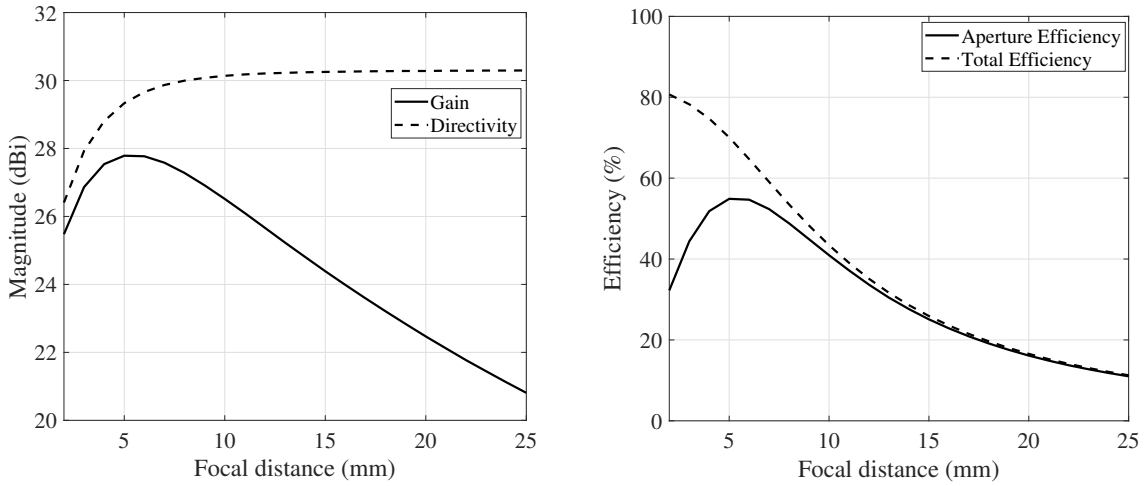

(a) (b)

Figure 5.6: Parametric analysis at the focal distance for a theoretical quartz transmitarray, showing (a) the gain and directivity, (b) the total and the aperture efficiency.

calculation, considering a margin area of 5 mm at each side of the transmitarray.

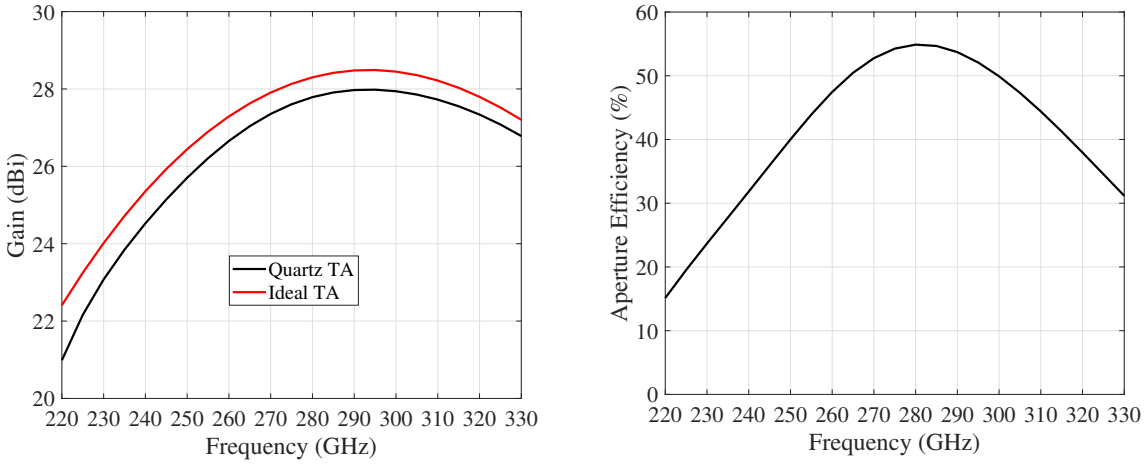

(a) (b)

Figure 5.7: Peak gain and aperture efficiency as a function of (a) the F/D and (b) the frequency for a quartz transmitarray, using both models reported in Chapter 2.

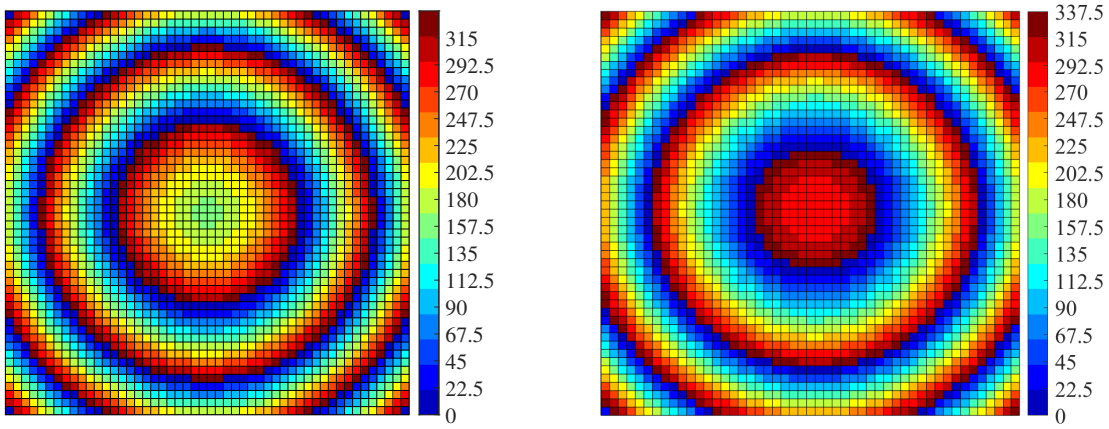

(a) (b)

Figure 5.8: Phase distribution of the quartz transmitarray antenna calculated using (a) the ray tracing and (b) the physical optics technique.

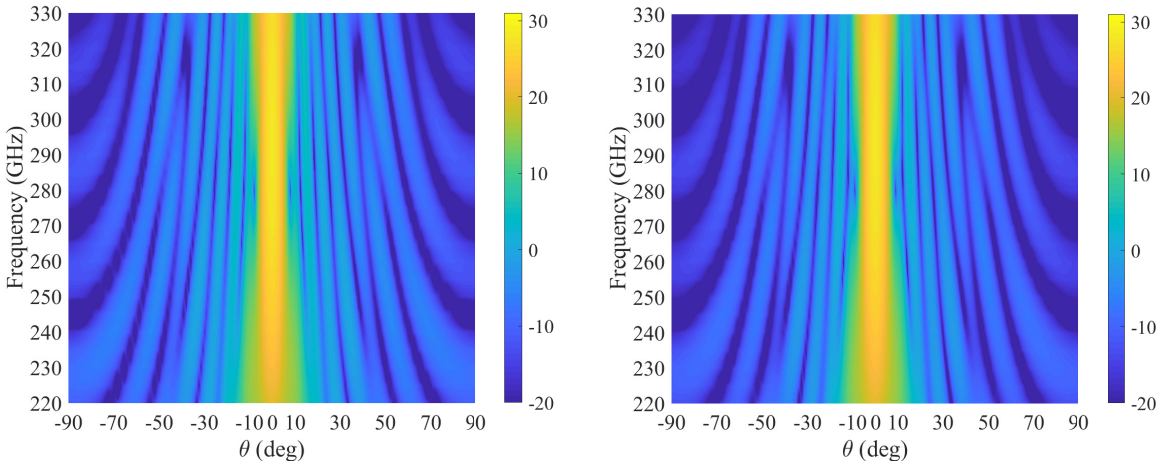

Figure 5.9: Co-polarized radiation pattern as a function of both the elevation angle and frequency for the (a) H- and (b) E-plane.

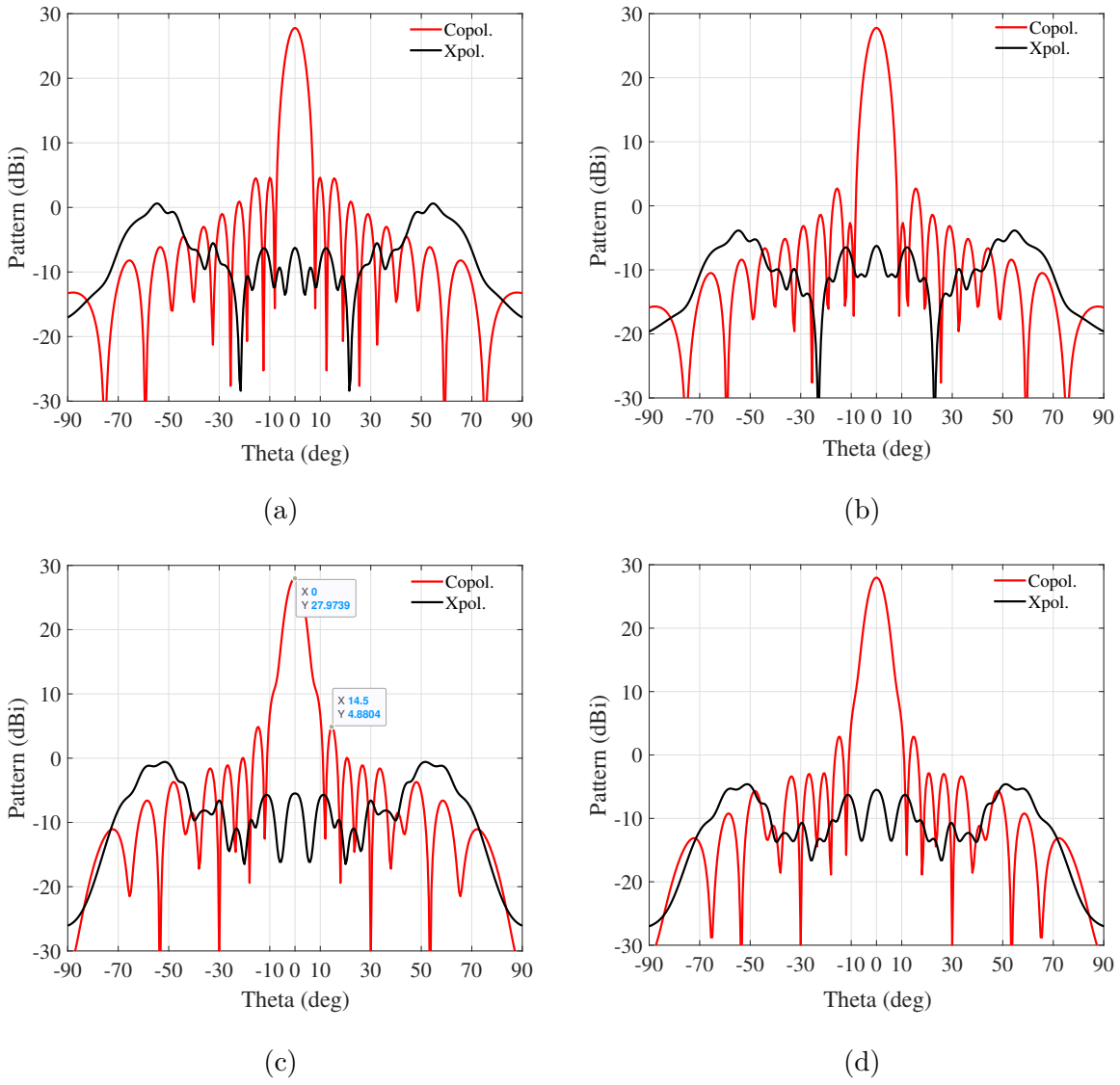

Figure 5.10: Co- and cross-polarized radiation pattern of quartz transmitarray using the physical optics technique to include the spillover radiation of the focal source. (a) H-plane at 280 GHz, (b) E-plane at 280 GHz, (c) H-plane at 300 GHz and (d) E-plane at 300 GHz.

5.4 Conclusion

The study and the design of a quartz-based transmitarray antenna was presented in this Chapter. Thanks to the fabrication process, a smaller periodical size and higher phase resolution were obtained. The designed unit-cells exhibit a more broadband behavior and are much less sensitive to the angle of incidence compared to the PCB design in Chapter 4. The positive features were also demonstrated by the design of a transmitarray antenna. Compared to an ideal lens, the gain loss was only 0.5 dB, while the final design exhibits 52.0% of aperture efficiency at the central frequency. To further validate the design approach and the newly tested fabrication process, one prototype was realized and will be measured in the future.

General Conclusions and Perspectives

Summary

The work presented in this thesis was carried out in the context of the "NEXT5G" project. As discussed in Chapter 1, in order to develop a wireless system concept with high-speed capabilities at 300 GHz, the efficient design of high-gain and wideband antennas is one of the most crucial tasks. In this context, different antenna technologies, suitable for such application, were mentioned. Several state-of-the-art prototypes with good or excellent performance were presented. However, in all cases the realization of the antenna was selected considering a trade-off between the cost and the final performance. Adding to this problem the necessity of enabling beam-steering capabilities, no low-cost antenna with high radiation performance was reported beyond the D-band. Among all discussed architectures, transmitarray antennas were a promising candidate, enabling the possibility of achieving high radiation efficiency using a low-cost planar fabrication process. However, no transmitarray design satisfying both criteria was reported at 300 GHz.

In Chapter 2, the theoretical modelling and design of the transmitarray antenna was reported. The main objective was to derive a fast approach to both analyze and synthesize large transmitarray antennas, trying to keep at the same time an accurate characterization of the radiated field. For this reason, two separate methods, both employing a mix of analytical modelling and full-wave simulations, were presented and compared. For a classical scenario, using a small size focal source, both methods showed almost perfect agreement. For cases of having a large size focal source, which is placed in close proximity, the second technique, named as physical optics approach, provided a more realistic description of the radiated field. A more accurate calculation of the spillover radiation, added in the final radiation, was also included with this approach.

In Chapter 3, a rigorous model based on cascaded sheet admittances to analyze and synthesize three-layer anisotropic transmitarrays, known as asymmetric linear polarizers (ALPs), was presented. The selection of the ALP design was primarily preferred over other

designs thanks to their high transmissivity over a wide bandwidth and the simple control of their properties using only three metal layers. In this thesis, a more general analysis of the unit-cell and a quantitative procedure to design it for maximum transmission and phase coverage were thoroughly described. It was rigorously demonstrated that the ALP can achieve at the design frequency both nearly perfect transmission and full phase coverage, as opposed to standard symmetric frequency-selective surface designs. It was shown that, following proper design guidelines, the transmission phase can be tuned by varying only one metallic sheet.

To validate both the transmitarray and the unit-cell model, different antenna prototypes fabricated using standard PCB technology were presented in Chapter 4. Despite the strict fabrication constraints imposed by the PCB at 300 GHz, all prototypes managed to exhibit very good performance and good agreement with the simulated results. Among the realized antennas, an ultra-high gain prototype, with 43.34 dBi gain and 39.0% aperture efficiency, suitable for large range backhaul-link communications, was reported. Another prototype with 37.0 dBi gain and 47.2% aperture efficiency, covering more than 85 GHz of 3 dB gain bandwidth, was also presented. These prototypes outperform some of the existing spatially fed architectures at frequencies beyond 100 GHz. The performance of these antennas was further highlighted by comparing their gain to an ideal transmitarray antenna. All prototypes exhibit gain losses equal or less than 2 dB. All the previous, combined with the standard PCB process, have given some of the first low-cost transmitarray antennas at 300 GHz, which can target the maximum achievable performance.

Finally, to further improve the performance of the unit-cell and the transmitarray antenna, another ALP design using lithography process on quartz substrate was presented in Chapter 5. Thanks to the employed technology, the final unit-cells cover more than 100 GHz with less than 1 dB insertion loss, exhibiting subwavelength size. One transmitarray antenna was numerically synthesized, exhibiting less than 0.5 dB of gain loss compared to an ideal transmitarray antenna.

Impact of the Research

The most important impact of this work was demonstrating that a low-cost PCB antenna design with high gain and aperture efficiency can be feasible at 300 GHz. This has been one of the main questions on the way of developing high-speed wireless communication systems avoiding the use of expensive antenna technologies.

From a theoretical point of view, this work gives a valuable insight on the study of the transmission performance limits of transmitarrays. Specifically, thanks to the proposed unit-cell model, it was proved that the three-layer anisotropic structure is the best candidate for a transmitarray. This conclusion, combined with the three-layer and via-less design, explain why the specific topology has been intensively employed for transmitarray antennas over the last three years. On top of that, the proposed synthesis approach allows targeting always at the maximum achievable performance, facilitating the study and synthesis of future ALP-based transmitarray designs.

Several publications including the studies and the results presented in Chapters 2 – 5 were reported. The novelty of the unit-cell model in Chapter 3 was highly appreciated, resulting in one nomination for Best Student Paper in the 2021 15th European Conference on Antennas and Propagation (EuCAP). In addition, the excellent performance of prototype D was presented in the 2021 European Microwave Conference (EuMC), which combined with the modelling approach, gave the prize for the Young Engineer.

Future Outlook

In the frame of next-generation wireless communications, an important and unanswered problem is the case of developing a reconfigurable transmitarray design. By leveraging on the dynamic beamforming, an increased channel capacity and a reduced interference can be achieved, which are both essential for such future system concept. Therefore, it is very important to assess all existing approaches or derive new ones, in order to overcome both main problems, i.e. the narrowband functionality and the individual control of each element, simultaneously.

Considering the results presented in this work, there are two parts that could be further investigated. The first one is the impact of the angle of incidence on the unit-cell performance inside the transmitarray. Specifically, despite the deteriorated performance of the PCB unit-cells simulated in the infinite periodic environment, the measurement results of both the transmitarrays and the unit-cell arrays did not show similar behavior. The second part is to further investigate the physical optics approach, especially for low-profile transmitarray designs. This could help overcoming the main problem of the volume occupancy and derive a fast and efficient approach for an antenna system that will be nearly impossible to investigate only through full-wave simulations.

A final study, related to this work, is to carry out a measurement campaign of the

fabricated quartz transmitarray prototype presented in Chapter 5. This will validate the design procedure and the novel fabrication process at these frequencies.

Appendix A

Fields radiated by an aperture

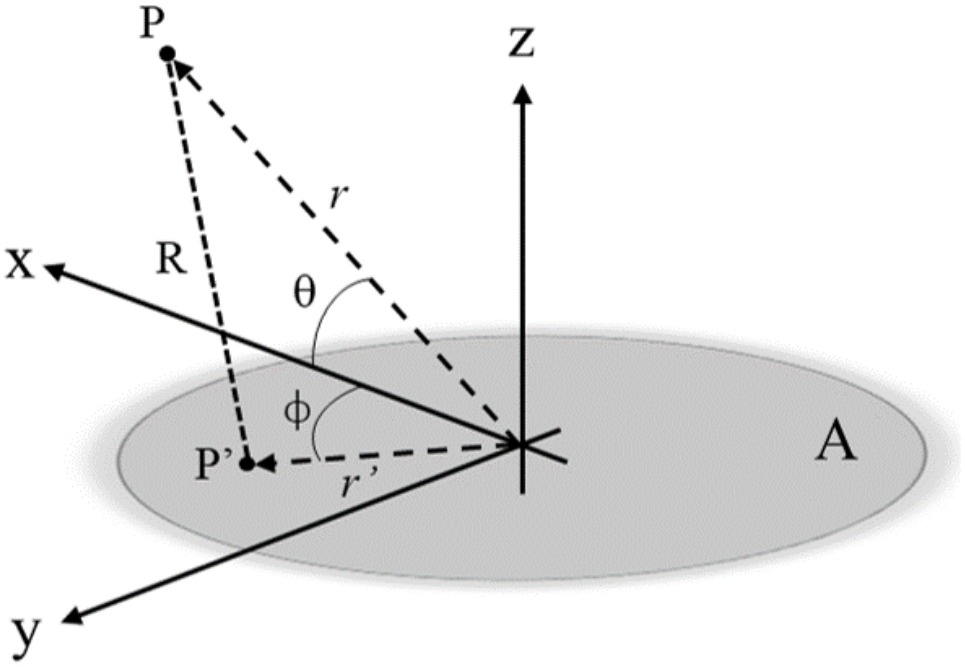

(a)

Figure A.1: Schematic view of fields radiated by an aperture A. P is the observation point and P' is the the source point, where a pair of dipoles is located.

Let's assume that an arbitrary two-dimensional aperture A is located on the xy-plane, as depicted in Figure A.1. The field distribution on that aperture can be expressed by a local dipole pair assumption. Specifically, each point of the aperture consists of two infinitesimal electric and magnetic dipoles acting in conjunction. The accuracy of this assumption depends on the number and size of the selected dipole pairs, i.e. the discretization step dS'. Normally, a subwavelength step must be chosen. Each dipole is described by an initial field $\overrightarrow{E}_a$ and $\overrightarrow{H}_a$, respectively. These fields may be replaced by equivalent sources as

$$\overrightarrow{J}_s = \hat{n} \times \overrightarrow{H}_a \,, \tag{A.1a}$$

$$\overrightarrow{M}_s = -\hat{n} \times \overrightarrow{E}_a \,, \tag{A.1b}$$

where $\hat{n}$ is the unit vector normal to the surface, in that case $\hat{n} \equiv \hat{z}$. Suppose that the dipole sources exhibit some electric and magnetic dipole moments, which are related to the currents as follows:

$$\overrightarrow{dp} = \overrightarrow{J}_s dS' \,, \tag{A.2a}$$

$$\overrightarrow{dm} = \overrightarrow{M}_s dS' \,. \tag{A.2b}$$

Using these dipole moments, the radiated electric and magnetic field can be calculated. If the point of observation is in the far-field of the dipoles, i.e. $kR >> 1$, where k is the wavevector, then these fields may be expressed as

$$\overrightarrow{dH}_e = \frac{jke^{-jkR}}{4\pi R}\overrightarrow{dp} \times \hat{R} \,, \;\; \overrightarrow{dE}_e = \eta_0 \overrightarrow{dH}_e \times \hat{R} \tag{A.3a}$$

$$\overrightarrow{dE}_m = -\frac{jke^{-jkR}}{4\pi R}\overrightarrow{dm} \times \hat{R} \,, \;\; \overrightarrow{dH}_m = \frac{1}{\eta_0}\overrightarrow{dE}_m \times \hat{R} \,. \tag{A.3b}$$

Therefore, the total electric and magnetic field coming from the dipole pair at the observation point are

$$\overrightarrow{dE} = \overrightarrow{dE}_e + \overrightarrow{dE}_m \,, \tag{A.4a}$$

$$\overrightarrow{dH} = \overrightarrow{dH}_e + \overrightarrow{dH}_m \,. \tag{A.4b}$$

Substituting (A.1) in (A.2), expressions (A.4) become

$$\overrightarrow{dE} = \frac{jke^{-jkR}}{4\pi R}(-\overrightarrow{M}_s \times \hat{R} + \eta_0(\overrightarrow{J}_s \times \hat{R}) \times \hat{R})dS' \tag{A.5a}$$

$$\overrightarrow{dH} = \frac{jke^{-jkR}}{4\pi R}(\overrightarrow{J}_s \times \hat{R} + \frac{1}{\eta_0}(\overrightarrow{M}_s \times \hat{R}) \times \hat{R})dS' \tag{A.5b}$$

Adding all dipole contributions on aperture A through integration in expressions (A.5), the total field at the observation point can be found.

When a transmitarray is added at the plane of observation, the transmitted field from

each dipole pair at the same point of observation becomes

$$\overrightarrow{dE}_t = \overline{\overline{S}}_{21}(\hat{R})\overrightarrow{dE} \tag{A.6a}$$

$$\overrightarrow{dH}_t = \boldsymbol{n}\overline{\overline{S}}_{21}(\hat{R})\boldsymbol{n}^{-1}\overrightarrow{dE}\,, \tag{A.6b}$$

where $\overline{\overline{S}}_{21}$ is the 2×2 transmission coefficient matrix of the unit-cell and $\boldsymbol{n}$ is the 90° rotation matrix

$$\boldsymbol{n} = \begin{bmatrix} 0 & -1 \\ 1 & 0 \end{bmatrix}. \tag{A.7}$$

In general, the transmission coefficient depends on the angle of incidence of the incoming wave, through the vector $\hat{R}$. Ideally, it must be considered in the integration, in order to calculate accurately the total radiated field at each unit-cell. The final expression of the total radiated field at each unit-cell becomes

$$\overrightarrow{E}_t = \frac{jk}{4\pi}\iint \overline{\overline{S}}_{21}(\hat{R})[\frac{e^{-jkR}}{R}(-\overrightarrow{M}_s \times \hat{R} + \eta_0(\overrightarrow{J}_s \times \hat{R}) \times \hat{R})]dS' \tag{A.8a}$$

$$\overrightarrow{H}_t = \frac{jk}{4\pi}\iint [\boldsymbol{n}\overline{\overline{S}}_{21}(\hat{R})\boldsymbol{n}^{-1}][\frac{e^{-jkR}}{R}(\overrightarrow{J}_s \times \hat{R} + \frac{1}{\eta_0}(\overrightarrow{M}_s \times \hat{R}) \times \hat{R})]dS' \tag{A.8b}$$

The expressions in (A.6) and (A.8) can be also used for the calculation of the far-field of the focal source and the transmitarray, respectively. Assuming the following approximations

$$R = |r - r'| \approx r\left(1 - \frac{(r \cdot r')}{r^2} + \frac{1}{2}\frac{(r' \cdot r')^2}{r^2}\right), \tag{A.9}$$

in the exponential phase, and

$$\frac{1}{R} \approx \frac{1}{R}\,, \quad \hat{R} \approx \hat{r}\,, \tag{A.10}$$

in the amplitude of the integral, the far-field expression of (A.6) and (A.8) becomes

$$\overrightarrow{E} \approx \frac{jke^{-jkr}}{4\pi r}\hat{r} \times \iint [\overrightarrow{M}_s - \eta_0(\overrightarrow{J}_s \times \hat{r})]e^{jk\hat{r}\cdot r'}dS'\,, \tag{A.11}$$

where in the case of the transmitarray, the currents can be calculated using the equivalence

principle. The corresponding magnetic field can be easily calculated as

$$\overrightarrow{H} = \frac{1}{\eta_0}\hat{r} \times \overrightarrow{E} \tag{A.12}$$

In order to obtain the spherical far-field components, the following approach is used. For a rectangular aperture, it is

$$\hat{r} \cdot \overrightarrow{r}' = sin\theta(x'cos\phi + y'sin\phi) + z'cos\theta\,. \tag{A.13}$$

Using the known relationship between the Cartesian and the spherical coordinate system, the spherical far-field components are eventually found [75] as

$$E_r = 0\,, \tag{A.14a}$$

$$E_\theta = \frac{jk}{4\pi}[N_x \cos\phi + N_y \sin\phi) + \eta_0 \cos\theta(-L_x \sin\phi + L_y \cos\phi)]\,, \tag{A.14b}$$

$$E_\phi = \frac{jk}{4\pi}[\cos\theta(-N_x \sin\phi + N_y \cos\phi) - \eta_0(L_x \cos\phi + L_y \sin\phi)]\,, \tag{A.14c}$$

where

$$\overrightarrow{N} = \iint \overrightarrow{E} e^{jk\hat{r}\cdot r'} dxdy\,, \tag{A.15a}$$

$$\overrightarrow{L} = \iint \overrightarrow{H} e^{jk\hat{r}\cdot r'} dxdy\,. \tag{A.15b}$$

The expressions in (A.14) have been normalized to the factor e^{-jkr}/r. The expressions (A.15) describe the two-dimensional Fourier transform of the radiated fields in the far-field region.

Appendix B

Derivation of Transmission for the Circuit of the ALP Unit-Cell

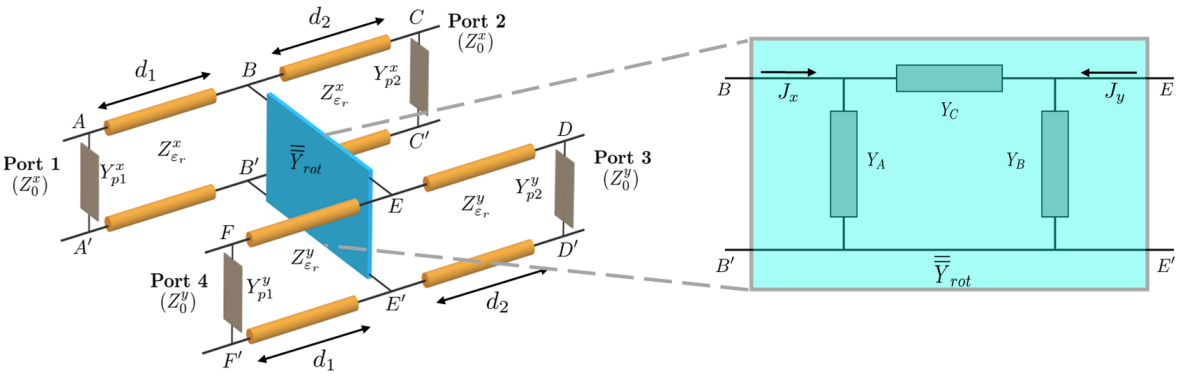

(a)

Figure B.1: Equivalent circuit model of the generic ALP unit-cell.

The scattering parameters of the four-port circuit in Figure B.1 are calculated using classical network theory [77]. The main interest is on the properties of the transmission coefficient S_{31}. The close-form expression of this coefficient, described in Chapter 3, is

$$S_{31} \triangleq T^{yx} = (Z_{AA'}^{-1} - Y_t)(1 + S_{11})K_1 K_2^{-1}\,. \tag{B.1}$$

The value $Z_{AA'}$ is the equivalent input impedance at Port 1 when all other ports are terminated by a matched load (Z_0). The value S_{11} is the reflection coefficient at Port 1, equal to

$$S_{11} \triangleq R^{xx} = \frac{Z_{AA'} - Z_0}{Z_{AA'} + Z_0} \tag{B.2}$$

In order to derive expression B.1, the ports 2, 3 and 4 must be terminated with matched loads, equal to Z_0. Then, the relation between transmitted and incident waves, V_3^- and

V_1^+, respectively, is derived. By doing so, the parameter K_1 in (B.1) is found to be

$$K_1 = Z_{\varepsilon_r}^{-1}(1-\Gamma_2) - Y_A(1+\Gamma_2) - Z_{P2}^{-1}(1+\Gamma_2) \tag{B.3}$$

The impedance Z_{P2} in (B.3) is equal to

$$Z_{P2} = Z_{\varepsilon_r}\frac{Z_{L1} + jZ_{\varepsilon_r}\tan(\beta d_2)}{Z_{\varepsilon_r} + jZ_{L1}\tan(\beta d_2)}\,, \tag{B.4}$$

where

$$Z_{L1} = \frac{Z_0}{1+Z_0Y_r} \tag{B.5}$$

The values Y_r and Y_t describe the case of reflection and transparency, respectively, for the two polarizers. Since they are considered identical, these parameters are

$$Y_{p1}^x = Y_{p2}^y = Y_t\,, \tag{B.6a}$$

$$Y_{p1}^y = Y_{p2}^x = Y_r\,. \tag{B.6b}$$

The coefficient Γ_1 is equal to

$$\Gamma_1 = \frac{Z_{L2} - Z_{\varepsilon_r}}{Z_{L2} + Z_{\varepsilon_r}}\,, \tag{B.7}$$

where

$$Z_{L2} = \frac{Z_0}{1+Z_0Y_t} \tag{B.8}$$

The coefficient Γ_2 is equal to

$$\Gamma_2 = \frac{Z_{in}^{BB'} - Z_{\varepsilon_r}}{Z_{in}^{BB'} + Z_{\varepsilon_r}} \tag{B.9}$$

The parameter $Z_{in}^{BB'}$ is the input impedance at BB', seen as the equivalent load of the first transmission line of Port 1. Similarly, the parameter K_2 can be found as

$$K_2 = \frac{(Y_B + Y_{in}^{EE'})(e^{j\beta d_2} + \Gamma_1 e^{-j\beta d_2})(e^{j\beta d_1} - \Gamma_2 e^{-j\beta d_1})}{Z_{\varepsilon_r}(1+\Gamma_1)} \tag{B.10}$$

The admittance $Y_{in}^{EE'}$ in (B.10) is the equivalent input admittance at EE', including Ports 3 and 4, seen by the rest of the circuit.

BIBLIOGRAPHY

[1] Ericsson Mobility Report: `https://www.ericsson.com/en/reports-and-papers/mobility-report`.

[2] G. P. Fettweis, "The tactile internet: applications and challenges", *IEEE Vehicular Technology Magazine*, vol. 9, *1*, pp. 64–70, 2014.

[3] H.-B. Liu, H. Zhong, N. Karpowicz, Y. Chen, and X.-C. Zhang, "Terahertz spectroscopy and imaging for defense and security applications", *Proceedings of the IEEE*, vol. 95, *8*, pp. 1514–1527, 2007.

[4] N. Llombart, K. B. Cooper, R. J. Dengler, T. Bryllert, G. Chattopadhyay, and P. H. Siegel, "Time-delay multiplexing of two beams in a terahertz imaging radar", *IEEE Transactions on Microwave Theory and Techniques*, vol. 58, *7*, pp. 1999–2007, 2010.

[5] K. B. Cooper, R. J. Dengler, N. Llombart, B. Thomas, G. Chattopadhyay, and P. H. Siegel, "Thz imaging radar for standoff personnel screening", *IEEE Transactions on Terahertz Science and Technology*, vol. 1, *1*, pp. 169–182, 2011.

[6] J. Ding, M. Kahl, O. Loffeld, and P. H. Bolívar, "Thz 3-d image formation using sar techniques: simulation, processing and experimental results", *IEEE Transactions on Terahertz Science and Technology*, vol. 3, *5*, pp. 606–616, 2013.

[7] S. Gu, C. Li, X. Gao, Z. Sun, and G. Fang, "Three-dimensional image reconstruction of targets under the illumination of terahertz gaussian beam—theory and experiment", *IEEE Transactions on Geoscience and Remote Sensing*, vol. 51, *4*, pp. 2241–2249, 2013.

[8] Z. Xu, J. Ding, G. Chen, G. Zhao, and Y. Zhang, "An approach to high frame rate radar imaging through electronically displaced-phase-center antenna", *IEEE Transactions on Geoscience and Remote Sensing*, vol. 58, *8*, pp. 5602–5611, 2020.

[9] Y. Nan, X. Huang, X. Gao, and Y. J. Guo, "3-d terahertz imaging based on piecewise constant doppler algorithm and step- frequency continuous-wave signaling", *IEEE Transactions on Geoscience and Remote Sensing*, vol. 59, *8*, pp. 6771–6783, 2021.

[10] A. Boriskin and R. Sauleau, *Aperture antennas for millimeter and sub-millimeter wave applications*. Springer, Sept. 2017.

[11] T. Tajima, H.-J. Song, K. Ajito, M. Yaita, and N. Kukutsu, "300-GHz step-profiled corrugated horn antennas integrated in LTCC", *IEEE Transactions on Antennas and Propagation*, vol. 62, *11*, pp. 5437–5444, 2014.

[12] S. Bhardwaj and J. L. Volakis, "Hexagonal waveguide based circularly polarized horn antennas for sub-mm-wave/terahertz band", *IEEE Transactions on Antennas and Propagation*, vol. 66, *7*, pp. 3366–3374, 2018.

[13] B. Aqlan, M. Himdi, L. Le Coq, and H. Vettikalladi, "Sub-THz circularly polarized horn antenna using wire electrical discharge machining for 6G wireless communications", *IEEE Access*, vol. 8, pp. 117 245–117 252, 2020.

[14] K. Konstantinidis, A. P. Feresidis, C. C. Constantinou, *et al.*, "Low-THz dielectric lens antenna with integrated waveguide feed", *IEEE Transactions on Terahertz Science and Technology*, vol. 7, *5*, pp. 572–581, 2017.

[15] M. Arias Campo, G. Carluccio, D. Blanco, O. Litschke, S. Bruni, and N. Llombart, "Wideband circularly polarized antenna with in-lens polarizer for high-speed communications", *IEEE Transactions on Antennas and Propagation*, vol. 69, *1*, pp. 43–54, 2021.

[16] M. Arias Campo, D. Blanco, S. Bruni, A. Neto, and N. Llombart, "On the use of fly's eye lenses with leaky-wave feeds for wideband communications", *IEEE Transactions on Antennas and Propagation*, vol. 68, *4*, pp. 2480–2493, 2020.

[17] M. Arias Campo, G. Carluccio, D. Blanco, S. Bruni, O. Litschke, and N. Llombart, "Dielectric-grating in-lens polarizer for beyond 5G communications", *in 2019 44th International Conference on Infrared, Millimeter, and Terahertz Waves (IRMMW-THz)*, 2019, pp. 1–2.

[18] J. Xu, Z. N. Chen, and X. Qing, "270-GHz LTCC-integrated high gain cavity-backed fresnel zone plate lens antenna", *IEEE Transactions on Antennas and Propagation*, vol. 61, *4*, pp. 1679–1687, 2013.

[19] H. Yi, S.-W. Qu, K.-B. Ng, C. H. Chan, and X. Bai, "3-D printed millimeter-wave and terahertz lenses with fixed and frequency scanned beam", *IEEE Transactions on Antennas and Propagation*, vol. 64, *2*, pp. 442–449, 2016.

[20] J. Zhu, Y. Yang, M. Li, *et al.*, "Additively manufactured millimeter-wave dual-band single-polarization shared aperture fresnel zone plate metalens antenna", *IEEE Transactions on Antennas and Propagation*, vol. 69, *10*, pp. 6261–6272, 2021.

[21] Z.-W. Miao, Z.-C. Hao, Y. Wang, B.-B. Jin, J.-B. Wu, and W. Hong, "A 400-GHz high-gain quartz-based single layered folded reflectarray antenna for terahertz applications", *IEEE Transactions on Terahertz Science and Technology*, vol. 9, *1*, pp. 78–88, 2019.

[22] A. Gomez-Torrent, M. García-Vigueras, L. Le Coq, *et al.*, "A low-profile and high-gain frequency beam steering subterahertz antenna enabled by silicon micromachining", *IEEE Transactions on Antennas and Propagation*, vol. 68, *2*, pp. 672–682, 2020.

[23] K. Tekkouk, J. Hirokawa, K. Oogimoto, *et al.*, "Corporate-feed slotted waveguide array antenna in the 350-GHz band by silicon process", *IEEE Transactions on Antennas and Propagation*, vol. 65, *1*, pp. 217–225, 2017.

[24] A. Gomez-Torrent, T. Tomura, W. Kuramoto, *et al.*, "A 38 dB gain, low-loss, flat array antenna for 320–400 GHz enabled by silicon-on-insulator micromachining", *IEEE Transactions on Antennas and Propagation*, vol. 68, *6*, pp. 4450–4458, 2020.

[25] H. Kaouach, L. Dussopt, J. Lanteri, T. Koleck, and R. Sauleau, "Wideband low-loss linear and circular polarization transmit-arrays in V-band", *IEEE Transactions on Antennas and Propagation*, vol. 59, *7*, pp. 2513–2523, 2011.

[26] C. Jouanlanne, A. Clemente, M. Huchard, *et al.*, "Wideband linearly polarized transmitarray antenna for 60 GHz backhauling", *IEEE Transactions on Antennas and Propagation*, vol. 65, *3*, pp. 1440–1445, 2017.

[27] K. T. Pham, A. Clemente, D. Blanco, and R. Sauleau, "Dual-circularly polarized high-gain transmitarray antennas at Ka-band", *IEEE Transactions on Antennas and Propagation*, vol. 68, *10*, pp. 7223–7227, 2020.

[28] A. Clemente, M. Smierzchalski, M. Huchard, C. Barbier, and T. L. Nadan, "Characterization of a low-profile quad-feed based transmitarray antenna at V-band", *in 2019 49th European Microwave Conference (EuMC)*, Paris, France, 2019, pp. 232–235.

[29] F. Foglia Manzillo, A. Clemente, and J. L. González-Jiménez, "High-gain D-band transmitarrays in standard PCB technology for beyond-5G communications", *IEEE Transactions on Antennas and Propagation*, vol. 68, *1*, pp. 587–592, 2020.

[30] Z.-W. Miao, Z.-C. Hao, G. Q. Luo, *et al.*, "140 GHz high-gain LTCC-integrated transmit-array antenna using a wideband SIW aperture-coupling phase delay structure", *IEEE Transactions on Antennas and Propagation*, vol. 66, *1*, pp. 182–190, 2018.

[31] S. L. Liu, X. Q. Lin, Z. Q. Yang, Y. J. Chen, and J. W. Yu, "W-band low-profile transmitarray antenna using different types of FSS units", *IEEE Transactions on Antennas and Propagation*, vol. 66, *9*, pp. 4613–4619, 2018.

[32] C. Pfeiffer and A. Grbic, "Millimeter-wave transmitarrays for wavefront and polarization control", *IEEE Transactions on Microwave Theory and Techniques*, vol. 61, *12*, pp. 4407–4417, 2013.

[33] A. H. Abdelrahman, A. Z. Elsherbeni, and F. Yang, "Transmitarray antenna design using cross-slot elements with no dielectric substrate", *IEEE Antennas and Wireless Propagation Letters*, vol. 13, pp. 177–180, 2014.

[34] M. Niroo Jazi, M. R. Chaharmir, J. Shaker, and A. R. Sebak, "Broadband transmitarray antenna design using polarization-insensitive frequency selective surfaces", *IEEE Transactions on Antennas and Propagation*, vol. 64, *1*, pp. 99–108, 2016.

[35] C.-Y. Hsu, L.-T. Hwang, T.-S. Horng, S.-M. Wang, F.-S. Chang, and C. N. Dorny, "Transmitarray design with enhanced aperture efficiency using small frequency selective surface cells and discrete jones matrix analysis", *IEEE Transactions on Antennas and Propagation*, vol. 66, *8*, pp. 3983–3994, 2018.

[36] X. Zhong, H.-X. Xu, L. Chen, W. Li, H. Wang, and X. Shi, "An FSS-backed broadband phase-shifting surface array with multimode operation", *IEEE Transactions on Antennas and Propagation*, vol. 67, *9*, pp. 5974–5981, 2019.

[37] Z. Zhang, X. Li, C. Sun, Y. Liu, and G. Han, "Dual-band focused transmitarray antenna for microwave measurements", *IEEE Access*, vol. 8, pp. 100 337–100 345, 2020.

[38] P. Y. Feng, S. W. Qu, and S. Yang, "Octave bandwidth transmitarrays with a flat gain", *IEEE Transactions on Antennas and Propagation*, vol. 66, *10*, pp. 5231–5238, 2018.

[39] Y. Ge, C. Lin, and Y. Liu, "Broadband folded transmitarray antenna based on an ultrathin transmission polarizer", *IEEE Transactions on Antennas and Propagation*, vol. 66, *11*, pp. 5974–5981, 2018.

[40] P. Y. Feng and S. W. Qu, "60-GHz 2D scan phased transmitarray with high gain and low profile", *in 2019 13th European Conference on Antennas and Propagation (EuCAP)*, Krakow, Poland, 2019, pp. 1–4.

[41] K. Mavrakakis, H. Luyen, J. H. Booske, and N. Behdad, "Wideband transmitarrays based on polarization- rotating miniaturized-element frequency selective surfaces", *IEEE Transactions on Antennas and Propagation*, vol. 68, *3*, pp. 2128–2137, 2020.

[42] P. Mei, G. F. Pedersen, and S. Zhang, "A broadband and FSS-based transmitarray antenna for 5G millimeter-wave applications", *IEEE Antennas and Wireless Propagation Letters*, vol. 20, *1*, pp. 103–107, 2021.

[43] K. Xu, Z. Xiao, J. Tang, D. Liu, and Z. Wang, "Ultra-broad band and dual-band highly efficient polarization conversion based on the three-layered chiral structure", *Physica E*, vol. 81, pp. 169–176, 2016.

[44] Y. Cheng, R. Gong, and L. Wu, "Ultra-broadband linear polarization conversion via diode-like asymmetric transmission with composite metamaterial for terahertz waves", *Plasmonics*, vol. 10, *12*, pp. 1113–1120, Aug. 2017.

[45] J. S. Li and F. Q. Bai, "Dual-band terahertz polarization converter with high-efficiency asymmetric transmission", *Opt. Mater. Express*, vol. 10, *8*, pp. 1853–1861, Aug. 2020.

[46] S. W. Qu and H. Yi, "Low-cost two-layer terahertz transmitarray", *in 2017 International Applied Computational Electromagnetics Society Symposium (ACES)*, Suzhou, China, 2017, pp. 1–2.

[47] L. Marnat, K. Medrar, and L. Dussopt, "Highly integrable high gain substrate-integrated planar lens for wide D-band applications", *in 2020 14th European Conference on Antennas and Propagation (EuCAP)*, Copenhagen, Denmark, 2020, pp. 1–4.

[48] K. Medrar, L. Marnat, L. Dussopt, *et al.*, "H-band substrate-integrated discrete-lens antenna for high data rate communication systems", *IEEE Transactions on Antennas and Propagation*, vol. 69, *7*, pp. 3677–3688, 2021.

[49] A. Clemente, L. Dussopt, R. Sauleau, P. Potier, and P. Pouliguen, "Wideband 400-element electronically reconfigurable transmitarray in X band", *IEEE Transactions on Antennas and Propagation*, vol. 61, *10*, pp. 5017–5027, 2013.

[50] P. Y. Feng, S. W. Qu, and S. Yang, "Phased transmitarray antennas for 1-D beam scanning", *IEEE Antennas and Wireless Propagation Letters*, vol. 18, *2*, pp. 358–362, 2019.

[51] A. Aziz, F. Yang, S. Xu, and M. Li, "A low-profile quad-beam transmitarray", *IEEE Antennas and Wireless Propagation Letters*, vol. 19, *8*, pp. 1340–1344, 2020.

[52] A. R. Vilenskiy, M. N. Makurin, C. Lee, and M. V. Ivashina, "Reconfigurable transmitarray with near-field coupling to gap waveguide array antenna for efficient 2-D beam steering", *IEEE Transactions on Antennas and Propagation*, vol. 68, *12*, pp. 7854–7865, 2020.

[53] J. G. Nicholls and S. V. Hum, "Full-space electronic beam-steering transmitarray with integrated leaky-wave feed", *IEEE Transactions on Antennas and Propagation*, vol. 64, *8*, pp. 3410–3422, 2016.

[54] J. Yang, S. T. Chen, M. Chen, *et al.*, "Folded transmitarray antenna with circular polarization based on metasurface", *IEEE Transactions on Antennas and Propagation*, vol. 69, *2*, pp. 806–814, 2021.

[55] H. Lei, Y. Liu, Y. Jia, Z. Yue, and X. Wang, "A low-profile dual-band dual-circularly polarized folded transmitarray antenna with independent beam control", *IEEE Transactions on Antennas and Propagation (Early Access)*, pp. 1–1, 2021.

[56] J. Zhu, Y. Yang, S. Liao, and Q. Xue, "Dual-band antenna hybridizing folded transmitarray and folded reflectarray", *IEEE Transactions on Antennas and Propagation (Early Access)*, pp. 1–1, 2021.

[57] G. Li, Y. Ge, and Z. Chen, "A compact multibeam folded transmitarray antenna at Ku-band", *IEEE Antennas and Wireless Propagation Letters*, vol. 20, *5*, pp. 808–812, 2021.

[58] ——, "Low profile folded transmitarray antenna with quadruple planar feeds at Ka-band", *in 2020 Cross Strait Radio Science Wireless Technology Conference (CSRSWTC)*, Fuzhou, China, 2020, pp. 1–3.

[59] M. Sazegar, Y. Zheng, C. Kohler, *et al.*, "Beam steering transmitarray using tunable frequency selective surface with integrated ferroelectric varactors", *IEEE Transactions on Antennas and Propagation*, vol. 60, *12*, pp. 5690–5699, 2012.

[60] S. V. Hum and J. Perruisseau-Carrier, "Reconfigurable reflectarrays and array lenses for dynamic antenna beam control: a review", *IEEE Transactions on Antennas and Propagation*, vol. 62, *1*, pp. 183–198, 2014.

[61] C. Huang, W. Pan, X. Ma, B. Zhao, J. Cui, and X. Luo, "Using reconfigurable transmitarray to achieve beam-steering and polarization manipulation applications", *IEEE Transactions on Antennas and Propagation*, vol. 63, *11*, pp. 4801–4810, 2015.

[62] J. G. Nicholls and S. V. Hum, "Full-space electronic beam-steering transmitarray with integrated leaky-wave feed", *IEEE Transactions on Antennas and Propagation*, vol. 64, *8*, pp. 3410–3422, 2016.

[63] F. Yang, P. Pitchappa, and N. Wang, "Terahertz reconfigurable intelligent surfaces (RISs) for 6G communication links", *Micromachines*, vol. 13, *2*, 2022.

[64] N. M. Monroe, G. C. Doqiamis, R. Stingel, P. Myers, X. Chen, and R. Han, "Electronic thz pencil beam forming and 2d steering for high angular-resolution operation: a 98 <tex>×</tex> 98-unit 265GHz CMOS reflectarray with in-unit digital beam shaping and squint correction", *in 2022 IEEE International Solid- State Circuits Conference (ISSCC)*, vol. 65, 2022, pp. 1–3.

[65] S. Li, Z. Zhang, B. Rupakula, and G. M. Rebeiz, "An eight-element 140-ghz wafer-scale IF beamforming phased-array receiver with 64-QAM operation in CMOS RF-SOI", *IEEE Journal of Solid-State Circuits*, vol. 57, *2*, pp. 385–399, 2022.

[66] S. Venkatesh, X. Lu, H. Saeidi, and K. Sengupta, "A high-speed programmable and scalable terahertz holographic metasurface based on tiled CMOS chips", *Nature Electronics*, vol. 3, *12*, pp. 785–793, 2020.

[67] M. R. M. Hashemi, S.-H. Yang, T. Wang, N. Sepúlveda, and M. Jarrahi, "Electronically-controlled beam-steering through vanadium dioxide metasurfaces", *Scientific Reports*, vol. 6, 2016.

[68] M. Jiang, F. Hu, L. Zhang, *et al.*, "Electrically triggered vo₂ reconfigurable metasurface for amplitude and phase modulation of terahertz wave", *Journal of Lightwave Technology*, vol. 39, *11*, 2021.

[69] P. Li, X. Yang, T. W. W. Maß, *et al.*, "Reversible optical switching of highly confined phonon–polaritons with an ultrathin phase-change material", *Nature Materials*, vol. 15, pp. 870–875, 2016.

[70] M. Wuttig, H. Bhaskaran, and T. Taubner, "Phase-change materials for non-volatile photonic applications", *Nature Photonics*, vol. 11, pp. 465–476, 2017.

[71] S. Gharbieh, A. Clemente, J. Milbrandt, and B. Reig, "Phase change material based reconfigurable transmitarray: a feasibility study", *in 2022 16th European Conference on Antennas and Propagation (EuCAP)*, 2022, pp. 1–4. DOI: Madrid,Spain.

[72] Q.-W. Lin, H. Wong, L. Huitema, and A. Crunteanu, "Coding metasurfaces with reconfiguration capabilities based on optical activation of phase-change materials for terahertz beam manipulations", *Advanced Optical Materials*, vol. 10, *1*, p. 2 101 699, 2022.

[73] S. Dash, C. Psomas, I. Krikidis, I. F. Akyildiz, and A. Pitsillides, "Active control of thz waves in wireless environments using graphene-based ris", *IEEE Transactions on Antennas and Propagation (Early Access)*, pp. 1–1, 2022.

[74] A. Clemente, *Design of transmitarrays with beamforming/beamtilting capability.* PhD thesis, University of Rennes 1, 2012.

[75] C. A. Balanis, *Antennna theory: analysis and design (4th ed.)* John Wiley, Sept. 2016.

[76] M. J. Mencagli, E. Martini, S. Maci, and M. Albani, "A physical optics approach to the analysis of metascreens", *IEEE Access*, vol. 8, 2020.

[77] D. M. Pozar, *Microwave engineering (4th ed.)* John Wiley, 2012.

[78] C. Pfeiffer and A. Grbic, "Bianisotropic metasurfaces for optimal polarization control: analysis and synthesis", *Phys. Rev. Applied*, vol. 2, p. 044 011, 4 Oct. 2014.

[79] B. A. Munk, *Frequency Selective Surfaces: Theory and Design.* John Wiley, Apr. 2000.

[80] R. Sauleau, P. Coquet, J. P. Daniel, T. Matsui, and N. Hirose, "Study of Fabry-Perot cavities with metal mesh mirrors using equivalent circuit models. Comparison with experimental results in the 60 GHz band", *J Infrared Millim Waves*, vol. 19, *12*, pp. 1693–1710, Dec. 1998.

[81] R. Sauleau, D. Thouroude, P. Coquet, and J. P. Daniel, "Theoretical reflection coefficient of metal grid reflectors at a dielectric boundary", *J Infrared Millim Waves*, vol. 20, *2*, pp. 325–340, Feb. 1999.

[82] M. Ando and Ken Takei, "Reflection and transmission coefficients of a thin strip grating for antenna application", *IEEE Trans. Antennas Propag.*, vol. 35, *4*, pp. 367–371, Apr. 1987.

[83] R. C. Compton, L. B. Whitbourn, and R. C. McPhedran, "Strip gratings at a dielectric interface and application of babinet's principle", *Appl. Opt.*, vol. 23, *18*, pp. 3236–3242, Sep. 1984.

[84] S. T. Shanahan and N. R. Heckenberg, "Transmission line model of substrate effects on capacitive mesh couplers", *Appl. Opt.*, vol. 20, *23*, pp. 4019–4023, Dec. 1981.

[85] T. Timusk and P. L. Richards, "Near millimeter wave bandpass filters", *Appl. Opt.*, vol. 20, *8*, pp. 1355–1360, Apr. 1981.

[86] A. M. Patel and A. Grbic, "Transformation electromagnetics devices based on printed-circuit tensor impedance surfaces", *IEEE Trans. Microw. Theory Techn.*, vol. 62, *5*, pp. 1102–1111, May 2014.

[87] D.-H. Kwon and D. H. Werner, "Transformation electromagnetics: an overview of the theory and applications", *IEEE Antennas and Propagation Magazine*, vol. 52, *1*, pp. 24–46, 2010.

[88] M. Borgese and F. Costa, "A simple equivalent circuit approach for anisotropic frequency-selective surfaces and metasurfaces", *IEEE Trans. Antennas Propag.*, vol. 68, *10*, pp. 7088–7098, Oct. 2020.

[89] A. H. Abdelrahman, A. Z. Elsherbeni, and F. Yang, "Transmission phase limit of multilayer frequency-selective surfaces for transmitarray designs", *IEEE Transactions on Antennas and Propagation*, vol. 62, *2*, pp. 690–697, 2014.

[90] Z. Qu, J. R. Kelly, and Y. Gao, "Analysis of the transmission performance limits for a multilayer transmitarray unit cell", *IEEE Transactions on Antennas and Propagation*, vol. 70, *3*, pp. 2334–2339, 2022.

[91] L. Marnat, K. Medrar, and L. Dussopt, "Highly integrable high gain substrate-integrated planar lens for wide d-band applications", *in 2020 14th European Conference on Antennas and Propagation (EuCAP)*, 2020, pp. 1–4.

[92] L. Dussopt, K. Medrar, and L. Marnat, "Millimeter-wave gaussian-beam transmitarray antennas for quasi-optical S parameter characterization", *IEEE Transactions on Antennas and Propagation*, vol. 68, *2*, pp. 850–858, 2020.

[93] A. H. Abdelrahman, F. Yang, A. Z. Elsherbeni, P. Nayeri, and C. A. Balanis. 2017.

[94] F. F. Manzillo, M. Śmierzchalski, N. di Pietro, A. Clemente, and M. Merluzzi, "Synthesis of transmitarrays via convex relaxation", *in 2020 IEEE International Symposium on Antennas and Propagation and North American Radio Science Meeting*, 2020, pp. 2017–2018.

List of Publications

Journals

- **O. Koutsos**, F. Foglia Manzillo, A. Clemente, R. Sauleau, "Analysis, Rigorous Design and Characterization of a Three-layer Anisotropic Transmitarray at 300 GHz,", *IEEE Transactions on Antennas and Propagation (Early Access)*, 2022 (in press).

Conferences

- **O. Koutsos**, F. Foglia Manzillo, A. Clemente and R. Sauleau, "Design of a 3-bit Transmitarray Antenna at 300 GHz using Asymmetric Linear Polarizers," *2020 IEEE International Symposium on Antennas and Propagation and North American Radio Science Meeting*, Montreal, QC, Canada, Jul. 2020, pp. 1505-1506.

- **O. Koutsos**, F. Foglia Manzillo, A. Clemente and R. Sauleau, "Analysis and Efficient Design of Sub-THz Transmitarrays with Three Anisotropic Layers," *2021 15th European Conference on Antennas and Propagation (EuCAP)*, Dusseldorf, Germany, Mar. 2021, pp. 1-5.

- **O. Koutsos**, R. Madi, F. Foglia Manzillo, M. Smierzchalski, A. Clemente and R. Sauleau, "Recent Achievements on Passive and Beam Steering Transmitarrays at Millimeter Waves," *2021 International Symposium on Antennas and Propagation (ISAP)*, Taipei, Taiwan, Oct. 2021, pp. 1-2.

- **O. Koutsos**, F. Foglia Manzillo, A. Clemente and R. Sauleau, "Wideband High-Gain Transmitarray Antenna for Point-to-Point Communications at 300 GHz," *2021 European Microwave Conference (EuMC)*, London, UK, 2022 (accepted).

- F. Foglia Manzillo, **O. Koutsos**, B. Fuchs, R. Sauleau, and A. Clemente, "Synthesis and Characterization of a Focused-beam Transmitarray Antenna at 300 GHz," *2022*

16th European Conference on Antennas and Propagation (EuCAP), Madrid, Spain, Mar. 2022, pp. 1-4.

- **O. Koutsos**, F. Foglia Manzillo, A. Clemente and R. Sauleau, "High-Resolution Quartz Transmitarray Antenna for Sub-THz Applications," *2022 IEEE International Symposium on Antennas and Propagation and North American Radio Science Meeting* (accepted).

- **O. Koutsos**, F. Foglia Manzillo, A. Clemente, M. Caillet and R. Sauleau, "Ultra-High Gain Transmitarray Antenna for Wireless Backhauling at 280 GHz," *2022 47th International Conference on Infrared, Millimeter and Terahertz Waves (IRMMW-THz)*, Delft, Netherlands, 2022 (accepted).

Deliverables

- A. Clemente, R. D'Errico, **O. Koutsos**, M. Lotti, R. Sauleau. D2.1 "NEXT5G system architecture and requirements," project NEXT5G (ANR), 2020.

- A. Clemente, **O. Koutsos**, O. de Sagazan, R. Sauleau. D4.1 "Report on the fabrication techniques," project NEXT5G (ANR), 2020.

- **O. Koutsos**, A. Clemente, F. Foglia Manzillo, R. Sauleau. D4.2 "Report on unit-cells and transmitarray designs," project NEXT5G (ANR), 2021.

Honors and Awards

- **Finalist** for the **Best Student Paper** in the *2021 15th European Conference on Antennas and Propagation (EuCAP)*, O. Koutsos, F. Foglia Manzillo, A. Clemente, R. Sauleau, "Analysis and Efficient Design of Sub-THz Transmitarrays with Three Anisotropic Layers".

- **Winner** of the **Young Engineer Prize** in the *2021 European Microwave Conference (EuMC)*, O. Koutsos, F. Foglia Manzillo, A. Clemente, R. Sauleau, "Wideband High-Gain Transmitarray Antenna for Point-to-Point Communications at 300 GHz".

DOCTORAT BRETAGNE LOIRE / MATHSTIC

UNIVERSITÉ DE RENNES 1

Titre : Étude, modélisation et conception d'antennes à réseaux transmetteurs à faisceau fixe à 300 GHz

Mot clés : réseau transmetteur, sub-THz, au-delà 5G, anisotropie, modélisation de circuits

Résumé : Le développement des communications sans fil à haut débit à des fréquences sub-THz est une solution prometteuse pour la croissance continue du trafic de données. À ces fréquences, le principal défi consiste à atténuer les pertes de propagation élevées en réalisant des antennes à gain élevé, efficaces et à large bande. Cependant, les contraintes de fabrication limite souvent les performances de l'antenne, ce qui encourage les technologies haute résolution et plus coûteuses.

Les antennes à réseaux transmetteurs sont des candidats appropriés, combinant les avantages des architectures alimentées spatialement avec des processus de fabrication planaires. Dans cette contribution, une approche synthétique pour l'analyse et la synthèse des réseaux transmetteurs passifs (faisceaux fixes) à 300 GHz est développée. La méthode proposée permet une conception rentable, tout en ciblant les performances maximales réalisables. Différents prototypes ont été fabriqués, en utilisant un circuit imprimé standard ou un procédé de lithographie au quartz. Les résultats expérimentaux ont démontré un gain élevé, jusqu'à 43,2 dBi, une efficacité d'ouverture très élevée, jusqu'à 48,6%, et des performances à large bande, jusqu'à plus de 30% de la bande passante relative, dans différents prototypes. Une méthode numérique basée sur l'optique physique pour les futures conceptions des réseaux transmetteurs à profil bas a été développée, comme alternative au modèle d'approche de lancer de rayons.

Title: Study, modelling and design of fixed beam transmitarray antennas at 300 GHz

Keywords: transmitarray antenna, sub-THz, beyond 5G, anisotropy, circuit modelling

Abstract: The development of high-speed wireless communications at sub-THz frequencies is a promising solution for the continuous growth of the data traffic. At these frequencies, the main challenge is to mitigate the high propagation losses by realizing high-gain, efficient and wideband antennas. However, the fabrication constraints often limit the antenna performance, encouraging for more expensive, high-resolution technologies.

Transmitarray antennas are suitable candidates, combining the advantages of spatially fed architectures with planar-based fabrication processes. In this contribution, a fast and rigorous approach for the analysis and synthesis of passive (fixed-beam) transmitarrays at 300 GHz is developed. The proposed method allows for a cost-effective design, while targeting for the maximum achievable performance. Different prototypes have been fabricated, using standard printed circuit board or quartz lithography process. The experimental results demonstrated high gain, up to 43.2 dBi, very high aperture efficiency, up to 48.6%, and wideband performance, up to more than 30% of relative bandwidth, in different prototypes. A numerical method based on physical optics for future low-profile transmitarray designs has been developed, as an alternative to the ray tracing approach model.